January 1997 • NREL/SR-520-22364

Wide Band Gap Solar Cells with High Stabilized Performance

Annual Technical Report
15 July 1995 - 15 July 1996

Wronski, C.R.; Collins, R.W.; Fujiwara, H.; Jiao, L.; Lee, Y.; Semoushkina, S.; Kim, S.; Lu, Z.; Liu, H.; and Koh, J.
Pennsylvania State University
University Park, Pennsylvania

National Renewable Energy Laboratory
1617 Cole Boulevard
Golden, Colorado 80401-3393
A national laboratory of
the U.S. Department of Energy
Managed by Midwest Research Institute
for the U.S. Department of Energy
under Contract No. DE-AC36-83CH10093

NREL/SR-520-22364 • UC Category: 1260 • DE97000103

Wide Band Gap Solar Cells with High Stabilized Performance

Annual Technical Report
15 July 1995 - 15 July 1996

Wronski, C.R.; Collins, R.W.; Fujiwara, H.; Jiao, L.; Lee, Y.; Semoushkina, S.; Kim, S.; Lu, Z.; Liu, H.; and Koh, J.
Pennsylvania State University
University Park, Pennsylvania

NREL technical monitor: B. von Roedern

National Renewable Energy Laboratory
1617 Cole Boulevard
Golden, Colorado 80401-3393
A national laboratory of
the U.S. Department of Energy
Managed by Midwest Research Institute
for the U.S. Department of Energy
under Contract No. DE-AC36-83CH10093

Prepared under Subcontract No. XAN-4-13318-03

January 1997

This publication was reproduced from the best available camera-ready copy submitted by the subcontractor and received no editorial review at NREL.

NOTICE

This report was prepared as an account of work sponsored by an agency of the United States government. Neither the United States government nor any agency thereof, nor any of their employees, makes any warranty, express or implied, or assumes any legal liability or responsibility for the accuracy, completeness, or usefulness of any information, apparatus, product, or process disclosed, or represents that its use would not infringe privately owned rights. Reference herein to any specific commercial product, process, or service by trade name, trademark, manufacturer, or otherwise does not necessarily constitute or imply its endorsement, recommendation, or favoring by the United States government or any agency thereof. The views and opinions of authors expressed herein do not necessarily state or reflect those of the United States government or any agency thereof.

Available to DOE and DOE contractors from:
Office of Scientific and Technical Information (OSTI)
P.O. Box 62
Oak Ridge, TN 37831
Prices available by calling (423) 576-8401

Available to the public from:
National Technical Information Service (NTIS)
U.S. Department of Commerce
5285 Port Royal Road
Springfield, VA 22161
(703) 487-4650

Printed on paper containing at least 50% wastepaper, including 20% postconsumer waste

TABLE OF CONTENTS

Executive Summary 1

1. Improved Understanding of Stability in Materials and Solar Cells 9

1.1 Stability in a-Si:H and a-$Si_{1-x}C_x$:H Materials 9

1.2 Stability in a-Si:H Solar Cells 13

1.3 Stability in a-Si:H Solar Cells: Customized Structures 25

1.4 Stability in a-$Si_{1-x}C_x$:H Solar Cells 40

2. Novel Intrinsic Materials Optimization 43

2.1 Wider-Gap a-Si:H versus Widegap a-$Si_{1-x}C_x$:H 43

2.2 Widegap a-Si:H Prepared by Microwave PECVD 50

2.3 a-$Si_{1-x}C_x$:H in Solar Cells and a Comparison with a-Si:H Cells Prepared with H_2-Dilution 51

2.4 Wider-Gap a-Si:H Prepared by H_2-Dilution: A Closer Look at Annealed and Degraded States 56

3. Solar Cells Optimized for p- and i-Layer Performance 63

3.1 Correlation between p-i-n Cell Performance and Deposition Conditions: H_2-Dilution, Substrate Temperature, Gas Pressure 63

3.2 Baseline a-Si:H p-i-n Cells from Single Chamber System 70

3.3 Customized p-i-n Solar Cells 74

3.4 a-Si:H n-i-p Solar Cells 84

4. Novel p-Type Materials 93

4.1 p-Type Materials Development and Optimization 93

4.2 n-i-p Solar Cells Incorporating Novel p-Layers 101

4.3 Optical Properties of the Doped Layers in the Device Configuration 109

4.4 Collaboration with USSC in Incorporating p-Layers in n-i-p Solar Cells 113

5. Solar Cell Interfaces 116

5.1 The Top Junction of the p(a-$Si_{1-x}C_x$:H)-i(a-Si:H)-n(a-Si:H) Solar Cell 116

5.2 The Bottom Junction of the p(a-$Si_{1-x}C_x$:H)-i(a-Si:H)-n(μc-Si:H) Solar Cell 123

5.3 Top Junction i/p Interfaces in n-i-p Cells 125

5.4 Real Time Spectroscopic Ellipsometry Characterization of Top Junction Formation for the n(a-Si:H)-i(a-Si:H)-p(μc-Si:H) Solar Cell 135

5.5 Role of Top Interfaces in Limiting V_{oc} 146

5.6 Compositional Grading at the p-i Interface in p-i-n Cells 148

6. Device Modeling 163

6.1 Schottky Barrier Solar Cell Structures 163

6.2 p-i-n and n-i-p Cell Performance Limitations 171

7. Bibliography 175

EXECUTIVE SUMMARY

1. Improved Understanding of Stability in Materials and Solar Cells

We have degraded films of a-Si:H and solar cells with a-Si:H *i*-layers using an ELH light source under different light intensities. It is found that a-Si:H films deposited with H_2-dilution of SiH_4 gas, not only show lower defect densities in the annealed state than the a-Si:H films prepared with pure SiH_4, but also better stability against light soaking. The improvement in material stability is found to translate directly into an improvement in device stability. Specifically, a direct correlation between the degradation of the diluted solar cells and their intrinsic films has been established in this study. Both diluted cells and films deposited at different substrate temperatures were found to reach a steady state of degradation under AM1 illumination within 100 hours. This distinct difference in kinetics from the undiluted materials and cells, and the ability to reach steady state degradation in less than 100 hours, are being utilized as a new probe for improving our understanding of the mechanisms limiting cell stability.

During this phase we also studied the stability of cells with atomic H treatments at the *p/i* interface as well as those with a-$Si_{1-x}C_x$:H absorber layers. We found that a combination of H_2-dilution during *i*-layer deposition of the *p-i-n* cells and atomic H treatment at the *p/i* interface resulted in substantial improvement in the V_{oc} of the a-Si:H cell and its stability against light soaking. Cells made with a-$Si_{1-x}C_x$:H *i*-layers give higher open-circuit voltages in the annealed state than these best a-Si:H cells, but this improvement is offset by a much poorer stability against light soaking. As a general conclusion, we find that *i*-layer material and solar cell stability show a close correlation including the observations that (i) H_2-dilution and atomic H treatments have led to improvements in the stability of both materials and cells; and (ii) incorporation of carbon into a-Si:H to make a-$Si_{1-x}C_x$:H alloys leads to significant reductions in the stability of both materials and cells, and (iii) the improvement in a-$Si_{1-x}C_x$:H materials and cells by H_2-

dilution is confined to the annealed state; the gains are offset by greater instability of materials and cells.

In order to establish and quantify the relative contributions of the bulk and p/i interface regions to the degradation of solar cells, degradation was investigated on customized cells consisting of p(a-SiC:H)-(x)i(diluted)-(4000Å-x)i(undiluted)-n(μc-Si) [x=50Å, 150Å, 300Å, 600Å] and p(a-SiC:H)-(300Å)i(undiluted)-(3700Å)i(diluted)-n(μc-Si). The results were compared with those of well characterized cells with single diluted and undiluted i-layers. The results indicate that the degradation kinetics of these cells are primarily controlled by the light induced changes in the bulk region rather than in the p/i interface region even though the p/i interface does play a key role in determining the V_{oc} in the annealed state.

2. Novel Intrinsic Materials Optimization

We have demonstrated that, while in the annealed state a-$Si_{1-x}C_x$:H *i*-layers prepared with H_2-dilution of source gases (*i.e.*, SiH_4 + CH_4) exhibit similar photoconductive properties to those of H_2-diluted a-Si:H materials, the gains made through H_2-dilution are largely lost in the degraded state. A similar behavior is reflected in the substantial degradation in open-circuit voltage and efficiency in the corresponding *p-i-n* solar cell study. Because of the instability of a-$Si_{1-x}C_x$:H materials and devices, emphasis has now been placed on obtaining wide bandgap a-Si:H films. The widening of the gap is being achieved by using hydrogen dilution and lower substrate temperatures. These diluted materials and their corresponding solar cells exhibit both higher stability and different degradation kinetics in comparison with those prepared without hydrogen dilution. In order to further understand the differences in stability and degradation kinetics between diluted and undiluted materials, studies were carried out on the degradation of these materials under 10 AM1 illumination. The experimental results show that, not only are the densities of light induced defects in the diluted materials lower, but also that their distributions (nature) are different than those in the undiluted materials. Numerical

modeling has been successfully used to fit the results for diluted films in which charged defects are included. Corresponding analysis is being carried out on the undiluted films.

3. Solar Cells Optimized for *p*- and *i*-Layer Performance

We have investigated the dependence of *p-i-n* solar cell performance in the annealed state on the deposition conditions. The variations in the deposition conditions included the deposition temperature of the *i*-layer (between 130°C and 240°C), H_2-dilution of SiH_4 gas during *i*-layer deposition, and atomic H treatment at the *p/i* interface. We have found that the open-circuit voltage of the cell increases at lower *i*-layer deposition temperatures as the bandgap of the *i*-layer is widened, and such an increase is more profound in cells prepared with H_2-diluted *i*-layers. It is also found that an atomic H *p/i* interface treatment results in a small but significant improvement in open-circuit voltage. (As noted above, this treatment also leads to higher stability.) By using the V_{oc} vs. light intensity characteristics combined with the simulations using AMPS, a picture is emerging as to what are the relative contributions from the p/i interface region, the bulk i-layer, and the built-in potential, V_{bi}, to the V_{oc} under different light intensities. Comparisons have been made between the V_{oc} vs. light intensity characteristics on different n-i-p solar cells including a very high V_{oc} (1.04V at AM1) USSC n-i-p cell and a PSU p-i/ USSC n/ITO cell.

We have been optimizing widegap p-layers in midgap n-i-p solar cells for high V_{oc}. The p-layers have been prepared using mixtures of SiH_4, CH_4 and TMB. The highest V_{oc} value achieved to date in our single-chamber system is 0.94 V, obtained by incorporating an a-Si:C:H p-layer prepared with high H_2 dilution ($R=[H_2]/[SiH_4]=120$). Further improvements through the incorporation of microcrystalline p-layers in the single-chamber n-i-p cells have been attempted, however, these efforts have not been successful ($0.85 \leq V_{OC} \leq 0.90$ V). There are two possible reasons for the observed lack of improvement. First, p-layers having a high crystalline quality have not been successfully obtained using the TMB dopant gas. In addition, it is necessary to apply a H_2-plasma treatment to the i-layer in order to obtain a high nucleation density for the microcrystalline

p-layers, and this process may need to be further optimized in order to obtain higher V_{oc}. In order to obtain further insights, we have applied spectroscopic ellipsometry (SE) to characterize the H_2-plasma treatments of the i-layer in greater detail. We have found that a number of processes occur simultaneously. First, we observe a decrease in the Si-Si bond packing density of the top 200-250 Å of the i-layer generated by H-incorporation (~4 at.%) that leads to a widening of the i-layer gap by 0.08 eV at the interface. This effect has a time scale of ~60 s. Second, we observe a gradually roughening of the i-layer that is due enhanced etching in the regions near weak bonds. This second effect occurs on a time scale of > 1 min, and does not saturate. Future work will focus on which of these effects lead to the nucleation enhancement, and which may be detrimental to the cell performance.

Efforts have been continued in order to evaluate the effects of interfaces, including the TCO/*p* interface, on the processing-property relationships for the baseline cells. Three different TCO's from Solarex, specular and textured SnO_2 and specular ZnO, were incorporated in the cell configuration with attempts to distinguish the processing effects on fill-factor and open-circuit voltage that are TCO-related from those are TCO-independent. For the current best midgap cell prepared in our single chamber system, it is found that the open-circuit voltage does not depend on TCO material, and in this case improved current-collection performance was observed for Solarex specular ZnO over specular SnO_2. In this study, we have incorporated B-graded p-layers into midgap a-Si:H (single-chamber) p-i-n cells in which the i-layer is prepared from pure SiH_4. In the graded p-layers, the doping level near the interface to the transparent conducting oxide (TCO) is a factor of 10 higher than that at the p/i interface. Such a gradient is found to increase the open circuit voltage for solar cells deposited on ZnO TCO and yield fill factors closer to those for single-chamber cells on textured SnO_2:F. It is suggested that a high B content near the ZnO/p-layer interface actually improves the contact in this case since B is an effective dopant for ZnO. Smaller improvements in V_{oc} also result for cells on SnO_2:F. In the latter case, a V_{oc} value of 0.88 V has been obtained by incorporation of the graded layer, an improvement comparable to that obtained upon H_2-dilution of the i-layer. In future, we intend to incorporate this p-layer process into a cell with a H_2-diluted i-layer.

4. Novel p-Type Materials Optimization

We have developed novel widegap amorphous and microcrystalline p-layers prepared using H_2-diluted and undiluted mixtures of SiH_4, CH_4, and $B(CH_3)_3$ (TMB) that are to be incorporated as the top layer in the *n-i-p* solar cell configuration. In this configuration, preparation of microcrystalline or amorphous *p*-layers with H_2-dilution does not suffer from the detrimental interactions between the H_2-rich plasma and the TCO material as in the case of the *p-i-n* configuration. High-quality amorphous Si:C:H p-layers doped with TMB have been obtained with a Tauc optical gap of 2.00eV, and cells prepared with these TMB doped amorphous p-layers appear to outperform those with diborane doping since the latter have problems caused by diborane CVD. However, the mixed-phase (microcrystalline+amorphous) materials prepared using H_2-diluted mixtures of SiH_4, CH_4, and TMB show poor crystallinity in comparison to intrinsic microcrystalline films prepared using SiH_4 + CH_4 and n-type microcrystalline films prepared using SiH_4 + PH_3. We have investigated the processes of B- and C- incorporation in the microcrystalline p-layers prepared with TMB. For these layers, the transport properties appear to be dominated by the amorphous component and are also detrimentally affected by their high void volume fraction. In the future, we plan to compare the microcrystalline films prepared using TMB as the dopant source to those obtained using BF_3 and B_2H_6.

In addition, using real time SE, we have characterized the optical properties and gaps of our microcrystalline p- and n- layers in the actual n-i-p and p-i-n device configurations. These have been compared with each other, with conventional doped amorphous layers, and with the thicker counterparts used for property evaluation. We have found that the p-layer material has a more defective microstructure than the n-layer material, including a higher fraction of voids and amorphous component. We have also found that the doped microcrystalline layers exhibit an absorption onset significantly different in shape than both the doped amorphous layers and single crystal Si. This suggests that size effects, possibly quantum mechanical in nature, control the optical properties of these layers. Such effects are characterized by an abrupt absorption onset in the region from 2.1 eV to 2.3 eV yielding much weaker absorption in the region from 1.7

to 2.0 eV in comparison with the amorphous layers. These effects are stronger in the microcrystalline n-layer than in the p-layer, and provides a means for assessing the quality and suitability of microcrystalline layers in cells.

5. Solar Cell Interfaces

We have extended our studies of the *p/i* interface to small sub-monolayer level discontinuities observed in the real time ellipsometry trajectories for interfaces formed with TMB *p*-layers. Similar but much larger shifts in the ellipsometric angle Δ have been observed for *p*-layers prepared with diborane and can be attributed to film formation on the sample surface during Ar flushing due to dopant gas-related contamination. However, the much smaller discontinuities associated with TMB-doped *p*-layers appear to be specific to the Ar gas flow rather than the presence of dopant gas related contamination. Similar discontinuities, but in the direction of film removal, were observed in this case immediately after the introduction of *i*-layer gases into the chamber, and this latter shift in Δ appears to be related to the H_2 flow. A more detailed assessment of the gas switching and flushing procedures including an assessment of possible fluctuations in near-surface film temperature is being undertaken.

We have also investigated the *i/p* interface in the *n-i-p* cell configuration with intended microcrystalline $Si_{1-x}C_x$ *p*-layers with high and low C-contents. It is found that high C-content microcrystalline layers do not reach sufficient coverage on the *i*-layer to form a bulk layer within the desired film thickness (~200 Å). The resulting incomplete coverage leads to an appreciably lower open-circuit voltage. We have developed H_2-plasma treatments of the i-layer surfaces that have been used to enhance the nucleation of the microcrystalline $Si_{1-x}C_x$ p-layers in the n-i-p solar cells. Initially, the H_2 plasma treatments have been performed under the same conditions as p-layer growth, but without the source and dopant gases. We have found that in contrast to the filament-treatments, significant roughening of the i-layer surface from 25 Å to ~60 Å occurs during a 2 min plasma treatment. Furthermore Si-H bond formation at the top of the i-layer saturates after <1 min with the plasma treatment, whereas more effective hydrogenation but at a much

slower rate (>50 min) appears to be possible with the filament. In the future, we plan to optimize the plasma method more carefully and compare the plasma and filament methods with regard to their effect on V_{oc} in the n-i-p cells.

We have extended our studies on carbon compositional grading at the *p/i* interface in this phase. We have studied buffer layers as a function of their thickness and bandgap gradient in order to obtain a reasonable collection of data from which one can model the cell performance using reliable parameters. The capability of monitoring the near surface structure and optical properties using a "pseudo-substrate" technique is critical in this methodology. First, a data base of dielectric functions of a-$Si_{1-x}C_x$:H for $0 \leq x < 0.25$ was obtained through bulk layer characterization. Using a general formula for the dielectric function of an amorphous semiconductor, we were able to establish a relationship between the C-content and the dielectric function through a parameterization based on the general formula. With this relationship and using least-squares regression analysis, we were able to characterize the time evolution of (i) the C-content in the top 10~20 Å of the bulk layer; (ii) the bulk layer instantaneous deposition rate; and (iii) the surface roughness layer thickness on top of the bulk layer during buffer layer growth. By integrating the instantaneous deposition rate and translating the C-content into the corresponding bandgap, we obtained a depth profile in the bandgap. This approach can turn out to be very useful not only for solar cell modeling but also for bandgap engineering of better devices.

6. Device Modeling

A new approach to device modeling was taken in this phase using AMPS which is less ambitious than that originally proposed due to the absence of reliable input parameters. The lack of such parameters limits the ability of AMPS to make reliable, quantitative predictions about the directions for improving the performance and stability of solar cells. This is particularly true for the p/i interface regions which are generally included in such modeling but whose parameters have as yet not been established in any detailed studies. In this approach the modeling of solar cell structures is carried out first to

establish material parameters that are self-consistent with those derived in detailed studies on intrinsic material thin films. This is currently being done with Schottky barrier solar cell structures, which do not have the uncertainties introduced by the p/i interface regions. The work carried out in the EPRI program has shown that self-consistent analysis can only be achieved by including charged defects and that useful "operational" parameters can be obtained using a three-Gaussian distribution. The analysis being carried out here relies heavily on the work being done in that program. Both the dark I-V's and QE's in these Schottky barrier structures are very sensitive to the bulk, and in particular to its light induced changes so they are very useful in the "fine-tuning" of the thin film material parameters for the self-consistent modeling of p-i-n cells with AMPS.

As an initial step in developing parameters that characterize the p/i interface regions, we have carefully measured the i-layer optical gap in a p-i-n cell after 100 Å deposition and after its completion (4500 Å). Identical results are obtained within the experimental error of ±10 meV. This information can be used as input in mathematical simulations of the performance of p-i-n solar cells. Specifically, detailed modeling of p-i-n solar cell performance has suggested that the i-layer material within 100 Å of the p/i interface is somehow different than that in the bulk. This modeling further suggests that band gap narrowing or a higher defect density (or a combination of both) occurs within this region. The real time SE provides an upper limit for the optical gap narrowing of 10 meV.

1. Improved Understanding of Stability in Materials and Solar Cells

1.1 Stability in a-Si:H and a-$Si_{1-x}C_x$:H Materials

It is known that a-Si:H films prepared with H_2-dilution are more stable against light soaking than a-Si:H films prepared without H_2-dilution and this statement appears to apply to *p-i-n* cells as well. In order to understand the degradation behavior under different light intensities, we have deposited a-Si:H films and cells with and without H_2-dilution, and degraded these films and cells under AM1 (~100 mW/cm^2) and 10AM1 (~1000 mW/cm^2) conditions. The sample surface temperatures during light soaking were about 28°C and 50°C for AM1 and 10AM1 light intensities, respectively.

For comparison of the role of H_2-dilution, the undiluted a-Si:H film was deposited with 15 sccm pure SiH_4 at 0.5 Torr and 200°C, while the H_2-diluted film was deposited under similar deposition conditions but with a H_2-dilution ratio $R=[H_2]/[SiH_4]=10$. In this case, the flows of SiH_4 and H_2 were 10 and 100 sccm, respectively, and the total pressure was 0.5 Torr. The photoconductivity measurements for both films and dual beam sub-bandgap photoconductivity measurements for the diluted film are used to obtain the degradation kinetics of the mobility-lifetime product, $\mu\tau$, as shown in Figure 1, where the reciprocal of is shown as a function of the AM1 soaking time. The corresponding densities of neutral dangling bonds, N_{D0}, estimated from the analysis of sub-bandgap absorption spectra, are shown as a function of the AM1 soaking time in Figure 2 for the H_2-diluted film. $\alpha(1.2eV)$, the absorption coefficient (in cm^{-1}) at 1.2 eV, is multiplied by 3×10^{16} to give an estimate of N_{D0} (in cm^{-3}). H_2-diluted films were also prepared as a function of substrate temperature for more detailed correlation with solar cell performance. These results are summarized in Fig. 3 where the reciprocals of the $\mu\tau$-products (obtained at a carrier generation rate of 10^{16} cm^{-3}s^{-1}) for films deposited at T_S values of 240, 200 and 170°C are plotted as a function of illumination time.

In Figure 1, both the H_2-diluted and undiluted films show fast degradation in $\mu\tau$ products from their annealed state values in the first few minutes of AM1 soaking. In the case of the H_2-diluted film, the $\mu\tau$ product dropped by over an order of magnitude and

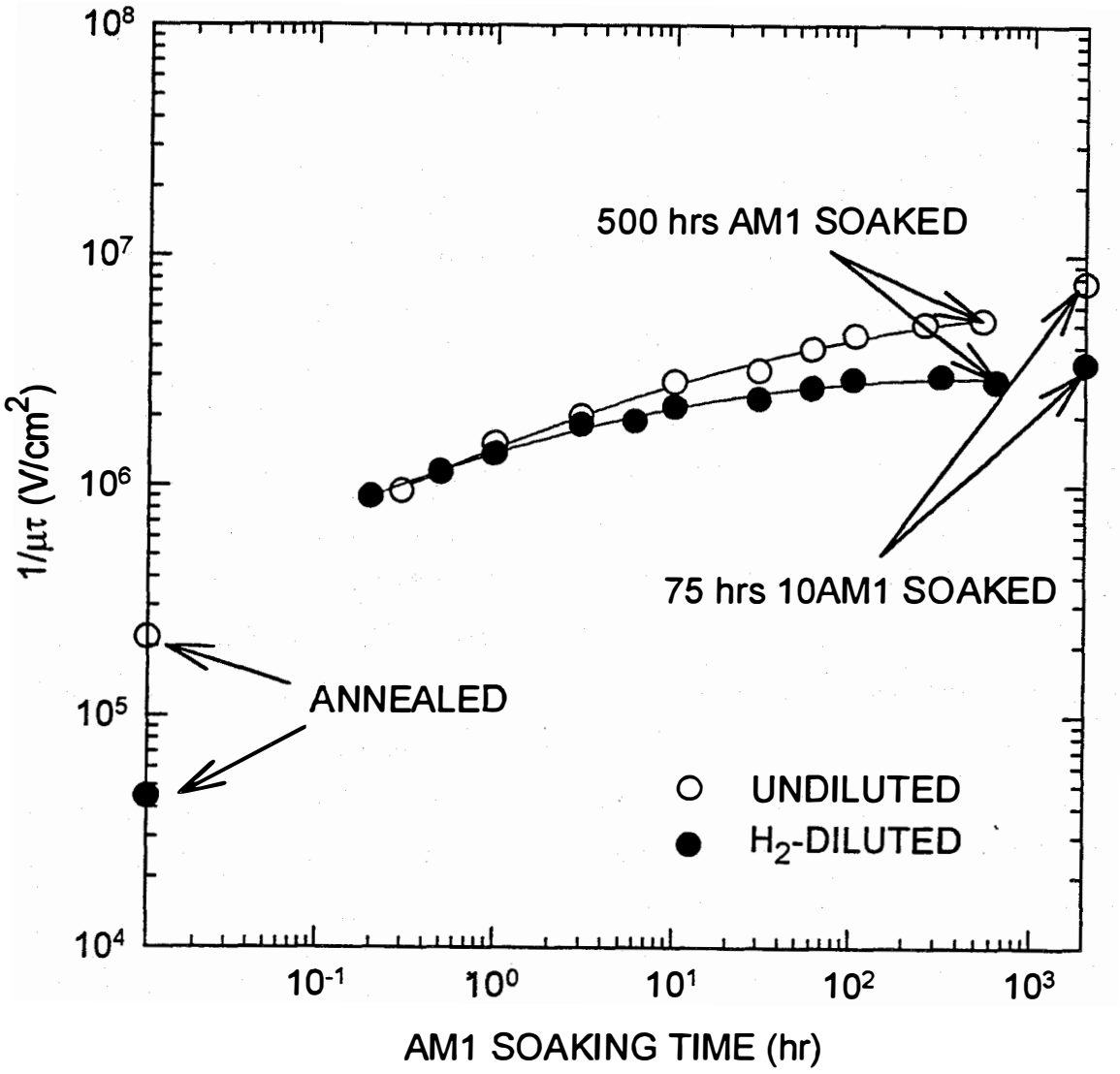

Figure 1 Dependence of the reciprocal of the mobility-lifetime product for undiluted and H_2-diluted a-Si:H films on AM1 soaking time. Data for the annealed state and 10AM1 degraded state are shown.

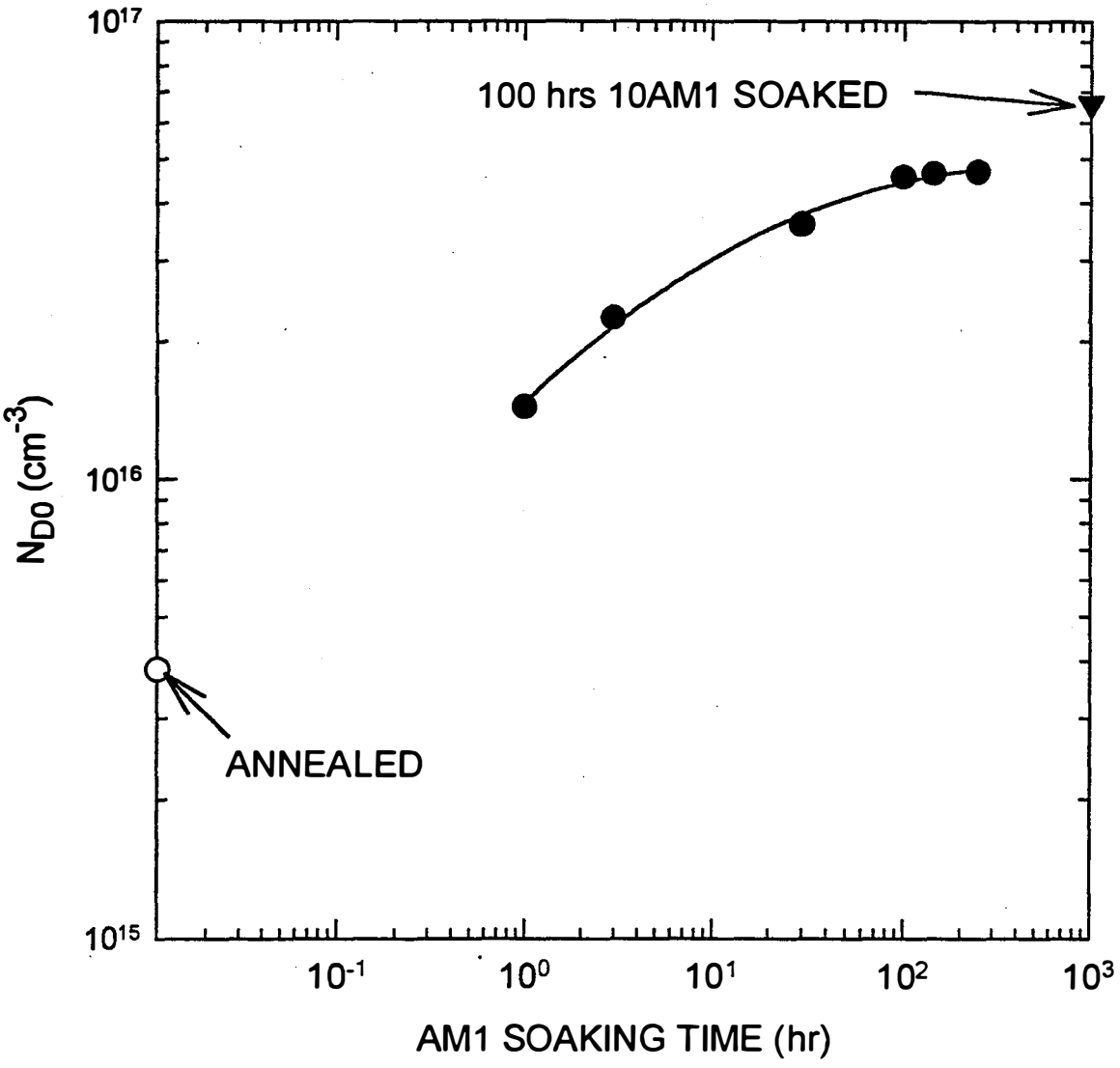

Figure 2 Density of neutral dangling bonds as a function of AM1 soaking time together with data for the annealed state and 100 hrs 10AM1 soaked state.

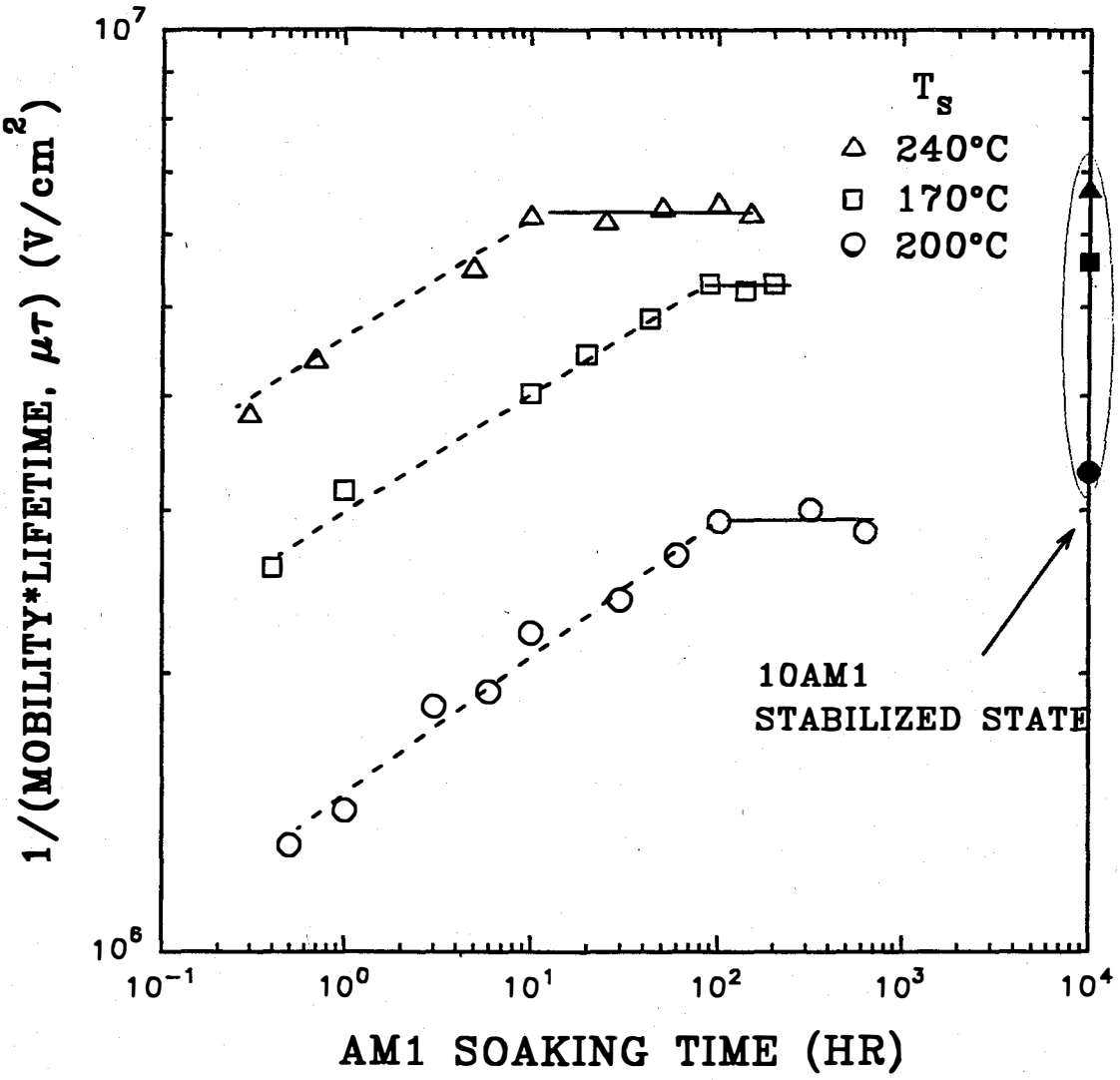

Figure 3 The degradation kinetics of the reciprocals of the electron mobility lifetime products under AM1 illumination for three hydrogen diluted films deposited at T_S of 170, 200, and 240°C. Also shown are the values for the stabilized degraded state under 10AM1 illumination. The stabilized degraded state is reached within 100 hours of AM1 soaking for the three films.

reached the stabilized degraded state after about 50 hrs of AM1 light soaking. In contrast, the undiluted film showed continuous degradation even after 500 hrs of AM1 soaking. Also included in Figure 1 are the $\mu\tau$ products under 10AM1 light soaking at 75 hrs for both films. It can be seen that there is a difference between the $\mu\tau$ value at the 75 hrs 10AM1 degraded state and that at the 500 hrs AM1 degraded state for the undiluted film. A smaller difference in $\mu\tau$ for the H_2-diluted film at the AM1 and 10AM1 stabilized degraded states is observed. The degradation kinetics of the densities of neutral dangling bonds, N_{D0}, shown in Figure 2, for the H_2-diluted film, however, does not show a corresponding fast increase in the first few minutes of soaking. The value of N_{D0} in the AM1 stabilized degraded state also shows a difference from that for that in the 10AM1 stabilized degraded state. Figure 3 which focuses on the approach to saturation reveals similar results to those in Fig. 1 for the H_2-diluted film. Detailed density of states modeling is currently being applied to further understand the correlation between the defect densities and the photoconductive properties of these materials.

1.2 Stability in a-Si:H Solar Cells

The properties of p(a-SiC:H)/i(a-Si:H)/n(μc-Si) solar cells and their i-materials prepared with hydrogen dilution were compared with cells and i-materials prepared without hydrogen dilution. The cells and the corresponding intrinsic films were fabricated in a multi-chamber PECVD system with pure silane (SiH_4) and silane diluted with hydrogen in the ratio $[H_2]/[SiH_4]=10$. The initial performance of both types of cells (~4000Å thick) fabricated without optical enhancement are quite similar but the diluted cells are more stable. Despite the reported importance of the interface regions in determining their solar cell characteristics as described later, a direct correlation between the degradation of the diluted solar cells and their intrinsic films has been further established in this study. Both H_2-diluted cells and films deposited at different substrate temperatures were found to reach a steady state of degradation under AM1 illumination within 100 hours. The normalized efficiencies, relative to the annealed state value, as a function of the AM1 soaking time for cells with *i*-layers deposited at 200°C and 170°C

with and without H_2-dilution are shown in Figure 4. It can be seen that the cells with H_2-diluted *i*-layers reached the stabilized degraded state after about 40 hrs AM1 light soaking, whereas the cells with undiluted *i*-layers were still degrading even up to 100 hrs of AM1 light soaking. These results in conjunction with those of Figs. 1 and 3 suggest that the stability of the *i*-layers, among other factors, plays a crucial role in determining the cell efficiency stability. The distinct difference in kinetics from the undiluted materials and cells, and the ability to reach steady state degradation in less than 100 hours, are being utilized as a new probe for improving our understanding of the mechanisms limiting cell stability.

This change in the functional dependence of cell performance on light soaking underscores the differences that can occur in the degradation of solar cells having different a-Si:H materials and cell structures. The fact that the stabilized states are reached in about 100 hours rather than 1000 hours, however, makes it practical to carry out detailed experiments on both the kinetics as well as the stabilized, "end-of-life", performance. The degraded steady state, just as the annealed state, constitutes a clearly defined "marker" for an unambiguous correlation of cells with materials in the degraded state. Such a "marker" is necessary for confirming the validity of any correlations between light induced changes in materials and the corresponding degradation in solar cells. Because of the difficulties with adhesion of diluted a-Si:H films to glass or quartz, particularly at low substrate temperatures, it has been difficult to obtain results on the materials used in diluted solar cells. The kinetics of degradation in the different cells with illuminations of AM1 and 10AM1 are also consistent with those reported by Solarex. The 4000Å p-i-n cells exhibited characteristics similar to those reported by them except for the J_{sc} values which were those expected for non-textured TCO's. The differences in the initial J_{sc} could be directly related to the differences in optical absorption, and the differences in V_{oc}, could be attributed at least in part to the differences in the corresponding bandgaps.

Under AM1 illumination the undiluted solar cells continuously degrade, whereas the diluted cells deposited at T_S of 200, 170, and 130°C exhibit a clearly defined steady state after less than 100 hours as illustrated in Fig. 5, where the normalized efficiencies for the three diluted cells are plotted versus the logarithm of the exposure time. The cell

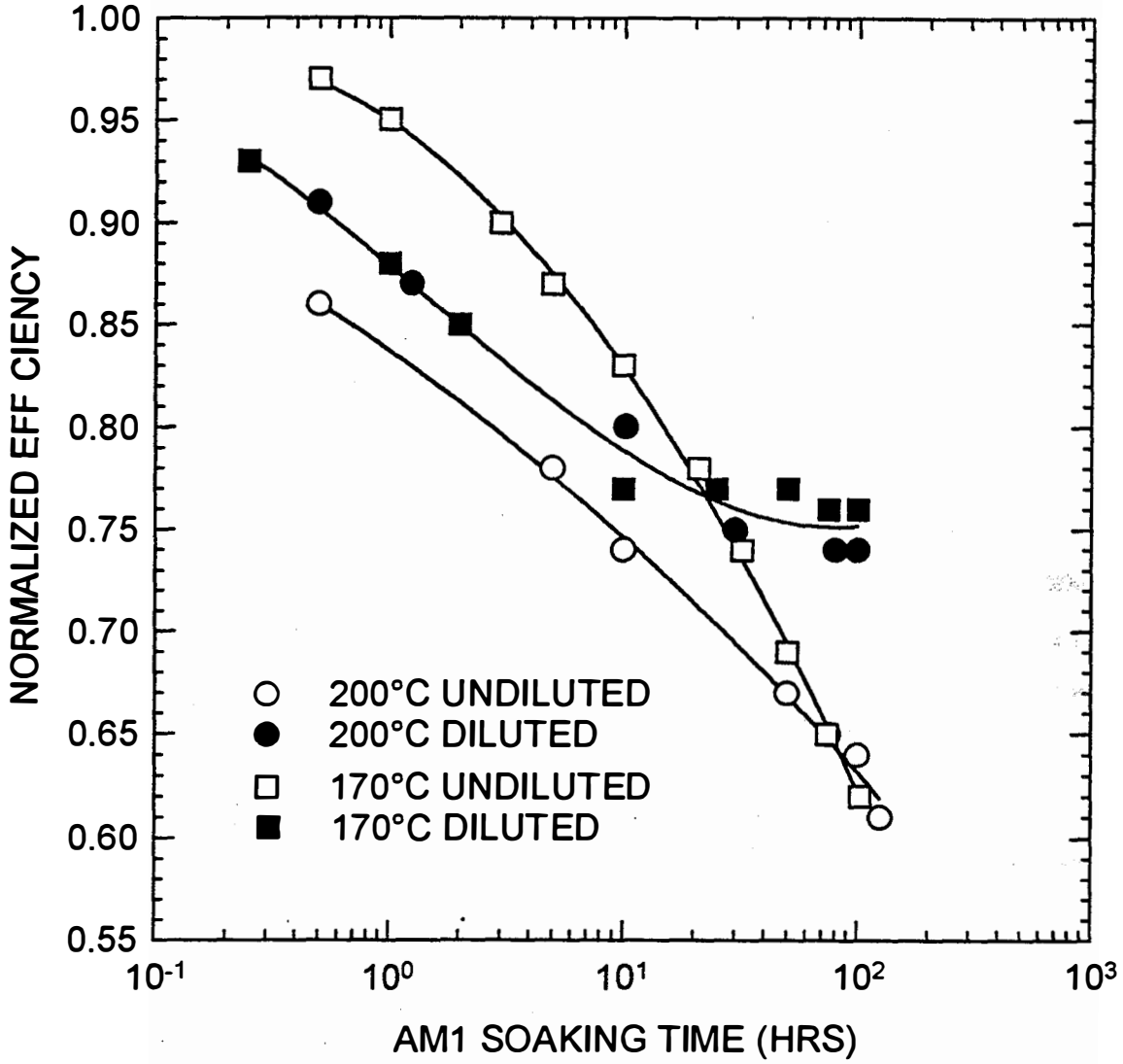

Figure 4 AM1 degradation of the normalized efficiencies of *p-i-n* cells with different *i*-layers. The cells with H_2-diluted *i*-layers show stabilization after 30-40 hrs soaking, while cells with undiluted *i*-layers do not stabilize even after 100 hrs AM1 soaking.

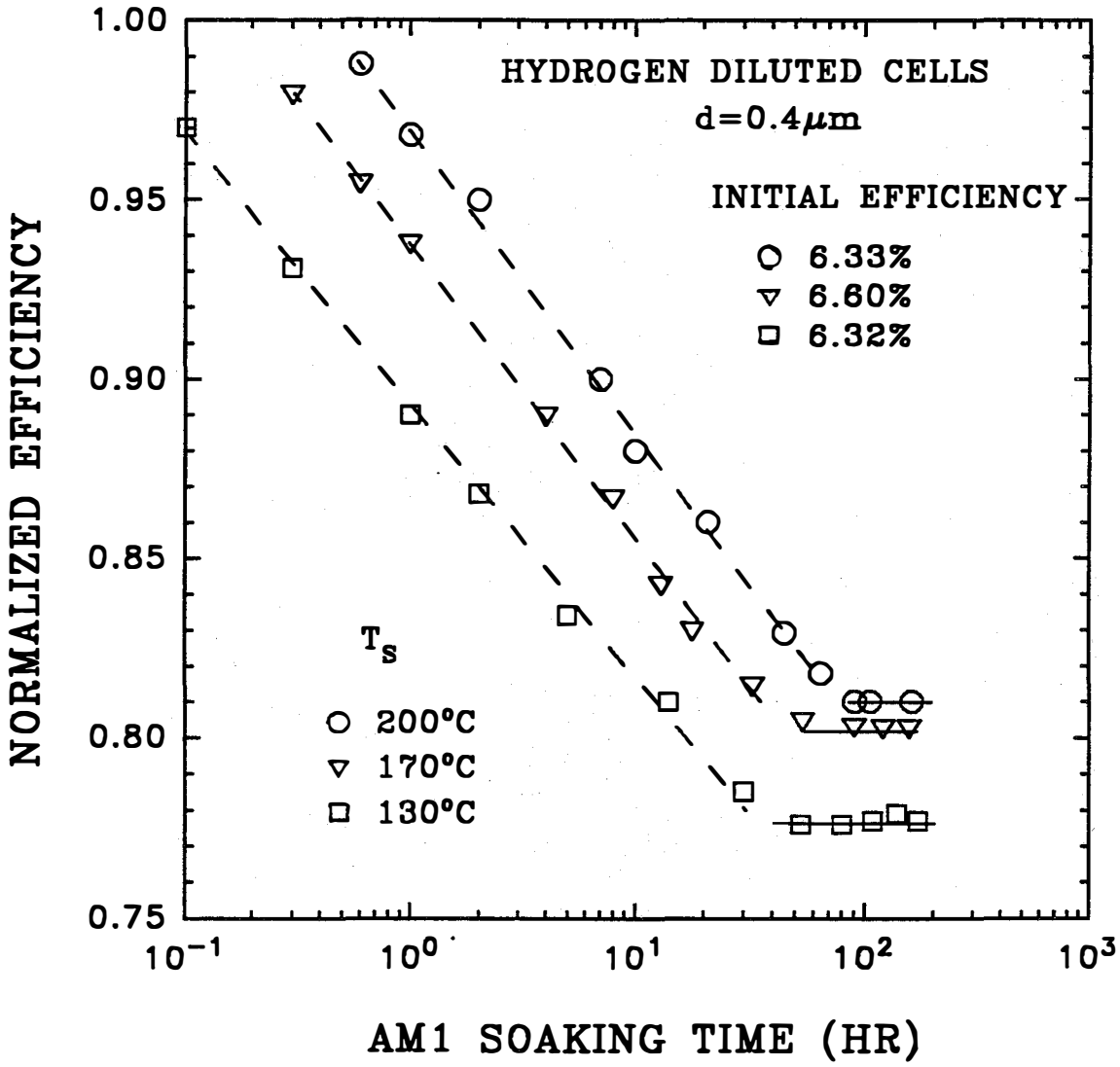

Figure 5 The degradation kinetics of the normalized efficiencies under AM1 illumination for three hydrogen diluted p-i-n solar cells deposited at T_S of 130, 170, and 200°C. The stabilized degraded state is observed for all three cases within 100 hours of soaking.

parameters in the annealed and stabilized degraded states are listed in Table 1. Differences were observed in the degraded steady states obtained with AM1 and 10AM1 illuminations. For example Fig. 6 shows results for cells that were deposited at 200°C with p-type a-SiC:H:B and n-type μc-Si:H:P layers having identical deposition conditions and 4000Å thick a-Si:H i-layers with (10:1) and without hydrogen dilution of SiH_4. It is important to note that for the diluted cell the steady state is reached in less than 100 hours with AM1 and the degraded stabilized state with 10AM1 illumination is reached in less than 10 hours but at a lower efficiency, which underscores the serious limitations on the estimates made for 'end-of-life' predictions based on any analysis of accelerated degradations carried out on undiluted cells and materials. In view of the previously reported lack of correlation between the properties of materials and cells, parallel studies were carried out on light induced changes in the i-layer films deposited at different T_S.

As in the case of solar cells the diluted films deposited at different T_S also reach steady states of degradation in less than 100 hours of AM1 illumination. This has been illustrated in Fig. 3 where the reciprocals of the electron mobility lifetime ($\mu\tau$) products obtained at a carrier generation rate of 10^{16} $cm^{-3}s^{-1}$ for films deposited at T_S's of 240, 200, and 170°C are plotted as a function of the AM1 illumination time. Although there is no unique correlation between $\mu\tau$ products and the types and densities of gap states, an inverse relationship is expected with quantitative correlations being obtained only after detailed studies. The results on the diluted solar cells clearly illustrate that direct correlations exist between the light induced changes in the bulk i-layers and those in p(a-SiC:H)/i(a-Si:H)/n(μc-Si) cells. This has not been previously demonstrated for "practical" solar cells having thicknesses less than ~5000Å. As indicated earlier, the distinctly different degradation kinetics in light induced changes in diluted and undiluted materials offer a new powerful probe for identifying the mechanisms limiting the performance and stability of solar cells. Studies on customized cell structures are being expanded with **well characterized** diluted and undiluted a-Si:H materials (see Sec. 1.3). Upon incorporation into the various regions of the cells, they allow their respective kinetics and the stabilized degraded states to be utilized not only in identifying but also in quantifying the different mechanisms of cell degradation.

Table 1 The parameters of solar cells with H_2-diluted i-layers prepared at T_s values of 200, 170, and 130°C in the annealed and AM1 stabilized steady states.

	Annealed State				AM1 Stabilized Degraded State			
Diluted p-i-n Cells	V_{oc} (V)	J_{sc} (mA/cm^2)	FF	Eff. (%)	V_{oc} (V)	J_{sc} (mA/cm^2)	FF	Eff. (%)
T_s=200°C	0.868	10.1	0.72	6.31	0.865	9.6	0.61	5.07
T_s=170°C	0.917	10.1	0.71	6.58	0.910	9.5	0.61	5.27
T_s=130°C	0.923	10.0	0.68	6.28	0.907	9.4	0.57	4.86

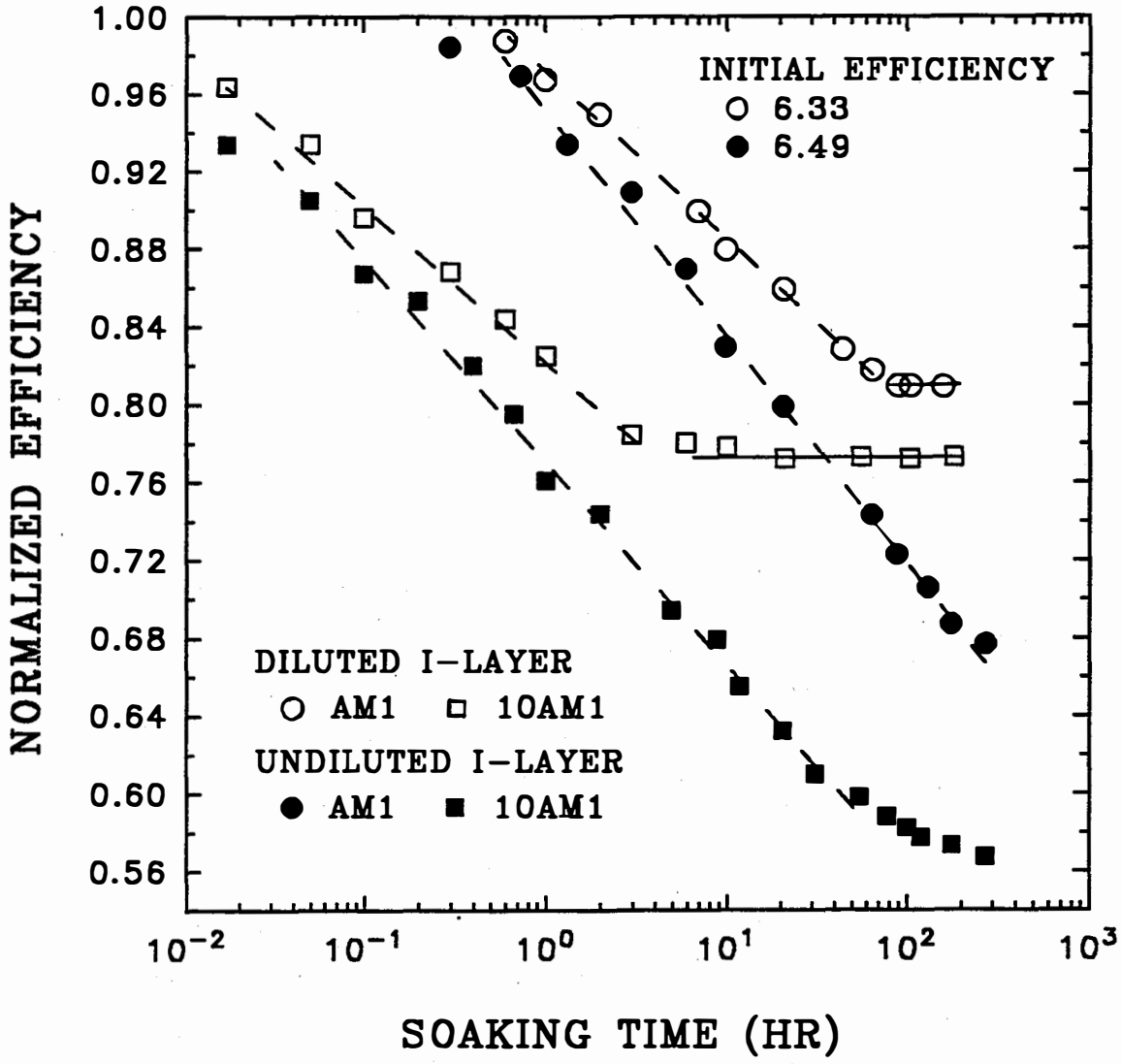

Figure 6 The degradation kinetics of the normalized efficiencies at different light intensities (AM1 at 28°C and 10AM1 at 50°C) vs. illumination time for diluted and undiluted cells.

The lack of reliable correlations between the characteristics of high performance cells and their intrinsic material properties was also addressed for undiluted solar cells. A systematic approach was developed for separating the effects of the bulk from those of the interface regions which is based on the self-consistent analysis on a variety of material and solar cell properties in the annealed and degraded states. The p-i-n cells, 0.4 to 1.0μm thick, are fabricated on specular SnO_2 substrates, so as not to have any optical enhancement effects. These cells exhibit parameters close to those for similar structures reported by industry, except (as expected) for J_{sc}, and the materials were what is commonly referred to as "device quality".

Since it is very difficult to obtain reliable information about the contributions of the bulk properties to solar cell performance from cells with one thickness, light I-V, dark I-V, and QE measurements were carried out on solar cells having different thicknesses. Examples of results are shown in Fig. 7 for a 0.4μm thick cell and in Fig. 8 for a 0.7μm thick p-i-n structure. The solid symbols represent the annealed state results and the open symbols represent the degraded state with 100 hours of AM1 illumination. In Fig. 8, the effect of the bulk can be seen in the much larger changes in the FF and J_{sc} in the thick structure, while the values and changes in the V_{oc} are about the same. Because there is no optical enhancement, the J_{sc} values in the two cells are directly determined by their thicknesses and the optical absorption so the changes can be accurately modeled. This is not the case for the comparable cells deposited on textured TCO where the differences are much smaller and the currents cannot be reliably quantified in terms of optical absorption. However because of the many adjustable parameters that are required in the analysis of light I-V's, reasonably good fits can still be made with different material and interface parameters. It is therefore necessary to measure and self-consistently fit other solar cell characteristics.

As expected, the degradation in the other cell characteristics of the thinner cells is significantly smaller. This is illustrated in Figs. 9 and 10, where the quantum efficiency results, measured without any light bias, are shown for the two cells. Because the characteristics undergo very small changes in the case of the 0.4μm cell, it is not possible to carry out reliable analysis in terms of the changes in bulk material properties.

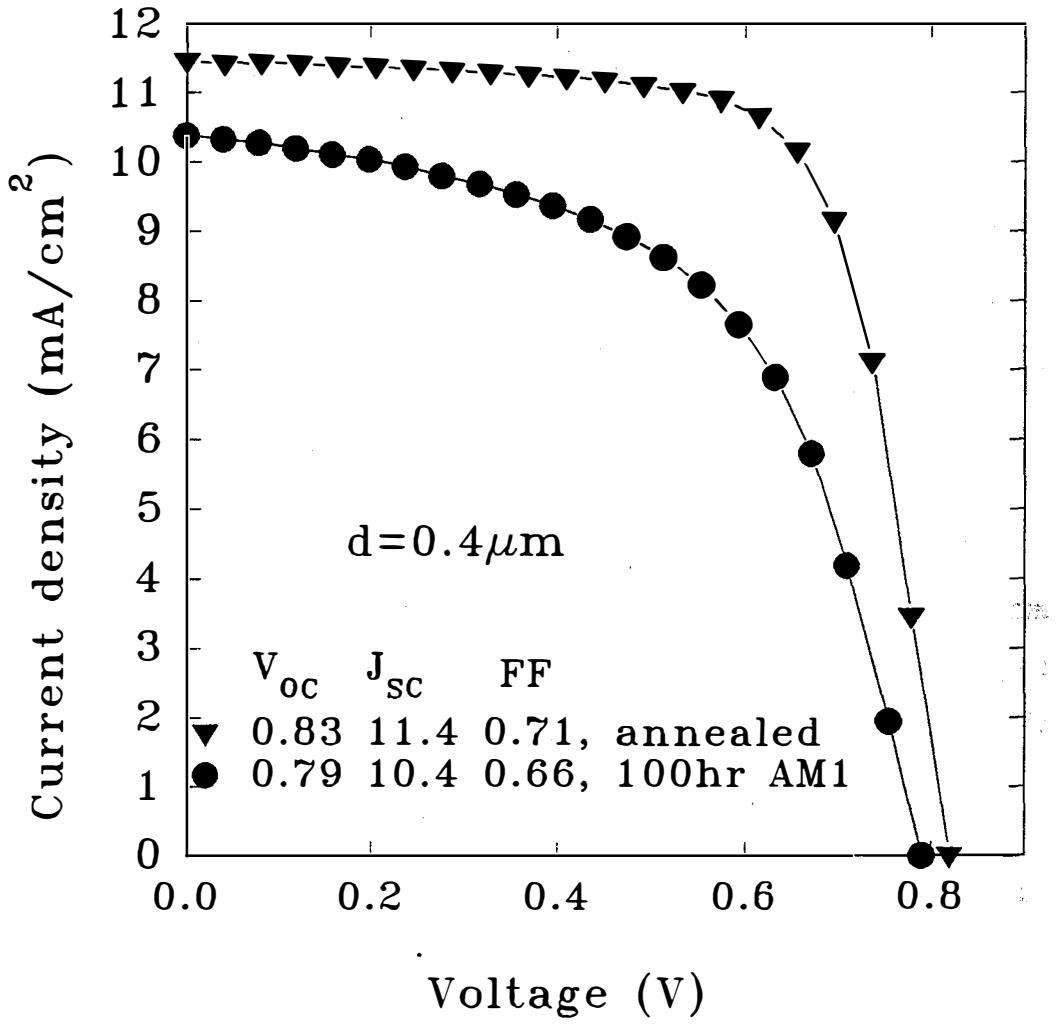

Figure 7 Light I-V's for a 0.4 μm thick p-i-n cell structure in the annealed and degraded state after 100 hours of AM1 light soaking.

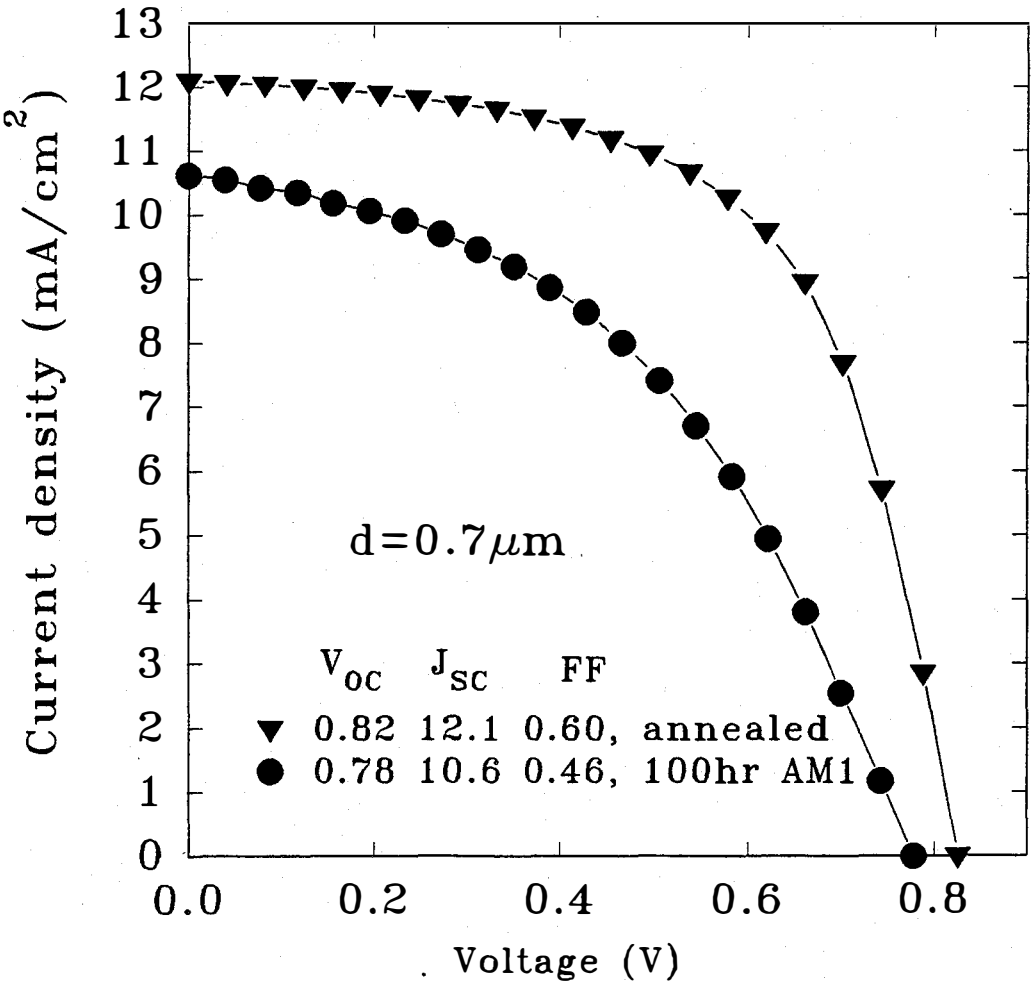

Figure 8 Light I-V's for a 0.7 μm thick p-i-n cell structure in the annealed and degraded state after 100 hours of AM1 light soaking.

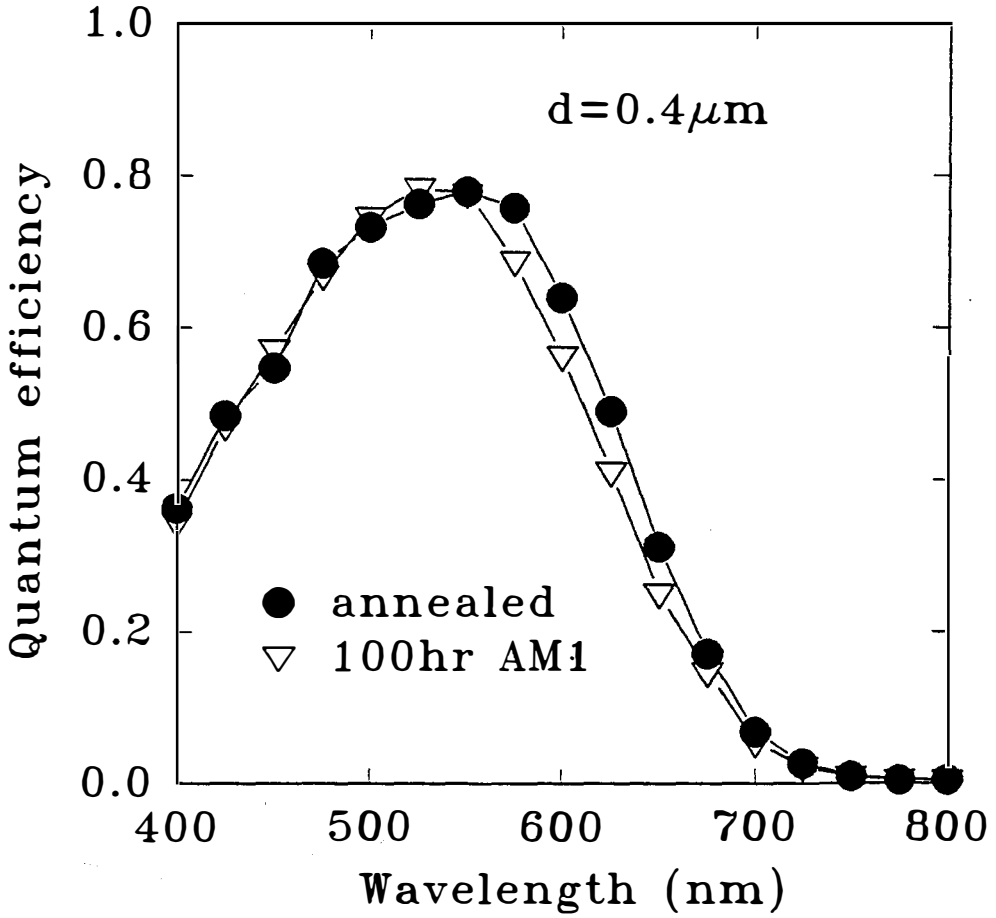

Figure 9 QE's without light bias for a 0.4 μm thick p-i-n cell structure in the annealed and degraded states after 100 hours of AM1 light soaking.

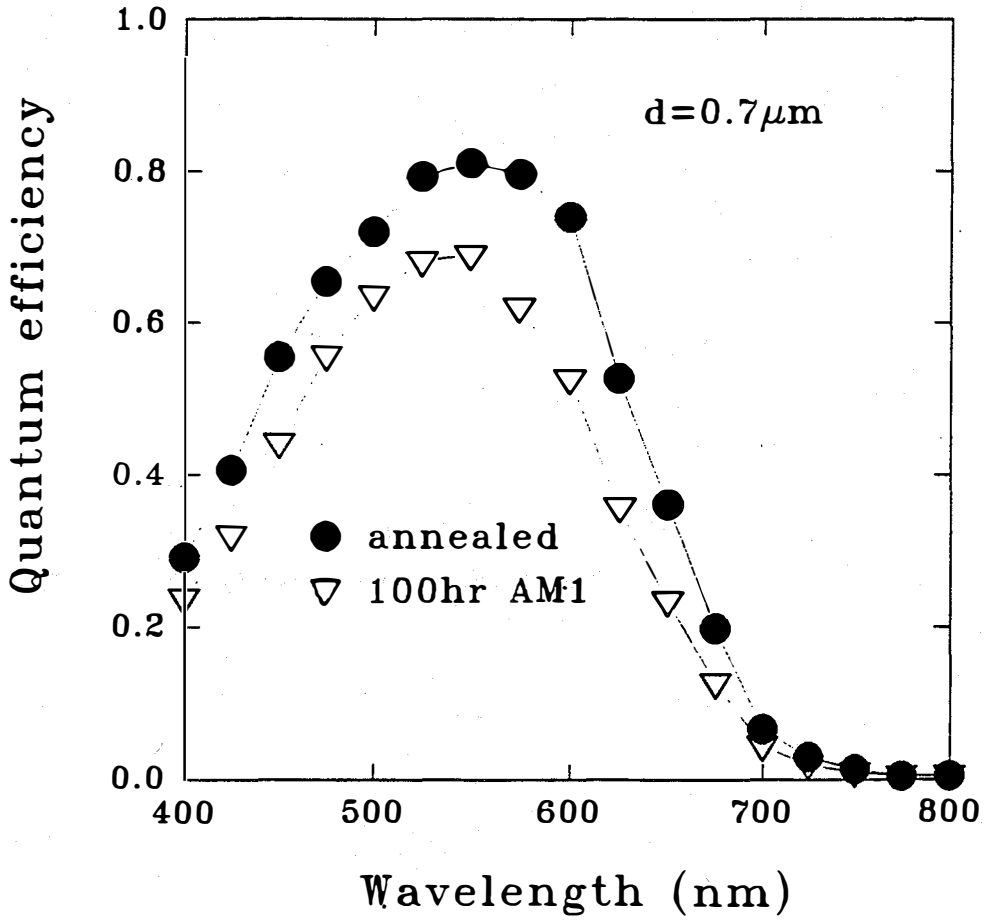

Figure 10 QE's without light bias for a 0.7 μm thick p-i-n cell structure in the annealed and degraded states after 100 hours of AM1 light soaking.

The thicker cells, on the other hand, offer characteristics in which the large effects can be more realistically analyzed. It is clear that even with well characterized materials, quantitative analysis should be carried out first on thick cells (>0.5μm) where the light induced changes in the bulk have a much larger effect on all of the cell characteristics.

Another characteristic that can be used in the analysis is the dark I-V of the p-i-n cell. It appears that in the I-V characteristics, the low forward bias exponential regions are controlled by carrier recombination/generation in the bulk and at the p/i interface. The far forward bias currents on the other hand are controlled by the space charge limited current flow through the bulk which is dominated by the bulk properties and hence the thickness of the p-i-n structures. As an example of this, the dark I-V characteristics are shown in Fig. 11 for thin (0.4μm) and thick (0.8μm) p-i-n structures, where the larger changes in the far forward dark I-V's of the thick structure are evident. The more dominant role in the p/i interfaces of the dark I-V's relative to the bulk in the thin structures is reflected in the corresponding difference in the far forward bias characteristics.

In addition, the metal Schottky barrier solar cell structures are also used because they offer a much more direct method for correlating the properties of thin film materials with device characteristics. They are also useful in further characterizing the bulk material properties in both the annealed and degraded states since both the dark I-V's and QE's are very sensitive to the bulk, and in particular to its light induced changes. They thus allow the "fine-tuning" of the material parameters derived from measurements and analysis of thin films for the self-consistent modeling of p-i-n cells with AMPS. This is discussed later when device modeling is treated.

1.3 Stability in a-Si:H Solar Cells: Customized Structures

Solar cell degradation studies were also carried out using the same setup as for film degradation in order to investigate the effects not only of H_2-dilution of the *i*-layers but also atomic H treatment at the *p/i* interfaces on the stability of *p-i-n* solar cells. The procedures for H_2-dilution and the *p/i* interface treatment are described elsewhere in this report. Four cells were made in our multi-chamber system for this customized cell study.

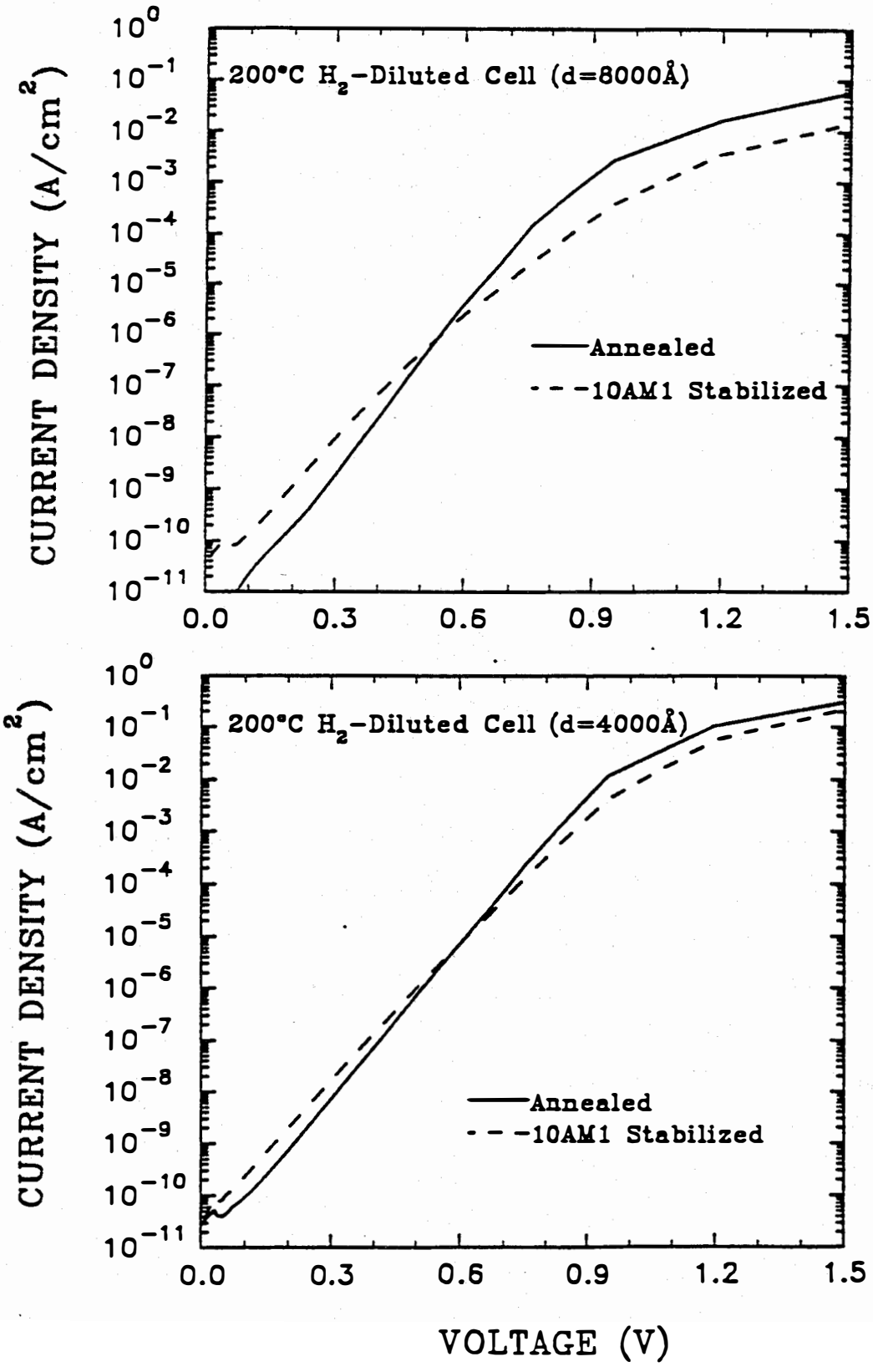

Figure 11 The dark I-V's of thick and thin p-i-n structures in both the annealed and the degraded states.

These cells are characterized by: (1) standard 200°C undiluted *i*-layer without interface treatment; (2) standard 200°C undiluted *i*-layer with atomic H *p/i* interface treatment; (3) 200°C H_2-diluted *i*-layer (R=10) without interface treatment; and (4) 200°C H_2-diluted *i*-layer with atomic H *p/i* interface treatment. The *p*-layers and *n*-layers were deposited under the same deposition conditions for all the cells.

These cells were characterized in both the annealed and degraded states. Degradation was carried out using ELH lamps with light intensities of AM1 and 10AM1 for up to 100 and 70 hrs, respectively. As far as the open-circuit voltage, V_{oc}, is concerned, cells with H_2-diluted *i*-layers show better stability than the corresponding cells with standard undiluted *i*-layers. When H_2-dilution of the *i*-layers is coupled with the atomic H *p/i* interface treatment, the V_{oc} stability is the best, as shown in Fig. 12. For example, the V_{oc} of the cell with standard *i*-layer and without interface treatment dropped from 0.84 V in the annealed state to 0.79 V in the 100 hrs AM1 degraded state, while that of the cell with both H_2-diluted *i*-layer and interface treatment degraded by less than 1%. Therefore applying H_2-dilution during *i*-layer growth along with atomic H treatment at *p/i* interface in a-Si:H *p-i-n* cell fabrication appears to improve cell V_{oc} stability.

Thus, to summarize the results of Fig. 10, we have shown the beneficial effects of atomic hydrogen treatment at the p/i interfaces on the performance of a-Si:H p-i-n cell structures. These atomic hydrogen treatments at the interfaces not only increase the V_{oc} in both solar cells in the annealed state, but also result in a more stable V_{oc} in both cases. We therefore conclude that in order to improve the initial, and more importantly the stabilized V_{oc}, not only do we need high quality and more stable bulk i-layer materials, achievable with H_2-diluted i-layers, but also improved p/i interfaces, such as those obtained with atomic hydrogen treatment of the p/i interfaces.

These conclusions have been further supported by studies of the stabilities of V_{oc} in n-i-p cell structures with i-layers deposited at lower substrate temperatures. These results are illustrated in Fig. 13 along with a comparison to the similar data from Fig. 12 for p-i-n cells. In Fig. 13, the cells with hydrogen diluted i-layers deposited at 170°C and atomic hydrogen treated p/i interfaces show better performance than their counterparts in both the annealed and degraded states. It can also be seen that at both 200° and 170°C, hydrogen

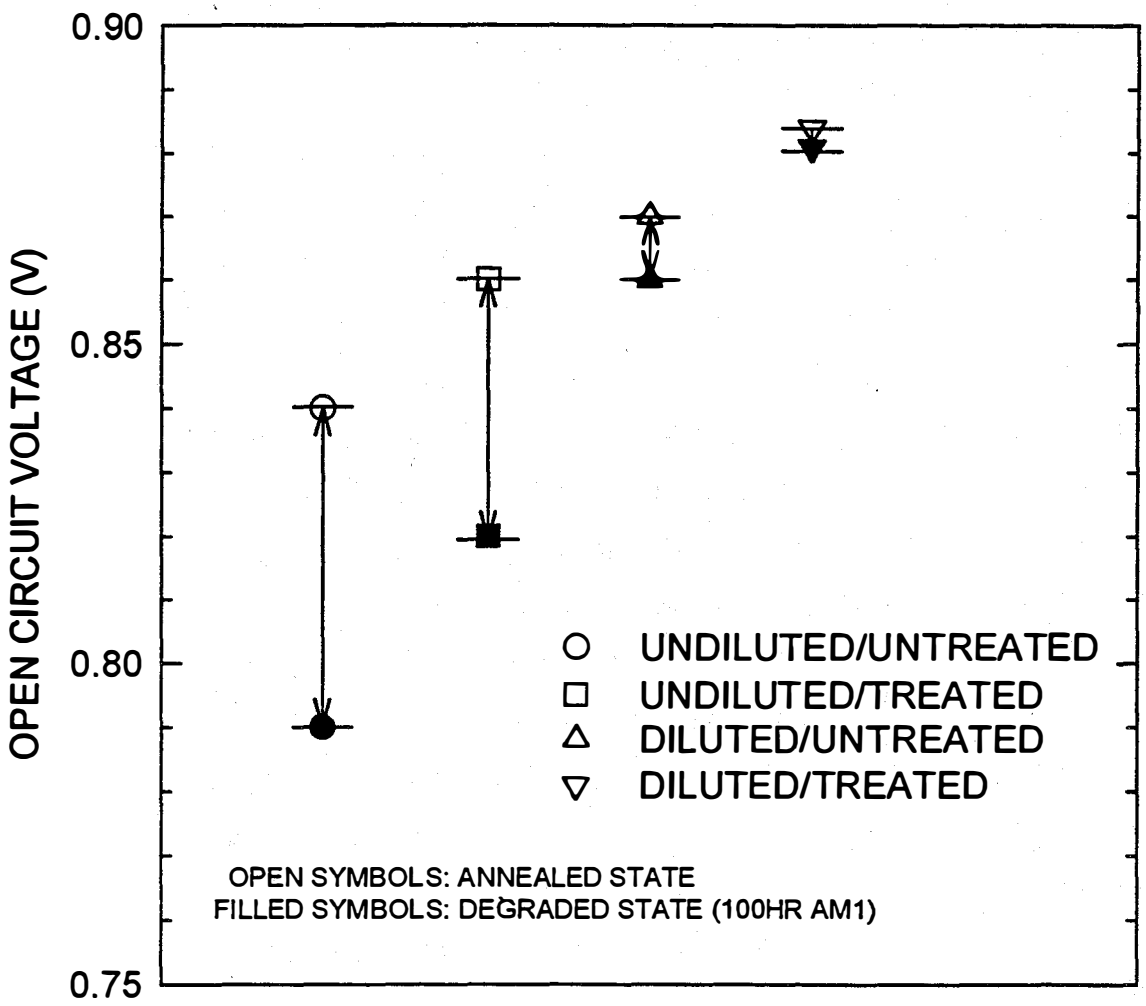

Figure 12 Degradation of open-circuit voltage for different *p-i-n* cells under 100 hrs AM1 illumination. Cells with *p/i* interface treatment show an improvement in V_{oc} and its stability.

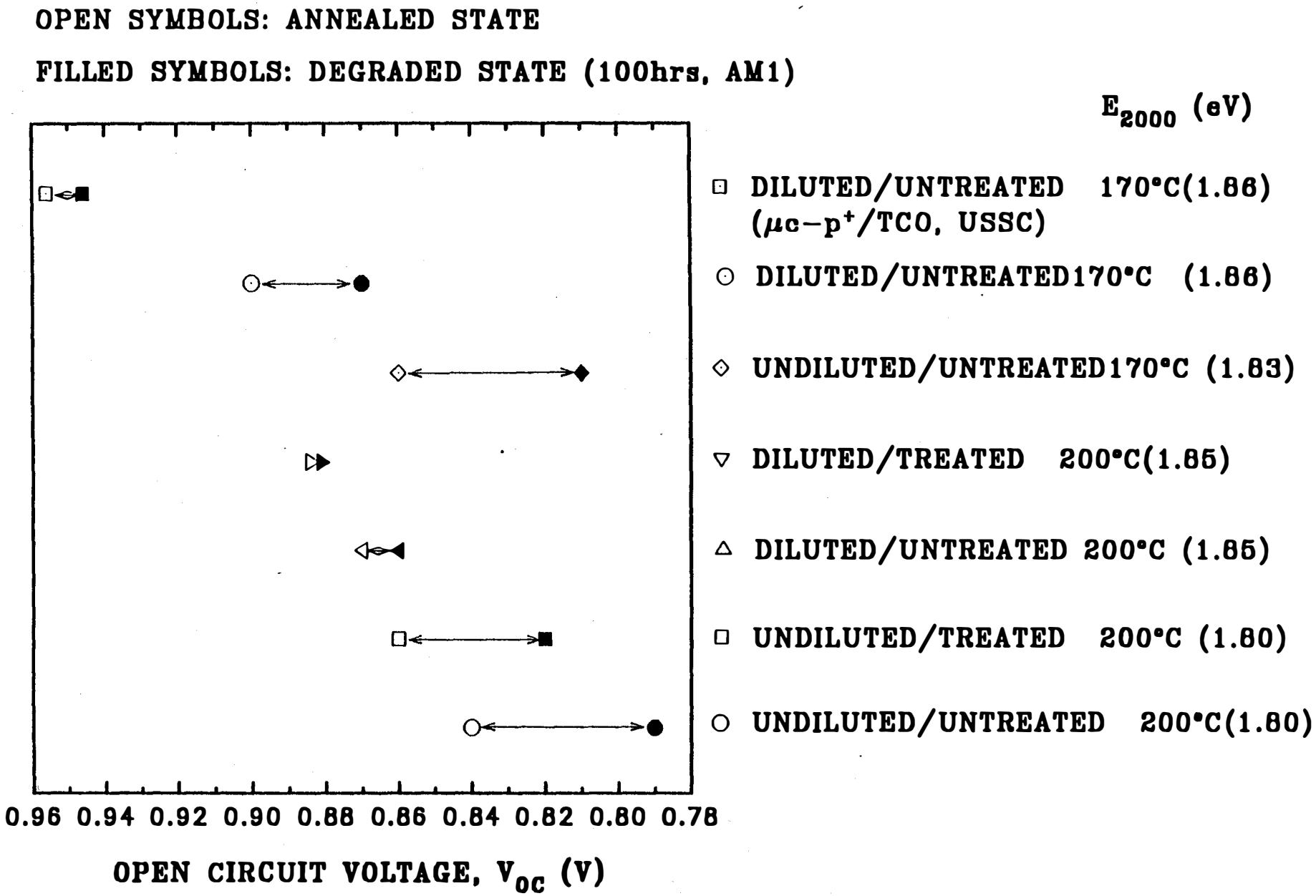

Figure 13 The effects of hydrogen dilution of the i-layers and atomic hydrogen treatment of the p/i interfaces on the annealed state V_{oc}'s and their stabilities for p-i-n (bottom four cells) and n-i-p (top three cells) structures.

dilution of the bulk i-layers results in a greater improvement in cell performance and stability than the atomic hydrogen p/i interface treatment that was used. These results can be understood if the hydrogen dilution used in the deposition of the i-layers improves both the bulk as well as p/i interface properties, while the atomic hydrogen treatment can only improve the p/i interfaces.

To further establish and quantify the relative contributions of the bulk and interface regions to the cell characteristics and their subsequent degradation under extended illumination, p-i-n cells were fabricated with thin H_2-diluted i-layers (150Å to 600Å) sandwiched between the p-layers and undiluted bulk i-layers. These customized cells were characterized in the annealed state as well as with extended 1 and 10AM1 degradations. In all the cells, the p-layers and n-layers were deposited under the same conditions and had the same thicknesses. To quantify real changes in J_{sc}, the cells were deposited onto specular TCO with non-reflecting Cr contacts.

The characteristics of cells with the sandwich structures were compared with those of cells with the standard diluted and undiluted i-layers. Examples of the light I-V's of these cells measured in the annealed state are shown in Fig. 14, where the cell with 300Å diluted interface and 3700Å undiluted bulk has the best overall performance. This cell has a FF of 0.73 and a V_{oc} of 0.864V, both of which are as high as those of the diluted cell; but it also has a J_{sc} of 11.4mA/cm^2, which is much higher than the corresponding diluted cell and similar to the undiluted cells. This effect would be expected for the higher optical absorption by the narrower gap i-layers. These results strongly indicate that in the annealed state the V_{oc} is primarily controlled by the p/i interface when the defect densities of the bulk material are low as in the case of these "device quality" bulk i-layers. On the other hand for such cells, the absorption by the bulk plays the major role in determining the J_{sc}, but the p/i interface can also affect the J_{sc} by modifying the electric field distribution. The highest J_{sc} of the diluted interface/undiluted bulk cell can be explained by the combination of the higher absorption by the bulk undiluted material and by a p/i interface region improved by hydrogen dilution. Since the fill factors are primarily determined by the bulk material properties, little difference is observed between these cells

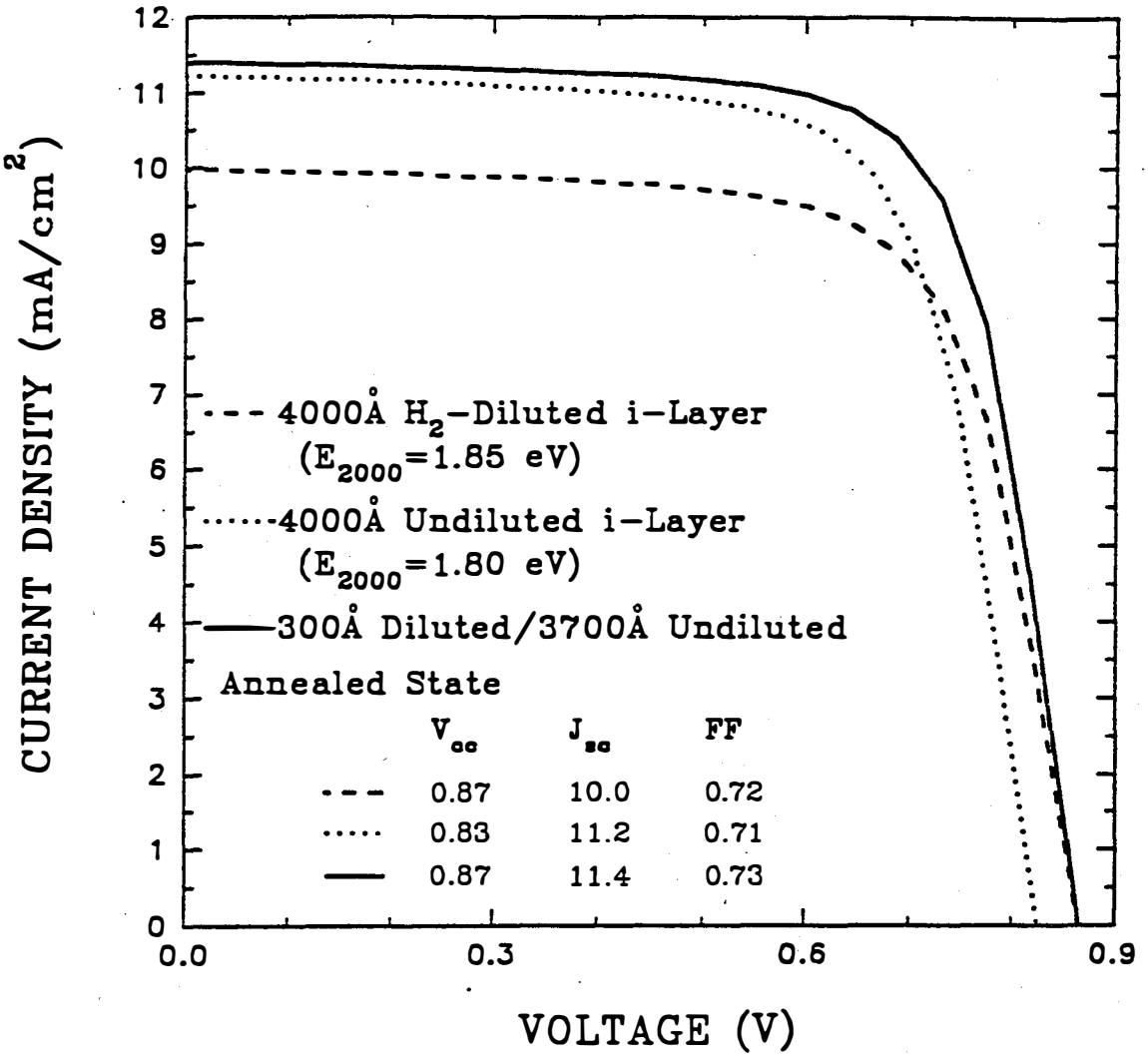

Figure 14 The annealed state light I-V's of the p-i-n structures with a pure diluted i-layer, a pure undiluted i-layer and a cell with diluted interface/undiluted bulk i-layer.

in the annealed state, since both the diluted and undiluted materials have been optimized and are of high quality.

A comparison of cells with different thicknesses of diluted interface layers were also carried out as shown in Fig. 15. The cells with 150Å, 300Å and 600Å thick diluted interfaces exhibit similar light I-V characteristics. The fill factors of all the cells are the same (0.73) because they are made with the same bulk materials. Since they have similar p/i interfaces, these three cells also have the higher V_{oc} (~0.865V).

The degradation studies of these p-i-n cells have been carried out using ELH light intensities of AM1 and 10AM1. The degraded state light I-V's after 100 hrs of 10AM1 light soaking for the 300Å diluted interface sandwich cell, together with the standard diluted and undiluted cells are shown in Fig. 16. Here it is seen that after 100 hrs of 10AM1 light soaking, the V_{oc} of the sandwich cell shows the largest voltage drop of 0.06V (from 0.87V to 0.81V) compared to the V_{oc} drop of only 0.01V (from 0.87V to 0.86V) for the cell with the diluted i-layer, as well as the V_{oc} drop of 0.04V (from 0.82V to 0.78V) for the cell with the undiluted i-layer. It can also be seen the V_{oc} of the sandwich cell, which has reached steady state in its degradation as in the diluted cell, lies between those of the diluted and undiluted cells, but is closer to that of the undiluted cell. These results clearly indicate that the degradation in the p-i-n cells is determined by the properties of both bulk i-layers and the p/i interfaces. The bulk i-layers appear to contribute more to the light-induced degradation when the defect densities in these layers are higher as in the case of the undiluted material. As expected, the sandwich cell has a stabilized efficiency between those of the cells with the pure diluted and undiluted i-layers due to the p/i interface, which is better than that of the undiluted cell, and the bulk i-layer, which is less stable than that of the diluted cell. The kinetics of the degradation in efficiencies of these three cells with 10AM1 illumination are shown in Fig. 17. Detailed studies on the changes in all the cell characteristics (dark I-V's, light I-V's, spectral response, etc.) are now being carried out in order to separate and quantify the relative contributions from the bulk and the interface regions to cell performance.

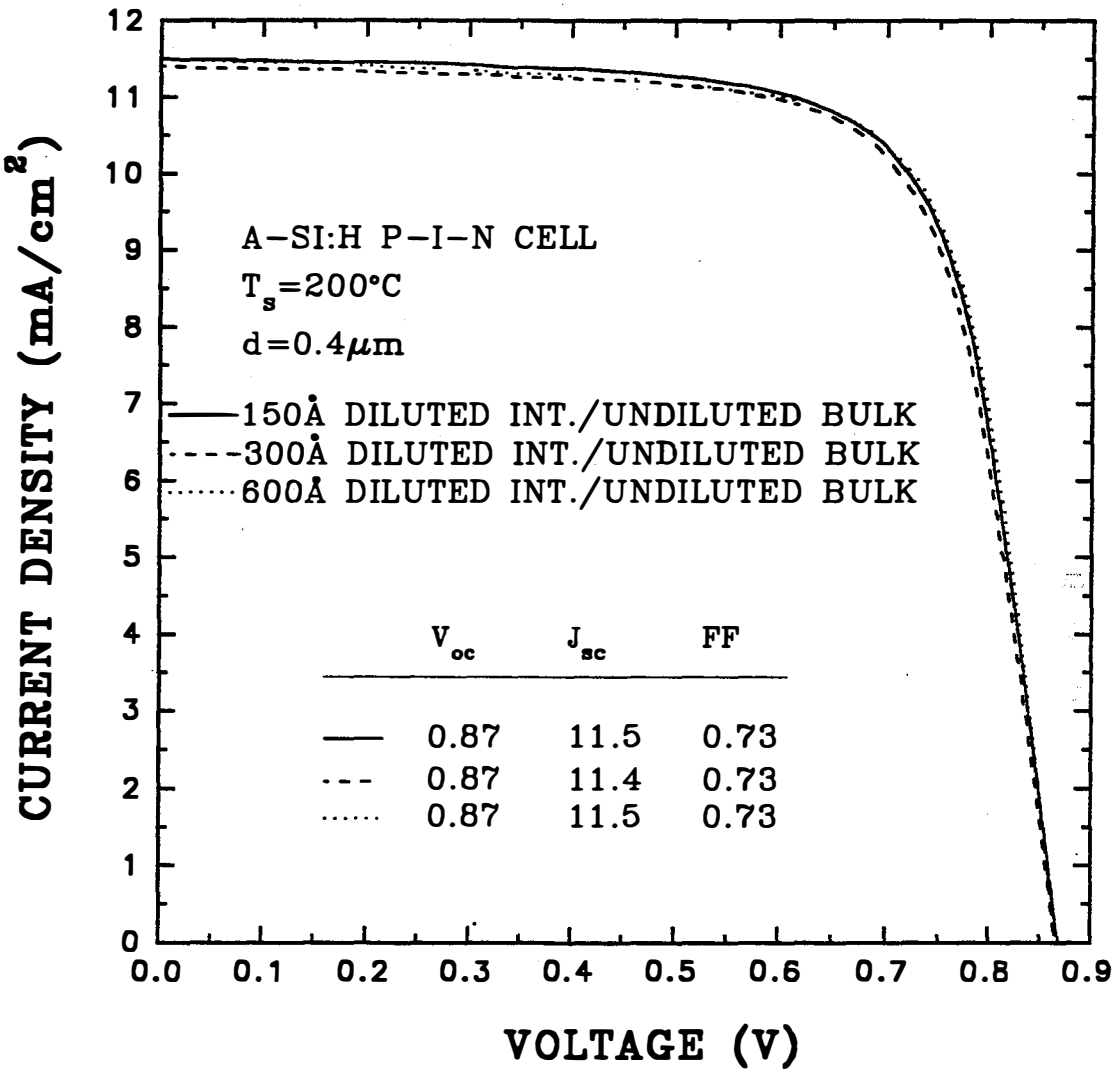

Figure 15 The annealed state light I-V's of p-i-n cells with three different thicknesses of diluted interface layers. The total i-layer thickness is 0.4 μm.

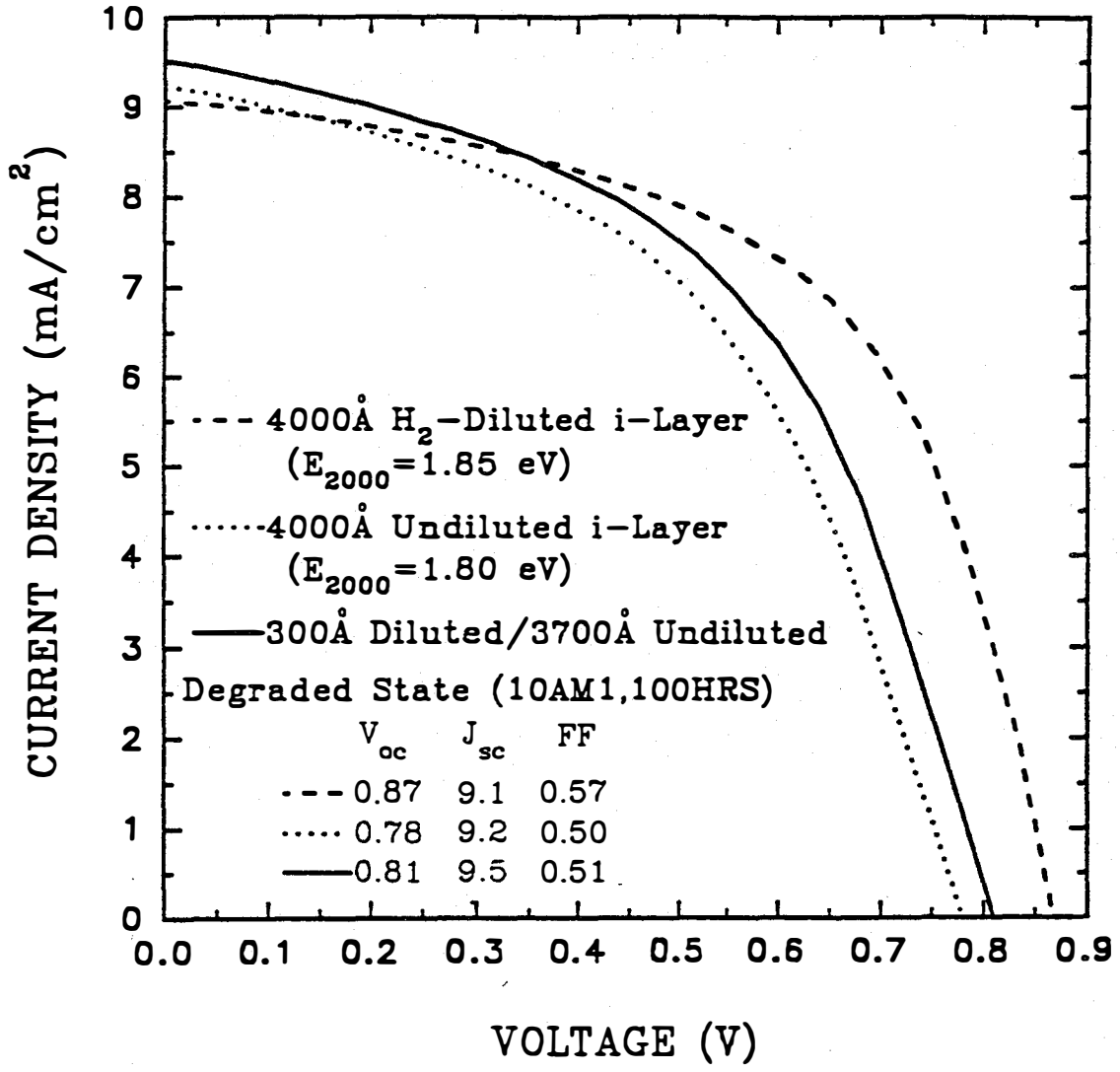

Figure 16 The degraded state light I-V's of the p-i-n cells with a pure diluted i-layer, a pure undiluted i-layer and a cell with diluted interface/undiluted bulk i-layer.

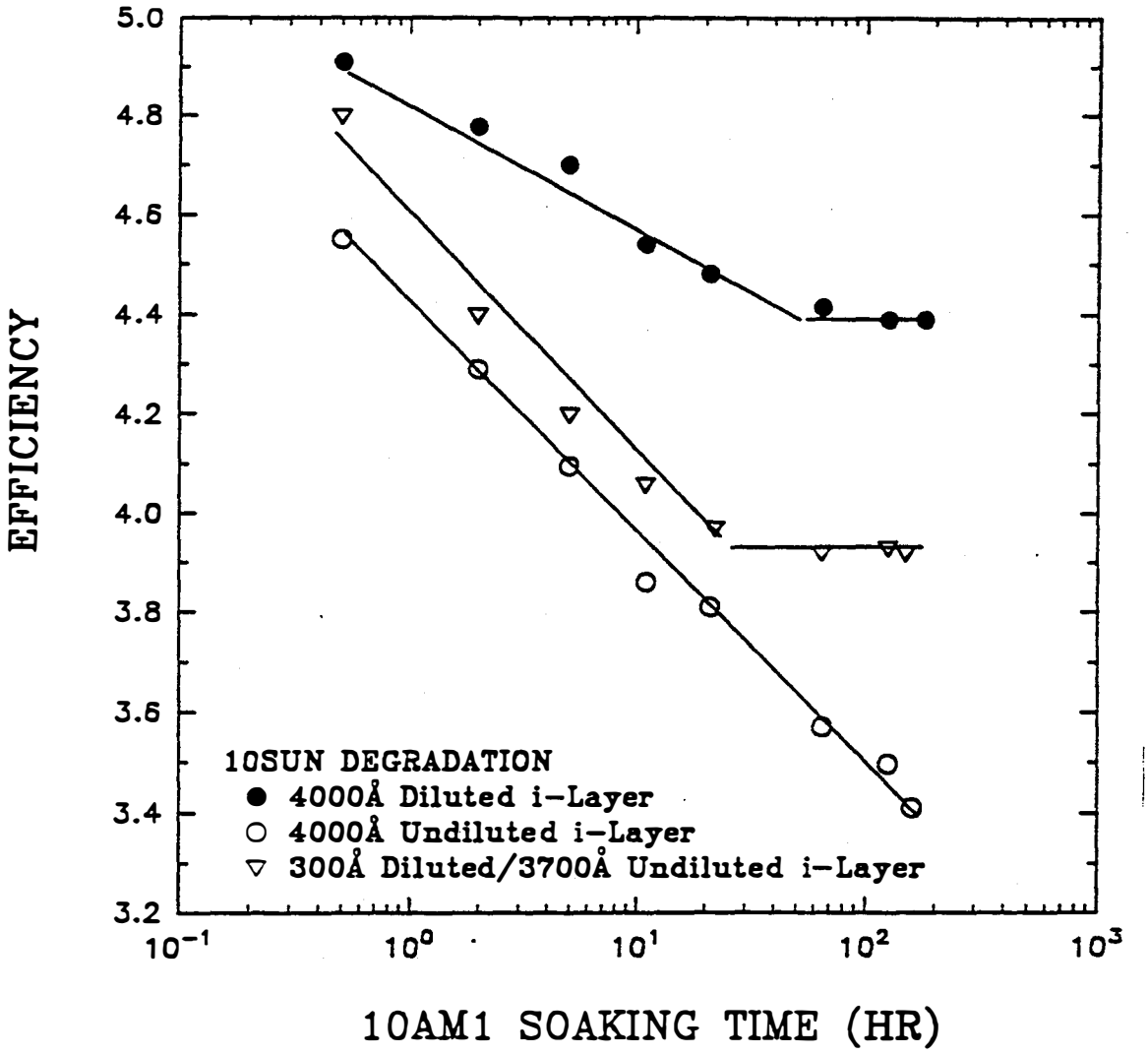

Figure 17 The degradation kinetics in the efficiencies of p-i-n cells with pure a diluted i-layer, a pure undiluted i-layer and a cell with diluted interface/undiluted bulk i-layer.

Computer modeling is also being employed in this detailed analysis. In the computer modeling, the role of the material parameters including densities of charged defects are studied.

Additional studies were performed in order to further quantify the relative contributions of the bulk and the p/i interface regions to the degradation of solar cells. Kinetics of degradation were investigated in detail on customized cells consisting of p(a-SiC:H)-(x)i(diluted)-(4000Å-x)i(undiluted)-n(μc-Si) [x=50Å, 150Å, 300Å, 600Å] and p(a-SiC:H)-(300Å)i(undiluted)-(3700Å)i(diluted)-n(μc-Si). These results were compared with those of well characterized p(a-SiC:H)-(4000Å)i(diluted)-n(μc-Si) and p(a-SiC:H)-(4000Å)i(undiluted)-n(μc-Si) cells. Additional information could be obtained on the role of the p/i interface regions and the bulk in determining degradation properties of the cells. This is illustrated in Fig. 18 where the efficiencies for the cell with the diluted bulk and undiluted interface region are shown together with those of the two standard cells. As seen in Fig. 6, the standard diluted cell reached a steady state in about 80 hours of AM1 soaking while the standard undiluted cell continuously degrades even after 200 hours soaking. On the other hand, the customized cell with 300Å undiluted p/i and 3700Å diluted bulk exhibits a degraded steady state in a time close to that taken by the standard diluted cell. The different cell parameters V_{oc}, J_{sc} and FF are shown in Fig. 19 where the contributions of the bulk can be clearly identified by the presence or absence of the steady state after less than 150 hours AM1 soaking. It is important to note that the customized cell with the 300Å undiluted p/i interface region exhibits similar degradation kinetics not only in J_{sc} and FF as the standard diluted cell, as would be expected based on their dependence on bulk properties, but also in V_{oc}. The standard undiluted cell does not show any signs of a degraded steady state in any of the parameters. These results indicate that in these cells the degradation kinetics are primarily controlled by the light induced changes in the bulk region rather than at the p/i interface, even though the interface plays a key role in determining the V_{oc} in the annealed state.

Figure 20 shows the degradation kinetics of V_{oc} for the standard diluted cell along with those for the customized cells with a total of 4000Å-x undiluted bulk and x=50Å, 150Å, 300Å, 600Å diluted p/i interface regions. It can be seen in Fig. 20 that the diluted

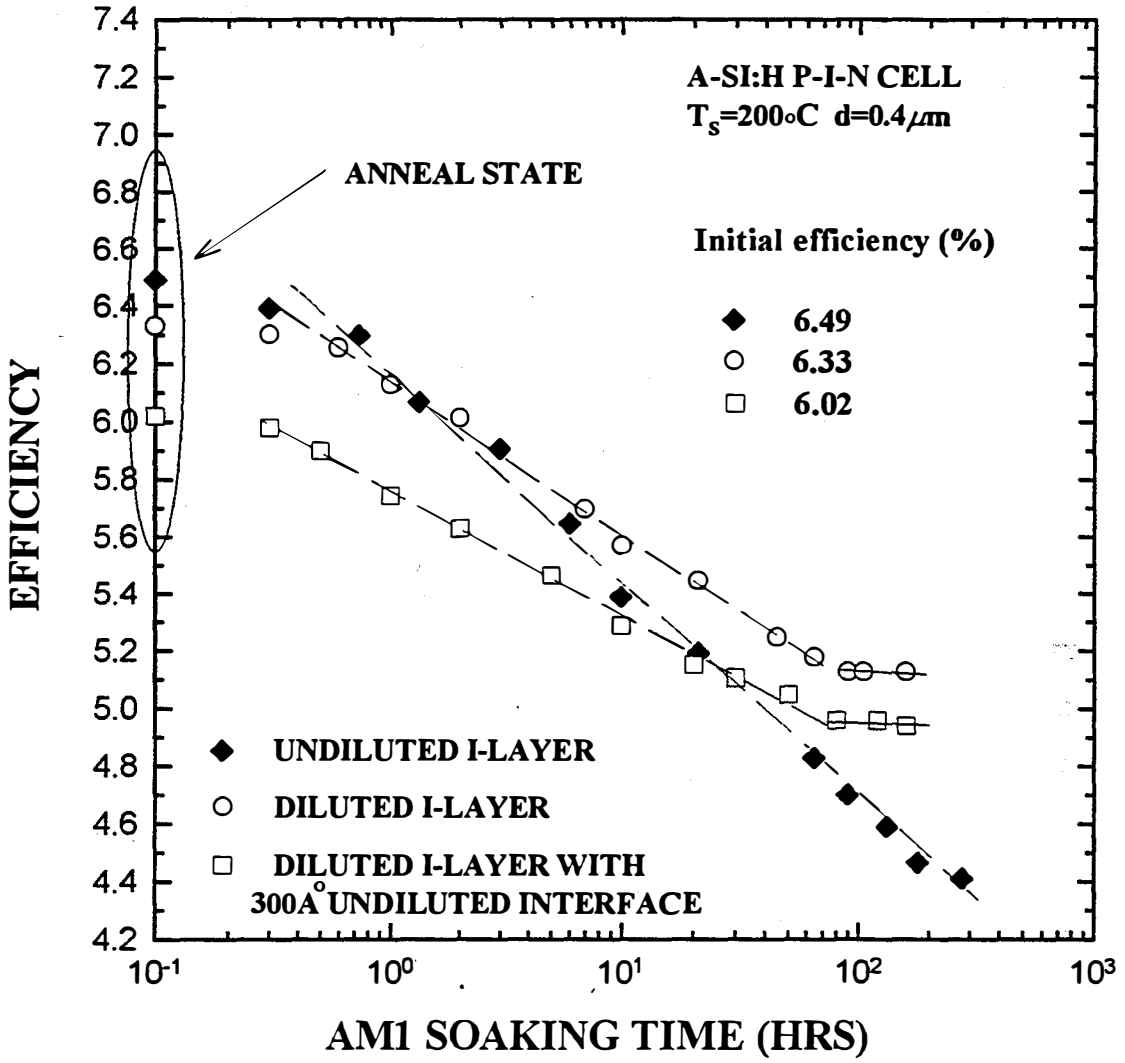

Figure 18 The degradation kinetics in the efficiencies versus AM1 illumination time for a standard diluted cell, a standard undiluted cell and a customized cell with undiluted i-layer and 300Å diluted interface layer. All the cells have the same bulk thickness of 0.4μm.

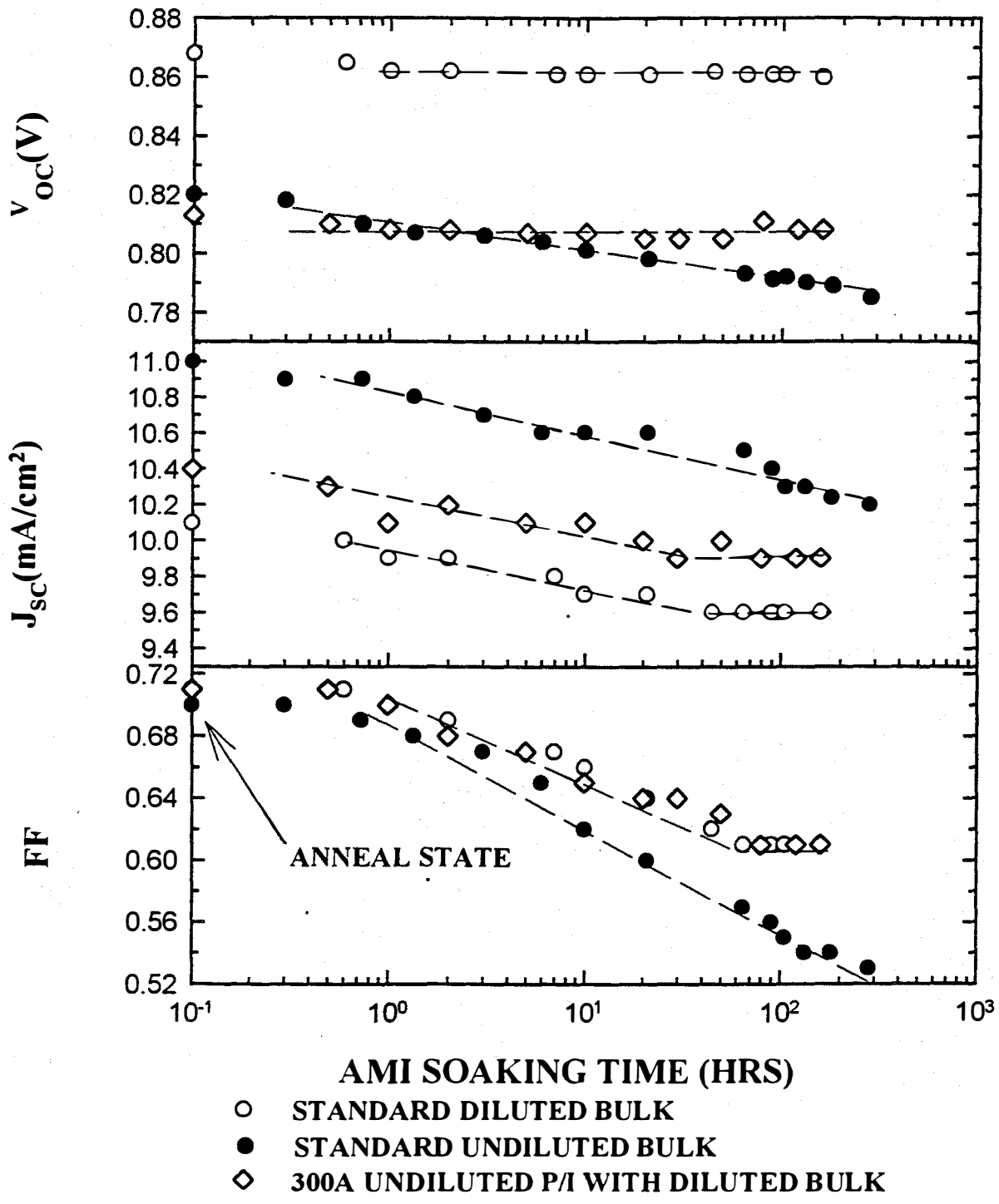

Figure 19 The degradation kinetics in V_{oc}, J_{sc} and FF versus AM1 illumination time for a standard diluted cell, a standard undiluted cell and a customized cell with undiluted i-layer and 300Å diluted interface layer.

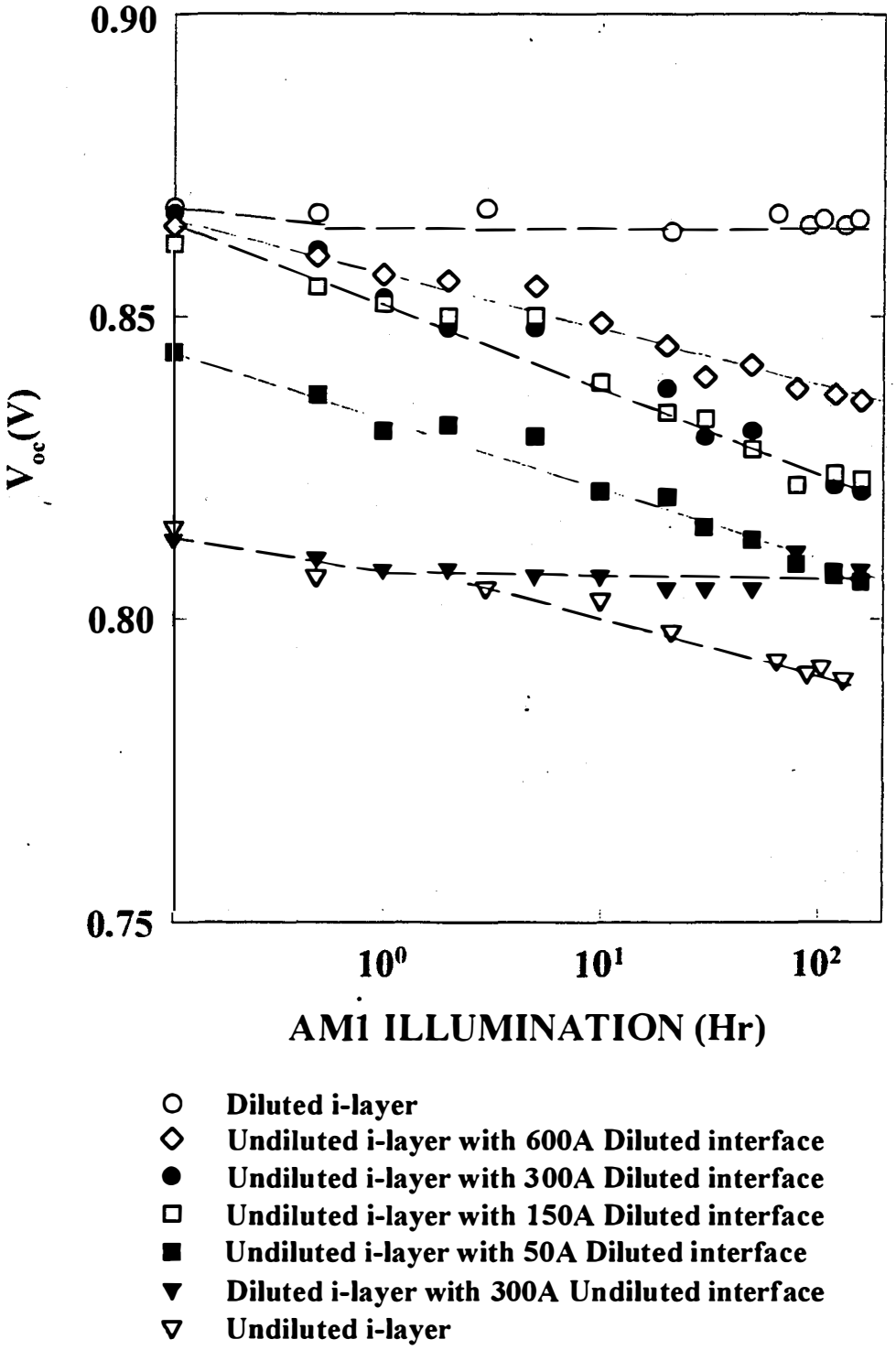

Figure 20 The degradation kinetics of V_{oc} versus AM1 illumination time for two standard cells and a series of customized cells which have undiluted bulk layers and different thickness diluted p/i interface layers, 50, 150, 300, 600Å.

p/i interface significantly improves the V_{oc} of the p-i-n solar cell compared with the undiluted bulk material. For thicknesses of the diluted region of 50, 150, 300, 600Å, the V_{oc} increases by 0.02, 0.04, 0.05 and 0.05V respectively. The largest change in V_{oc} occurs from x=0 to x=150Å. After a thickness of 150Å there is little difference in V_{oc} from that of a standard diluted cell. These results indicate that the thickness of the p/i interface regions in these p-i-n cells is around 100Å. Thus the results clearly show that in the annealed state the V_{oc} is determined by the p/i interface. In spite of this, their degradation kinetics depend on the bulk material as indicated by the corresponding results in Fig. 19. For example, V_{oc} continues to decrease beyond 100 hours of soaking for the standard undiluted bulk cells as well as those with 50, 150, 300 and 600Å diluted interface regions cells while the standard diluted cell show very little degradation. For the cell with 600Å p/i diluted interface region the V_{oc} degrades more slowly, but this is not surprising since 600Å is no longer negligible when compared to the 3400Å bulk undiluted material.

It has been found that these customized cells, consisting of diluted and undiluted a-Si:H, are becoming very useful in reliably quantifying the contributions of the interface regions and the bulk in both the annealed and degraded state. Detailed measurements are being carried out on a variety of cell characteristics, and subsequent analysis of the results is being used to quantify these contributions.

1.4 Stability in a-Si_{1-x}:C_x:H Solar Cells

Another approach to increase the open-circuit voltages of *p-i-n* solar cells even further is to use a-$Si_{1-x}C_x$:H layers as the absorber layers. However, a-$Si_{1-x}C_x$:H materials generally have larger defect densities than those of a-Si:H layers in the annealed state, and they degrade much faster under light soaking than a-Si:H layers. Early in Phase II, we incorporated 2000 Å thick a-$Si_{1-x}C_x$:H layers as the absorber layers in the fabrication of *p-i-n* solar cells for stability studies. We also introduced a H_2-dilution graded layer at the *p/i* interface in an attempt to better understand the effects of H_2-dilution on the open-circuit voltage of *p-i-n* cells.

In order to study the stability of *p-i-n* cells with different a-$Si_{1-x}C_x$:H *i*-layers and with interface graded layers, we made three different *p-i-n* cells as outlined in the following. The a-$Si_{1-x}C_x$:H:B *p*-layers and a-Si:H *n*-layers are identical for all three cells. The deposition temperature was 200°C. The H_2-dilution graded layers were discussed in greater detail in Phase I.

p-i(R=5)-*n*: a-$Si_{1-x}C_x$:H *i*-layer with R=[H_2]/{[SiH_4]+[CH_4]}=5

p-i(R=20)-*n*: a-$Si_{1-x}C_x$:H *i*-layer with R=20

p-h-i(R=20)-*n*: A H_2-dilution graded layer, ***h***, is inserted between *p*- and *i*-layers. R was adjusted continuously to achieve R=2 at the *p/h* interface to R=20 at the *h/i* interface. The intended thickness of the H_2-dilution graded layer ***h*** was 200 Å.

The cell parameters in the annealed state and in the AM1 degraded state are listed in Table 2. As can be seen in the table, we can change the open-circuit voltage by using different H_2-dilution ratios for the a-$Si_{1-x}C_x$:H *i*-layers as noted in the final report of Phase I. These a-$Si_{1-x}C_x$:H cells have relatively low efficiencies (~3%) in the annealed state in part due to the thinness of the a-$Si_{1-x}C_x$:H *i*-layer. However after 100 hrs AM1 light soaking, approximately 50% of the initial efficiency is lost. The poorer stability against light soaking of individual a-$Si_{1-x}C_x$:H films as compared to pure a-Si:H films translates into poorer long term stability of cells made from them. Thus such a conclusion is common not only in comparing the stability of H_2-diluted and undiluted a-Si:H materials and cells (see Secs. 1.1-1.2), but also in comparing pure a-Si:H and a-$Si_{1-x}C_x$:H alloy materials and cells (see Sec. 2.1).

Table 2 Comparison of the cell parameters of devices in the annealed and 100 hrs AM1 degraded states for selected a-$Si_{1-x}C_x$:H *p-i-n* structures having 2000 Å *i*-layers prepared with different H_2-dilution ratios. One of the cells was prepared with a H_2-dilution graded buffer layer at the p/i interface (last row).

CELL	STATE	V_{oc} (V)	J_{sc} (mA/cm^2)	FF	Eff. (%)
p-i(R=5)-*n*	Annealed	0.914	5.4	0.61	3.01
	Degraded	0.868	4.5	0.42	1.64
p-i(R=20)-*n*	Annealed	0.880	7.0	0.48	2.96
	Degraded	0.847	5.2	0.38	1.67
p-h-i(R=20)-*n*	Annealed	0.882	5.7	0.50	2.51
	Degraded	0.836	4.9	0.40	1.64

2. Novel Intrinsic Materials Optimization

2.1 Wider-gap a-Si:H versus Widegap a-$Si_{1-x}C_x$:H

Optimization of a-$Si_{1-x}C_x$:H materials as the absorber layers has continued in the early part of Phase II. Optimized a-$Si_{1-x}C_x$:H materials and solar cells have been compared with wider bandgap a-Si:H materials and solar cells prepared with hydrogen dilution. Real time optical measurements, along with *ex situ* electronic characterization were combined to optimize a-$Si_{1-x}C_x$:H alloys as a function of the H-dilution ratio $R=[H_2]/\{[CH_4]+[SiH_4]\}$ and substrate temperature, T_S. In Phase I, it was shown that the optimum H_2-dilution ratio of R = 20 to 25 is the maximum that can be sustained without the formation of Si microcrystals in the films. Results on subgap absorption using Dual-Beam Photoconductivity (DBP) on the a-$Si_{1-x}C_x$:H films deposited at different substrate temperatures are shown in Fig. 21 where it can be seen that the values of the annealed state α (1.2 eV), the absorption coefficient at 1.2 eV, remain relatively constant over the substrate temperature range between 175°C and 250°C. These results indicate that high quality a-$Si_{1-x}C_x$:H material, with R=20, is obtained in this range of substrate temperatures.

Emphasis has been given to a-$Si_{1-x}C_x$:H materials because of their high optical bandgaps which are useful in obtaining high values of V_{oc} in solar cells. Materials have been optimized with E_{2000} as high as 1.97eV. The concurrent studies on increasing the bandgap of a-Si:H materials through hydrogen dilution have shown that bandgaps as high as E_{2000}=1.90eV can be obtained at substrate temperatures between 170°C and 200°C and further increases in bandgap are being pursued by fabricating films at lower substrate temperatures. Previous studies on a-$Si_{1-x}C_x$:H and a-Si:H materials in Phase I have indicated that the properties of the optimized a-$Si_{1-x}C_x$:H materials degrade much more than those of a-Si:H prepared with hydrogen diluted SiH_4. The magnitude of this can be clearly seen in Fig. 22, where the results of the subgap absorption both in the annealed state and in the degraded states after 10AM1 illumination for 100 hours are shown for an a-$Si_{1-x}C_x$:H film ($x \approx 0.05$) prepared under the optimized condition at T_S=175°C and a wider-gap a-Si:H prepared at T_S=170°C. This a-$Si_{1-x}C_x$:H material has E_{2000}=1.97eV,

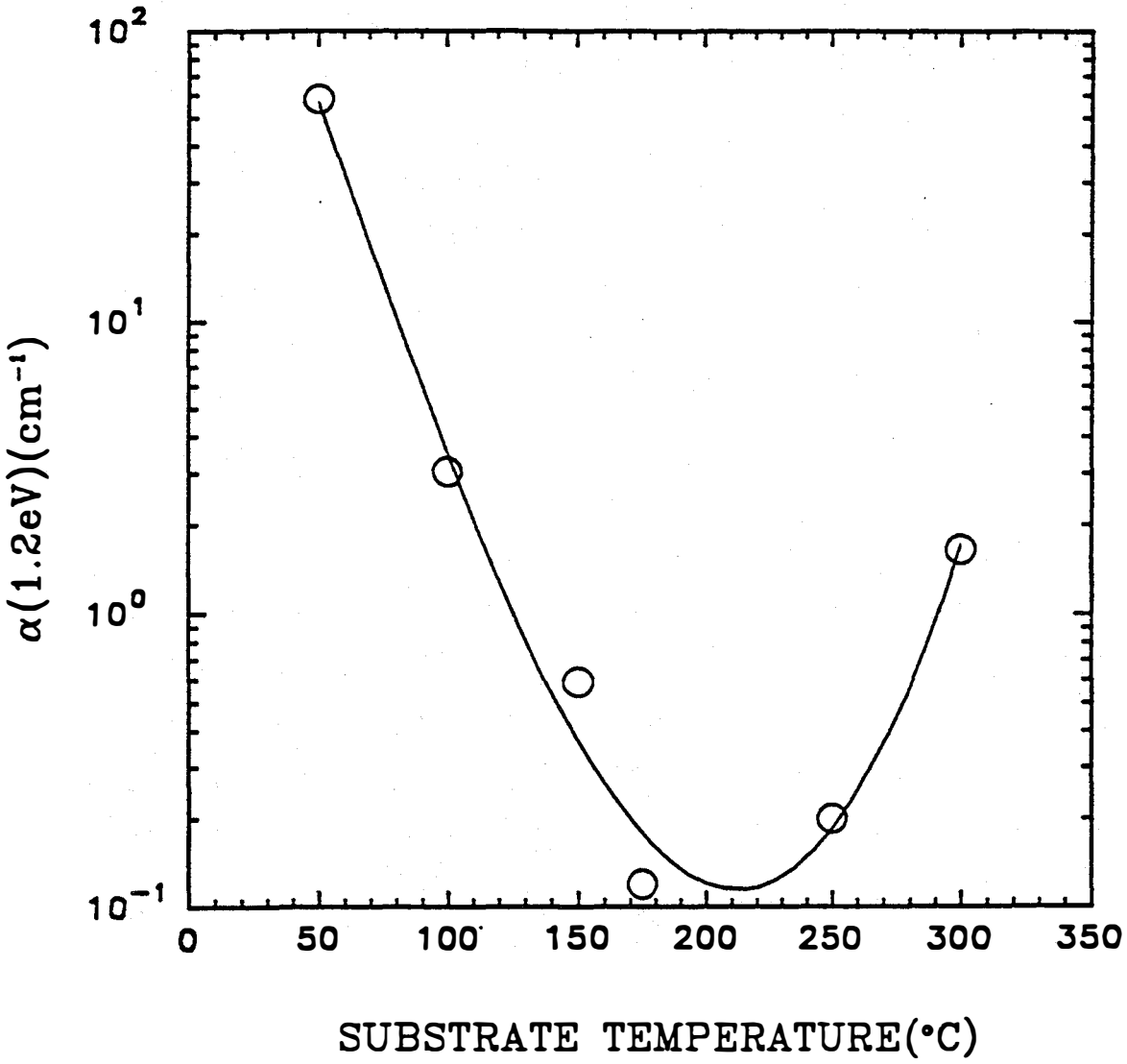

Figure 21 The subgap absorption coefficient, α(1.2eV), as a function of substrate temperature, T_S, for a-$Si_{1-x}C_x$:H films.

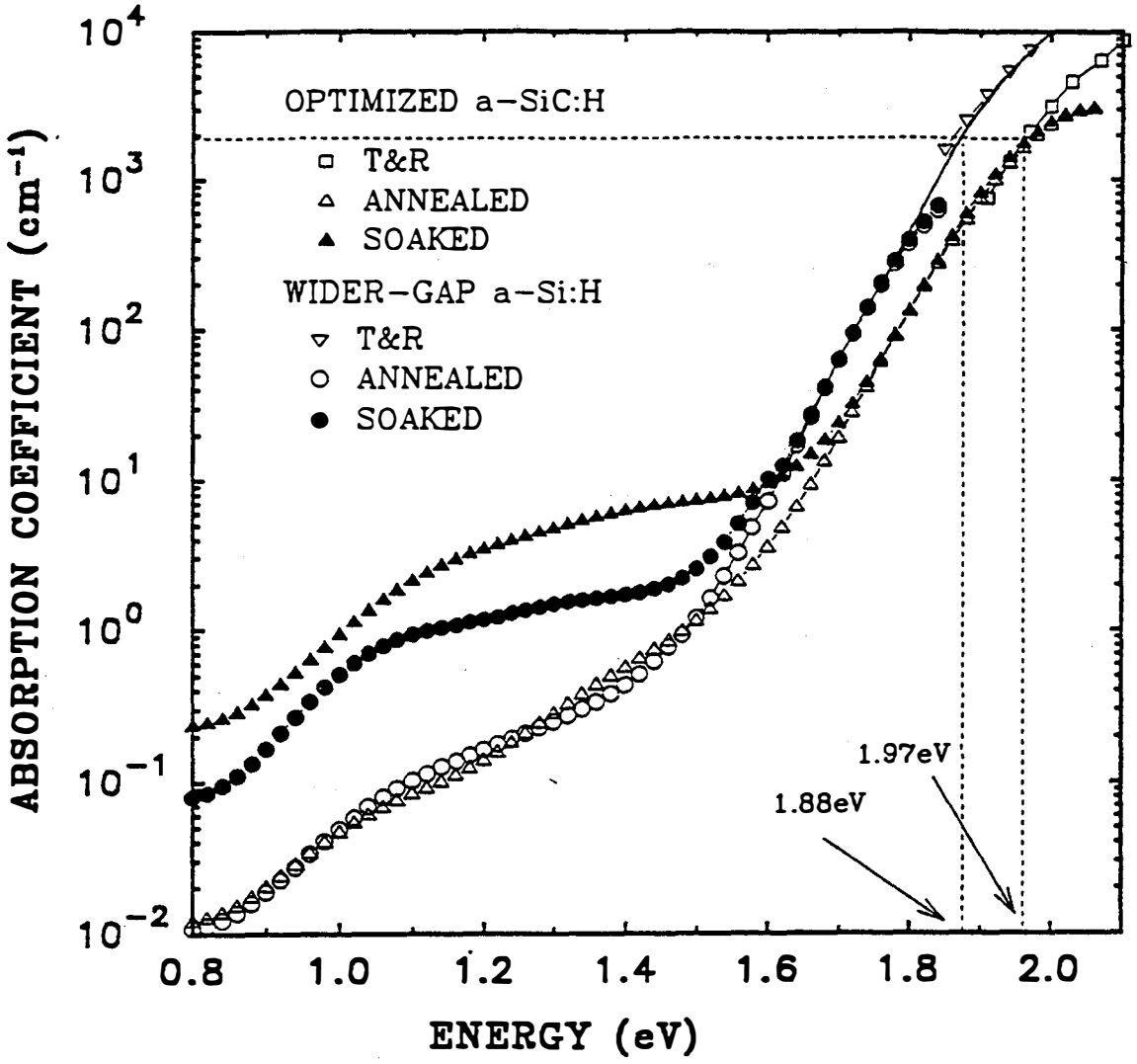

Figure 22 The subgap absorption spectra in the annealed and degraded states for an a-$Si_{1-x}C_x$:H film prepared at T_S=175°C and a wider-gap a-Si:H film prepared at T_S=170°C.

which is significantly higher than hydrogen diluted a-Si:H material, E_{2000}=1.88eV. It is interesting to note here that the subgap absorption, in particular α (1.2eV), is virtually the same for both materials in the annealed state. After degradation, however, the subgap absorption of a-$Si_{1-x}C_x$:H becomes much higher than that of the a-Si:H material. This larger increase in the midgap densities of defects in the a-$Si_{1-x}C_x$:H material is also reflected in the decrease in the a-$Si_{1-x}C_x$:H electron mobility-lifetime products. The mobility-lifetime products of the two materials are shown in Fig. 23 in both the annealed and degraded states. Again, in the annealed state, the mobility-lifetime products for the two materials are virtually the same. After degradation, however, the a-$Si_{1-x}C_x$:H values are much lower than those of the a-Si:H material. Table 3 summarizes the results of the subgap absorption and $\mu\tau$-product measurements of widegap a-$Si_{1-x}C_x$:H and wider-gap a-Si:H. In fact, it can be noted that the gains made in the fundamental properties of a-$Si_{1-x}C_x$:H through H_2-dilution are to a large extent lost in the stabilized degraded state. The significantly larger degradation in the a-$Si_{1-x}C_x$:H materials noted in Table 3 is expected to generate much larger degradation in their solar cells based on the discussions of Secs. 1.1-1.2.

Fig. 24 shows the evolution of the additional Si-H volume fraction averaged over the top ~200Å of a thick a-Si:H and a-SiC:H films, generated during a weak 1 hr filament-generated atomic H-treatment. The Si-H volume fraction is proportional to the concentration of Si-Si bonds that are broken and converted to Si-H bonds. For both a-Si:H and a-SiC:H samples, the substrate was maintained at 250°C during film growth, and the sample was maintained between 240°C and 250°C during the H-exposure process. It is clear that there is little change in the optical response of the a-SiC:H upon H-treatment compared with that of a-Si:H. SIMS shows that the H penetrates the a-$Si_{1-x}C_x$:H, e.g., via the Si-Si bonds or void structure, but once there does not effect a change in bonding. Because the a-$Si_{1-x}C_x$:H already contains ~20-25 at.% H (as opposed to the 8 at.% in the a-Si:H), its network may already be relaxed and further Si-Si bond breaking may not be energetically favorable. In conclusion, unlike a-Si:H, a-SiC:H shows little bonding relaxation upon chemical annealing by filament-generated atomic H. This suggests

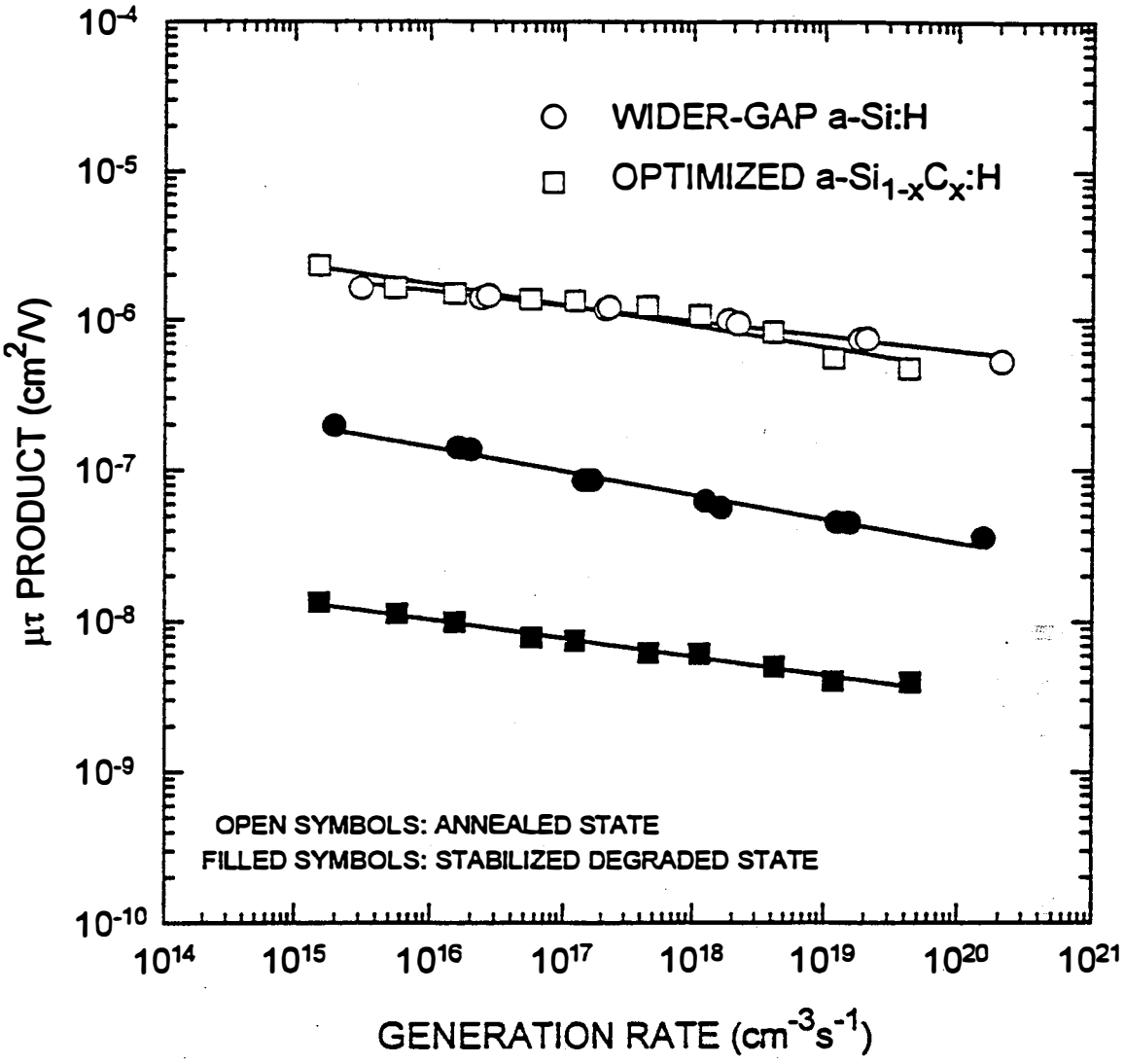

Figure 23 Mobility lifetime products versus generation rate in the annealed and stabilized degraded states for wider-gap a-Si:H and widegap a-$Si_{1-x}C_x$:H the latter optimized versus H_2-dilution and substrate temperature.

Table 3 Comparison of the annealed and degraded properties of wider-gap a-Si:H prepared from H_2-diluted SiH_4 and widegap a-$Si_{1-x}C_x$:H optimized for intrinsic material characteristics with H_2-dilution and substrate temperature.

	a-Si:H, R=10, T_s=200°C		a-$Si_{1-x}C_x$:H; R=20, T_s=175°C	
E_{2000} (eV)	1.85		1.97	
STATE	ANNEALED	DEGRADED	ANNEALED	DEGRADED
α(1.2 eV) a-Si:H (cm^{-1})	0.12	0.6		
α(1.3 eV) a-$Si_{1-x}C_x$:H (cm^{-1})			0.23	3.5
E_u (meV)	46	48	52	52
$\mu\tau$ (cm^2/V) (G=10^{19} $cm^{-3}s^{-1}$)	8×10^{-7}	4.5×10^{-8}	7×10^{-7}	4×10^{-9}

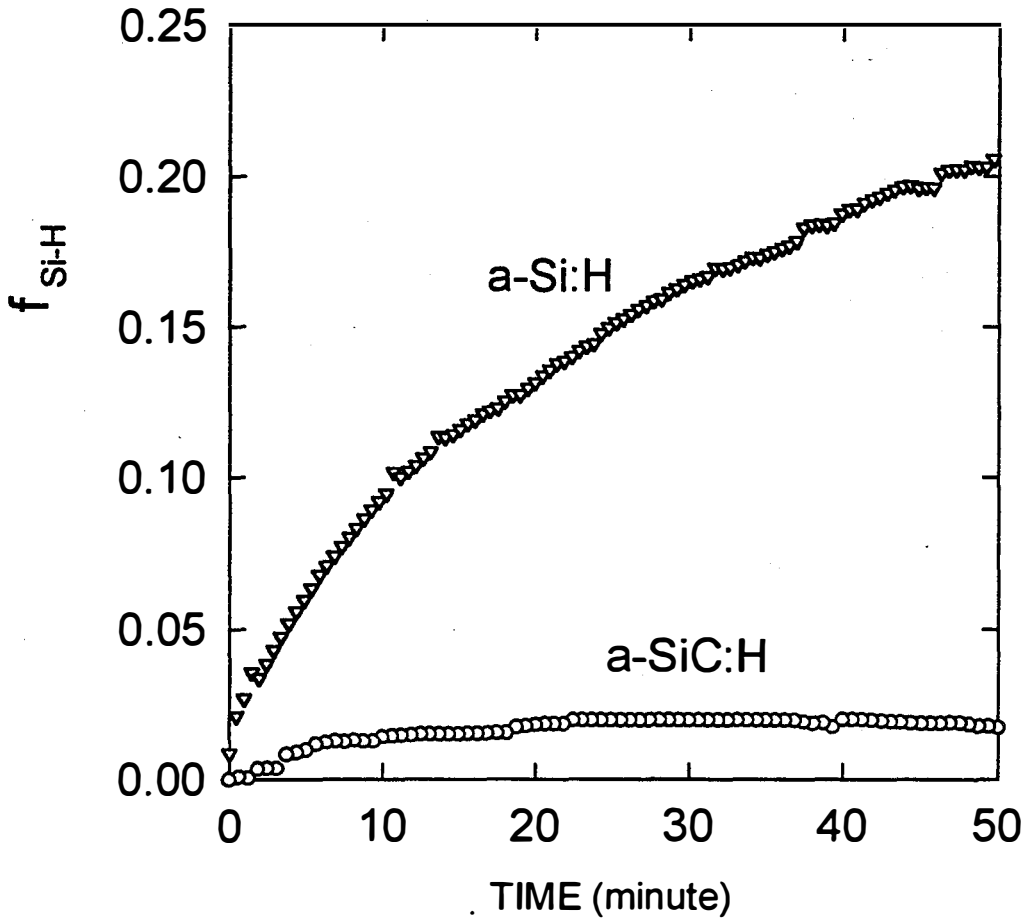

Fig. 24 Evolution of relative Si-H component volume fraction in the top 200Å of a-Si:H and a-SiC:H (R=0) during exposure of opaque films to atomic hydrogen generatred by a heated filament. The substrate was maintained at 250°C during film growth, and the sample was maintained between 240 and 250°C during the H-exposure process.

a fundamental difference in the bonding of the two materials, and the effects of H on the bonding that may provide clues to understanding the differences in stability.

2.2 Widegap a-Si:H Prepared by Microwave PECVD

The advantage of a-$Si_{1-x}C_x$:H over a-Si:H prepared with H_2-diluted SiH_4 has been the ability to attain wider gaps in the optimized material. Our previous studies have shown that optimum H_2-dilution of SiH_4 to make a-Si:H can lead to an optical gap that is 0.1 eV higher than the standard midgap material (with E_{2000} increasing from 1.75 to 1.85 eV). In contrast, a-$Si_{1-x}C_x$:H can be made with optical gaps more than 0.2 eV higher than the standard midgap material (with E_{2000} increasing from 1.75 to 1.97 eV) without a significant increase in the Urbach energy E_u and α (1.2-1.3eV) as shown in Table 3. This difference is shown in the complete optical spectra of Fig. 22, where the E_{2000} gaps are indicated. The C-alloying capability yields more flexibility and also leads to very widegap *p*-layer that can be incorporated readily into the cell. However, unless stability problems can be overcome, we may be forced to retreat to pure a-Si:H *i*-layers and consider novel methods for widening its optical gap further than is possible with conventional H_2-dilution in order to provide materials with E_{2000} >1.9 eV for widegap *i*-layers and *p*-layers.

A promising approach is that being pursued by Professor I. Shimizu at the Tokyo Institute of Technology. His group is alternating growth and atomic H-exposure at low temperatures (~100°C) in order to generate pure a-Si:H of apparently high quality with E_{2000} gaps as high as 2.1 eV. The a-Si:H growth process is standard parallel-plate deposition whereas the H-exposure employs a remote microwave plasma source. In our earlier studies, we have also pursued the chemical annealing approach in producing a more stable wider gap a-Si:H. In our case, we used a tungsten filament heated in low pressure (~5-10 mTorr) H_2 to generate atomic H. However, our technique is more cumbersome since the growth and H-exposure are performed at very different pressures and the chamber must be pumped down once every cycle during the growth process. The major benefits of our approach to date, however, have been related to single atomic H treatments at device interfaces, for example to improve V_{oc} and its stability for solar cells with pure

a-Si:H i-layers. (See Figure 12 and associated discussion of Sec. 1.3.) In this situation the filament approach is advantageous because it is simple, inexpensive, and easy to implement in any parallel plate PECVD reactor. For the alternating monolayer-by-monolayer approach, however, the microwave atomic H source has the advantage of being able to operate at the same pressure as the pure SiH_4 discharge, and is thus more readily automated.

Figure 25 shows the first optical absorption data from transmission and reflection (T&R) measured at Penn State for one of the Tokyo Inst. Technol. samples in which the substrate temperature was held at 100°C and 10 s a-Si:H growth was alternated with 20 s H-exposure. The E_{2000} gap for this material is found to be 2.09 eV, much wider than any a-Si:H materials that can be made by conventional H_2-dilution techniques in the parallel plate PECVD configuration at similar temperature. Fig. 25 shows that this growth system may have the same flexibility as the C-alloy system in its ability to prepare materials with E_{2000} gaps ranging from 1.75 to 2.1 eV. The next step in this research is to obtain possibly better material that has a gap comparable with our optimized a-$Si_{1-x}C_x$:H (E_{2000}~1.95 eV). Then we will (i) measure the sub-bandgap absorption spectra and electronic transport in the material; (ii) determine these properties in the stabilized degraded state; (iii) incorporate the material as a 2000 Å *i*-layer in a solar cell; and (iv) measure the stability of the resulting solar cell for comparison with the data in Table 2. Thus at every step we will assess the material in comparison with our existing data on a-$Si_{1-x}C_x$:H.

2.3 a-$Si_{1-x}C_x$:H in Solar Cells and a Comparison with a-Si:H Cells Prepared with H_2-Dilution

The larger degradation in a-$Si_{1-x}C_x$:H has been confirmed through studies of the stability of p-i-n cells having different a-$Si_{1-x}C_x$:H i-layers including cells with graded interface layers. Cells with 2000Å i-layers deposited at 200°C showed the best initial performance among all the a-$Si_{1-x}C_x$:H absorber p-i-n structures, and their degradation kinetics have been investigated by using AM1 illumination for up to 100 hrs. The initial and stabilized state performances of these a-$Si_{1-x}C_x$:H cells were compared with those of

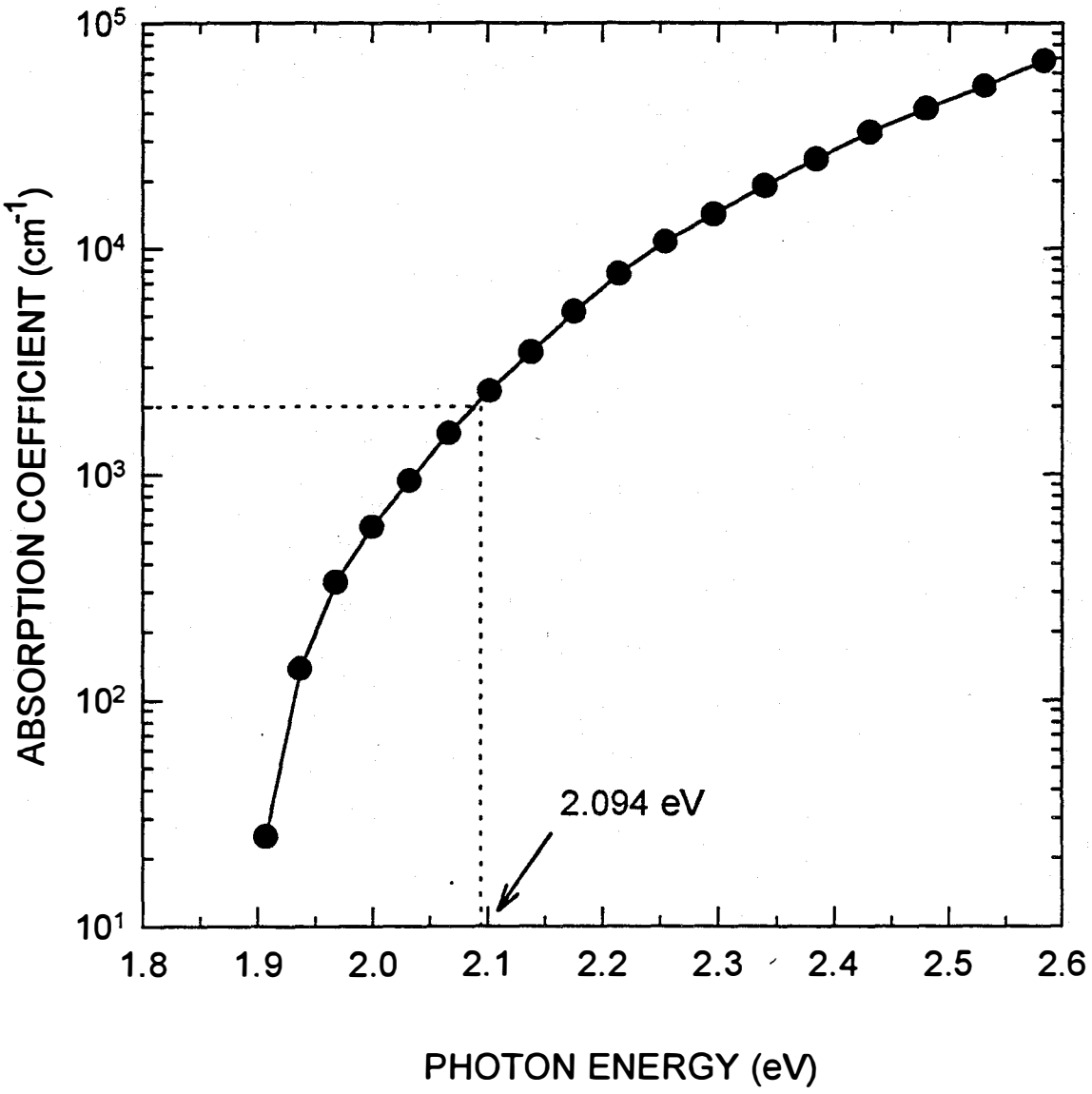

Figure 25 Optical spectra of a-Si:H prepared by chemical annealing at 100°C by the group at Tokyo Institute of Technology. These results were deduced from transmission and reflection measurements. The arrow shows the E_{2000} gap.

p-i-n structures fabricated with wider bandgap absorber a-Si:H i-layers. To highlight the extent of the degradation in the a-$Si_{1-x}C_x$:H cells, in Fig. 26 a comparison is made between such a 2000Å cell and an a-Si:H cell, the latter with a 4000Å thick diluted i-layer also deposited at 200°C. Fig. 26 shows the light I-V curves of these two cells in both the annealed and the degraded states. As expected, the J_{sc} of the a-$Si_{1-x}C_x$:H absorber cell in the annealed state is much lower than that of the a-Si:H cell due to its thickness and to the poor absorption in the bulk. Even though the thicknesses of the intrinsic a-Si:H layers are much higher, the a-$Si_{1-x}C_x$:H absorber cell exhibits a lower FF which can be attributed not only to poor transport in the a-SiC:H bulk but also to a poorer p/i interface. In the annealed state, the V_{oc} (0.92V) of this a-SiC:H absorber cell is higher than that (0.87V) of the corresponding a-Si:H diluted cell. However, the use of intrinsic a-$Si_{1-x}C_x$:H as an absorber layer does not show any advantage in the degraded state, since the a-$Si_{1-x}C_x$:H cell shows a much larger deterioration in V_{oc} than the cell with the diluted a-Si:H i-layer. As a result, values of V_{oc} in the degraded state are the same for the two cells. It is also worth noting that the V_{oc} of the diluted a-Si:H cell saturates after 40 hrs of the AM1 degradation, while the V_{oc} of the a-SiC:H absorber cell does not show any sign of saturation even after 100 hrs of illumination. Furthermore, the FF of the a-SiC:H cell is also much worse, 0.42, compared to that of the diluted a-Si:H cell, 0.61, even though it is only 2000Å thick. In addition, the degradation in J_{sc} of about 20% is much larger than the 5% observed in the a-Si:H cell. In conclusion, p-i-n cells with H_2-diluted i-layers provide much lower and stabilized degradation in all the cell parameters than the cells with a-$Si_{1-x}C_x$:H absorber layers.

Possible improvements in the performance of a-$Si_{1-x}C_x$:H absorber layer solar cells were investigated using different p/i interface layers and intrinsic a-$Si_{1-x}C_x$:H i-layers with different dilution ratios. It is found that, even with extensive optimization of the p/i interfaces and bulk i-layers, no significant improvements were obtained in the stabilities of the a-$Si_{1-x}C_x$:H absorber cells. Results for some of these cells are listed in Table 2. These results are repeated in Table 4 along with new data for a cell that includes a C-graded buffer layer. In all the a-$Si_{1-x}C_x$:H absorber cells listed, the efficiencies degrade by more than 35% after 100 hrs. of AM1 light soaking, compared to degradations of less than 20%

Table 4 Degradation results for four different a-$Si_{1-x}C_x$:H p-i-n solar cells.

Cell Structure	State	Voc (V)	Jsc (mA/cm^2)	FF	Effncy%
CC3 B: 2:3 to 3:2 I: R=5	Annealed AM1,100HRS	0.950 0.854	5.3 2.8	0.50 0.31	2.52 0.74
W4 I: R=5	Annealed AM1,100HRS	0.914 0.868	5.4 4.5	0.61 0.42	3.01 1.64
W5 H: R=2 to 20 I: R=20	Annealed AM1,100HRS	0.882 0.836	5.7 4.9	0.50 0.40	2.51 1.64
W1 I:R=20	Annealed AM1,100HRS	0.880 0.847	7.0 5.2	0.48 0.38	2.96 1.67

B: Buffered Layer $[SiH_4]$:$[CH_4]$=2:3 to 3:2
H: H_2-dilution gradation R=2 increasing to R=20
I: a-SiC:H i-layer
R=$[H_2]/([SiH_4]+[CH_4])$

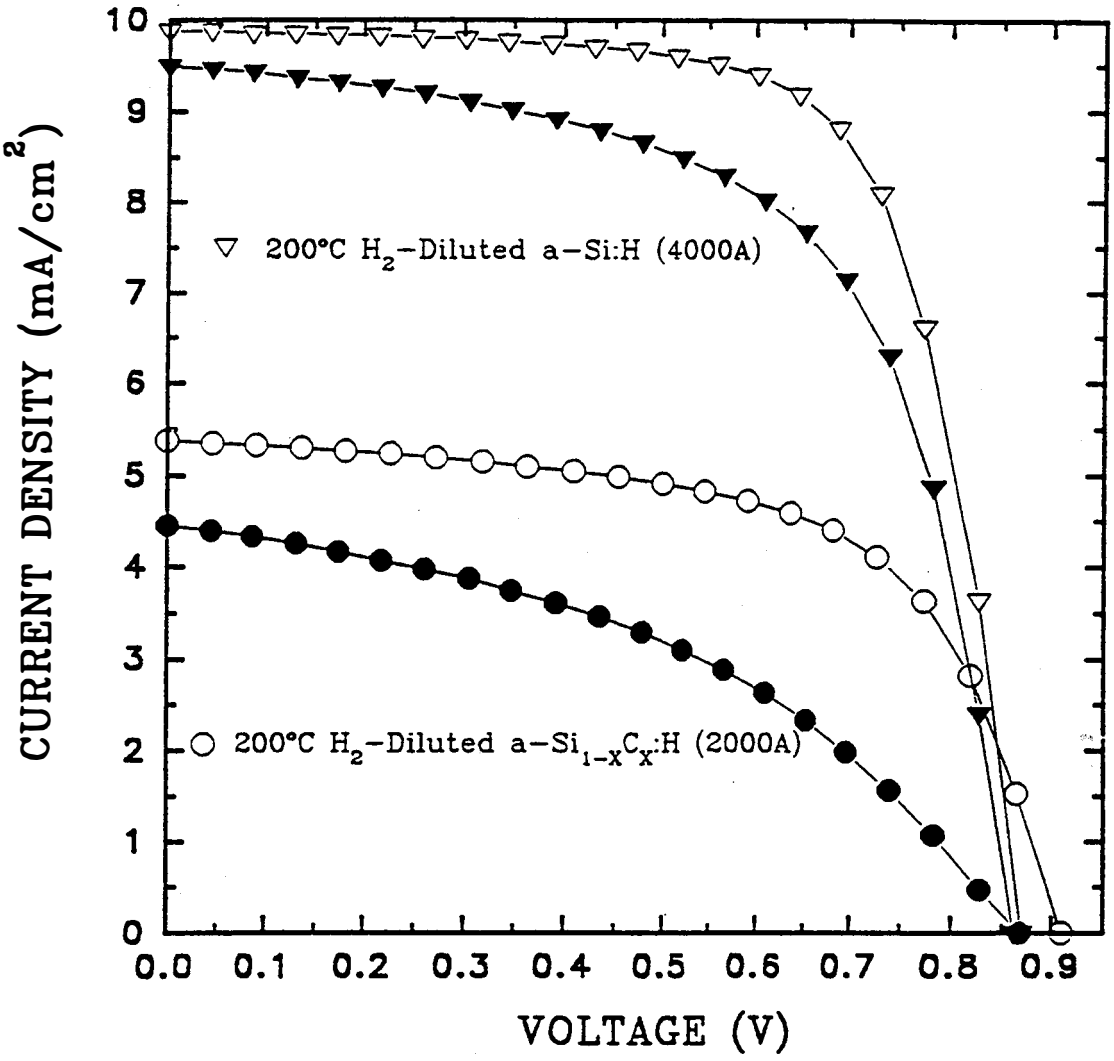

A-Si:H (4000Å, E_{2000}=1.86 eV)
▽ ANNEALED ▼ STABILIZED (100hr, AM1)

V_{OC}	▽ 0.87	▼ 0.86
J_{SC}	▽ 9.9	▼ 9.5
FF	▽ 0.72	▼ 0.61

A-$Si_{1-x}C_x$:H (2000Å, E_{2000}=1.97 eV)
○ ANNEALED ● DEGRADED (100hr, AM1)

V_{OC}	○ 0.92	● 0.87
J_{SC}	○ 5.4	● 4.6
FF	○ 0.61	● 0.48

Figure 26 The light I-V's of an a-Si:H p-i-n cell with a diluted i-layer and an a-$Si_{1-x}C_x$:H p-i-n cell, both in annealed and degraded states.

for much thicker diluted a-Si:H cells. Although the incorporation of a C-graded buffer layer leads to a high annealed state V_{oc} of 0.95V, its degradation becomes even worse. This is attributed to the additional C-incorporation near the p-i interface.

2.4 Wider-Gap a-Si:H Prepared by H_2-Dilution: A Closer Look at Annealed and Degraded States

Because of the instability of intrinsic a-$Si_{1-x}C_x$:H films and solar cells as discussed in Sec. 2.3, emphasis has been placed on obtaining wider bandgap a-Si:H films. The widening of the gap is being achieved by using hydrogen dilution and lower substrate temperatures. These diluted materials and their corresponding solar cells exhibit both higher stability and different degradation kinetics as discussed in Section 1. In order to understand the causes of these differences, studies have been undertaken on characterizing these diluted materials and comparing them with undiluted materials from this as well as from other laboratories.

In these studies the electron mobility-lifetime products and subgap absorption obtained over a wide range of carrier generation rates are used to obtain the information about the gap states and their evolution under light illumination. We find that for different films (with/without hydrogen dilution) not only the magnitude of the electron mobility-lifetime products ($\mu\tau$), but also its functional dependence on carrier generation rates, are quite different. This is illustrated in Fig. 27 which shows the electron mobility-lifetime products as a function of generation rates for diluted and undiluted films prepared at 200°C and 170°C. It is clearly seen that the same recombination kinetics cannot be used to explain both sets of results. It can also be seen that differences at the low generation rates are larger than at the high (AM1) generation rate ranges. This indicates that measurement of the photoconductivity at one intensity, particularly AM1, is not a true reflection of the differences in a-Si:H films. The differences in the functional dependence of $\mu\tau$ on carrier generation rates are significant and are not taken into account when materials are characterized solely by AM1 photoconductivity measurements.

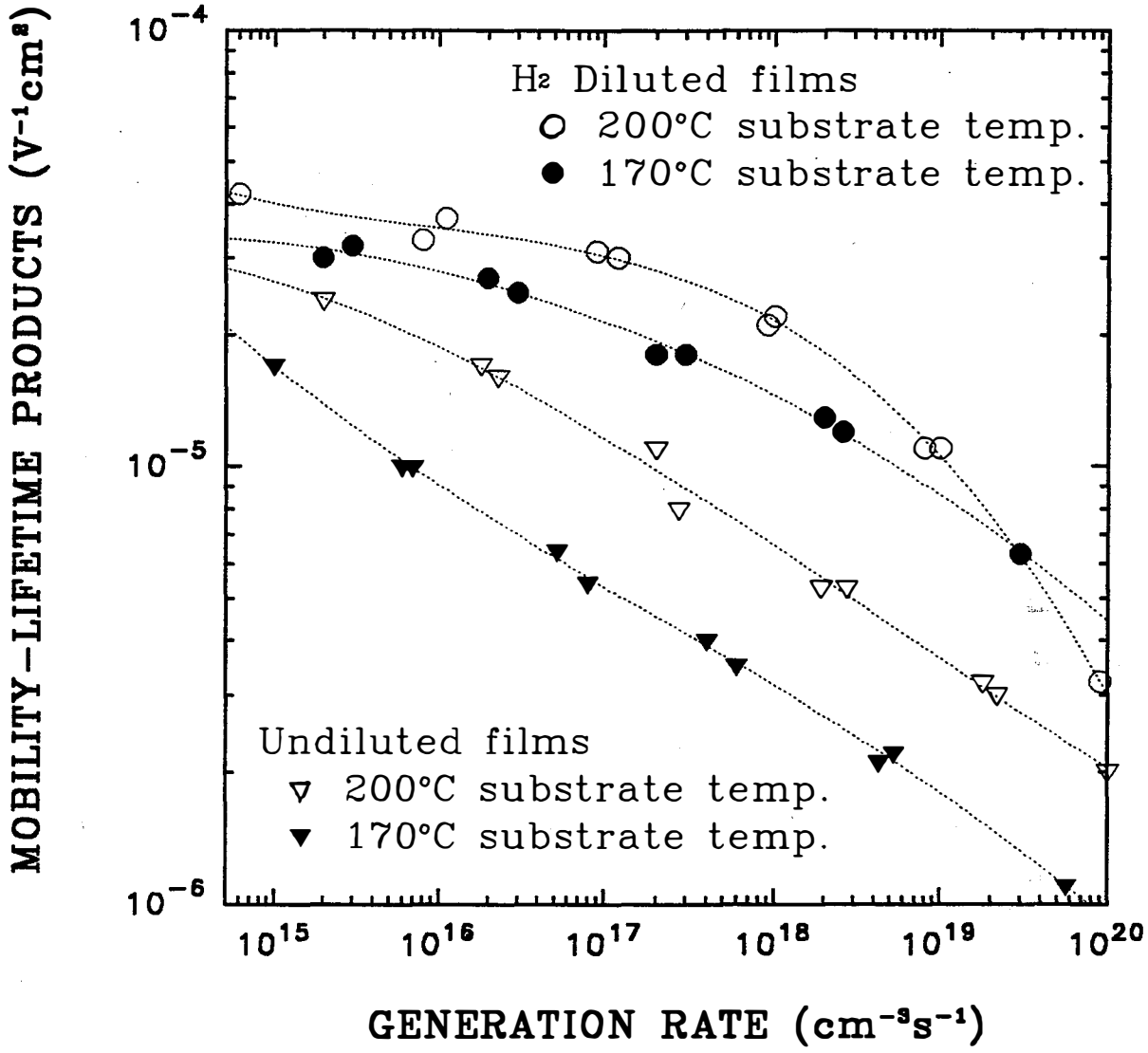

Figure 27 The electron mobility-lifetime products as a function of generation rate for diluted and undiluted films deposited at substrate temperatures of 200°C and 170°C.

The importance of these characteristics is further reinforced by the significant differences that are present in the subgap absorption spectra as measured by Dual Beam Photoconductivity. These differences are illustrated in Fig. 28 which shows the subgap absorption spectra for diluted and undiluted films deposited at a substrate temperature of 200°C which have different optical band gaps. There is a distinct difference in the shape of the subgap region below ~1.5 eV where the undiluted film has a much more pronounced shoulder. This difference indicates problems with some of the basic ideas about a-Si:H:

(1) The values of α (1.2eV) do not directly reflect the densities of neutral dangling bonds, D^o.

(2) Integration of the subgap region below the exponential region cannot be readily related to the densities of midgap states and certainly not by using the same constant for different films.

Such differences in subgap absorption and electron mobility-lifetime products can only be explained by taking charged defect states in the gap into account. We use the Subgap Absorption Model (SAM) and a three-gaussian distribution of gap states (D^+, D^o, D^-) to obtain the "Operational" parameters for both the charged (D^+, D^-) and the neutral (D^o) defect states. The self-consistent analysis being developed and carried out in the EPRI program is being applied to obtain reliable gap state parameters in the different films. Such parameters can be used in the quantitative correlation of these materials with their corresponding solar cells.

Figs. 27 and 28 demonstrate the electron mobility-lifetime products ($\mu\tau$) and the subgap absorption obtained over a wide range of carrier generation rates for different diluted and undiluted materials are quite different in the annealed state. Significant differences in the stability and degradation kinetics of materials prepared with and without hydrogen dilution are also observed. Because light induced steady states in undiluted films cannot be reached within 100 hrs of AM1 illumination, their stability was also evaluated using 10 AM1 illumination.

In these studies, the films were first annealed at 170°C in a N_2 environment for 4 hrs then were soaked under 10 AM1 illumination. The temperature of the films under illumination was kept at about 50°C. After about 50 hrs, the diluted films reached their

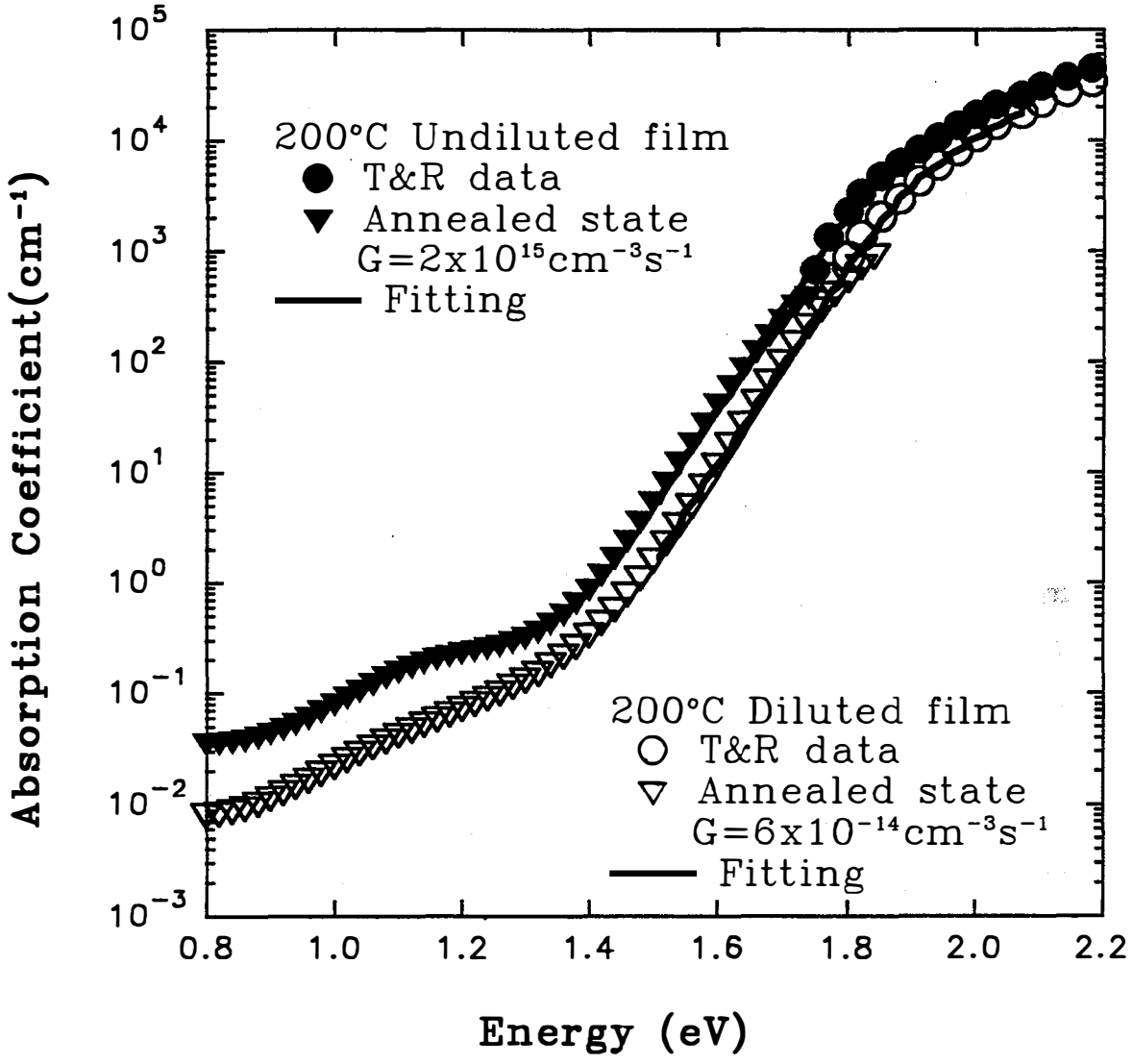

Figure 28 The subgap absorption spectra of a diluted and an undiluted film deposited at a substrate temperature of 200°C measured by Dual Beam Photoconductivity (DBP).

degraded steady states, and the undiluted films reached theirs after about 80 hrs. The electron $\mu\tau$ products and subgap absorption obtained over a wide range of carrier generation rates were used to obtain the information about the gap states in these degraded steady states. It is found that both the magnitude of the electron $\mu\tau$ products and their functional dependence on carrier generation rates are different for diluted and undiluted films. This is illustrated in Fig. 29 where the electron $\mu\tau$ products are shown as a function of carrier generation rates for diluted and undiluted films deposited at 200°C and 170°C. It can be seen that $\mu\tau$ products of the diluted films deposited at different substrate temperatures have a similar functional dependence on the carrier generation rate but different values. In the steady state, the diluted film at 200°C has the higher $\mu\tau$ product (i.e., photoconductivity) than that at 170°C. Both the magnitude and the functional dependence of the $\mu\tau$ products for the undiluted films are different from those for the diluted films. Again the values for the film deposited at 170°C is much smaller than that deposited at 200°C but with a similar dependence on the generation rate. A comparison of the $\mu\tau$ products - particularly at high generation rates - for films deposited at the same substrate temperature indicate that the diluted films are much more stable. In addition, the differences in the $\mu\tau$ characteristics imply that not only are the densities of light induced defects lower but also that their distributions (i.e., nature) are also different.

The differences between the diluted and undiluted films in the steady states were also investigated by studying their subgap absorption spectra by Dual Beam Photoconductivity. Fig. 30 shows the subgap absorption spectra for both the diluted and undiluted films deposited at a substrate temperature of 200°C obtained with generation rates of 6×10^{14} and 2×10^{15} cm^{-3}, respectively. A wider bandgap for the diluted film (E_{2000}=1.85eV versus 1.79eV for the undiluted film) can be seen as well, as a lower absorption coefficient in the region of $E < 1.5$eV arising from a somewhat lower density of light induced defects. In Fig. 30, the absolute values of subgap absorption and the shape of the spectra are both slightly different for the diluted and undiluted films. If these differences are considered solely in terms of the densities neutral dangling bonds, D^o, they cannot explain the much larger differences in the $\mu\tau$ results such as shown in Fig. 29. To understand these differences, the Subgap Absorption Model and a three-gaussian

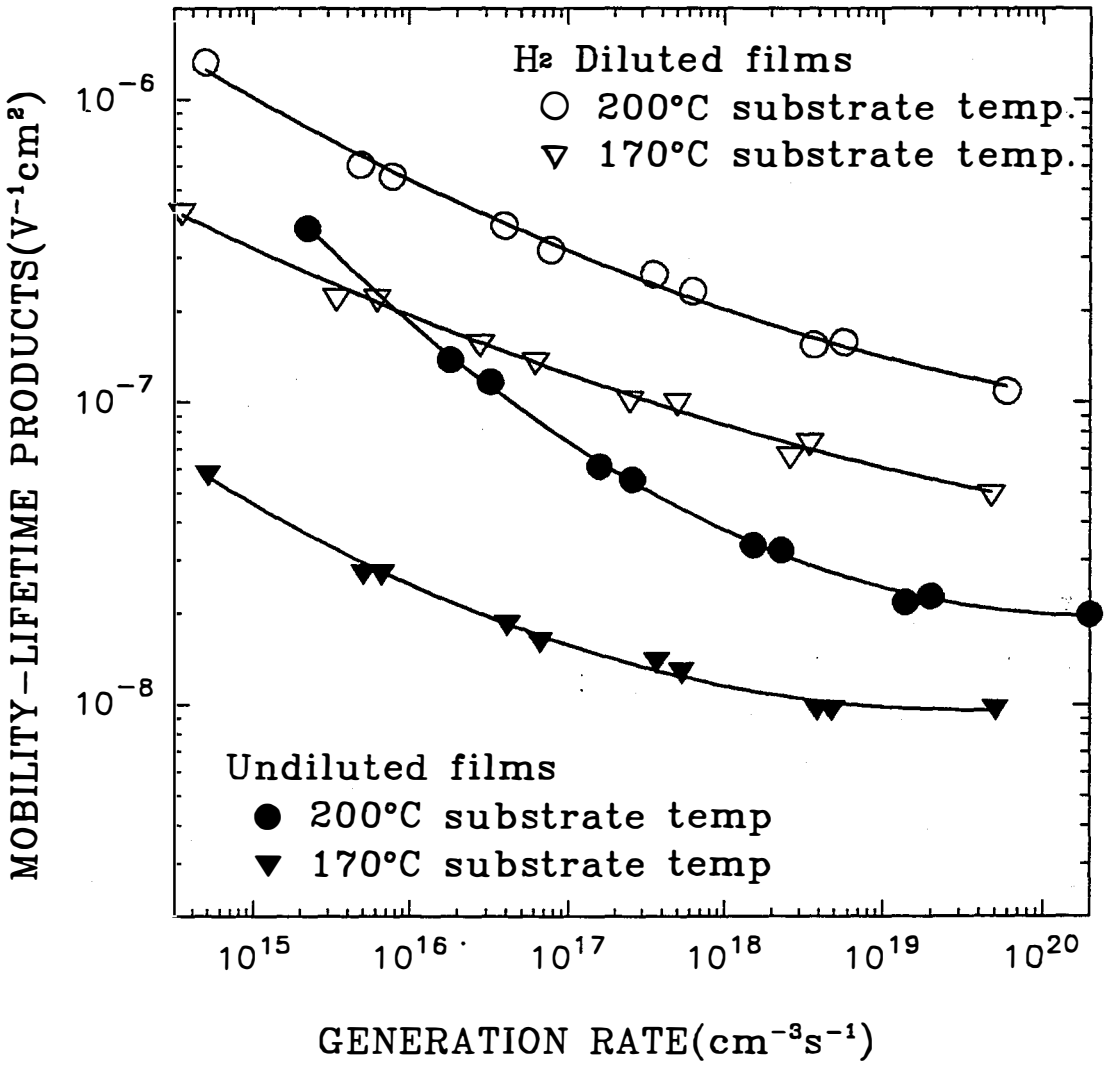

Figure 29 The electron mobility-lifetime products ($\mu\tau$) as a function of carrier generation rate in the degraded steady states for diluted and undiluted films deposited at 200°C and 170°C.

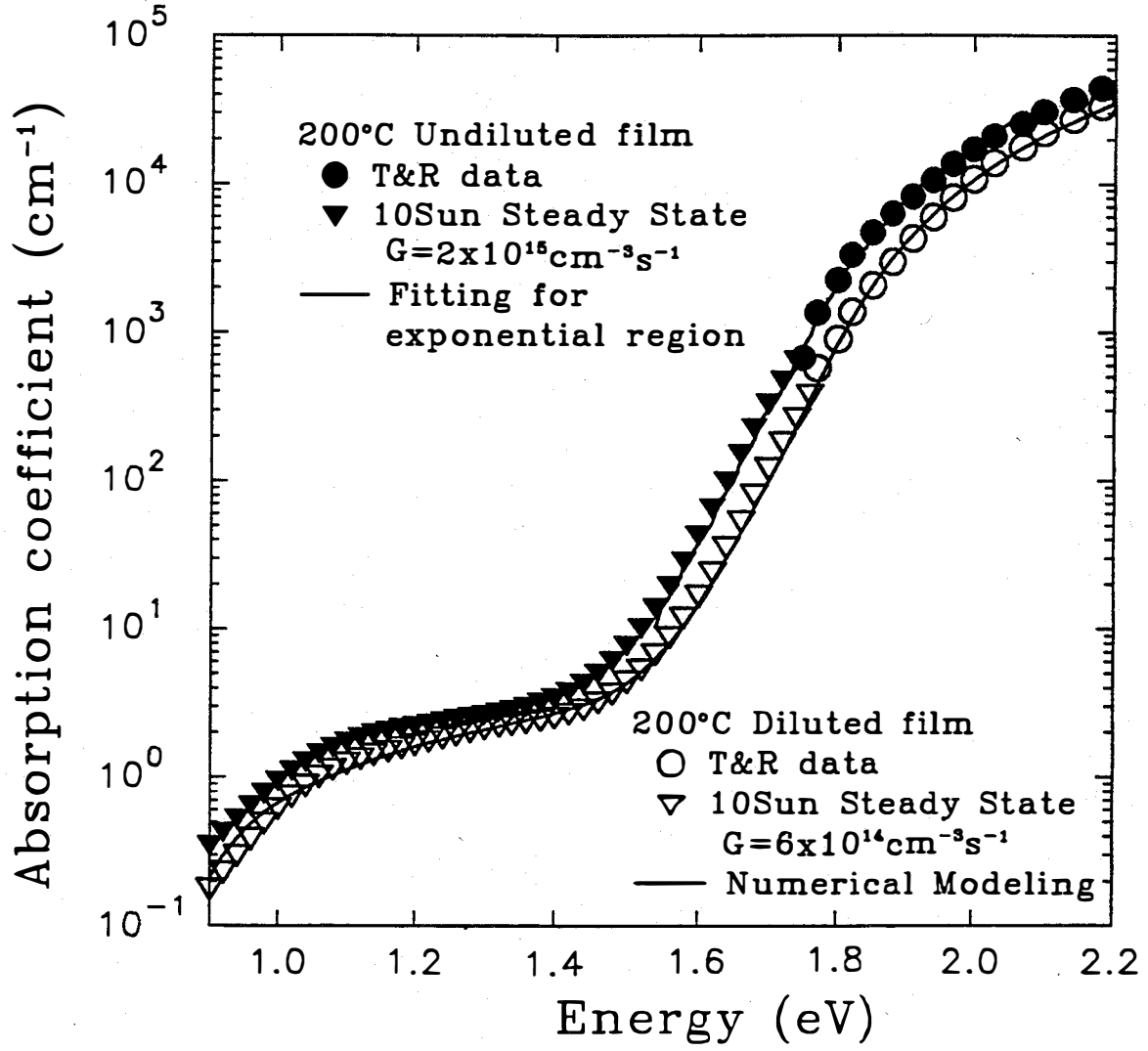

Figure 30 Subgap absorption spectra measured by DBP in the degraded steady states for the diluted and undiluted films deposited at 200°C.

distribution of gap states (D^+, D^o, D^-) are used to fit the experimental results self-consistently using both $\mu\tau$ as well as the differences in DBP obtained with different generation rates. The fitting of the subgap absorption spectrum of the 200°C diluted film is shown in Fig. 30 as the solid line which was obtained by using the gap state densities, $D^+ = 9 \times 10^{16}$ cm^{-3}, $D^o = 2 \times 10^{17}$cm^{-3} and $D^- = 9 \times 10^{16}$cm^{-3}. We can see that, in addition to the increase in neutral dangling bonds, D^o, the charged defects also increase with light illumination. Similar good fits using these same parameters were also obtained to the characteristics of Schottky barrier cell structures. Numerical modeling is now being carried out on the undiluted films in order to establish the differences, not only in the annealed states, but also in the degraded states.

3. Solar Cells Optimized for *p*- and *i*-Layer Performance

3.1 Correlation between p-i-n Cell Performance and Deposition Conditions: H_2-Dilution, Substrate Temperature, Gas Pressure

During this phase we investigated the dependence on deposition conditions of the annealed state parameters, V_{oc}, J_{sc}, and FF, of a-Si:H *p-i-n* cells. The parameter space explored includes *i*-layer deposition temperatures between 130°C and 240°C, with and without H_2-dilution, and cells with and without atomic H treatment at the *p/i* interface. The main goal of this study was to identify the roles of *i*-layers and *p/i* interface treatments in determining the cell parameters, with an emphasis on V_{oc}.

A series of *p-i-n* cells was deposited on specular SnO_2 substrates in our multi-chamber system. The *p*- and *n*-layers are deposited under identical conditions for all cells. The *p*-layers are deposited at 200°C using a gas mixture of 10 sccm SiH_4, 10 sccm CH_4, and 5 sccm of 2% TMB in He with thicknesses of 200-250 Å. Highly conductive microcrystalline *n*-layers are deposited with a gas mixture of 1.4 sccm SiH_4, 0.6 sccm of 1% PH_3 in SiH_4, and 100 sccm H_2 with thicknesses of 300-350 Å. The *i*-layer thicknesses were controlled for cells at each deposition temperature for a valid comparison of J_{sc} and

FF. However, relatively thin H_2-diluted *i*-layers (0.2 μm) were used in an attempt to raise FF and to improve V_{oc} stability of the 130°C cell. The H_2-dilution ratio for all cells with H_2-diluted *i*-layers was R=[H_2]/[SiH_4]=10 except for the 130°C cell, in which case R=5 was used. (Although we generally do not encounter adhesion problems for cells with H_2-diluted *i*-layers deposited on SnO_2 substrates at low temperatures, we have not succeeded in depositing such films on glass substrates at R=10 using substrate temperatures lower than 170°C.) The undiluted a-Si:H layers were deposited using 15 sccm pure SiH_4. Table 5 lists the annealed state parameters for these cells. It is seen from Table 5 that cells with H_2-diluted *i*-layers show better V_{oc} and FF than the corresponding cells with undiluted *i*-layers at all temperatures investigated. The improvement in V_{oc} and FF could be due to (i) reduced bulk defect densities in diluted *i*-layers and/or (ii) increased optical and mobility gaps with H_2-dilution.

To address the critical role of the *p/i* interface, atomic H treatments of this interface were performed for cells both with and without H_2-diluted *i*-layers. The treatment was carried out according to the following procedure:

1. A *p*-layer was deposited onto the SnO_2 substrate.
2. An *i*-layer of 100-150 Å was subsequently grown on top of the *p*-layer.
3. A hot tungsten filament was used to generate thermal atomic H to penetrate the 100-150 Å *i*-layer and passivate the *p/i* interface. The filament parameters were established based on real time spectroscopic ellipsometry (RTSE) studies. The power applied to the filament was about 12 W with an exposure time of 1 hr. Higher powers resulted in etching of the layers. Exposure times longer than 1 hr have been tried but did not result in any significant differences.
4. The remaining *i*-and *n*-layers were subsequently grown.

The 100-150 Å intrinsic layer was deposited before the treatment because we wanted to treat the *p/i* interface only after it is formed. The 100-150 Å *i*-layer thickness range was chosen because an earlier SIMS study performed with a deuterium treatment demonstrated that atomic H generated by a hot tungsten filament under the corresponding

Table 5 Comparison of the annealed state cell parameters for a succession of midgap and wider-gap a-Si:H *p-i-n* solar cells prepared in the multi-chamber system at different substrate temperatures with and without *i*-layer H_2-dilution. The thickness of the *i*-layer in each cell is also indicated for J_{sc} and FF evaluation.

T_s (°C)	*i*-LAYER	V_{oc} (V)	J_{sc} (mA/cm^2)	FF	Eff (%)
130	undiluted (0.34 μm)	0.854	8.8	0.50	3.76
	H_2-diluted (0.20 μm)	0.886	9.3	0.61	5.03
170	undiluted (0.62 μm)	0.857	9.6	0.55	4.52
	H_2-diluted (0.65 μm)	0.870	10.2	0.56	4.97
200	undiluted (0.48 μm)	0.835	11.7	0.66	6.45
	H_2-diluted (0.41 μm)	0.861	10.0	0.68	5.85
240	undiluted (0.51 μm)	0.796	11.1	0.60	5.30

conditions would be able to penetrate effectively through the *i*-layer to the *p/i* interface. This results in a widening the optical bandgap near the interface and passivating defects without damaging the *p*-layer as may occur in a direct plasma process.

Table 6 lists the annealed state cell parameters for cells with and without atomic H treatment at the *p/i* interface. As seen in Table 6, the interface treatment also improves V_{oc} and improves or maintains the FF for all cells regardless their *i*-layer deposition conditions (*i.e.*, with or without H_2-dilution).

The results above show that the V_{oc} increase for a given increase in optical gap is greater for cells with H_2-diluted *i*-layers in comparison with cells with undiluted *i*-layers, as indicated in Fig. 31. For cells with H_2-diluted *i*-layers, a gain of ~10 meV in the optical gap corresponds to an ~30mV increase in the open-circuit voltage, whereas for cells with undiluted *i*-layers, a gain of ~80meV in the optical gap contributes to only ~60mV in the open-circuit voltage. In this study, the optical gap is derived by extrapolating the linear behavior in $(\varepsilon_2)^{1/2}$ vs. photon energy to zero in the region of the absorption onset (*i.e.*, via the Cody method). The smaller increase in V_{oc} for cells with undiluted *i*-layers at larger optical gaps could be due to a concurrent increase in defect densities at the p/i interface which, among other effects, limits V_{oc} in spite of the optical gap increase in the *i*-layers. These results are currently being studied by computer modeling in order to further understand the details.

We also studied the effect of total gas pressure in the preparation of the H_2-diluted i-layer on the annealed-state V_{oc} improvement. Fig. 32 shows V_{oc} values for a set of five p-i-n cells prepared on specular SnO_2 using i-layer H_2-dilution ratios of R=5 and 10, plotted as a function of total gas pressure. It is interesting to note that at the lowest pressure of 0.2 Torr, H_2-dilution does not lead to an increase in V_{oc} over the undiluted i-layers. At the highest pressure of 0.9 Torr, however the increase in V_{oc} is the largest, 0.08eV. There are two possible origins of the improvement in V_{oc} with pressure. First, at low pressure ionic H from H_2-dilution may generate more damage at the *p/i* interface or in the bulk i-layer as it is prepared. This effect would be ameliorated at higher pressure due to the reduced mean free path of ionic species. Alternatively, the higher pressures lead to a more confined plasma which may result in reduced contamination nearest the *p/i* interface that arises from

Table 6 Comparison of the annealed state cell parameters for a succession of midgap and wider-gap a-Si:H *p-i-n* solar cells prepared in the multi-chamber system at 200°C with and without *i*-layer H_2-dilution and atomic H treatment at the *p/i* interface. The thicknesses of the *i*-layers are 0.46-0.48 μm for all four cells.

H_2-DILUTION	H-TREATMENT	V_{oc} (V)	J_{sc} (mA/cm^2)	FF	Eff. (%)
w/o	w/o	0.835	11.7	0.66	6.45
w/o	w	0.859	10.8	0.69	6.40
w	w/o	0.861	10.0	0.68	5.85
w	w	0.884	9.5	0.68	5.71

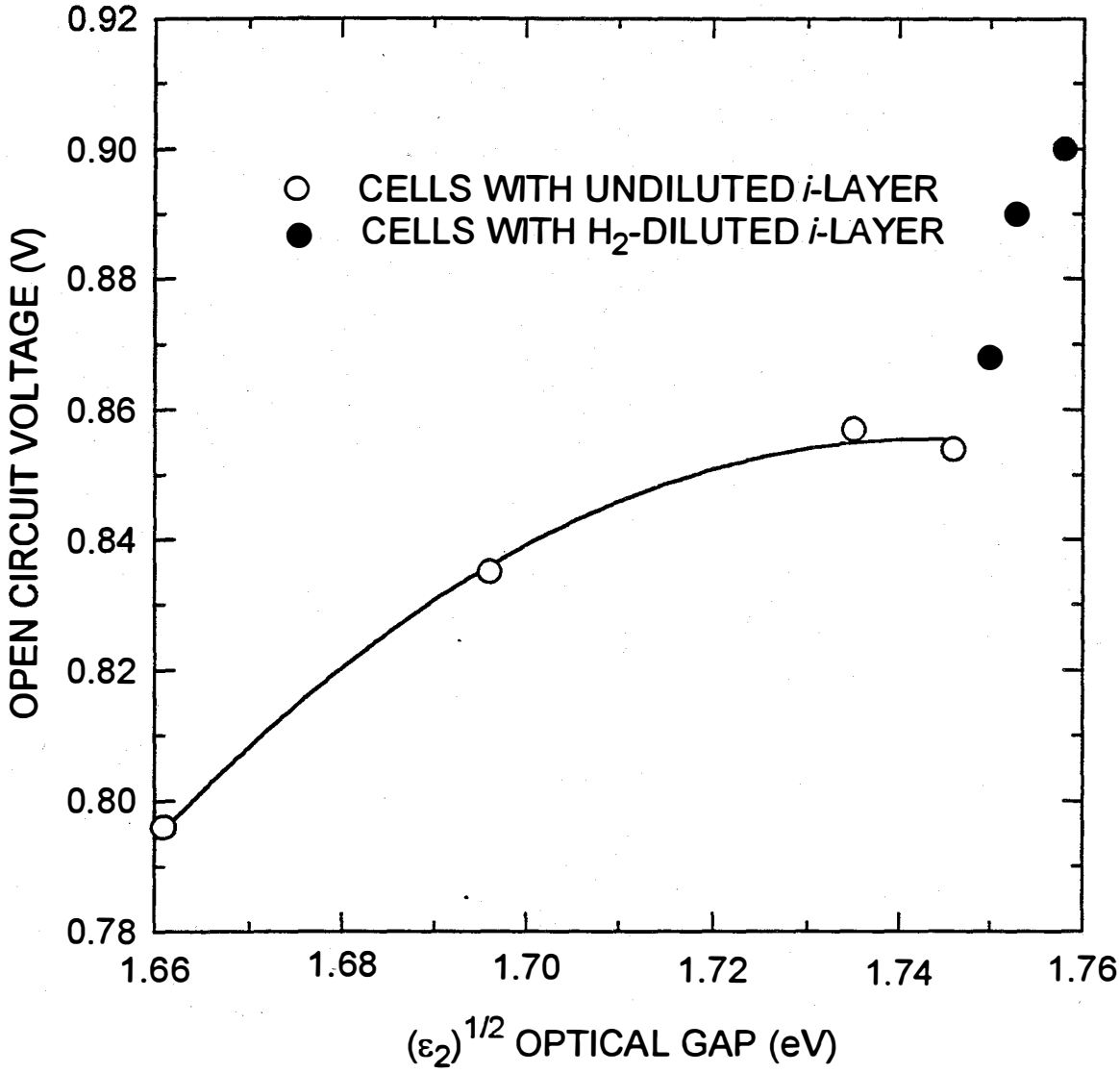

Figure 31 Open-circuit voltage as a function of the *i*-layer optical bandgap obtained using the $(\varepsilon_2)^{1/2}$ extrapolation method of Cody for two sets of *p-i-n* solar cells, one with H_2-diluted *i*-layers and the other with undiluted *i*-layers. These results show that cells with H_2-diluted *i*-layers exhibit higher open-circuit voltages.

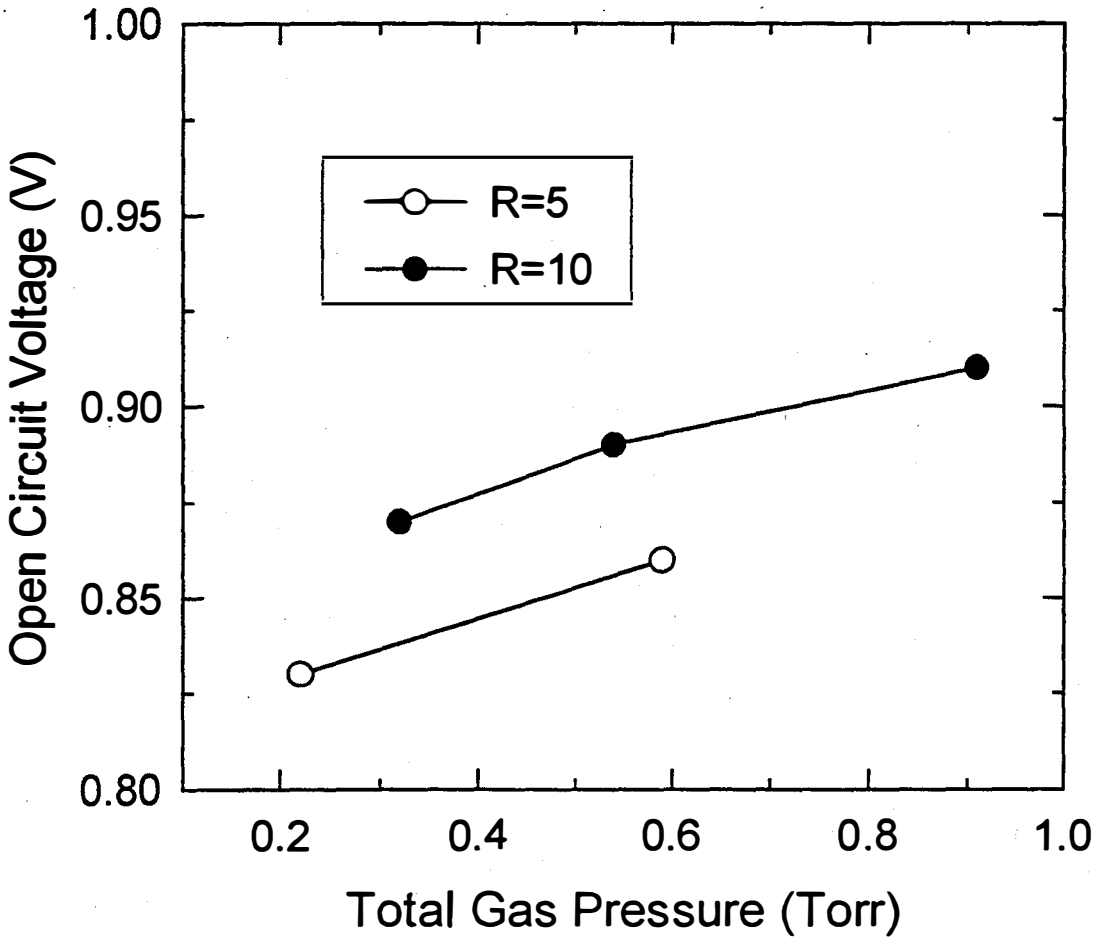

Figure 32 Open circuit voltage as a function of total i-layer gas pressure using two different H_2-dilution ratios of R=5 and 10.

wall-effects. Further studies of the stability of the high-pressure H_2-diluted cells with V_{oc}=0.91V are planned. In addition, the effect of deposition system will be considered (single- vs. multi-chamber).

3.2 Baseline a-Si:H p-i-n Cells from Single Chamber System

We have continued our attempts to improve midgap baseline *p-i-n* cells prepared in the single chamber system used in conjunction with our RTSE studies. This baseline data is used for three purposes. First we seek to better understand the processing-property relationships for standard midgap cells, especially with respect to the role of the interfaces at the top junction. Second, the baseline cell performance is used for comparison with the performance of midgap and widegap cells incorporating novel *i*-layers or *p*-layers in order to assess the new approaches. Third, we need to ensure that the solar cells from the single-chamber system with RTSE monitoring are comparable with similarly-prepared cells from the multi-chamber system. Recently, we have standardized to glass substrates coated with three different TCO materials. These substrates have been supplied by Solarex and include specular and textured SnO_2 and specular ZnO. The motive here is to attempt to distinguish the processing effects on fill-factor and open-circuit voltage that are related to the TCO/*p* interface (which would be specific to the TCO) from those related to the *p/i* interface (which would be independent of the TCO).

Table 7 includes the evolution of the performance parameters for cells with intended ~5000 Å thick *i*-layers on textured SnO_2, starting with our first cell obtained near the start of the Phase I program, and ending with the baseline cell. The increase in fill-factor between the cells of the first two rows was attributed to a reduction in a high B-content layer right at the *p/i* interface. It is possible, particularly at high temperatures (250°C), that B at the *p/i* interface diffuses into the bulk layer, which leads to the FF degradation. The reduction in the interface layer appears to have occurred as a result of improvements in our gas shutdown procedure; namely, the *p*-layer gas and plasma were shutdown simultaneously in order to minimize the effects of diborane CVD. The absence of a similar improvement in V_{oc} between these two runs is not fully understood, however.

Table 7 Comparison of annealed state cell parameters for a succession of a-Si:H *p-i-n* solar cells prepared in the single chamber system on textured SnO_2, showing the improvements over time that have occurred with differences in processing procedure. The cells had intended ~0.5 μm thick *i*-layers from pure SiH_4 and were monitored with real time spectroscopic ellipsometry. These results provide a running baseline for development of new processes and materials to be incorporated into widegap cells based on insights from RTSE. The last entry shows the results for a cell prepared on textured TCO with a H_2-diluted layer.

i-LAYER T_s (°C), R	*p*-GAS	J_{sc} (mA/cm^2)	V_{oc} (V)	FF	Eff. (%)
250 R=0	B_2H_6	12.5	0.78	0.53	5.2
250 R=0	B_2H_6	13.7	0.74	0.65	6.6
200 R=0	B_2H_6	12.9	0.83	0.71	7.6
200 R=0	TMB	15.1	0.84	0.66	8.4
200 R=10	TMB	11.9	0.86	0.60	6.1

In particular, the effect of a high B-doped layer at the *p/i* interface on the V_{oc} is unclear at this time. The improvement in reducing the substrate temperature from 250°C to 200°C (between the second and third rows in Table 7) appears to result from a further reduction in the *p/i* interface layer. This is expected to improve the fill-factor even further since diffusion into the *i*-layer may be reduced at the lower temperature. Because the thicknesses of the *i*-layers for the cells of rows two and three in Table 7 are very close, the higher optical gap at the lower substrate temperature accounts for a reduction in the J_{sc}. The fourth row shows results for a cell that incorporates TMB as a dopant gas. Although RTSE results presented in Phase I and discussed in greater detail below suggest that the *p/i* interface contamination is reduced with the use of TMB, the fill-factor actually decreases. At present it is not known why this occurs. Further attempts at process improvement are ongoing in particular, focusing on contamination of the i-layer by residual dopants within the chamber. Such attempts are necessary since run-to-run variations in FF have been observed which appear to depend on deposition history. It is notable that the V_{oc} and FF for the fourth entry of Table 7, prepared by single-chamber deposition without H_2-dilution of the i-layer are identical to those shown in the first entry of Table 6, prepared similarly but by multi-chamber deposition. The last entry of Table 7 shows the effect of H_2-dilution of the i-layer on the p-i-n cells prepared by single-chamber deposition. In this case, the increase in V_{oc} is identical to that obtained by multi-chamber deposition. However, there is reduction in FF that appears to be attributable to a reduction in bulk layer quality due to dopant contamination associated with single-chamber deposition, as noted above.

Figure 33 shows the initial state light I-V characteristics of the midgap a-Si:H *p-i-n* solar cell on textured SnO_2, given in the fourth row of Table 7 (circles). In this case, cells co-deposited on three different TCO's are compared, the textured SnO_2 result from Table 5, along with specular SnO_2 (squares) and ZnO (triangles). For this deposition the dopant gas is TMB with a gas flow ratio of $D=[TMB]/\{[SiH_4]+[CH_4]\}=0.02/10$ (in sccm). The most interesting observation is that the open-circuit voltage does not depend on the TCO material. The fill-factor is slightly lower for the specular substrates than for the textured

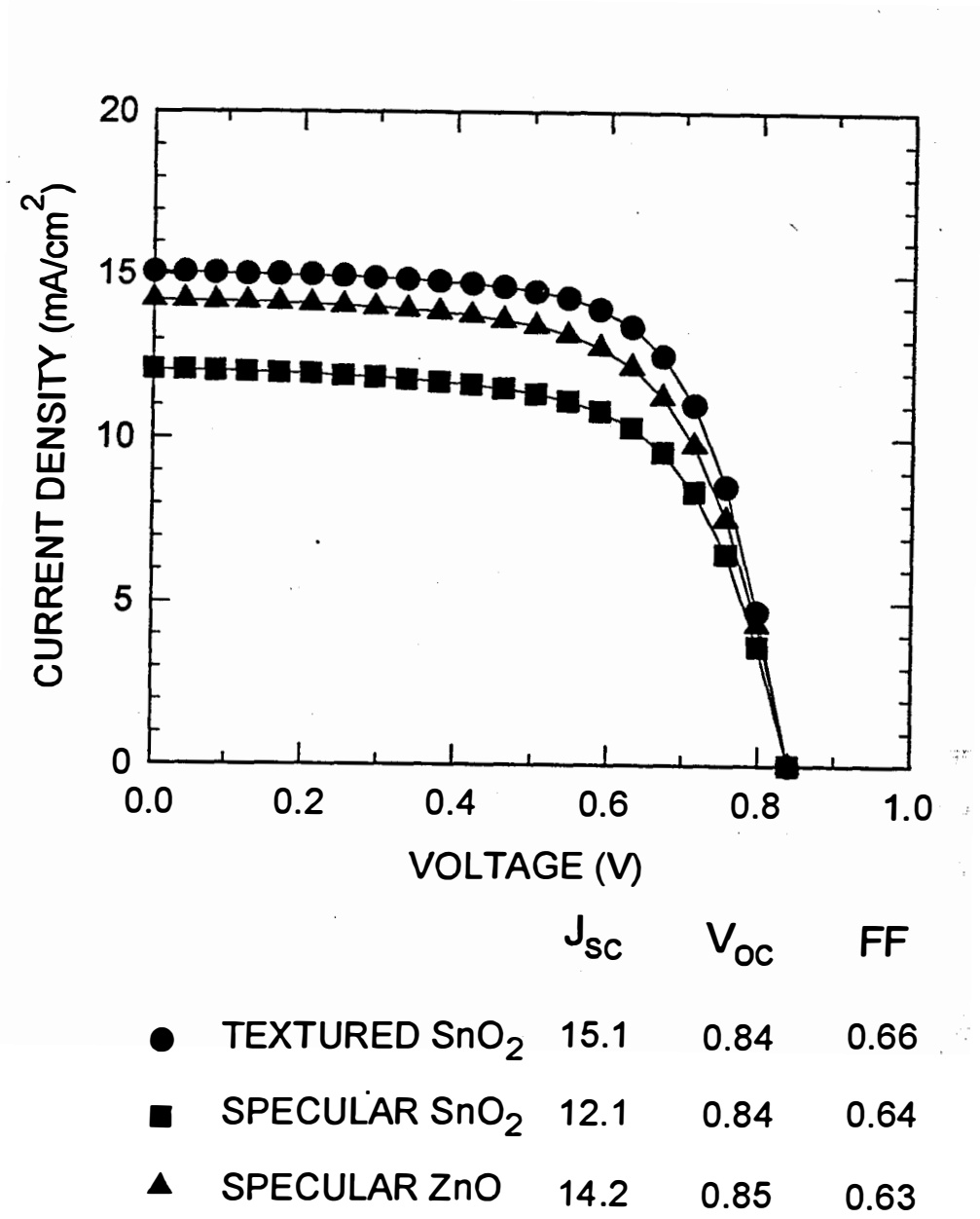

Figure 33 Annealed state light I-V characteristic of the midgap a-Si:H *p-i-n* solar cell on textured SnO_2, given in the fourth row of Table 7 (circles). In this case, cells co-deposited on three different TCO's are compared; the result from Table 7 for textured SnO_2, along with specular SnO_2 (squares) and ZnO (triangles) are included. For this cell deposition the dopant gas is TMB with a doping gas flow ratio of D= [TMB]/{[SiH_4]+[CH_4]}=0.02/10 (in sccm).

one. It is also interesting that the specular ZnO exhibits improved current-collection performance over the specular SnO_2.

3.3 Customized p-i-n Solar Cells

In Sec. 3.1 we demonstrated the beneficial effects of H_2-dilution and atomic hydrogen treatments on the open circuit voltage, V_{oc}, of a-Si:H p-i-n solar cells. We presented data showing an increase in the open circuit voltage when comparing p-i-n cells deposited at 200°C substrate temperature having H_2-diluted i-layers with those having i-layers deposited using pure silane. As shown extensively in Sec. 1, the stability of V_{oc} against light soaking is also drastically improved when a H_2-diluted i-layer is incorporated in the solar cells. In Secs. 1 and 3.1, we showed the effects on V_{oc} of an atomic hydrogen treatment at the p/i interface which was performed in an attempt to increase the optical gap at the interface and to reduce the p/i interface defect density. The atomic hydrogen treatment at the interface was found not only to increase open circuit voltage in solar cells both with and without H_2-diluted i-layers, but also to result in a more stable open circuit voltage in both cases. We concluded that in order to improve the open circuit voltages, and more importantly to achieve more stable open circuit voltages, we need not only high quality (low defect density) and high stability i-layer materials with wider bandgaps, but also superior p/i interfaces. The high quality wide bandgap materials can be obtained when H_2-diluted a-Si:H i-layers are deposited at relatively low substrate temperatures (<200°C), while superior interfaces can be realized either by incorporating low defect density wide optical gap interface layers, or by atomic hydrogen p/i interface treatments.

To further investigate the contribution to the open circuit voltage from the bulk and from the interface, we made p-i-n cells with thin H_2-diluted i-layers (150Å to 600Å) sandwiched between the p-layer and the undiluted i-layer. In order to make a direct comparison with the previous a-Si:H p-i-n cells deposited at 200°C, we made several p-i-n cells with the same conditions except that the i-layer was deposited at a lower substrate temperature of 170°C. By depositing the i-layers at a lower substrate temperature with and

without H_2-dilution, we effectively increased the optical bandgap. However, we found that the increase in optical gap is not as large with undiluted i-layers as with H_2-diluted i-layers.

In comparing p-i-n cells with i-layers at two different deposition temperatures, we observed that the increase in open circuit voltage is higher (0.87V at 200°C and 0.90V at 170°C) in the cells with H_2-diluted i-layers than in cells with undiluted i-layers (0.84V at 200°C and 0.86V at 170°C), as shown in Fig. 13. This is so even though the increase in optical gap is larger in the two undiluted films (E_{2000}=1.80eV at 200°C and 1.83eV at 170°C) as compared to that in the H_2-diluted films (E_{2000}=1.85eV at 200°C and 1.86eV at 170°C). This has been discussed in Sec. 3.1, where it was shown that the open circuit voltage increases more rapidly with the optical gap in cells with hydrogen diluted i-layers than those with undiluted i-layers (see Fig. 31). Differences were also found in the stability of the open circuit voltages for the cells fabricated with diluted and undiluted a-Si:H i-layers, as discussed extensively in Sec. 1. In the case of the undiluted i-layers after 100 hours of 1 sun ELH light soaking, the 170°C cells showed similar degree of open circuit voltage drop (V_{oc} from 0.86V to 0.81V, a drop of 0.05V) as those deposited at 200°C (V_{oc} from 0.84V to 0.79V, a drop of 0.05V). However, not only does the open circuit voltage degradation in cells with hydrogen diluted i-layers reach a steady state in less than 100 hours of the same light soaking, but these cells also show smaller overall degradation. For the 170°C cells, the V_{oc} decreased from 0.90V to 0.87V, a drop of 0.03V, whereas for the 200°C cells, the V_{oc} decreased from 0.87V to 0.86V, a drop of 0.01V.

These degradation experiments and the results shown in Fig. 13 allow several conclusions to be drawn. *First of all*, the open circuit voltage depends, among other factors, on the mobility gap (and the optical gap) of the absorber i-layer; a higher open circuit voltage can be obtained with higher optical gaps in the absorber layer. *Secondly*, the open circuit voltage stability is influenced by the i-layer stability; cells with hydrogen diluted i-layer have more stable open circuit voltages than the cells fabricated with undiluted i-layers. *Thirdly*, atomic hydrogen treatment at the p/i interface not only increases the open circuit voltage in cells with and without H_2-dilution but it also improves the open circuit voltage stability, especially in cells with H_2-diluted i-layers. The effects of the atomic hydrogen treatment of the p/i interface are twofold: (i) to widen the optical gap

at the interface allowing more light to come into the absorber i-layer, (ii) to reduce the defect densities at the p/i interface region thus reducing carrier recombination at the interface, which can adversely affect the open circuit voltage. Since cells made with hydrogen diluted i-layers already have an improved p/i interface *in-situ*, because of the high hydrogen influx at the formation of p/i interface, we expect that the higher open circuit voltages are inherent in the cells with diluted i-layers. In the undiluted counterparts, the p/i interface quality is expected to be worse. So truly stable open circuit voltages are expected in cells fabricated with hydrogen diluted i-layers and atomic hydrogen p/i interface treatments.

To investigate and quantify the contributions of the p/i interfaces to the open circuit voltage, we made a series of p-i-n cells with customized thin interface layers sandwiched between the p-type a-SiC:H and the undiluted i-layer. The compositions of these structures are summarized below:

1) glass/TCO/a-SiC:H p^+/Diluted i/μc-n^+/Cr

2) glass/TCO/a-SiC:H p^+/Undiluted i/μc-n^+/Cr

3.1) glass/TCO/a-SiC:H p^+/h1/Undiluted i/μc-n^+/Cr; (h1:150Å of Diluted i)

3.2) glass/TCO/a-SiC:H p^+/h2/Undiluted i/μc-n^+/Cr; (h2:300Å of Diluted i)

3.3) glass/TCO/a-SiC:H p^+/h3/Undiluted i/μc-n^+/Cr; (h3:600Å of Diluted i)

(The thicknesses are: a-SiC:H p^+-layer:~250Å; μc-n^+-layer:~350Å; i-layer+interface layer:~4000Å)

The solar cell parameters of the different cells in the annealed state are listed in Table 8. It is important to note that by inserting a diluted i-layer, as thin as 150Å, in the cells with undiluted i-layers it is possible to increase the open circuit voltages from 0.825V to 0.868V, the same values as obtained in the cells with diluted i-layers. The increase in the open circuit voltages with these interface layers, from 0.825V to 0.868V, is a gain of 43mV. This is better than that obtained with the atomic hydrogen treatments of the cells with undiluted i-layers which showed an increase of about 22mV in the open circuit voltage, from 0.835V to 0.857V. Although these atomic hydrogen treatments at the p/i

Table 8 Parameters for customized p-i-n solar cells with different interface regions. The labelling scheme is given in the text.

	Status	Voc (V)	Jsc (mA/cm^2)	FF	Eff%
1)	Annealed	0.868	10.0	0.72	6.25
2)	Annealed	0.825	11.2	0.71	6.56
3.1)	Annealed	0.868	12.3	0.73	7.79
3.2)	Annealed	0.864	11.4	0.73	7.19
3.3)	Annealed	0.865	11.5	0.73	7.26

interface for the cells with undiluted i-layers were not optimized it appears that extensive work would be needed not only to increase the open circuit voltage beyond what has already been achieved, but also to stabilize their values.

More recently, such studies have been extended to additional thicknesses and we find that for thicknesses about 100Å the full beneficial effect of the interface layer is achieved. This is illustrated in Fig. 34, where the light I-V's are shown for cells with 4000Å thick i-layers, which are totally undiluted, undiluted+50Å diluted, undiluted+150Å diluted, and totally diluted layers. As reported earlier, no difference is found when the diluted interface region is increased to 300Å and 600Å.

We have also performed studies of the factors limiting the open circuit voltage using i-layers fabricated at different substrate temperatures and having different mobility gaps. Results are shown in Fig. 35 for the dependence of V_{oc} on illumination intensity for p(a-SiC:H)/i(a-Si:H)/n(μc-Si) cells with i-layers deposited at 200, 170, and 130°C. The mobility gaps for the 200 and 170°C i-layers are 1.87eV and 1.90eV, respectively. (No measurements could be carried out on films deposited at 130°C as the peeling problems at these temperatures have not yet been solved.) It can be noted here that all the cells studied showed a linear dependence of J_{sc} on light intensity over the entire range. There is a clear correlation of V_{oc} with the bandgap at all intensities, particularly at intensities less than AM1, where dependence on the bulk is indicated by the device modeling to be discussed in the Sec. 6. Although it was shown that the built-in potential, V_{bi}, in the cells studied (both diluted and undiluted) were higher than those reported in the literature, the factors limiting the open circuit voltage at AM1 are being further investigated using different solar cell structures.

The experimental results described above (see also Section 1) have demonstrated the importance of (and to a certain degree quantified) the contributions of these regions relative to the bulk. It has been suggested from preliminary modeling using AMPS that the insertion of a 50Å layer of heavily p-doped material at the p/i interface could be used to enhance the open circuit voltage even more efficiently than the above approach. This result seemed to run counter to our intuition and also to the RTSE observations (see Table 7 and Sec. 4). As a result, we fabricated a solar cell with a high B-doped interface layer,

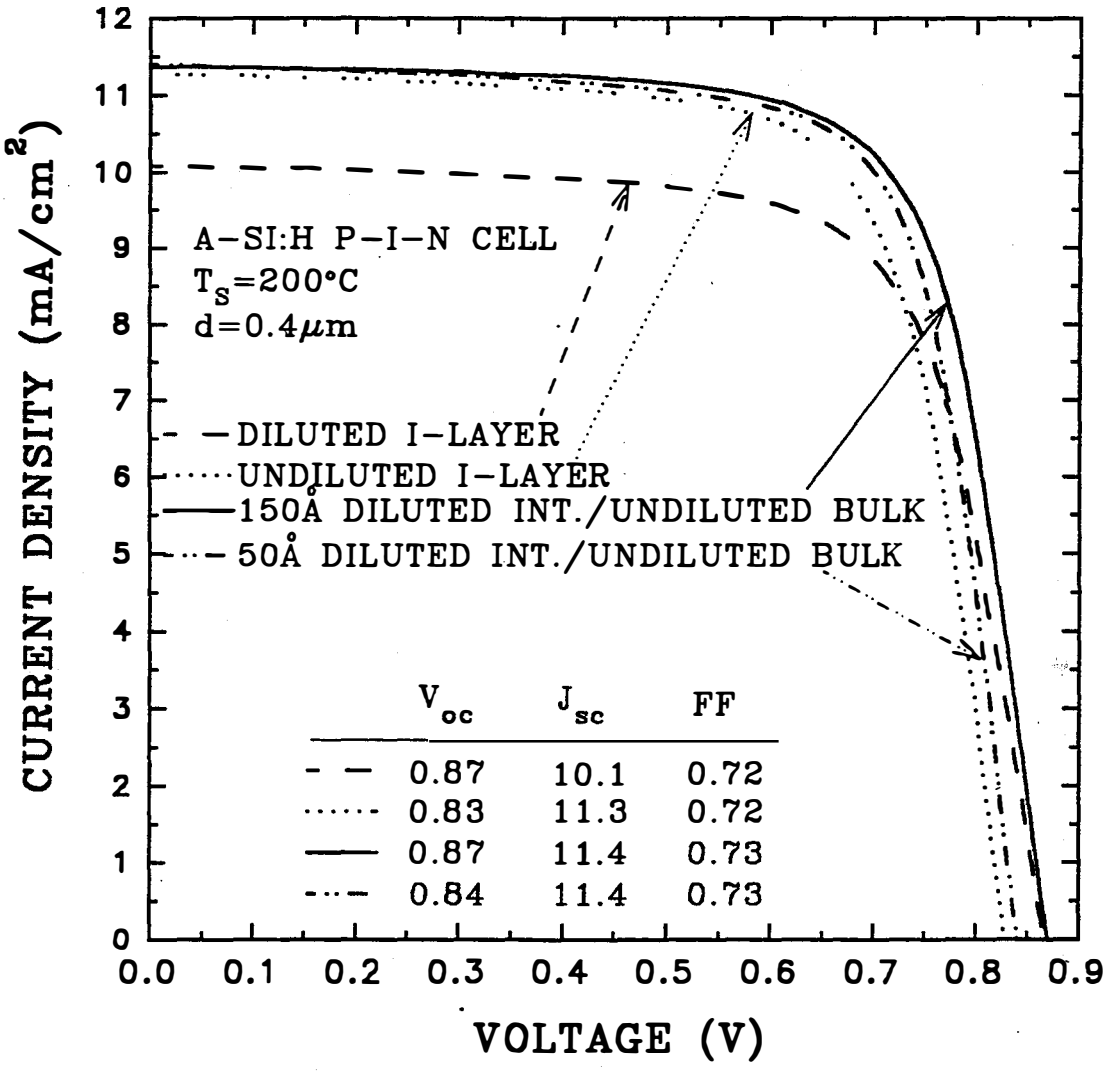

Figure 34 The annealed state light I-V characteristics of two standard p-i-n cells, one with hydrogen dilution and the other without hydrogen dilution, and two "customized" p-i-n cells. One of the customized cells has 50Å of standard hydrogen diluted material at the p/i interface and the other has 150Å of this material at the p/i interface. Both customized cells have the same standard undiluted bulk i-layer.

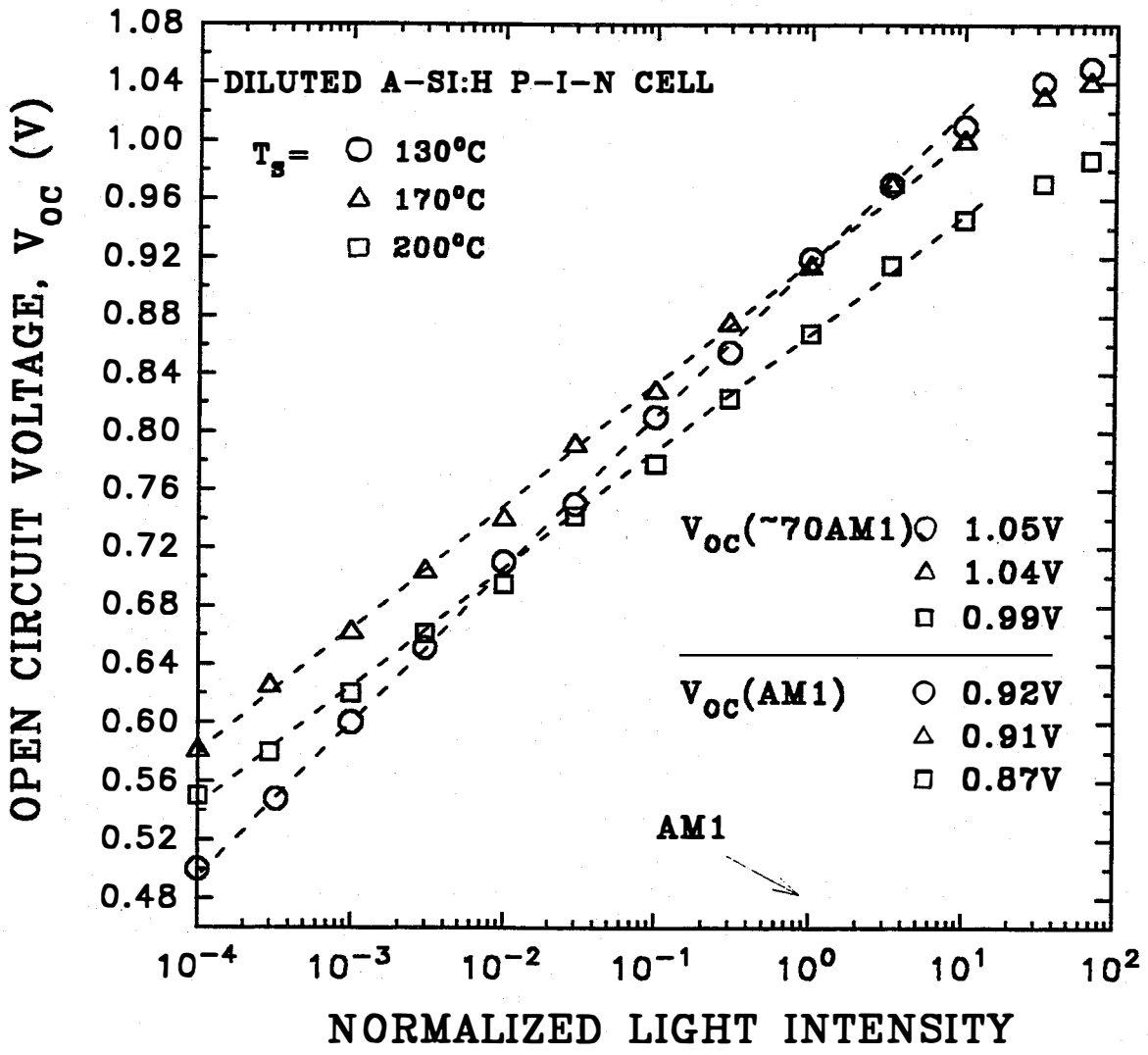

Figure 35 The dependence of the open circuit voltage, V_{oc}, on the normalized illumination light intensity for three hydrogen diluted p-i-n solar cells. It can be noted that the short circuit current, J_{sc}, maintains a good linear relationship with illumination light intensity over the entire intensity range studied. V_{oc} follows a relationship described by $V = \frac{kT}{q} \ln \frac{J}{J_o}$ until approximately 10AM1, from which point it starts to deviate, revealing the limitations due to other factors.

using our standard undiluted a-Si:H p-i-n structures. The data comparing the standard cell and the p-doped interface cell are shown in Fig. 36. It can be seen from the two light I-V characteristics that the open circuit voltage drops from 0.825V to 0.760V when the p-doped interface layer is inserted, while the short circuit current and the fill factor remain comparable. This is consistent with the single-chamber results of Table 7, in which a high level of B-related contamination as observed by RTSE, leads to V_{oc} values in the range 0.74~0.78V, whereas low levels of contamination led to V_{oc} values in the range of 0.83~0.84V. This clearly indicates the limitations of predictions from the modeling of solar cell characteristics which are not based on **accurate self-consistent material parameters**. This example also reinforces the importance of having such parameters, which unfortunately are only just now being established. We are thus proceeding in directions indicated by our experimental results which have established the importance of the interface and the necessity of maintaining low defect densities at the p/i interface, such as are obtained with proper p-layer gases and gas handling, hydrogen treatments, and hydrogen dilution. We feel that more reliable parameters must be established, as is being done, before one can rely on modeling results as valid predictors of directions to be taken.

Additional interesting results have been obtained on tailoring the B-doping profile in our p-i-n cell single-chamber preparations. In these studies we have included both specular ZnO and SnO_2:F coated glass substrates in the deposition, in addition to textured SnO_2:F glass substrates. In most cases, we have found that the V_{oc} value and the fill-factor for the cells on ZnO are inferior to those on textured SnO_2:F. The origin of this problem is unclear. It is possible that the contact between ZnO and the p-layer is not as intimate as that between SnO_2:F and the p-layer. For example, some small amount of reduction of the SnO_2:F may actually be beneficial in forming the contact. For the ZnO TCO, we have found that modest improvements in V_{oc} and fill-factor appear possible by intentionally incorporating a B-gradation in the p-layer, with a high gas phase B-content at the TCO/p interface dropping by an order of magnitude to its usual value after 200 Å. Table 9 shows the results for a control cell and two cells with B-graded p-layers. For all three cells the i- and n- layers were identical, and the i-layer was prepared without H_2-dilution. For the control cell, the p-layer was prepared from a 6:4:0.01:0.5 gas flow ratio of

Table 9. Performance results for a control p-i-n cell and two cells with B-graded p-layers. For all three cells, the i- and n- layers were identical, and the i-layer was prepared without H_2-dilution. For the control cell, the p-layer was prepared from a 6:4:0.01:0.5 gas flow ratio of SiH_4:CH_4:TMB:He. For the B-graded p-layers the ratios were varied from 6:4:0.1:5 to 6:4:0.01:0.5 continuously during the growth of the p-layer.

Cell	TCO	V_{oc} (V)	J_{sc} (mA/cm^2)	FF	eff.
Control	specular ZnO	0.80	14.8	0.52	6.15
B-graded p-layer	specular ZnO	0.85	14.2	0.63	7.60
B-graded p-layer	specular ZnO	0.86	14.4	0.59	7.31

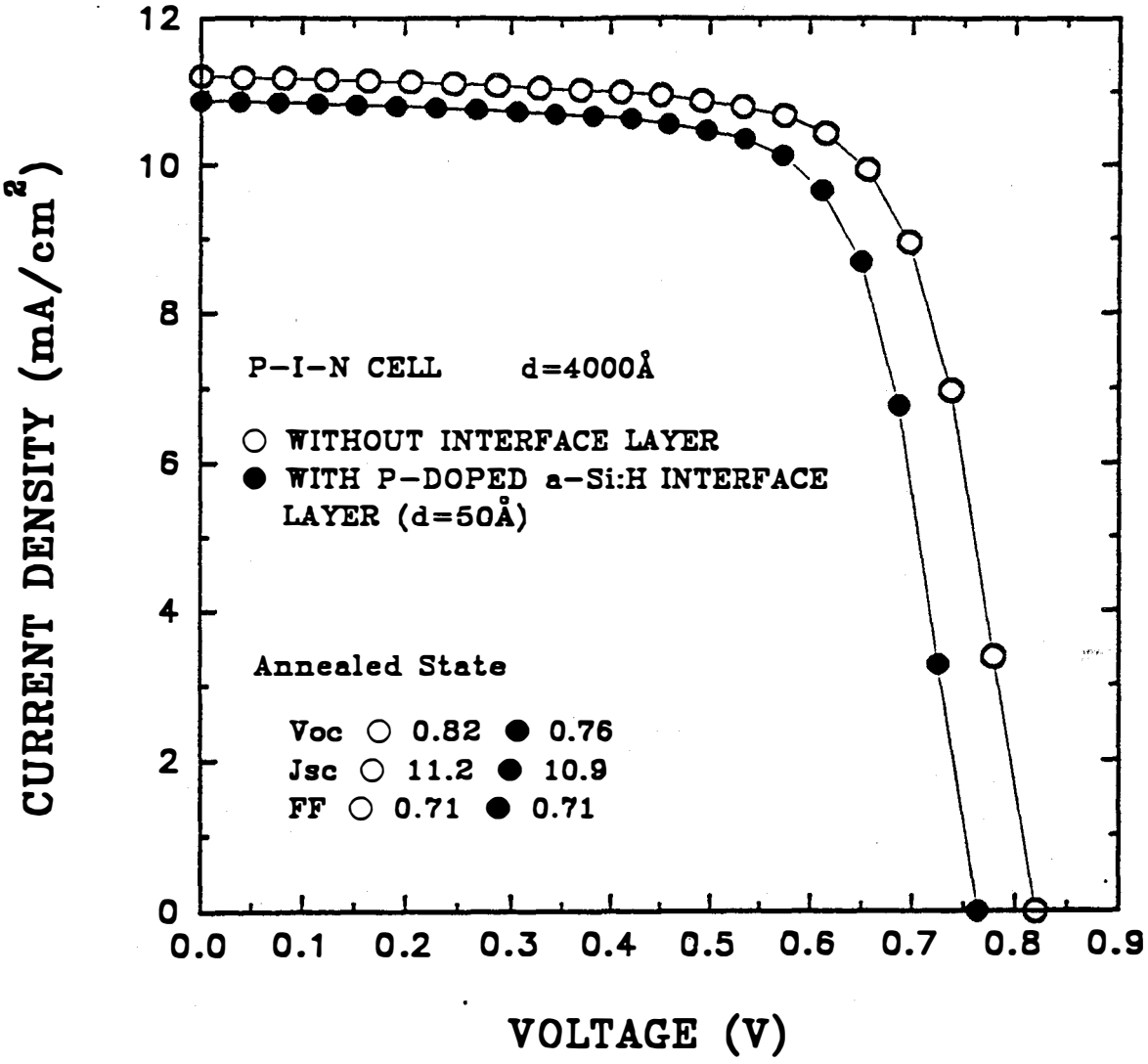

Figure 36 The detrimental effect on the light I-V for a p-doped a-Si:H layer deposited between the a-$Si_{1-x}C_x$:H p-layer and the a-Si:H i-layer in a p-i-n solar cell in comparison with a control cell without any interface layer.

SiH_4:CH_4:TMB:He. For the B-graded p-layers the ratios were varied from 6:4:0.1:5 to 6:4:0.01:0.5 (The He is included because our TMB is diluted at 2% in He.). The results of Table 9 show that the graded layer leads to an increase in V_{oc} of 50- 60 mV; an increase in fill-factor is also observed. In fact, the increase in V_{oc} is similar to that obtained with H_2-dilution of the i-layer. For textured SnO_2:F substrates, there is a weaker increase in V_{oc}, typically from 0.85 V to about 0.88 V. In the future, we intend to explore the effect of B-graded layers in optimized widegap cells in greater detail. Stability studies will also be performed at that time.

3.4 a-Si:H n-i-p Solar Cells

We also extended our studies of open circuit voltage issues to n-i-p solar cell structures made by multi-chamber deposition. In these studies, both a-SiC:H p^+/semi-transparent Cr and μc-p^+/TCO contacts were used. In addition to our standard n^+-layers, hydrogen diluted i-layers, and a-SiC:H p^+-layers, μc-p^+/TCO contacts made at USSC were used. We found that the a-SiC:H p^+ n-i-p cells give essentially the same open circuit voltages at AM1.5 as those in the standard p-i-n configuration. In contrast, an open circuit voltage increase of about 60mV, from 0.90V to 0.96V, was obtained for cells incorporating a-Si:H layers deposited at 170°C when the top p^+-layer is changed from the standard a-SiC:H to the USSC μc-p^+. In addition, the stability of the open circuit voltage in the n-i-p cell with the μc-p^+-layer is also better. This is illustrated in Fig. 37, where the light I-V's are shown for the n-i-p cell with the μc-p^+-layer in the annealed state and after illumination at 10AM1.5 for 100 hours. There is an 11mV drop in the V_{oc} for the n-i-p cell with the μc-p^+-layer. In contrast, a 50mV decrease of V_{oc} is seen in the p-i-n counterpart with the a-SiC:H p^+-layer under the same degradation conditions. The dramatic difference in the open circuit voltage between the two cell structures can be attributed to two factors. First, even though the a-Si:H i-layer surface was exposed to air for an extended period of time prior to the deposition of the top μc-p^+-layer, the resultant p/i interface is better than that in the a-Si:H/p^+-a-SiC:H solar cells. That this would be the case is consistent with our extensive studies on p/i interfaces in which the beneficial effects of atomic hydrogen

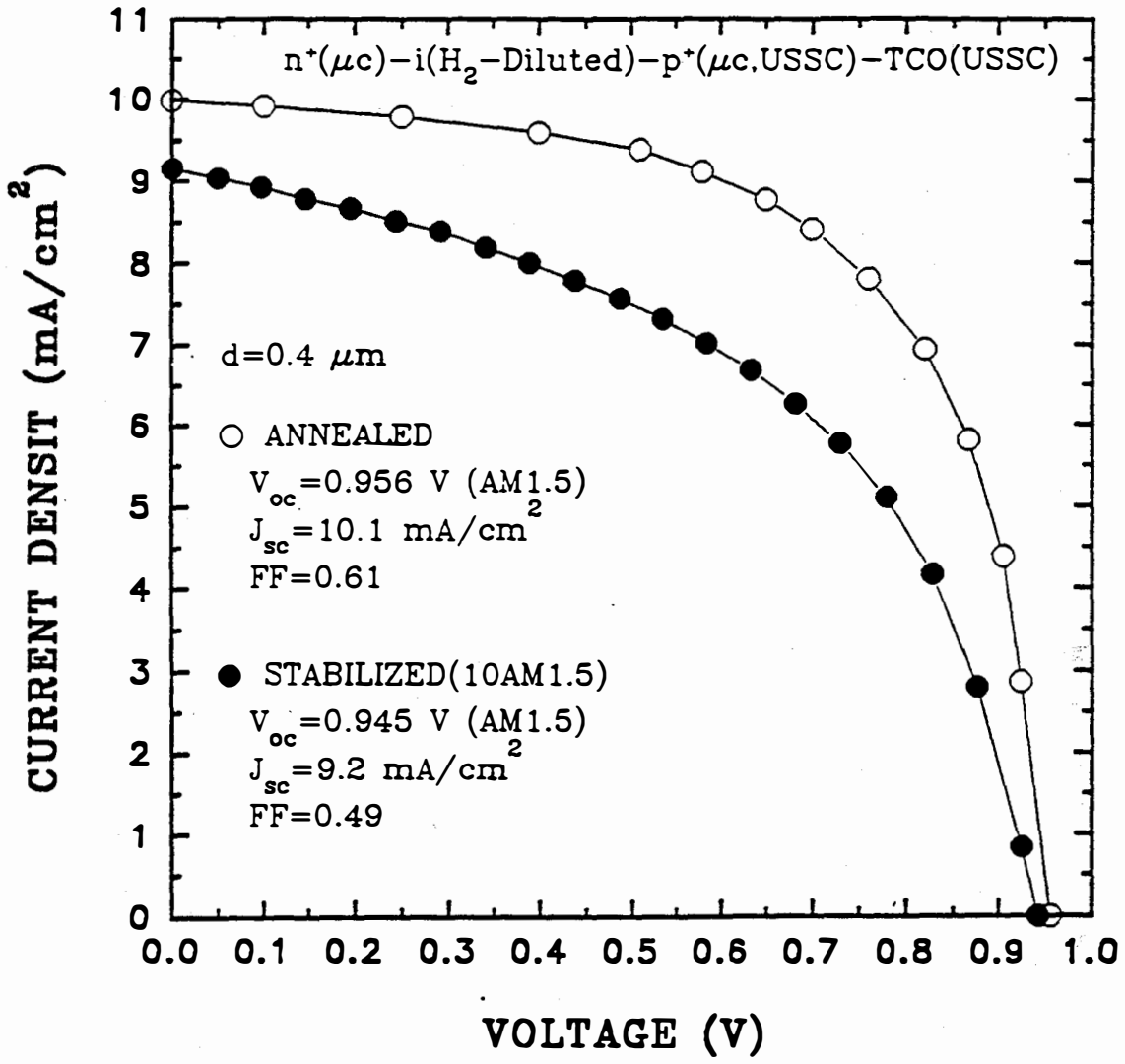

Figure 37 The light I-V's of an n-i-p cell with a μc-p^+-layer in both annealed and 10AM1 degraded states. The substrate temperature for the i-layer is 170°C.

treatments on this interface have been demonstrated. In the process of depositing the μc-p^+-layers, there is a large flux of atomic hydrogen generated (high hydrogen dilution and power) which, depending on the substrate temperature can penetrate as much as 200Å into the a-Si:H. The second possibility that has been suggested elsewhere is that the open circuit voltages with a-SiC:H p-layers at or above 0.9 volts become limited by the built-in potentials in such cells.

To establish the limitations imposed by the built-in potentials, which have been suggested by the results of V_{bi} measurements using the electroabsorption technique, we undertook a study of the J_{sc}-V_{oc} characteristics over a wide range of light intensities up to ~50 AM1. The J_{sc}-V_{oc} characteristics obtained for the standard a-SiC:H/a-Si:H p-i-n cells are shown in Fig. 38, for diluted a-Si:H layers deposited with substrate temperatures of 130°C and 200°C. It can be seen in Fig. 38 that in both cases there is an approximately linear relationship of the $\ln J_{sc}$-V_{oc} characteristics, corresponding to the equation $V_{OC} \cong \frac{nkT}{q}\ln(\frac{J_{sc}}{J_0})$, which holds very well over five orders of magnitude of J_{sc} (and light intensity). With illuminations of about 50AM1, it was possible to increase the open circuit voltage by as much as 120mV above the value obtained at AM1. If the V_{oc} was limited by V_{bi}, a "saturation" in V_{oc} should be observed with no further increase in V_{oc} with illumination as in J_{sc}. Since no such saturation is observed in both cases it can be concluded that the AM1 V_{oc}'s are not limited by the built-in potentials and also that the V_{bi}'s are greater than about 1.0V for the 130°C cell (V_{oc} at AM1.5 is 0.91V) and 0.99V in the 200°C cell (V_{oc} at AM1.5 is 0.87V). This is a clear demonstration that the built-in potentials are not a limiting factor in our standard p-i-n cells and would not be even for V_{oc} values as high as 1 volt. In the case of the n-i-p solar cell with the μc-p^+/TCO contact, this relationship of the $\ln J_{sc}$-V_{oc} characteristics also holds over more than five orders of magnitude as is shown in Fig. 39. However, in this case the open circuit voltage is 1.07V at the maximum available illumination of 50AM1, a value which is ~110mV above that at AM1 (0.96V). Thus 1.07V is a lower limit for the V_{bi}. The facts that the built-in potentials are not limiting the V_{oc} in both a-SiC:H and μc-p^+-layer cells and that (for the same a-Si:H materials deposited at 170°C) the respective AM1 V_{oc} values are 0.9V and 0.96V, are

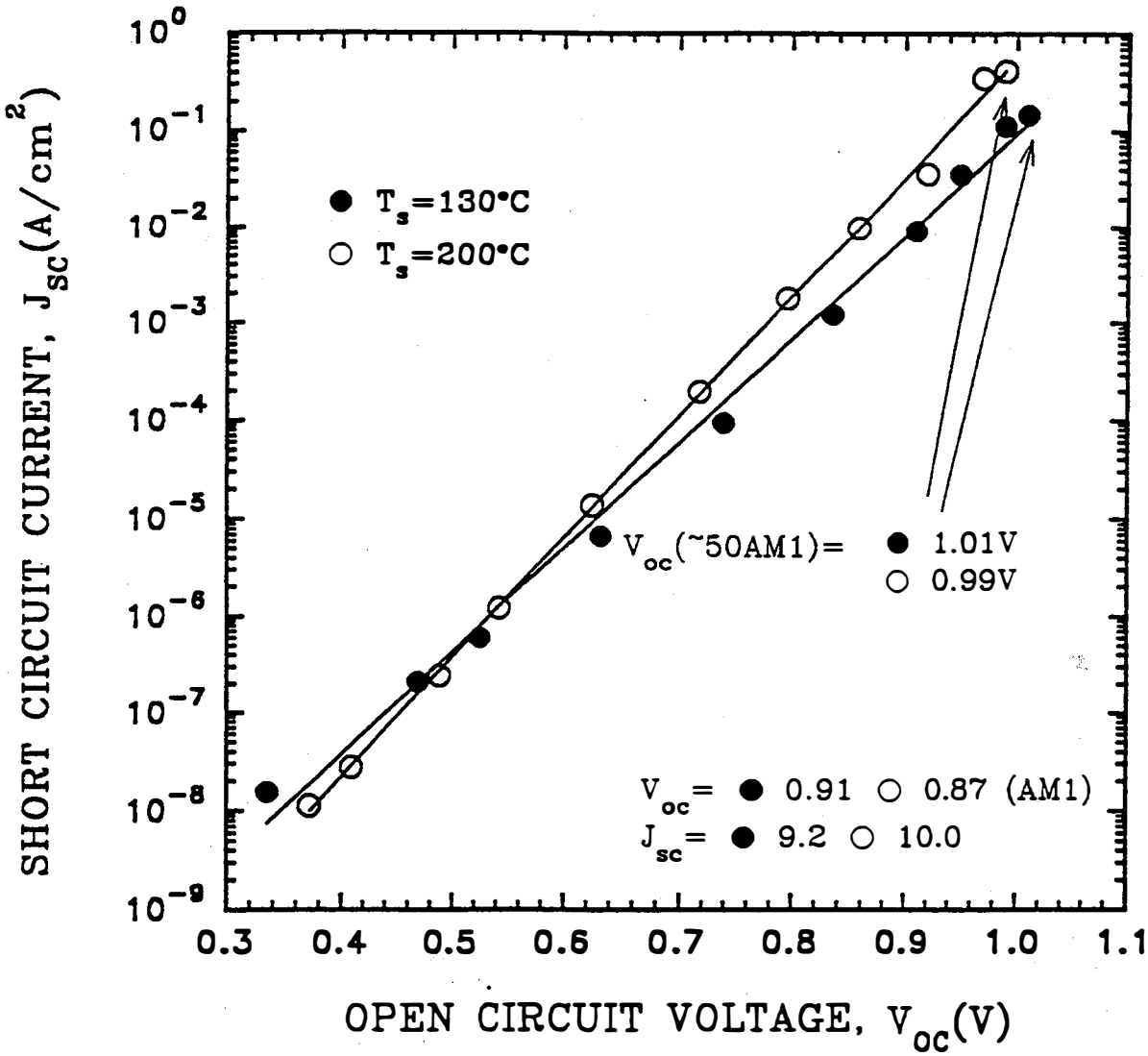

Figure 38 The J_{sc}-V_{oc} characteristics of two p-i-n cells deposited at two substrate temperatures. The maximum light intensity is about 50 suns.

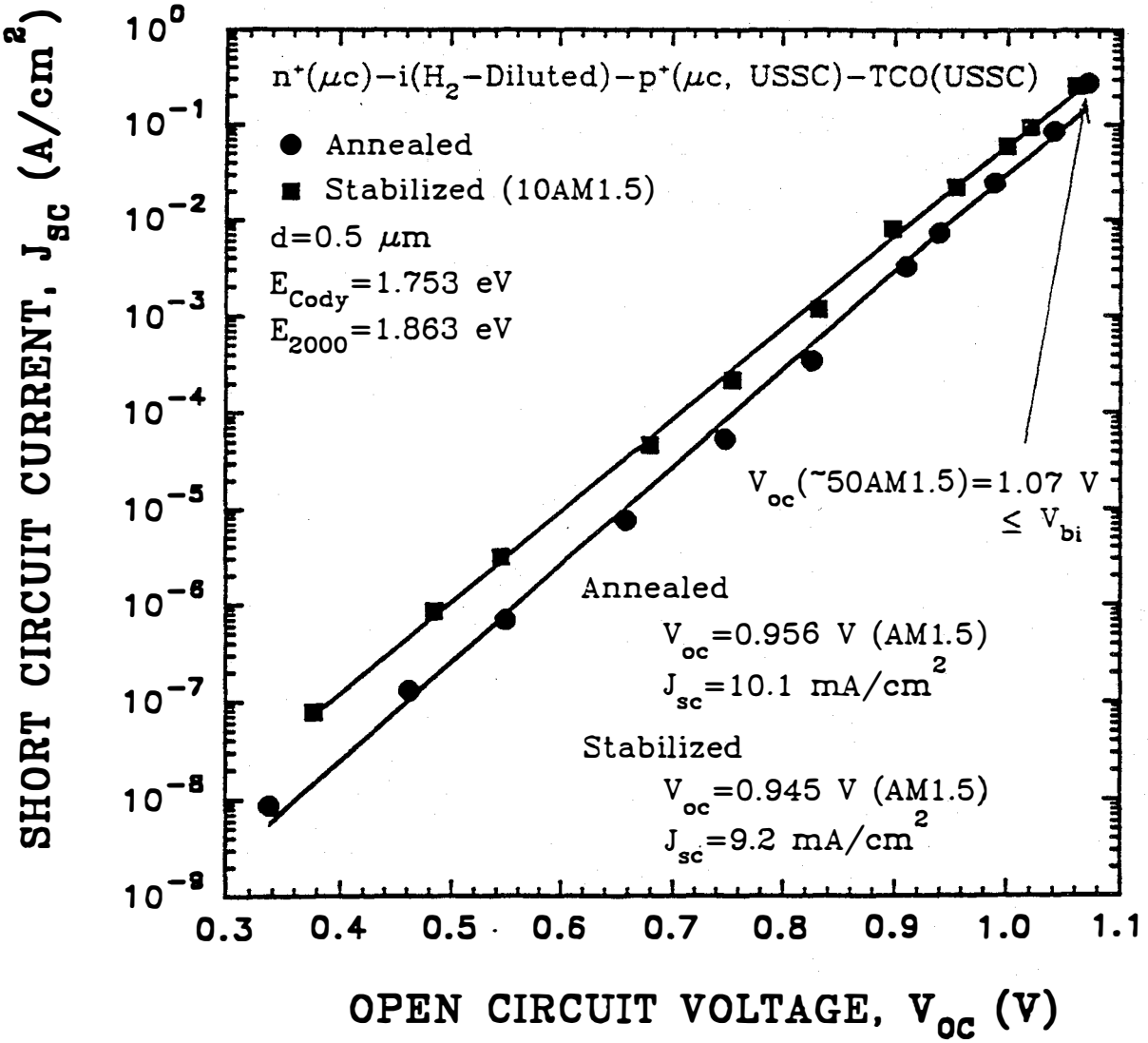

Figure 39 The J_{sc}-V_{oc} characteristics of an n-i-p cell with a μc-p-layer/TCO contact in both annealed and 10 sun degraded states.

consistent with our conclusion that the p/i interface regions are different for the two different p-contacts. It also indicates that open circuit voltages of about 1.1 volts may be obtainable with appropriate i-layers and p/i interfaces.

The above studies were carried out concurrently with those in which real time spectroscopic ellipsometry (RTSE) was used to obtain the full structural evolution and optical properties during n-i-p solar cell preparation. An example of these results is presented next. The analysis procedure for the n-i-p cells is similar to that for the p-i-n solar cells discussed in Phase I. The full analysis procedure has been applied to an n-i-p cell with a widegap amorphous p-layer whose V_{oc} is 0.94V. The n-i-p solar cell was prepared in the single chamber system with RTSE capability using a Cr-coated c-Si substrate held at 200°C. The plasma power-flux densities were 70mW/cm^2 for both i- and n-layers and 700mW/cm^2 for the p-layer. The a-Si:H:P n-layer was prepared onto the Cr surface first using a flow ratio of [SiH_4]:[PH_3]=10:0.2 (in sccm). For the i-layer, a-Si:H was deposited without H_2-dilution (i.e., a midgap cell) using a 20 sccm flow of SiH_4 at 0.19 Torr. The widegap p-layer was prepared using flow ratios of [SiH_4]:[TMB]:[H_2]=1.0:0.05:120 (in sccm) at a total pressure of 0.58 Torr. Surprisingly, this led to an amorphous p-layer in spite of the high H_2-dilution. Evidently the incorporation of TMB in the process thwarts the development of crystallinity as described in Sec. 4. The V_{oc} performance of the cell was assessed by depositing semitransparent metal (Cr) contacts (~150Å) on top of the p-layer.

The upper two panels of Figs. 40(a) and (b) show the final results of the analysis for n- and i-layer growth on the Cr and n-layer, respectively. In this plot, f_i, d_s, and d_b represent the volume fraction of the depositing material that fills the modulations in the substrate film roughness layer, the thickness of the surface roughness layer for the depositing material, and the bulk layer thickness, respectively. The inset in Fig. 40(b) depicts the entire range of d_b and d_s for i-layer growth. The effective or mass thicknesses of n- and i-layers, determined according to the equation '$d_{mass}=d_i f_i+d_b+0.5d_s$' (all final film values), are 308Å and 5112Å. These values are close to the intended ones of 300Å and 5000Å, respectively. The upper two panels of Fig. 40(c) show the evolution of d_b and d_s for widegap amorphous p-layer growth on the a-Si:H i-layer. The scatter in the roughness

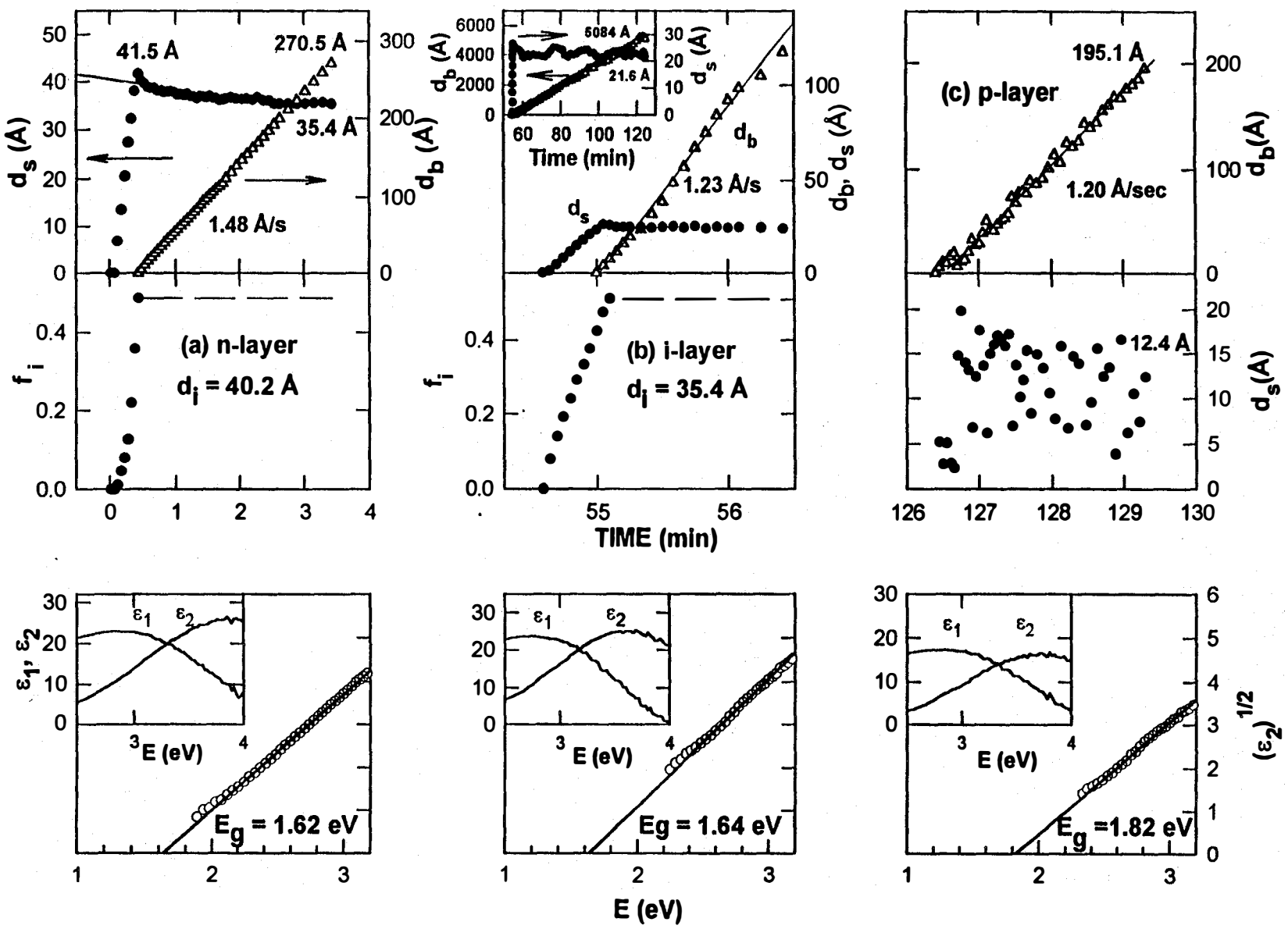

Figure 40 Layer thicknesses and volume fractions (upper two panels), and the optical properties at 200°C (lower panel) obtained in a post-deposition analysis of RTSE data acquired during n-i-p solar cell fabrication. Results are provided for: (a) n-type a-Si:H ; (b) undoped a-Si:H ; (c) widegap a-Si:H:B:C. The thicknesses d_s, d_i and d_b are for the surface and interface roughness and bulk layers, respectively, and f_i is the volume fraction of the film that forms within the modulations of the substrate roughness. The optical gap E_g is obtained assuming a constant dipole matrix element from plots of $(\varepsilon_2)^{1/2}$ vs. energy, where the dielectric function is $\varepsilon=\varepsilon_1+i\varepsilon_2$ (see insets, low panel).

layer here is attributed to the fact that the p-layer is much more transparent than the i- and n-layers. In such a case, roughness is more difficult to detect optically. At the end of p-layer deposition, we find that the effective layer thickness is 201Å which is in excellent agreement with the intended thickness of 200Å for the p-layer.

The lower panels of Fig. 40 show the dielectric functions of each layer in the insets (which are obtained along with the microstructural parameters in the analysis) and the optical gaps determined using the constant dipole (CD) analysis. The resulting optical gaps at 200°C are 1.62, 1.64, and 1.82 eV for the n, i, and p-layers, respectively. These values are ~0.18 eV lower than the Tauc gaps measured by T & R at room temperature. Finally, it should be pointed out that the key advantage of RTSE is its ability not only to deduce the final effective layer thicknesses but also the deposition rates and the optical gaps for the separate n, i, and p-layers in the actual cell structures.

We have also incorporated differently-prepared widegap p-layers (Tauc gap ~ 2.00 eV) from SiH_4, CH_4, and TMB into midgap n-i-p cells fabricated in the single chamber system using guidance from RTSE. For all cells, the substrate temperature was 200°C, and the i-layer was made from pure SiH_4 at 20 sccm flow. The goal of the study was an attempt to optimize widegap p-layers in n-i-p structures from the standpoint of V_{oc}. Further characterization of the p-layers in the actual solar cell configuration using RTSE is required to obtain an improved understanding of the cell results. Such results are reported in Sec. 5. Table 10 lists the p-layer gas mixtures along with the resulting V_{oc} for the n-i-p solar cells. For the first entry of Table 10, the Si:C:H p-layer was fully amorphous in both thin film (200 Å) and also thick film (~1 μm) forms. This is the cell whose RTSE results appear above in Fig.40. For the second entry, the p-layer was a mixed phase amorphous+microcrystalline material as determined in its thick film form. Furthermore nucleation of this material on the i-layer in the n-i-p solar cell configuration occurred at low density, as might be expected for a microcrystalline structure. However, an RTSE analysis has yet to reveal clear evidence of the crystalline phase in this 200 Å p-layer material, possibly because of the small grain size or its low crystalline volume fraction. It is the low nucleation density that leads to the very low V_{oc} value for the second entry of Table 10. For the third entry, the p-layer conditions were kept the same as for the second

Table 10 V_{oc} values measured on midgap n-i-p solar cells whose n- and i-layers were prepared under identical conditions, but whose widegap p-layers were prepared using different mixtures of SiH4/CH_4/TMB. The variable parameters used in p-layer preparation are the H2-dilution ratio R (R=[H2]/{[SiH_4]+[CH_4]}), the source gas ratio Z (Z=[CH_4]/[SiH4]), and the doping gas ratio D (D=[TMB]/{[SiH4]+[CH4]}). For the last three entries, the i-layer surface was exposed to an H2-plasma prior to p-layer growth.

p-layer preparation conditions				Cell Performance	
Z	R	D	H_2-plasma	structure	V_{oc} (V)
0	120	0.05	0	amorphous	0.94
0.67	200	0.2	0	μc in thick layer	0.36
0.67	200	0.2	133 s	μc in thick layer	0.85
0.67	200	0.05	133 s	μc in thick layer	0.89
0	200	0.05	133 s	amorphous	0.88

entry, except that a H_2 plasma treatment of the i-layer was performed prior to p-layer nucleation. This has led to a higher nucleation density and improved V_{oc}. For the fourth and fifth entries, the deposition conditions were altered by either reducing the doping level or the CH_4 content in the plasma. Although a small improvement is obtained by reducing the doping level, the improvement is not sufficient to lead to results comparable with the a-Si:C:H p-layer (first entry). There are two possible explanations for this effect. First, it is possible that the microcrystalline layers prepared with TMB are relatively defective. Evidence that this is the case is presented in Sec. 4. Another possibility is that the H_2 plasma treatment of the i-layer surface, required in order to generate a high nucleation density for the p-layer, is not optimized. This possibility will be discussed further in Sec. 5.

4. Novel *p*-Type Materials

4.1 p-Type Materials Development and Optimization

In the first part of this Phase, we developed widegap $Si_{1-x}C_x$ *p*-layers to be used as the top-most junction in *n-i-p* solar cells. In such a cell configuration, microcrystalline or high H_2-dilution amorphous *p*-layers can be prepared without concern for the interaction between the H_2-rich plasma and the transparent conductor (which is a major problem, of course, in the *p-i-n* configuration). In our first attempts, however, we prepared a-$Si_{1-x}C_x$:H *p*-layers for the *n-i-p* solar cells in the same way as has been done earlier for *p-i-n* cells. The fourth row of Table 11 shows the relevant properties of our standard a-$Si_{1-x}C_x$:H *p*-layer, prepared to a thickness of ~0.82 μm at a substrate temperature of 200°C, using a $[CH_4]/[SiH_4]$ gas flow ratio of Z=4/6 (in sccm) and a dopant gas flow ratio of $D=[TMB]/\{[SiH_4]+[CH_4]\}= 0.02/10$ (in sccm). These conditions lead to an E_{2000} optical gap of 1.89 eV which is typically ~0.05 eV less than the corresponding gap of similarly prepared undoped material. If the energy E_σ or E_{2000}-E_σ is taken as a measure of the quality of doped amorphous materials, then we would conclude that TMB doping leads to a somewhat inferior bulk a-$Si_{1-x}C_x$:H *p*-layer than diborane gas doping. This is seen by

Table 11 Electrical and optical properties of ~1.1-2.3 μm thick microcrystalline $Si_{1-x}C_x$ layers prepared at 200°C using mixtures of SiH_4/CH_4, TMB, and H_2, compared with corresponding results for a-$Si_{1-x}C_x$:H prepared without additional H_2 dilution, the latter doped using either diborane or TMB. Here, we present the E_{2000} gap, defined as the photon energy at which α=2000 cm^{-1} in order to compare the absorption properties of mixed-phase microcrystalline films with those that are purely amorphous.

SAMPLE	{[B_2H_6] or [TMB]} /{[SiH_4] + [CH_4]	E_{2000} (eV)	E_σ (eV)	E_{2000} - E_σ (eV)	THICKNESS (μm)
μc-Si/a-$Si_{1-x}C_x$:H:B (as-dep., R=120, Z=0.67)	0.2 (TMB)	*	0.50	*	2.28
μc-Si/a-$Si_{1-x}C_x$:H:B (as-dep., R=200, Z=0.67)	0.05 (TMB)	1.83	0.60	1.23	1.09
μc-Si/a-$Si_{1-x}C_x$:H:B (as-dep., R=200, Z=0.67)	0.2 (TMB)	*	0.52	*	1.14
a-$Si_{1-x}C_x$:H:B (as-dep., Z=0.67)	0.002 (TMB)	1.89	0.55	1.34	0.8
a-$Si_{1-x}C_x$:H:B (as-dep., Z=0.67)	0.001 (B_2H_6)	1.87	0.50	1.37	0.8

* rough surface; accurate T&R data not available

comparing the fourth and fifth rows of Table 11, the latter being for our standard diborane-gas-doped a-$Si_{1-x}C_x$:H, prepared to a similar thickness. In spite of this, the interface problems generated by diborane CVD (as documented in earlier reports and discussed in more detail below) have led us to adopt TMB for *p*-layer doping in the *p-i-n* solar cells. Thus, we start out with the same TMB-based a-$Si_{1-x}C_x$:H:B formula in our first *n-i-p* cells as described in the next section.

We have been studying widegap microcrystalline $Si_{1-x}C_x$ *p*-layers prepared using mixtures of CH_4/SiH_4, H_2 and TMB. Results for the electrical and optical properties are included in Table 11 and Figs. 41 and 42. Figure 41 shows the conductivity versus temperature for the microcrystalline films in the second and third rows of Table 11 prepared with $R=[H_2]/\{[SiH_4]+[CH_4]\}=200$, $Z=[CH_4]/[SiH_4]=4/6$, and $D=[TMB]/\{[SiH_4]+[CH_4]\}=0.05$ and 0.2. Also shown for comparison are the corresponding results for the standard TMB-doped a-$Si_{1-x}C_x$:H. Figure 42 provides the dielectric functions of the final films from which an assessment of the crystallinity and structure can be made. In similarity to undoped $Si_{1-x}C_x$ films prepared with high H_2-dilution, the films of the second and third rows of Table 11 consist of a mixture of a-$Si_{1-x}C_x$:H, c-Si, and void, quantified by effective medium modeling (see values provided in Fig. 42). This modeling approach is expected to yield a lower limit on the Si crystallite content because of size effects in the Si nanocrystals, however the relative void volume is expected to be accurate.

As has been suggested by earlier more detailed studies of undoped (but otherwise similar) μc-Si:H/a-$Si_{1-x}C_x$:H mixed-phase materials, we assume that the a-$Si_{1-x}C_x$:H phase is characteristic of the purely amorphous material prepared at lower R (*i.e.*, R=20) but with the same value of Z (*i.e.*, Z=0.67 for the materials of the second and third rows of Table 11). The earlier results showed that the crystallites forming at R>30, are pure Si and exclude C from the network, leading to a lower net C content (by volume) in the film. This conclusion appears to be valid in the doped film situation as well. It is also possible that if C fails to be incorporated within the Si crystallites, B may also be excluded. This would occur if the C_3-B bonding units are so strong that they are not dissociated in the plasma. The experimental results appear to be consistent with this type of scenario for the

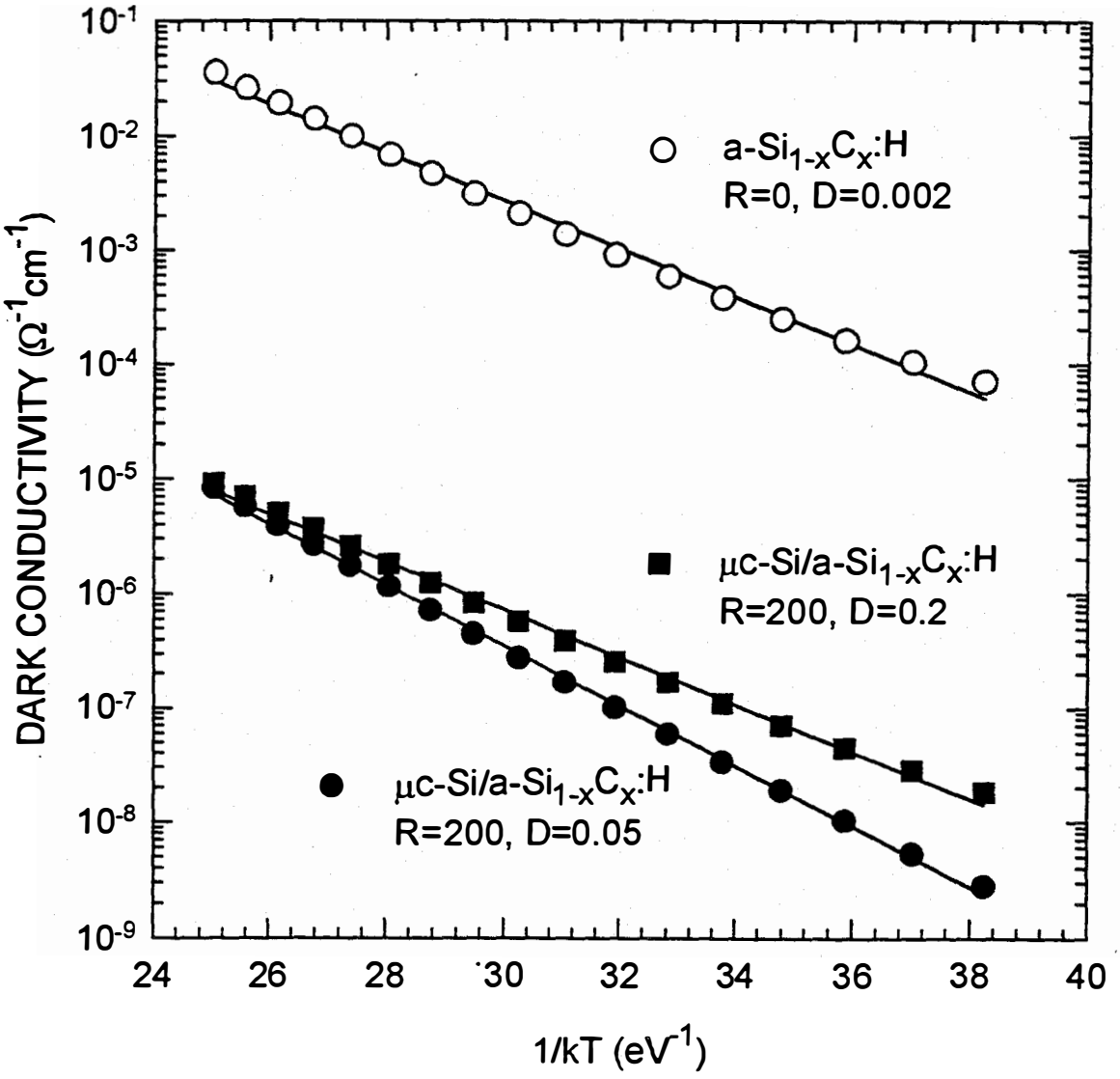

Figure 41 The conductivity versus inverse temperature for 1.0-1.2 μm thick B-doped microcrystalline $Si_{1-x}C_x$ layers (rows 2 and 3 of Table 11) compared with a 0.82 μm thick B-doped a-$Si_{1-x}C_x$:H layer (row 4 of Table 11). The doping gas in all these cases was TMB.

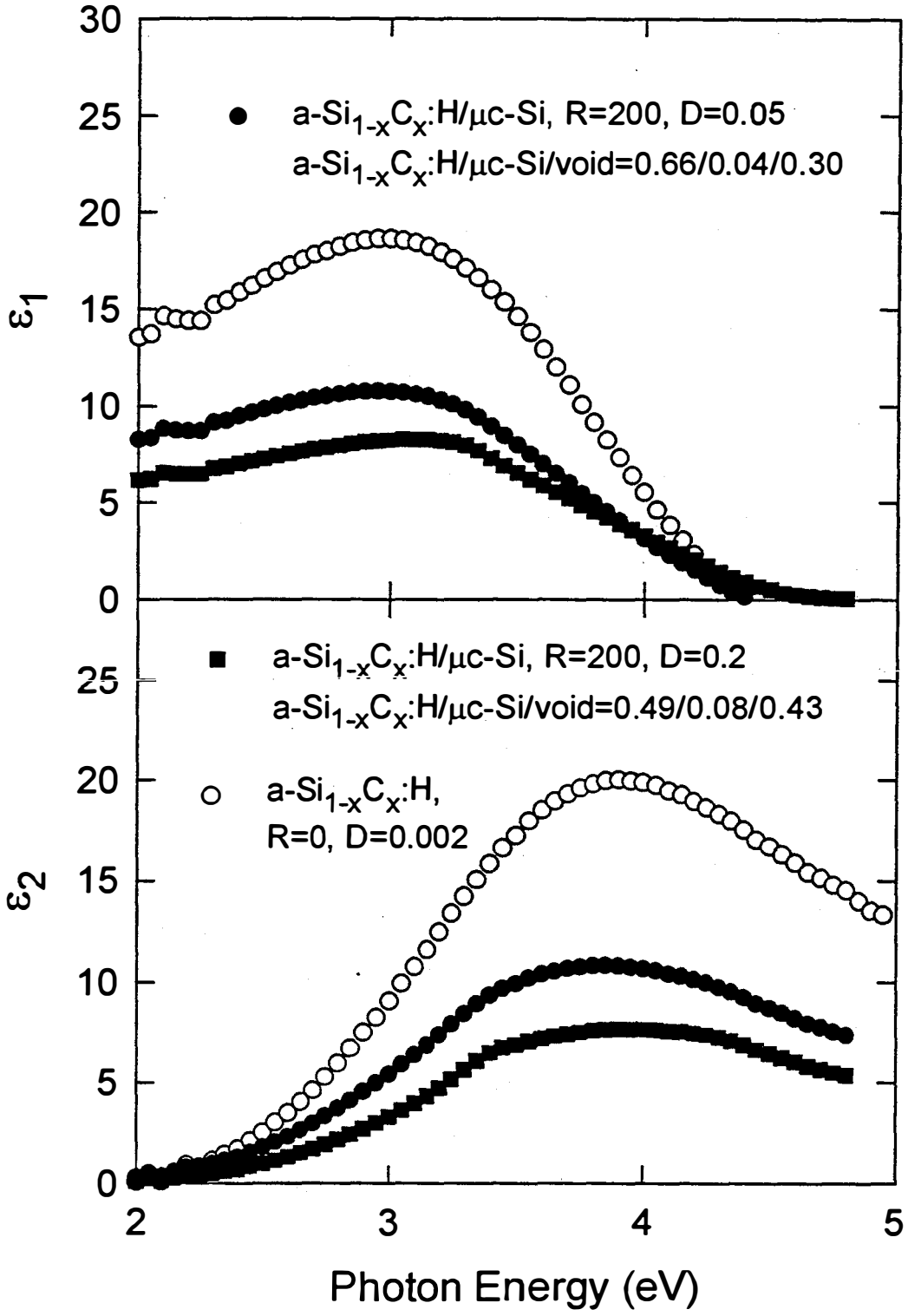

Figure 42 The dielectric functions of the 1.0-1.2 μm thick B-doped microcrystalline $Si_{1-x}C_x$ layers (rows 2 and 3 of Table 11) compared with a 0.82 μm thick B-doped a-$Si_{1-x}C_x$:H layer (row 4 of Table 11). The doping gas in all these cases was TMB. Also provided are the compositions of the mixed-phase materials estimated from effective medium theory modeling of the dielectric functions.

following two reasons. (i) The conductivity activation energy is high, considering the high value of D. This suggests one of two possibilities: either the B is entering the film in a non-doping configuration or the B is being excluded from the film as proposed above. (ii) The values of the conductivity activation energy for the mixed-phase microcrystalline films are similar to those for doped a-$Si_{1-x}C_x$:H, suggesting that the conductivity may be controlled by the amorphous phase. The much lower conductivity values for the mixed phase films may suggest that a lower volume fraction of the film is contributing to the conductivity. This may be consistent with the high void volume fractions in the films. If the ideas presented here are correct, then it important to disconnect the processes of B- and C-incorporation in the films. Further problems with the doped microcrystalline $Si_{1-x}C_x$ materials will be discussed next.

Our studies suggest that the microcrystalline $Si_{1-x}C_x$ p-type materials made with TMB are more defective and have a smaller crystallite size than similarly-prepared intrinsic materials prepared without TMB. As an example Table 12 shows microstructural and critical point analyses of two mixed phase films prepared from mixtures of $SiH_4/CH_4/H_2$. The first is an intrinsic layer prepared with $Z=[CH_4]/[SiH_4]=0.67$, R=80, D=0, and T_S=250°C, and the second is a p-type layer prepared with Z=0.67, R=120, D=0.2, and T_S=200°C. The latter film exhibits much broader electronic transitions as indicated by lower c-Si content even though prepared at a higher H_2-dilution level. Although the lower T_S may play a role in this effect, we feel that the incorporation of TMB in the process is the key factor in reducing crystalline grain size and the degree of crystallinity. This work suggests that we should convert our dopant source to either B_2H_6 or BF_3 for better optimization of microcrystalline p-layers in n-i-p cells. Further discussion and verification of the problems encountered here will be provided below where the n-i-p cell performance characteristics will be presented.

For comparison with the microcrystalline $Si_{1-x}C_x$ p-type films prepared at high H_2-dilution from SiH_4/CH_4/TMB, we also prepared several films without the CH_4 additions. Figure 43 shows the dielectric functions of microcrystalline $Si_{1-x}C_x$ films prepared with $R=[H_2]/\{[SiH_4]+[CH_4]\}$=120 and 200, $Z=[CH_4]/[SiH_4]$=4/6, and $D=[TMB]/\{[SiH_4]+[CH_4]\}$=0.2 (filled squares and triangles, respectively).

Table 12 Microstructural and critical point analyses of two mixed-phase films prepared from mixtures of $SiH_4/CH_4/H_2$. The first is an intrinsic layer prepared with $Z=[CH_4]/[SiH_4]=0.67$, R=80, D=0, and $T_S=250°C$, and the second is a p-type layer prepared with Z=0.67, R=120, D=0.2, and $T_S=200°C$.

Sample		Intrinsic Layer	p-type Layer
E_o'-E_1	E (eV)	3.413 ± 0.083	3.371 ± 0.150
	Γ (eV)	0.398 ± 0.083	0.484 ± 0.150
E_2	E (eV)	4.261 ± 0.057	4.249 ± 0.288
	Γ (eV)	0.243 ± 0.057	0.603 ± 0.288
Bulk Layer	a-Si	0.596 ± 0.033	0.602 ± 0.047
	c-Si	0.335 ± 0.032	0.053 ± 0.012
	void	0.069 ± 0.006	0.352 ± 0.072
Surface Roughness Thickness (Å)		22.8 ± 11.6	57.75 ± 6.05
Surface Roughness Layer	a-Si	0.523 ± 0.192	0.5 fixed
	c-Si	0.106 ± 0.113	0
	void	0.371 ± 0.155	0.5 fixed

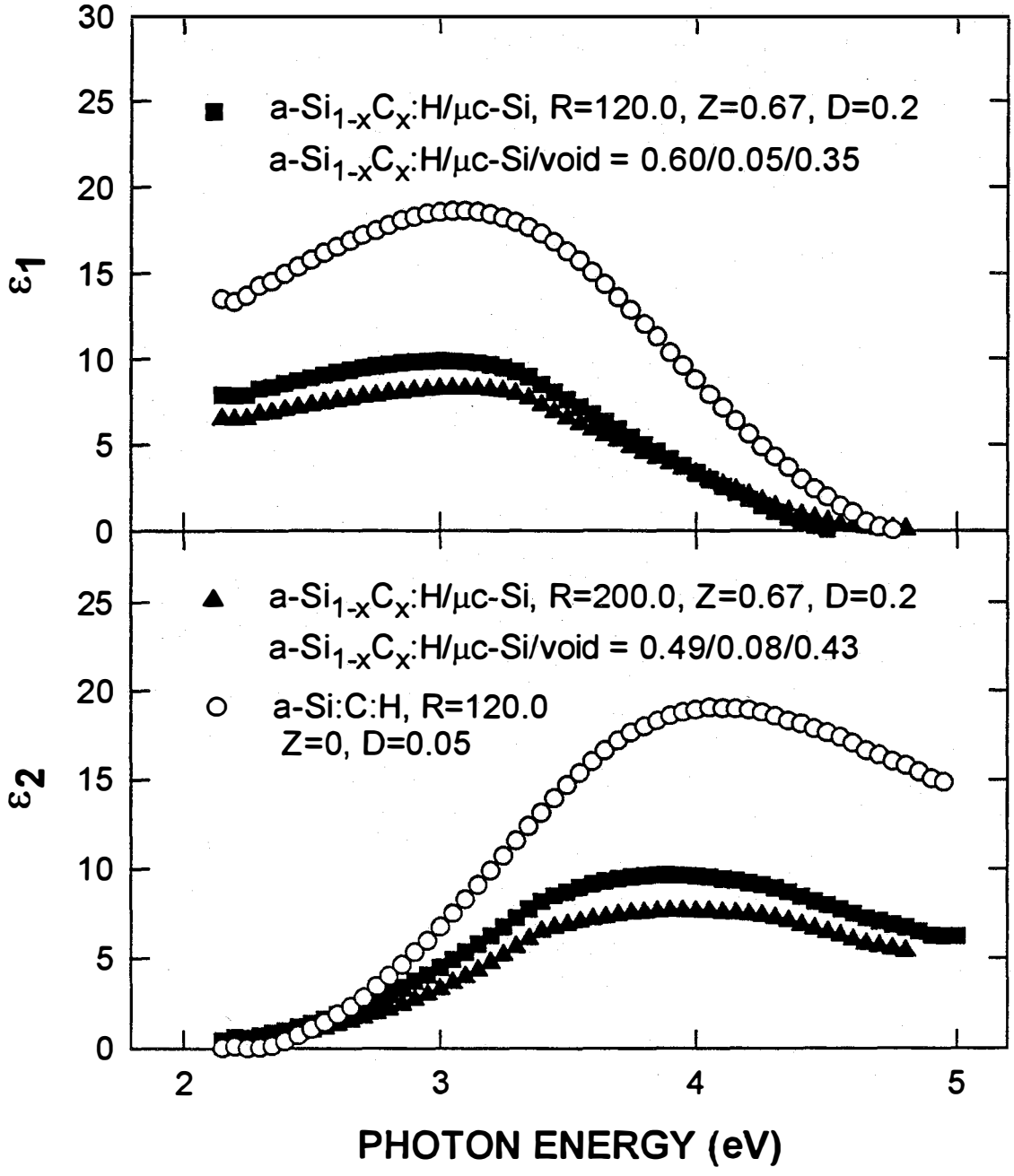

Fig.43 The dielectric functions of B-doped $Si_{1-x}C_x$ layers. The doping gas in all these cases was TMB. Also provided are the compositions of the mixed-phase materials estimated from effective medium theory modeling of the dielectric functions.

These films consist of a mixture of a-$Si_{1-x}C_x$:H, c-Si, and void, as quantified by effective medium theory modeling (see values provided in Fig. 43). The film with the dielectric function shown in Fig. 43 as the open circles was prepared with high H_2-dilution (R=120), D=0.05, but without the CH_4 addition (i.e., Z=0). The dielectric function of this film prepared to a thickness of ~0.8μm, appears to be characteristic of a purely amorphous material, in spite of the high-H_2-dilution. The constant dipole (or Cody) optical gap (E_{CD}) of this material deduced from RTSE data at 200°C is 1.84eV, and the value of E_{2000} deduced from T & R at room temperature is 1.98eV. These values are higher than those of the p-layers discussed above. As a result, we expect this material to be promising as a novel p-layer candidate. In fact, the highest V_{oc} value obtained to date for an n-i-p solar cell with a midgap i-layer (i.e., no H_2-dilution) has been obtained using this material as the p-layer (see Secs. 3 and 4.2).

These studies of the high H_2-dilution a-Si:C:H prepared from SiH_4/TMB (no CH_4) suggest that the TMB, employed as a dopant, thwarts the development of microcrystals. As an example, Table 13 shows the microstructural analysis of two thick (~0.8-1.6 μm) doped Si layers. The first is a p-type layer prepared from a 120/1 gas flow ratio (in sccm) of H_2/SiH_4 ($R=[H_2]/[SiH_4]=120$) with $D=[TMB]/[SiH_4]=0.05$ and a substrate temperature (Ts) of 200°C. The second is an n-type layer prepared from a 100/2 gas flow ratio (in sccm) of H_2/SiH_4 (R=50) with $D=[PH_3]/[SiH_4]=0.009$ and T_S=200°C. This comparison shows that the p-type layer is amorphous, whereas the n-layer is microcrystalline, even though the latter was prepared at much lower H_2-dilution level.

4.2 n-i-p Solar Cells Incorporating Novel p-Layers

We have prepared a series of n-i-p midgap solar cells on Cr-coated c-Si substrates held at 200°C. The depositions were performed in our single chamber system with real time monitoring by spectroscopic ellipsometry (RTSE). The mixed-phase microcrystalline and amorphous $Si_{1-x}C_x$ p-layers discussed in Sec. 4.1 have been incorporated into the cells.

Table 13. Microstructural analysis of two thick, doped Si layers. The first is a p-type layer prepared from a 120/1 gas flow ratio (in sccm) of H_2/SiH_4 ($R=[H_2]/[SiH_4]=120$) with $D=[TMB]/[SiH_4]=0.05$. The second is an n-type film prepared from a 100/2 gas flow ratio (in sccm) of H_2/SiH_4 ($R=50$) with $D=[PH_3]/SiH_4]= 0.009$.

Sample	Bulk Layer			Surface Roughness Thickness (Å)	surface Roughness Layer		
	a-Si	c-Si	void		a-Si	c-Si	void
B-doped p-layer	0.77 ± 0.01	0	0.23 ± 0.01	24 ± 5	0.5	0	0.5 fixed
P-doped n-layer	0.44	0.26 ± 0.10	0.30 ± 0.03	128 ± 11	0.28 ± 0.03	0.22 ± 0.03	0.5 fixed

The n- and i- layers were prepared using the same conditions as for our standard midgap p-i-n cells. The performance of the n-i-p cells was assessed by depositing semitransparent metal (Cr) contacts (~150Å thick) on top of the p-layers and illuminating through the contacts. Table 14 includes the values of V_{oc} for cells with p-layers prepared using different gas mixtures. The best V_{oc} of 0.942V is obtained for the widegap p-layer prepared under the conditions (R=120, Z=0, D=0.05) which yielded purely amorphous material in the thick-film studies as is shown in Fig. 43 (open circles). This V_{oc} value is in fact ~100 meV larger than that of the standard p-layers prepared without high H_2 dilution. Figure 44 shows the results for the time evolution of void volume fraction and thickness for three n-i-p solar cells with different $Si_{1-x}C_x$ p-layers. These results were obtained in a simplified analysis of RTSE data assuming a single layer model for p-layer growth on the i-layer. The validity of this model will be discussed further in Sec. 5. The top figure shows the results for the cell in the first row of Table 14 with an intended a-$Si_{1-x}C_x$:H/μc-Si:H mixed phase p-layer whose dielectric function in thick film form is given in Fig. 43 as the squares. For this p-layer, additional carbon was incorporated using Z=$[CH_4]/[SiH_4]$=0.67. The results in the middle and at the bottom in Fig. 43 are for the high V_{oc} cells in the second and third rows of Table 14 with the purely amorphous widegap p-layer whose dielectric functions in thick film form are given by the open circles in Fig. 43. In this case, the carbon in the films comes only from the TMB dopant gas whose concentration is maintained at a lower value than those used in the other p-layer depositions as shown in Fig. 43 and Table 14. One of the goals of our research is to use RTSE for improved control of the the p-layer thickness in order to obtain the desired value of 200Å. The difference between the middle and the bottom panels of Fig. 44 is due to the difference in the p-layer thicknesses. The middle figure was obtained in a growth process without p-layer thickness control, and the results suggest that the thickness may be too large for the low carbon content p-layer cell. For the cell in the bottom figure, the thickness is controlled to be ~200Å by terminating the deposition at the correct time. The p-layer thickness control appears to account for the increase in V_{oc} from 0.89 to 0.94 V, as shown in Table 14. Figure 45(a) shows a $3\times3\mu m^2$ AFM image of the top surface for the best V_{oc} solar cell of Table 14. The root-mean-square (rms) roughness layer thickness extracted

Table 14 Open circuit voltages for midgap a-Si:H n-i-p cells prepared with different $Si_{1-x}C_x$ p-layers doped with TMB.

sample (p-layer)	H_2 (sccm)	CH_4 (sccm)	SiH_4 (sccm)	TMB (sccm)	V_{oc} (V)
mixed-phase μc-Si/a-$Si_{1-x}C_x$:H:B	120.0	0.4	0.6	0.2	0.664
a-Si:H:B:C (thickness not controlled: d=245Å)	120.0	0	1.0	0.05	0.891
a-Si:H:B:C (thickness controlled: d=199Å)	120.0	0	1.0	0.05	0.942
mixed-phase μc-Si/a-$Si_{1-x}C_x$:H:B (No H-treatment)	200.0	0.4	0.6	0.2	0.360
mixed-phase μc-Si/a-$Si_{1-x}C_x$:H:B (H_2-plasma treatment)	200.0	0.4	0.6	0.2	0.820

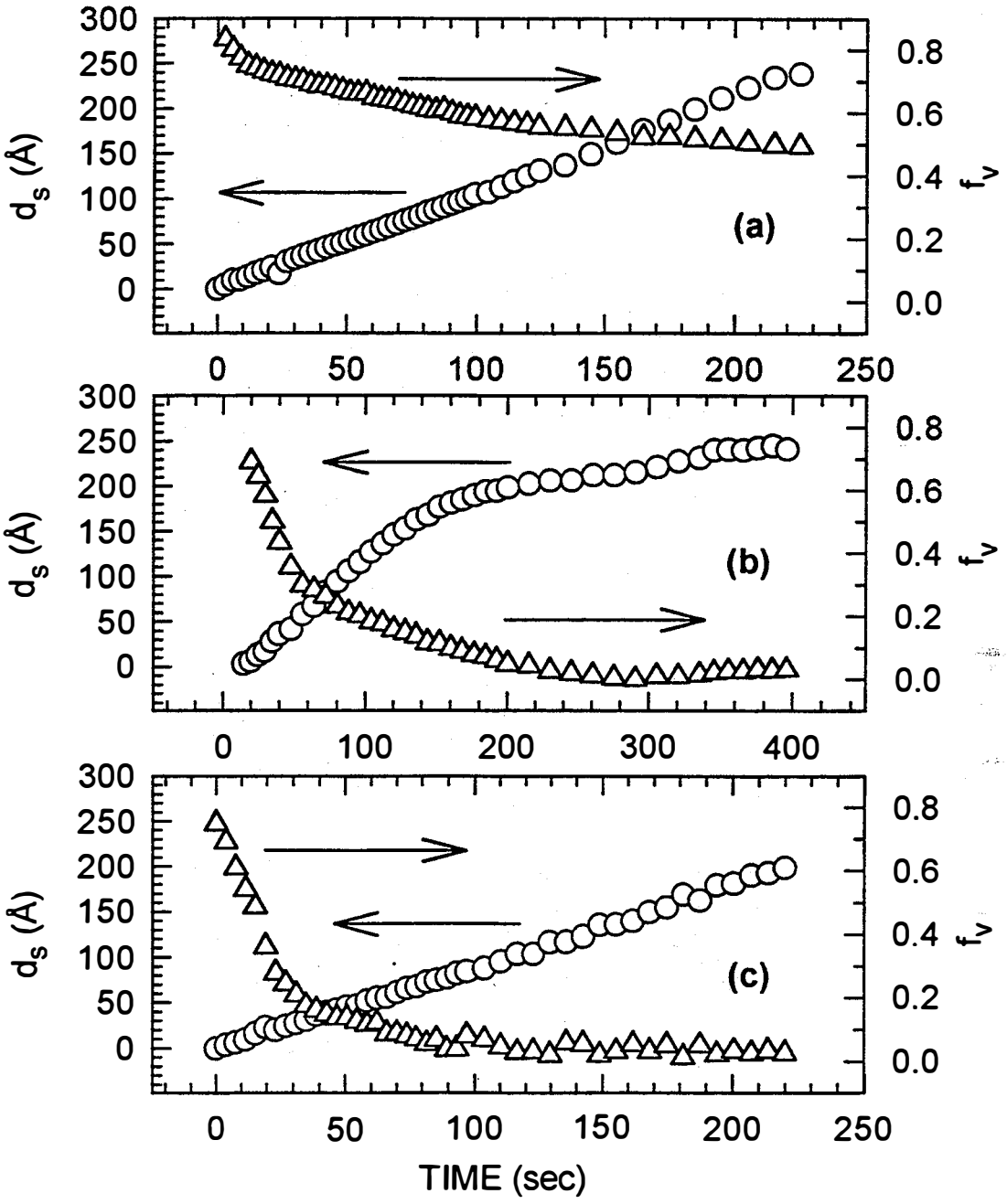

Fig. 44 Time evolution of void volume fraction and thickness for n-i-p solar cells with amorphous (middle and bottom) and microcrystalline (top) $Si_{1-x}C_x$ p-layers. For the data at the top, the cell properties appear in the first row of Table14. For the data at the middle and bottom, the cell properties appear in the second and third rows of Table 14. The p-layer compositions are same for the middle and bottom data. The only difference is the thickness of the p-layers.

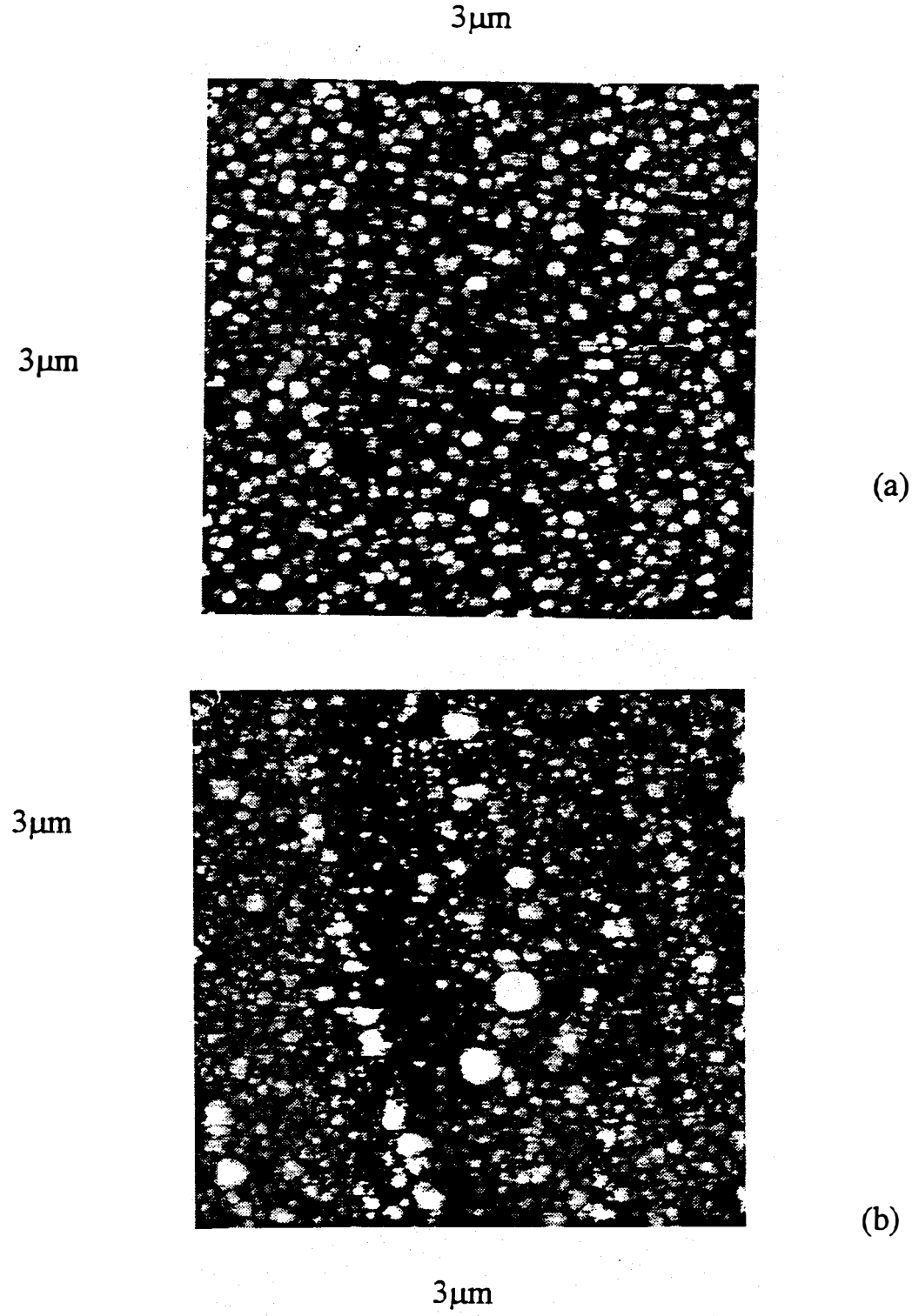

Figure 45 Surface roughness as imaged by Atomic Force Microscopy (AFM), The rms values of surface roughness deduced by the AFM measurement are 12 and 21Å for the top and bottom pictures. For the p-layer surfaces at the top and bottom, the corresponding cell properties appear in the third and fourth rows of Table 14, respectively.

from the AFM data is 12Å. From monitoring the growth of this film with RTSE we obtained a value of ~13Å for the final thickness of surface roughness based on the effective medium approximation (EMA) analysis and a two-layer model [Fig. 40].

Next, we will provide some insights into the reason why the V_{oc} is for the microcrystalline layers in the first and fourth rows of Table 14 are so low. We propose that in the initial stages of growth, carbon is incorporated into the near surface of the i-layer. This carbon stabilizes the network and thwarts the ability of the atomic hydrogen in the gas phase to penetrate the sub-surface where it is able to break Si-Si bonds and thus allowing the network to relax which leads to nucleation sites at the i-layer surface. In order to check this idea, experiments were carried out using an initial H_2-plasma treatment of the i-layer surface before p-layer growth. The results of this test are shown in Table 14 and Fig. 46. The results shown in Fig. 46 (open and filled circles) correspond to the cells given in the fourth and fifth rows in Table 14, respectively. The improvement of V_{oc} (0.36V to 0.82V) may be explained by the greatly enhanced nucleation densities of the p-layer material. For the low V_{oc} solar cell, the layer thickness is ~160Å when the void content drops below ~50 vol.%. This low density suggests that the nuclei are just starting to coalesce at 200Å, which is the final desired p-layer thickness. In contrast, for the H_2-plasma treated layer, the p-layer (filled circles in Fig. 46) reaches the critical 50 vol.% void density point at a thickness of ~90Å. In conclusion, the H_2-plasma treatment is effective in generating nucleation sites before the surface is exposed to carbon. The results in Fig. 46 indicate possible further improvement of V_{oc} (i.e., over 0.82V). The data given by the filled circles suggest that the thickness of the p-layer may be too small. Although the intended thickness was 200Å, the actual thickness is found to be ~150Å. This problem can be rectified by extending the deposition time in the next cell fabrication.

The AFM image is shown in Fig. 45(b) for the top surface of the low V_{oc} cell whose characteristics are listed in the fourth row in Table 14. The rms value of the roughness layer thickness deduced from AFM is 21Å. This result suggests that the magnitude of surface roughness for the microcrystalline p-layer is relatively high compared with the amorphous p-layer. This may be attributed to a lower nucleation density for the former p-layers, observed by comparing Figs. 44 (bottom panel) and 46 (open circles).

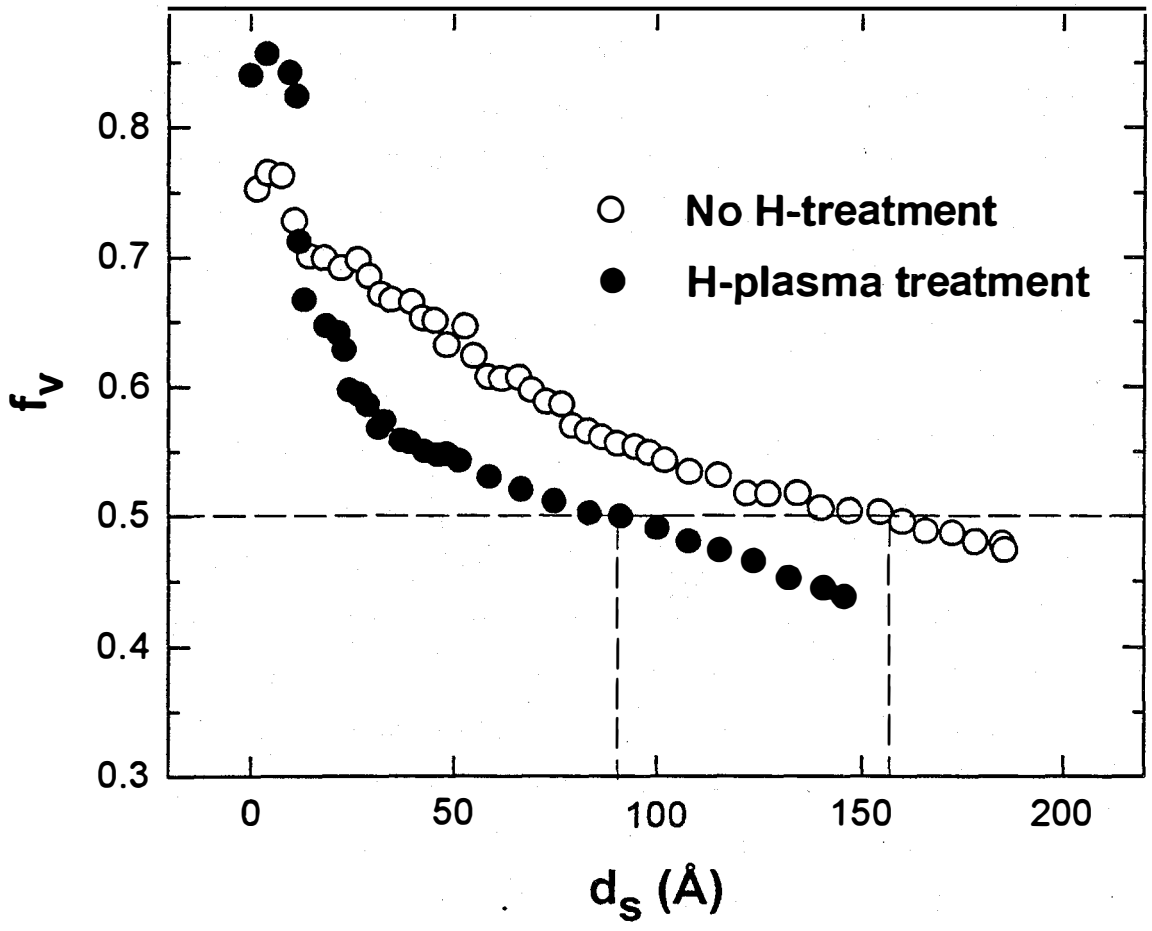

Fig. 46 Evolution of the void volume fraction with thickness for two microcrystalline $Si_{1-x}C_x$ p-layers of n-i-p solar cells. For the open and filled circles, the cell properties appear in the fourth and fifth rows of Table 14. For the data given by the filled circles, the initial i-layer surface was exposed to an H_2 plasma to enhance the p-layer nucleation.

4.3 Optical Properties of the Doped Layers in the Device Configuration

In extending the RTSE studies, we have determined the optical properties of thin microcrystalline p- and n-layers in situ in the actual device configuration. To our knowledge, this is the first time such results have been obtained. Because of this, and because of the importance of these layers in device performance and modeling, it is of interest to compare the results obtained here for the thin microcrystalline films to those obtained for their thick film counterparts and the conventional amorphous doped layers. In Sec. 4.2, we assumed that, because doped layers were microcrystalline in thick film form, their thin film counter-parts were also microcrystalline. This assumption is not necessarily correct, and must be tested on a case-by-case basis. We do this here for the p-layer in the cell given by the fifth entry of Table 14, and also for an n-layer prepared under high H_2-dilution conditions.

Figs. 47 and 48 show the dielectric functions of p- and n-type microcrystalline layers prepared with R=200 (Table 14, fifth entry) and R=50, respectively, along with the corresponding results for conventional doped amorphous layers with R=0, all obtained in the device configuration. Three points can be made concerning the differences between the two pairs of spectra. First, the doped amorphous layers have a larger dielectric function magnitude than the microcrystalline layers. This suggests a higher void volume fraction in the bulk for the latter layers. Second, the absorption onsets are shifted to higher energy for the microcrystalline films, and this provides evidence for their microcrystalline nature, even though the E^1 critical point in the dielectric functions near 3.3 eV is not evident. Third, the shift in the absorption onset for the doped microcrystalline materials leads to a significant reduction in the absorption amplitude below 2.5 eV. It is this effect that will lead to the device improvements, as long as the other doped-layer properties are not degraded. Figure 49 shows a direct comparison between the dielectric functions of the microcrystalline n- and p-type layers of Figs. 47 and 48. These results suggest that the p-type material is more defective, having higher contents of voids and amorphous component.

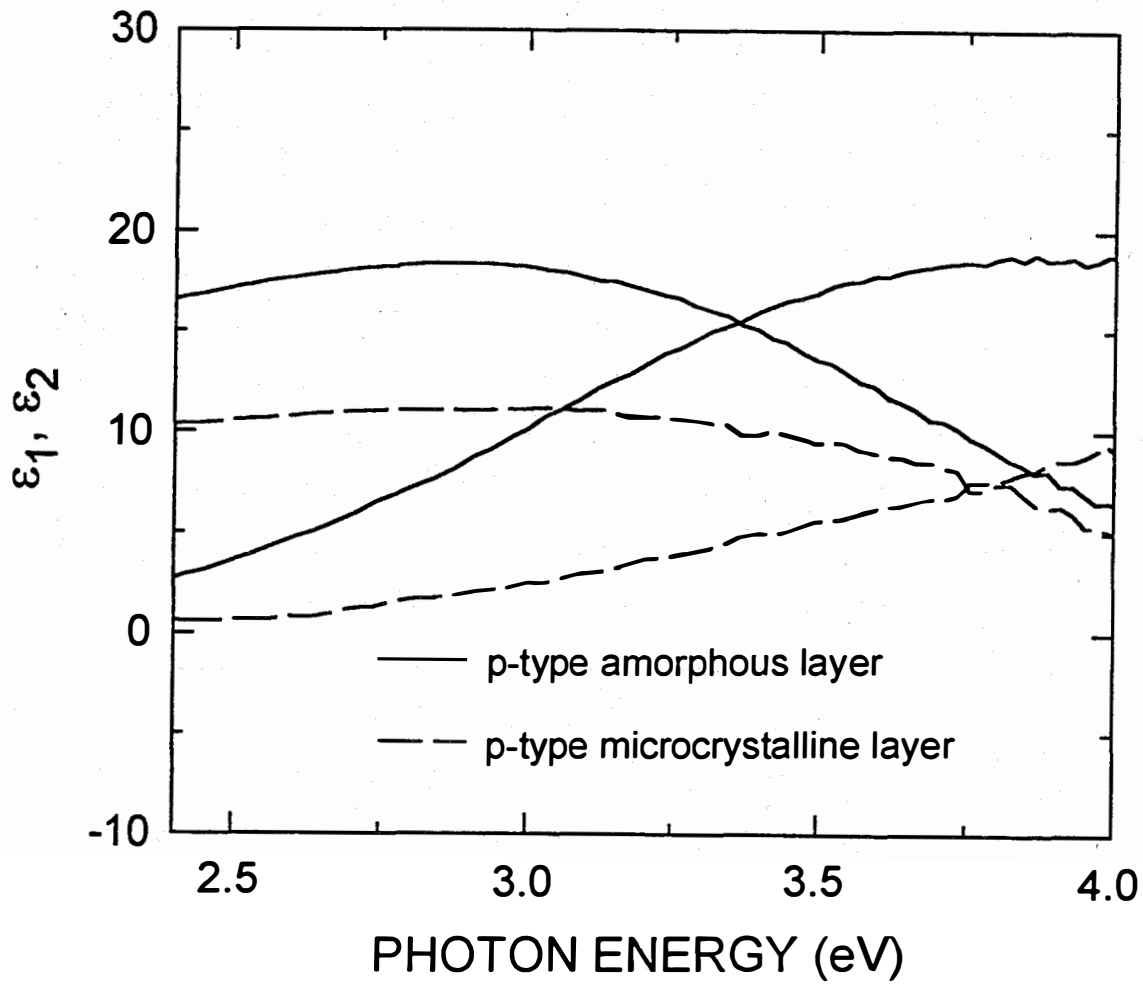

Figure 47 The dielectric function of the p-type microcrystalline layer in the cell given as the fifth entry of Table 14. This p-layer was prepared from gas flow ratios of SiH_4:CH_4:TMB:He:H_2 given by 0.6:0.4:0.2:10:200, with an rf power density of 700 mW/cm^2, and a pressure of 0.9 Torr. Corresponding results are also shown for a conventional p-type amorphous layer prepared from SiH_4:CH_4:TMB:He of 6:4:0.02:1, with an rf power density of 70 mW/cm^2, and a pressure of 0.13 Torr. All results were obtained in the device configuration.

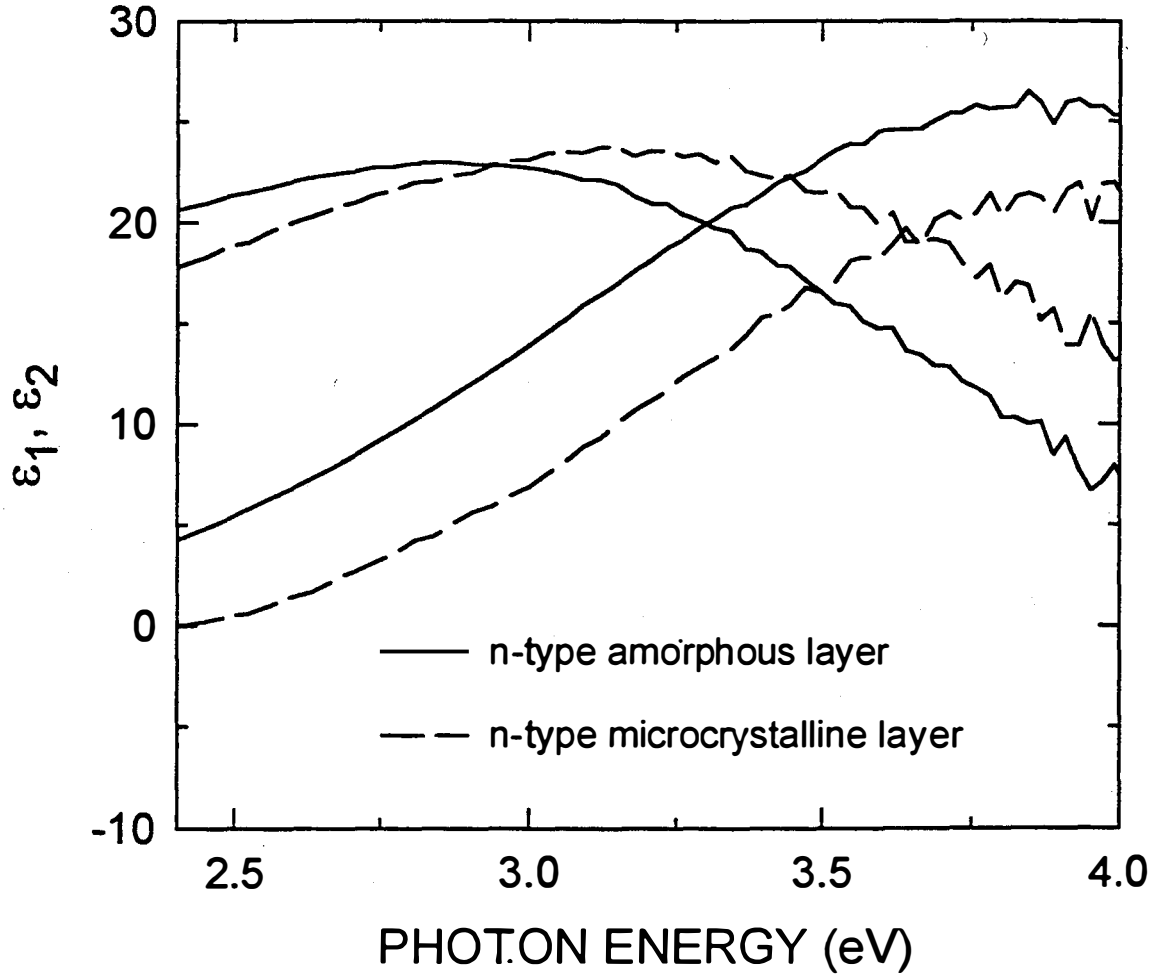

Figure 48 The dielectric function of an n-type microcrystalline layer prepared from a gas flow ratio of SiH_4:PH_3:H_2 given by 2:0.012:100, with an rf power density of 700 mW/cm^2, and a pressure of 0.5 Torr. Corresponding results are also shown for a conventional n-type amorphous layer prepared from SiH_4:PH_3 of 10:0.2, with an rf power density of 70 mW/cm^2, and a pressure of 0.12 Torr. All results were obtained in the device configuration.

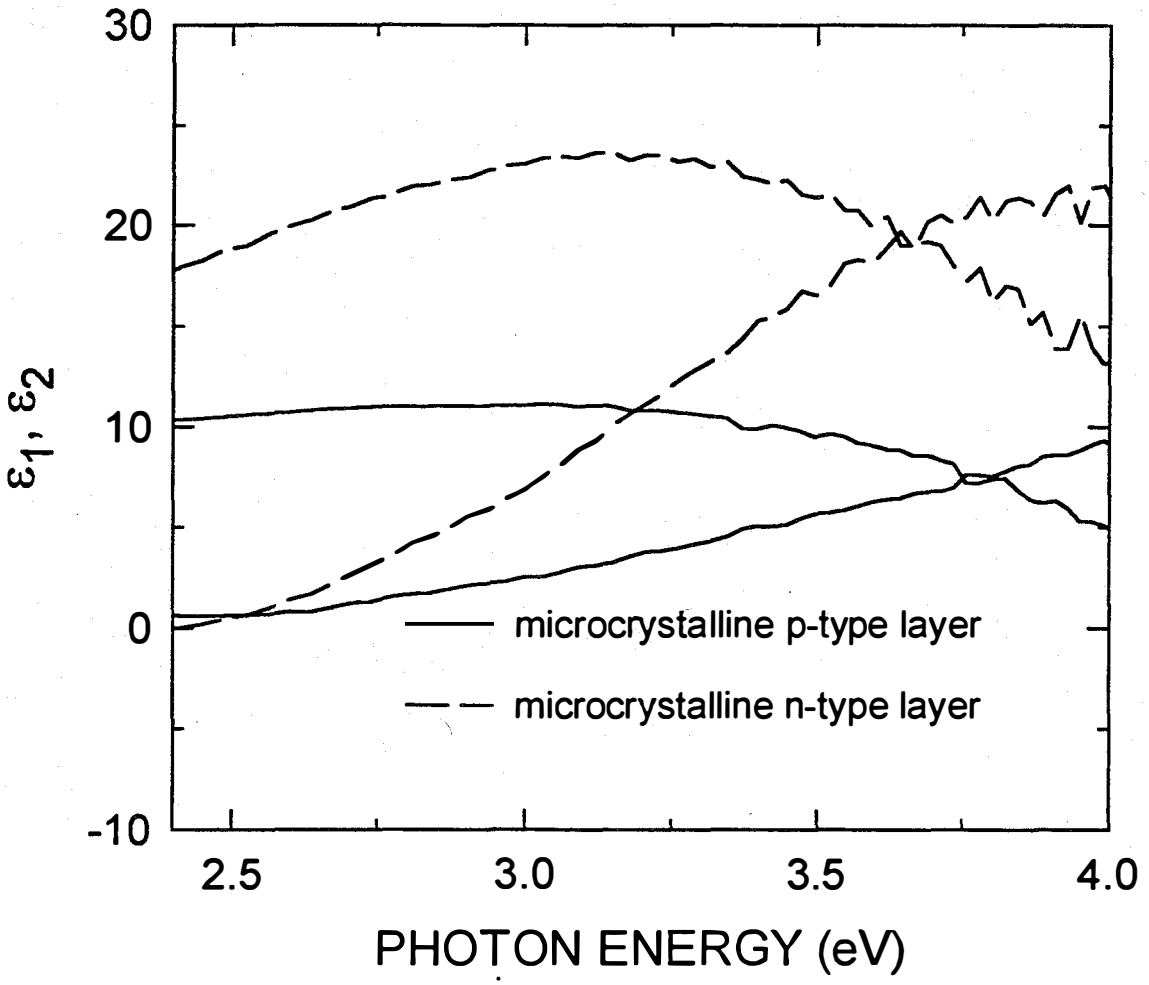

Figure 49 A direct comparison between the dielectric functions of the microcrystalline p- and n-type layers of Figs. 47 and 48. These results suggests that the p-type material is more defective with higher contents of voids and amorphous component.

Finally, in Figs. 50 and 51 comparisons are shown between the pseudo-dielectric functions of thin (200-300 Å) doped layers in the device configuration and the thick layers used for property evaluation. These data are obtained directly from the ellipsometric spectra without correcting for the surface roughness or bulk (doped-layer) transparency. The data were collected ex situ at room temperature in order to obtain a wider spectral range (to 4.8 eV) so that the sharpness of E_2 transition in Si near 4.2 eV can be assessed. Three conclusions can also be drawn from these data. First, the amplitudes of the dielectric function are reduced in the thick layers. This effect can be attributed to a much thicker surface roughness layer on the thick layers. Second, the E_2 transition is sharper in the thicker films due to the larger grain size (which also contributes to the thicker surface roughness layer). Finally, the absorption onset for the thinner films appears to be sharper. The exact origin of this effect is unclear. It is possible that quantum size effects in the smaller crystallites in the thin films generate such an effect. This leads to a blue shift of the band gap and behavior closer to that observed in direct gap materials (i.e., an abrupt absorption onset).

4.4 Collaboration with USSC in Incorporating p-Layers in n-i-p Solar Cells

Studies have been performed on the n-i-p cell structures fabricated in our multi-chamber system in addition to those fabricated in the single chamber system equipped with real time spectroscopic ellipsometry (RTSE) capabilities as reported in Secs. 4.1-4.3. The n-i-p structures fabricated so far in our multi-chamber system are summarized in the following:

T_s=200°C

1. Stainless Steel/ n^+(μc-Si)/ i(undiluted a-Si:H)/ p^+(a-SiC:H)/ ITO (by USSC)
2. Stainless Steel/ n^+(μc-Si)/ i(undiluted a-Si:H)/ p^+(a-SiC:H)/ Cr
3. Stainless Steel/ n^+(μc-Si)/ i(undiluted a-Si:H)/ p^+(μc-Si, by USSC)/ ITO (by USSC)

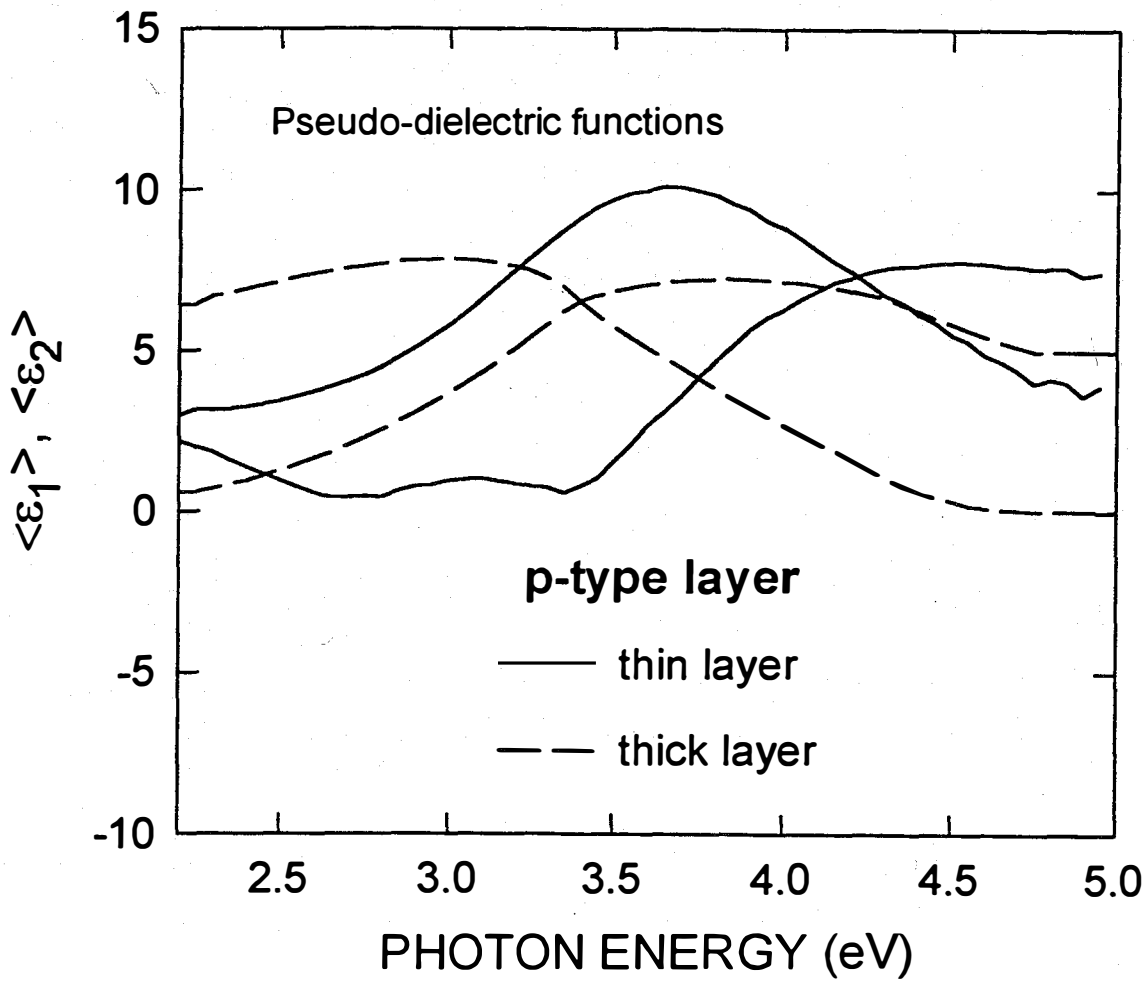

Figure 50 A comparison between the pseudo-dielectric function of the thin (~240 Å) p-layer of the cell of Table 14, fifth entry, in the actual device configuration and that of an identically-prepared thick layer (~0.5 μm) used for property evaluation. These results are obtained directly from the ellipsometric spectra (ψ, Δ) without correcting for surface roughness or doped layer thickness (hence "pseudo-dielectric function"). The data were collected ex situ at room temperature in order to obtain a wider spectral range (to 4.8 eV) so that the sharpness of the E_2 transition in Si can be assessed.

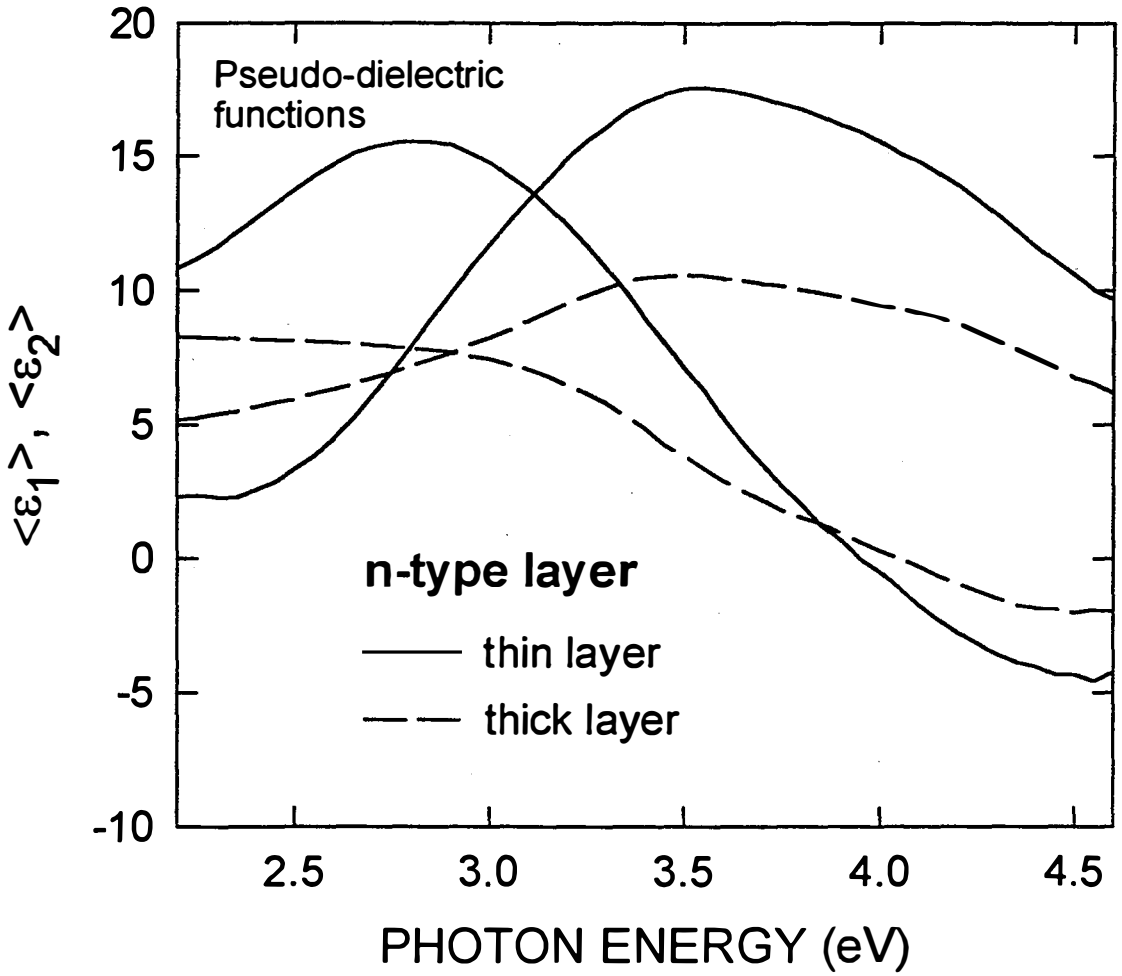

Figure 51 A comparison between the pseudo-dielectric function of a thin (~270 Å) n-layer in the device configuration and that of an identically-prepared thick layer (~1.4 μm) used for property evaluation. These results are obtained directly from the ellipsometric (ψ, Δ) spectra without correcting for surface roughness or doped layer thickness (hence "pseudo-dielectric function"). The data were collected ex situ at room temperature in order to obtain a wider spectral range (to 4.8 eV) so that the sharpness of the E_2 transition in Si can be assessed.

T_s=170°C

4. Stainless Steel/ n^+(μc-Si)/ i(diluted a-Si:H)/ p^+(a-SiC:H)/ Cr
5. Stainless Steel/ n^+(μc-Si)/ i(diluted a-Si:H)/ p^+(μc-Si, by USSC)/ ITO (by USSC)

These structures were utilized in studies related to V_{oc} in which the effects of p-contacts were investigated after the deposition of ITO at USSC. The open circuit voltages obtained with the μc-Si p-contacts (deposited after a long exposure to air between State College, PA and Troy, MI) were ~40mV higher than those with the a-SiC:H p-contacts for the diluted cells deposited at T_s=170°C and ~90mV higher for the undiluted cells deposited at T_s=200°C. It should be noted that both these n-i-p (a-SiC:H) cells had the same values of J_{sc}, V_{oc} as the corresponding p (a-SiC:H)-i-n cells. However, thus far we have not been able to obtain fill factors in the n-i-p (a-SiC:H) cells which are the same as those in the corresponding p (a-SiC:H)-i-n cells. In the p-i-n structures the fill factors are greater than 0.7, whereas in the n-i-p cells they were around 0.6 depending on the i-layers. At this time, the reason for this dramatic change is not known but studies are being undertaken to identify the causes and then to rectify them.

5. Solar Cell Interfaces

5.1 The Top Junction of the p(a-$Si_{1-x}C_x$:H)-i(a-Si:H)-n(a-Si:H) Solar Cell

We have studied *p/i* interface effects in p-i-n cells in greater detail in an attempt to understand the residual processes that give rise to small sub-monolayer level interface discontinuities in the real time ellipsometry trajectories even for optimized interfaces formed with TMB-prepared *p*-layers.

Figures 52 and 53 provide a review of the phenomena involved. In Fig. 52, we present a comparison of the trajectories in the ellipsometry parameters at 2.45 eV near the *p/i* interface for (a) a midgap a-Si:H cell incorporating an *i*-layer from pure SiH_4 and an a-$Si_{1-x}C_x$:H:B *p*-layer from a B_2H_6 doping source and (b) an a-$Si_{1-x}C_x$:H alloy cell

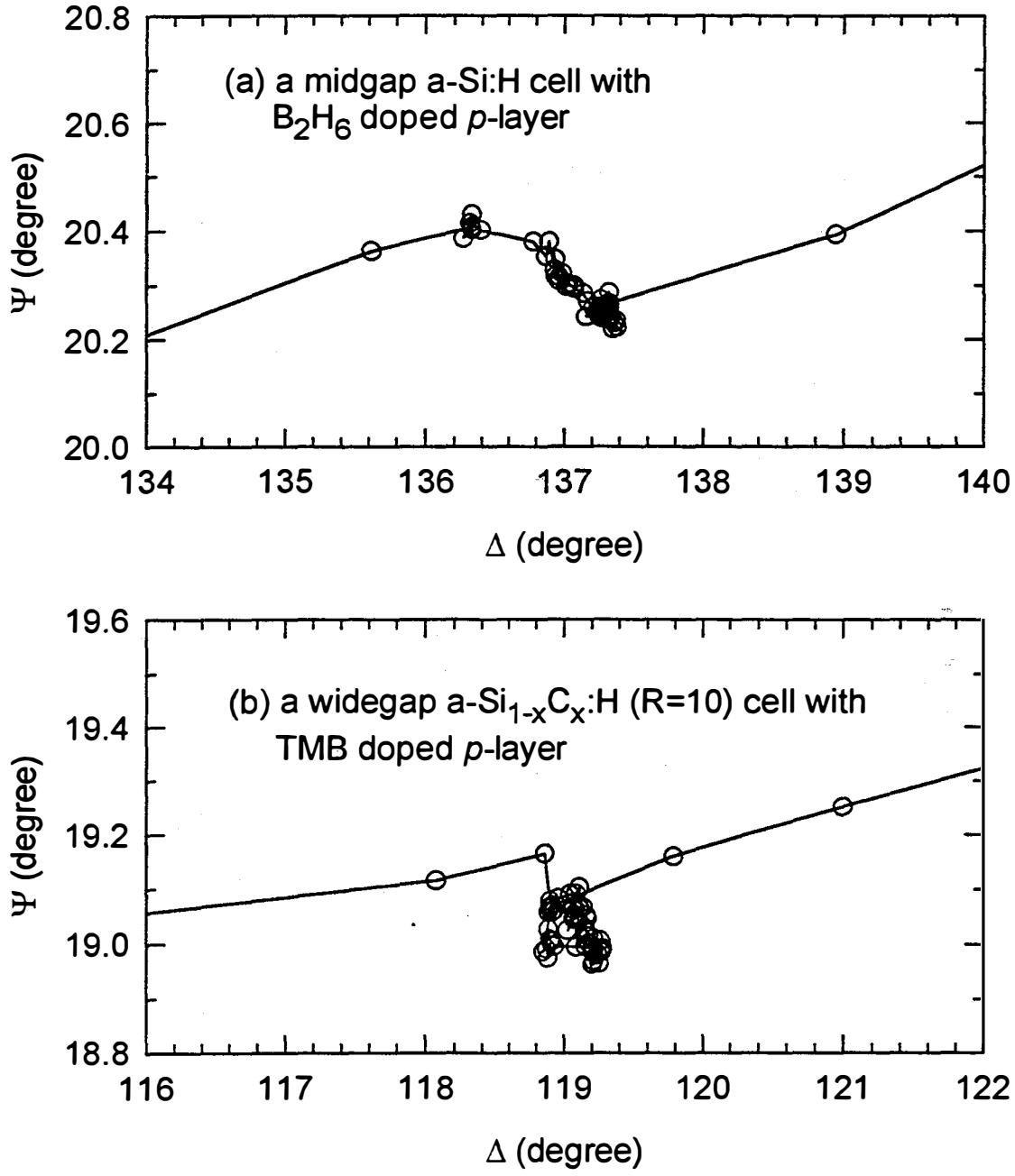

Figure 52 A comparison of the trajectories in the ellipsometry parameters (ψ,Δ) at 2.45eV near the *p/i* interface for (a) a midgap a-Si:H cell incorporating an *i*-layer from pure SiH_4 and an a-$Si_{1-x}C_x$:H:B *p*-layer from a B_2H_6 doping source and (b) an a-$Si_{1-x}C_x$:H alloy cell incorporating an *i*-layer prepared with R=10 and an a-$Si_{1-x}C_x$:H:B *p*-layer from a TMB doping source. In both cases, the *p*-layer gas is terminated at the same time as the plasma and a 50 minutes Ar^+ flush is used before bringing in the *i*-layer gas.

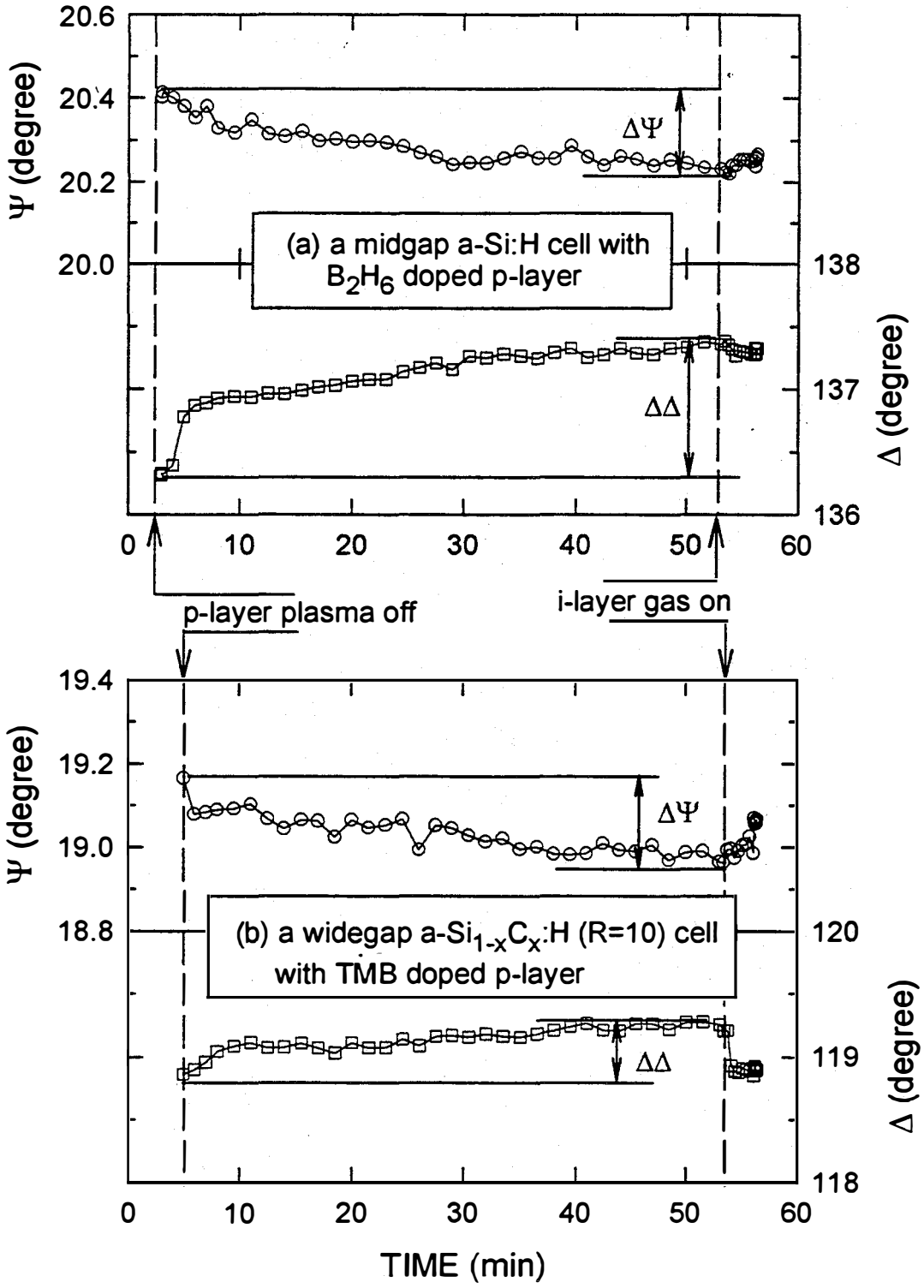

Figure 53 Time evolution of the ellipsometric parameters (ψ Δ) at 2.45eV during the *p/i* interface formation processes for (a) the a-Si:H solar cell of Figure 52(a) and (b) the a-$Si_{1-x}C_x$:H cell of Figure 52(b). The quantities $\Delta\Psi$ and $\Delta\Delta$ indicate the magnitude of the discontinuity in the data that develops between turning off the *p*-layer plasma and gas source and turning on the *i*-layer gas source.

incorporating an *i*-layer prepared with R=10 and an a-$Si_{1-x}C_x$:H:B *p*-layer from a TMB doping source. In both cases, the substrate temperature was 200°C, the *p*-layer gas was terminated at the same time as the plasma, and a 50 minutes Ar flush was performed before bringing in the *i*-layer gas. In Fig. 53, we present the time evolution of the ellipsometric parameters (ψ, Δ) at 2.45 eV during the same two *p/i* interface formation processes. In the case of the *p*-layer doped with B_2H_6, there is a >1° shift to higher Δ during the Ar flush. The resulting discontinuity in the ellipsometric angles Ψ and Δ between the end of the *p*-layer and the start of the *i*-layer is attributed to film formation on the surface during the Ar flush due to dopant gas-related contamination. This effect corresponds to the formation of a mass thickness of about a monolayer (1.7Å).

The discontinuity in Ψ and Δ between the end of the *p*-layer and the start of the *i*-layer is much weaker in the case of the *p*-layer prepared from TMB (<0.2° in Δ). However, there is still an effect that is occurring at the level equivalent to 0.1 monolayer contaminant coverage. This process has two interesting characteristics (see Figure 53): (i) a very small shift to higher Δ that occurs in the initial stages of the Ar flushing and (ii) an almost complete reversal of this shift that occurs when the *i*-layer gas (with R=10 and Z=0.67) is brought into the chamber before striking the *i*-layer plasma. In our current research, we are attempting to (i) understand these residual effects that are observed under our present optimum interface formation procedure and (ii) possibly eliminate the effects and improve interfaces even further with an appropriate processing procedure.

In the recent studies, we have made the following observations with regard to the shift to higher Δ during the Ar purge:

(1) The residual small shift to higher Δ (in the direction of film formation) as in Fig. 52(b) when the Ar purge gas is brought into the chamber is observed even when the previous film is intrinsic a-Si:H or a-$Si_{1-x}C_x$:H. As a result, this small shift cannot be attributed to dopant-related contamination. This does not invalidate our conclusions based on flushing after the B_2H_6 grown *p*-layer, since in that case the Δ shift is always much larger. [Compare Fig. 53(a) and (b).]

(2) Flowing pure SiH_4 or SiH_4+CH_4 over the surface of any amorphous material (*p*- or *i*-type; a-Si:H or a-$Si_{1-x}C_x$:H) after its deposition does not lead to any significant shift in Δ. This suggests that the shift in Δ is specific to the Ar gas flow.

Three scenarios are possible. (i) The Ar gas, because of its higher flow (100 sccm) in comparison with the reactive gases (SiH_4+CH_4; ~10 sccm), is physically sweeping contaminants from the walls. We need to perform experiments as a function of Ar flow to test this possibility. (ii) The Ar gas contains contaminants such as H_2O that react with the surface. This seems unlikely since we are using ultrapure Ar (99.9995% pure); however, with the high flow and submonolayer detectivity we cannot rule out this possibility. (iii) The Ar is being physisorbed onto the film surface.

Observations made in regard to the small shift to lower Δ during the *i*-layer gas flow are the following:

(1) The shift to lower Δ (in the direction of film removal) as in Fig. 52(b) when the *i*-layer gases are brought into the chamber is observed even when the previous film is intrinsic a-Si:H or a-$Si_{1-x}C_x$:H.

(2) The shift is due primarily to the H_2 component of the gas mixture. There appears to be an optimum pressure of H_2 for the apparent film removal process. In our a-$Si_{1-x}C_x$:H film growth process, this occurs when R=10, corresponding to a partial H_2 pressure of ~0.5 Torr.

Here again at least two scenarios are possible. (i) Molecular H_2 is physically or chemically removing weakly-bonded species from the film surface. Because of the stability of H_2, a second possibility is more likely. Namely, (ii) H_2 is being dissociated by the internal components of our heaters within the chamber and some of the atomic H is reacting with the surface to remove weakly-bound material. The optimum H_2 pressure could be related to a mean free path effect in that at lowest pressures there is a lower concentration of H_2 (and thus less atomic H), but at the highest pressures the atomic H can recombine in the gas phase before it reaches the surface.

Another interesting possibility for both the Ar and i-layer gas flushing effects is related to temperature changes at the film surface. In our initial assessment of these changes, we relied on an internal thermocouple to reach the conclusion that the sample

temperature increase during Ar flushing and the decrease during H_2 gas flow is insufficient to account for the residual changes in Δ. However, if the temperature changes at the film surface are much larger than previously thought, then our conclusion could be in error. We plan to assess these changes using c-Si as a thermometer based on optical detection, as we have done in our diamond film growth studies. An assessment of these changes is also important to the extent that the true surface and nominal substrate temperatures may be quite different under certain high flow, high pressure processing conditions. Thus, research in Phase III will be undertaken in an attempt to sort out all these possibilities and improve the *p/i* interface for improved solar cell performance.

In modeling the performance of a-Si:H p-i-n solar cells, one needs to know the basic bulk properties of the material components and how these properties are modified due to the particular conditions that exist in the formation of the actual solar cell structure. For example, in modeling cell performance, it has been found that the detailed cell characteristics can only be explained if the properties of the i-layer close to the p-i interface (first 100Å) are different than those in the bulk. For example, either a narrowing of the optical gap or an increase in the density of gap states (or a combination of both) can generate an effect needed to explain the experimental results. This is an area where RTSE can make an impact on our understanding of devices. Figure 54 shows the optical gaps for the i-layer in a p-i-n cell deduced assuming that the layer is uniform. The measurements were collected at two different stages of the growth process: (a) after 100 Å of growth on the p-layer surface, and (b) at the end of the growth process after 4500 Å is deposited. The optical gaps in these two cases differ by no more than 10 meV, which is the experimental error in the measurements. Thus, in modeling the cell performance, one cannot appeal to a band gap narrowing effect of more than 10 meV in the first 100 Å of the i-layer.

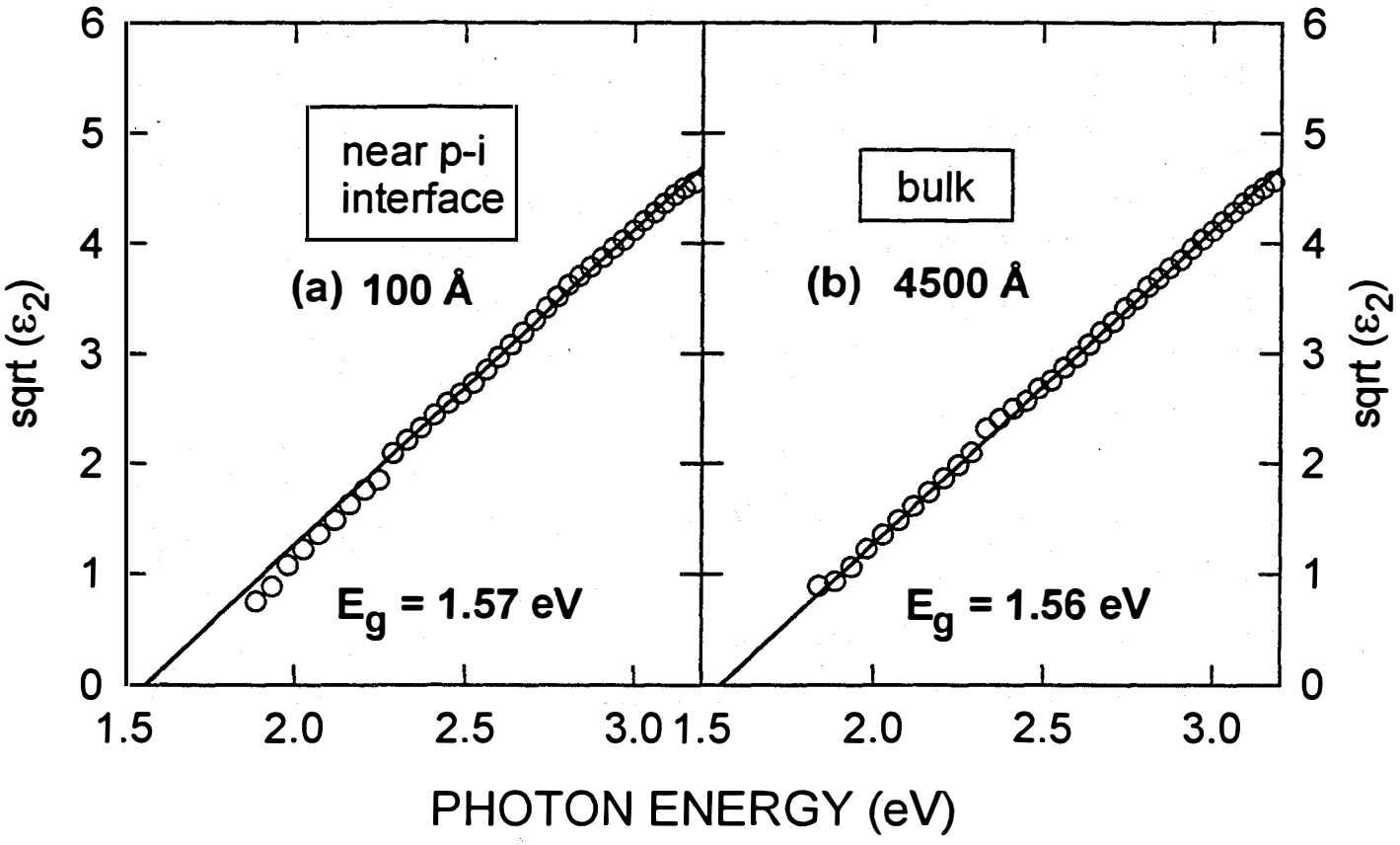

Figure 54 Optical gap determinations for the i-layer in a p-i-n cell deduced assuming that the layer is uniform. The measurements were collected at two different stages of the growth process: (a) after 100 Å of growth on the p-layer, and (b) at the end of the growth process after 4500 Å is deposited. The gaps in these two cases differ by no more than 10 meV, which is the experimental error in the measurements.

5.2 The Bottom Junction of the p(a-$Si_{1-x}C_x$:H)-i(a-Si:H)-n(μc-Si:H) Solar Cell

Although the top junction of the a-Si:H p-i-n cell is of greatest interest for improving cell performance, real time monitoring of the entire cell including the bottom junction is also of interest, especially when a microcrystalline Si n-layer is used. Figure 55 shows the microstructural evolution of a μc-Si:H n-layer prepared on an i-layer using gas flow ratios of 2:0.012:100 SiH_4:PH_3:H_2, an rf power density of 700 mW/cm^2, and a pressure of 0.5 Torr. A H_2 plasma pretreatment of the i-layer prior to microcrystalline n-layer growth was not found necessary to ensure a solar cell performance similar to that of an a-Si:H:P n-layer. In spite of this, future efforts will look into the effects of such pretreatments at the bottom junction of the p-i-n cells. Specifically, the cell of Fig. 55 showed a V_{oc} of 0.84 V, identical to that for a similarly-prepared cell with an a-Si:H:P n-layer.

Three structural parameters are shown in Fig. 55: (a) the volume fraction of additional Si-H bonds that form in the near-surface (top 200Å) of the underlying i-layer (as a result of its exposure to the H-rich plasma during nucleation of the n-layer), (b) the bulk n-layer thickness, (c) the roughness thickness on the n-layer, and (d) the volume fraction filling of the surface roughness on the i-layer to yield interface roughness between the i- and n-layers. In the analysis of Fig. 55, we assume that once the bulk n-layer begins to grow (i.e., after interface filling), the underlying i-layer is no longer modified. This approach is reasonable since it takes 30 s for the bulk layer to form, and this is about the same time required to modify the i-layer to saturation with a pure H_2 plasma under similar conditions (i.e., rf power density of 700 mW/cm_2, and a pressure of ~0.9 Torr). Figure 55 shows that in the initial 30 s, the 25 Å thick surface roughness modulations on the i-layer fill with n-layer material, the i-layer is modified such that ~0.14 volume fraction of new Si-H bonds form (corresponding to ~3.5±1 at.% additional bonded H), and the n-layer surface roughness develops to a thickness of ~25 Å. With the start of bulk n-layer formation at 30 s, the underlying structure is assumed to be stable, and the bulk layer grows linearly as a function of time with a rate of 0.77 Å/s. Concurrently, roughness on the n-layer gradually increases to a thickness

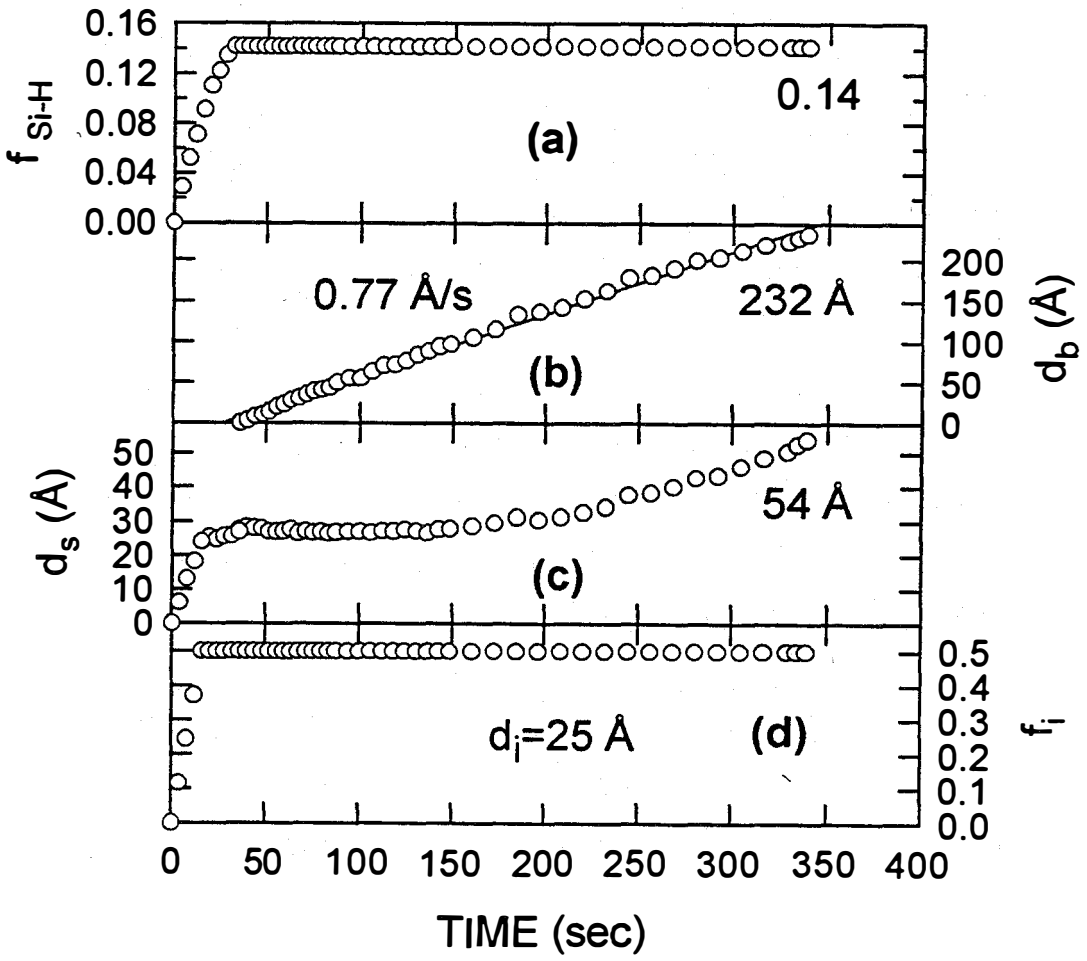

Figure 55 Microstructural evolution of a μc-Si:H n-layer prepared on the i-layer of a p-i-n cell using ratios of PH_3:SiH_4:H_2=0.012:2:100, an rf power density of 700 mW/cm^2, and a pressure of 0.5 Torr. Three structural parameters are shown: (a) the volume fraction of additional Si-H bonds that form in the near-surface (top 200-250Å) of the underlying i-layer (as a result of its exposure to the H-rich plasma), (b) the bulk n-layer thickness, (c) the roughness thickness on the n-layer, and (d) the volume fraction filling of the surface roughness on the i-layer to yield interface roughness between the i- and n-layers. In the analysis, we make the assumption that once the bulk n-layer begins to grow (i.e., after interface filling), the underlying i-layer is no longer modified. The final effective thickness of the n-layer including contributions from the interface roughness, bulk, and surface roughness layers is 272Å, which is somewhat less than the intended value of 300Å.

of 54 Å. The final effective thickness of the layer is 272 Å, which is somewhat less than the intended value of 300 Å.

Figure 56 shows the dielectric function and optical gap for the n-layer deduced in the same analysis as was used to obtained the results on the microstructure in Fig. 55. If one were to use the $\varepsilon_2^{1/2}$ approach for obtaining the optical gap, a value of 2.28 eV is obtained. This translates into a room temperature gap of 2.38 eV if the temperature coefficient of the gap for this material is the same as that of a-Si:H. In fact, measurements of the cell at room temperature yield a 2.39 eV gap, as obtained by the same $\varepsilon_2^{1/2}$ extrapolation approach. The very high value for the 200°C gap in Fig. 56 suggests that this layer is in fact microcrystalline, and that in determining the gap, the crystallites play an important role. Thus, the $\varepsilon_2^{1/2}$ approach for determining the gap is likely to be incorrect since it is based on the assumption of an amorphous material.

5.3 Top Junction *i/p* Interfaces in *n-i-p* Cells

We have prepared a series of *n-i-p* midgap a-Si:H solar cells on Cr-coated c-Si substrates held at 200°C. The depositions were performed in our single chamber system with real time monitoring by spectroscopic ellipsometry (RTSE). Both amorphous and mixed-phase microcrystalline $Si_{1-x}C_x$ *p*-layers have been incorporated into the cells. The properties of similarly prepared, but much thicker *p*-layers were presented in Table 11 above. The *n*- and *i*-layers were prepared using the same conditions as for our standard midgap *p-i-n* cells. The performance of the cells was assessed by depositing semitransparent metal (Cr) contacts on top of the *p*-layer and illuminating through these contacts.

Table 15 includes the V_{oc} values for cells having *p*-layers prepared using different *p*-layer gas mixtures. The fourth entry in the table shows the results for our standard a-$Si_{1-x}C_x$:H:B doped using TMB gas. All preparation parameters for this cell match those used for the 8.4% efficient *p-i-n* cell of Table 7, deposited in the same single chamber system. We find that the V_{oc} values for the two cells are very close (0.84 V for *p-i-n* vs. 0.83 V for *n-i-p*). At this point, Table 15 shows that the best V_{oc} of 0.94 V is obtained for

Table 15 Open-circuit voltages for midgap a-Si:H *n-i-p* cells prepared with either intended microcrystalline $Si_{1-x}C_x$ or a-$Si_{1-x}C_x$:H *p*-layers doped with TMB using preparation techniques described under Section 4.

sample (*p*-layer)	H_2 (sccm)	CH_4 (sccm)	SiH_4 (sccm)	TMB (sccm)	V_{oc} (V)
mixed-phase μc-Si/a-$Si_{1-x}C_x$:H:B	120.0	0.4	0.6	0.2	0.664
a-Si:C:H:B	120.0	0	1.0	0.2	0.726
a-Si:C:H:B	120.0	0	1.0	0.05	0.942
a-$Si_{1-x}C_x$:H:B	0	4.0	6.0	0.02	0.832

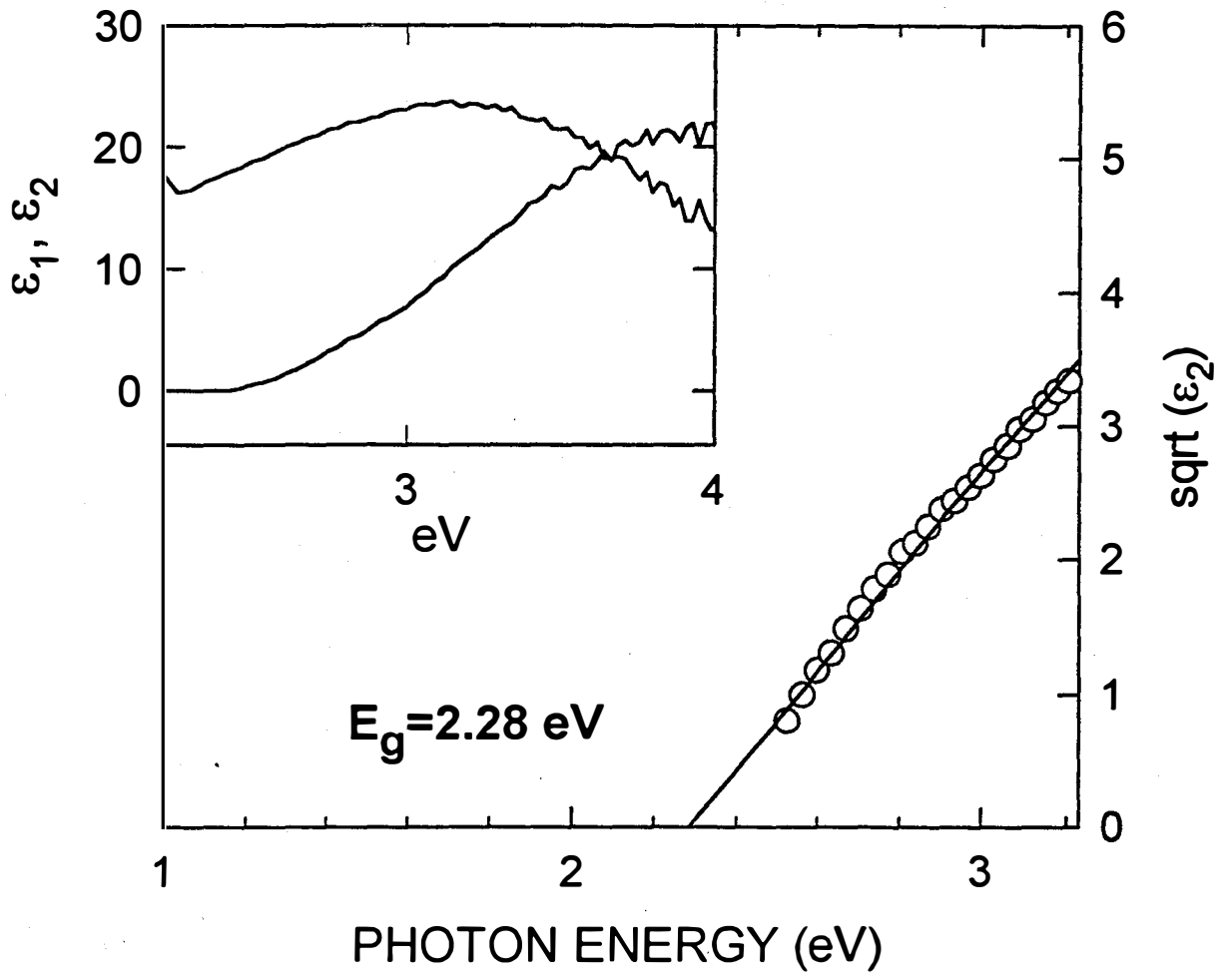

Figure 56 Dielectric function at 200°C and optical gap determination for the n-layer of Fig. 55. As usual, the optical gap is obtained by extrapolation of $\varepsilon_2^{1/2}$. The wide optical gap is attributed to the effects of Si crystallites.

an a-Si:C:H *p*-layer in which the lower doping gas ratio of D=[TMB]/{[SiH_4]+[CH_4]}=0.05 is used, and the only C in the film comes from the TMB doping gas source (*i.e.*, Z=0, so no CH_4 is added).

In the absence of RTSE measurements, very little understanding can be gained from an inspection of the results in Table 15. In the particular application of microcrystalline film nucleation, however, RTSE is a very valuable tool that can establish the directions of future optimization experiments. Earlier results reported in Sec. 3 have shown that the evolution of the layer thicknesses and the optical gaps of the separate layers can be deduced from the RTSE data. Here, we focus on the nucleation of the *p*-layer on top of the *i*-layer. For the a-$Si_{1-x}C_x$:H:B *p*-layer deposited on the a-Si:H *i*-layer (Table 15, row 4), the scale of nucleation is smaller than the *i*-layer surface roughness thickness (~20Å) and so is undetectable. In this case, the filling of the *i*-layer surface modulations by *p*-type material is the dominant observable process. In contrast, for the case of the mixed-phase μc-Si:H/a-$Si_{1-x}C_x$:H:B (Table 15, row 1), nucleation is expected to be detectable, and an approximate nucleation density and the evolution of void volume fraction with *p*-layer thickness may be extracted from RTSE data in a simplified one-layer analysis. Figure 57 shows results for the time evolution of void volume fraction and thickness obtained from the simplified analysis for two *n-i-p* solar cells with widegap *p*-layers. The results at the top are for the cell of the first row of Table 15 in which the p-layer is a mixed-phase μc-Si/a-$Si_{1-x}C_x$:H material and additional C was incorporated into the *p*-layer using Z=[CH_4]/[SiH_4]= 0.67. The results at the bottom are for the highest V_{oc} cell of the third row of Table 15. In this latter case, the p-layer is purely amorphous (a-Si:C:H:B) and the only C in the film comes from the TMB dopant gas which is maintained at a lower flow ratio than for any of the microcrystalline *p*-layer depositions.

A comparison of the results in the two panels of Figure 57 provides some insight into the reason why V_{oc} for the high C-content microcrystalline layer is so low. At the end of the deposition when the high C-content microcrystalline *p*-layer reaches ~220Å, the layer still contains ~50 vol.% voids. This low density suggests that the nanocrystal nuclei are just starting to make contact. If the nuclei were hemispherical in shape and arranged on a square grid, 50% voids in a 22 Å thick film would imply an average spacing of

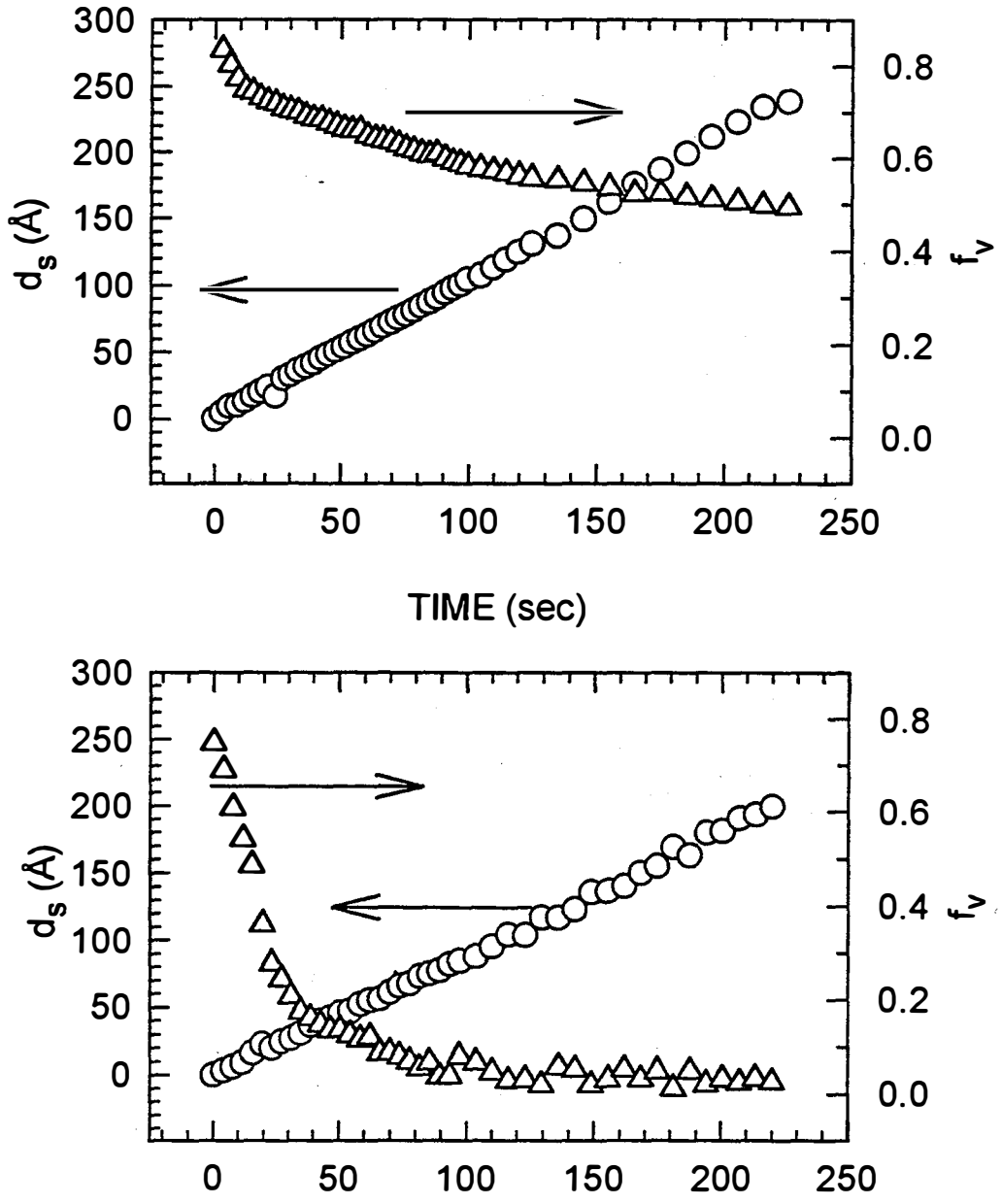

Figure 57 Time evolution of void volume fraction and thickness for two *n-i-p* solar cells with widegap *p*-layers. For the data at the top, the cell properties appear in the first row of Table 15. In this case, the layer is mixed-phase (μ-Si + a-$Si_{1-x}C_x$:H) and additional C was incorporated into the *p*-layer with Z=[CH_4]:[SiH_4]=4/6. For the data at the bottom, the cell properties appear in the third row of Table 15. In this case, the layer is a-Si:C:H:B and the only-C in the film comes from the TMB dopant gas.

~400-500Å between nuclei. Because the nuclei are actually randomly distributed, we expect that there will remain some regions of the *i*-layer that have not been covered by *p*-type material. Such a microstructure would give rise to *p*-layer shunting and could account for the low V_{oc}. In contrast, the a-Si:C:H:B *p*-layer reaches the critical 50% density point only after about 30Å. In fact, after ~200Å, a bulk density structure is reached. Thus, we attribute the improvement in V_{oc} from 0.66 to 0.94 V for the *n-i-p* cells to an enhancement in the nucleation process for the amorphous p-layer. This enhancement leads to a thinner film at which coalescence occurs and a denser microstructure in comparing films of similar thickness.

We have studied the role of H_2-plasma treatments in improving the nucleation of widegap microcrystalline p-layers on the i-layers of a-Si:H midgap n-i-p solar cells. Figure 46 shows the effect of a H_2-plasma treatment of the i-layer on the initial nucleation of a microcrystalline p-layer. The preparation conditions for the p-layer in this case are given in Table 10 (second and third entries) and discussed further in Sec. 4. The H_2-plasma treatment was performed for about 2 min using the same plasma power as is used for p-layer preparation (10 times higher than that used for the i-layer). In Figure 46, the void volume fraction in the nucleating film is plotted versus film thickness. In this way, one can obtain a good relative estimate of the thickness at which nuclei make contact ("contact thickness"). The contact thickness is obtained as the thickness at which the void volume fraction drops below 0.5. We have proposed that the factor of two reduction in the contact thickness that occurs as a result of the H_2-plasma treatment leads to a more completely covered i-layer surface and the significant increase in V_{oc} from an unacceptably low value of 0.36 V to a more reasonable value of 0.85 V. However, as mentioned above, even with the H_2-plasma treatment and microcrystalline growth conditions, we have been unable to raise V_{oc} above 0.90 V. Although we have mentioned that the source of the problem could be the TMB-doped microcrystalline p-layer (sec. 4), an unoptimized H_2-plasma treatment may also cause the problem.

We have begun to study the H_2 plasma treatments in greater detail, comparing their effects to the filament-treatments that we have developed earlier. In fact, Figure 58 includes the evolution of the Si-H bond volume fraction in the top 200Å of an a-Si:H

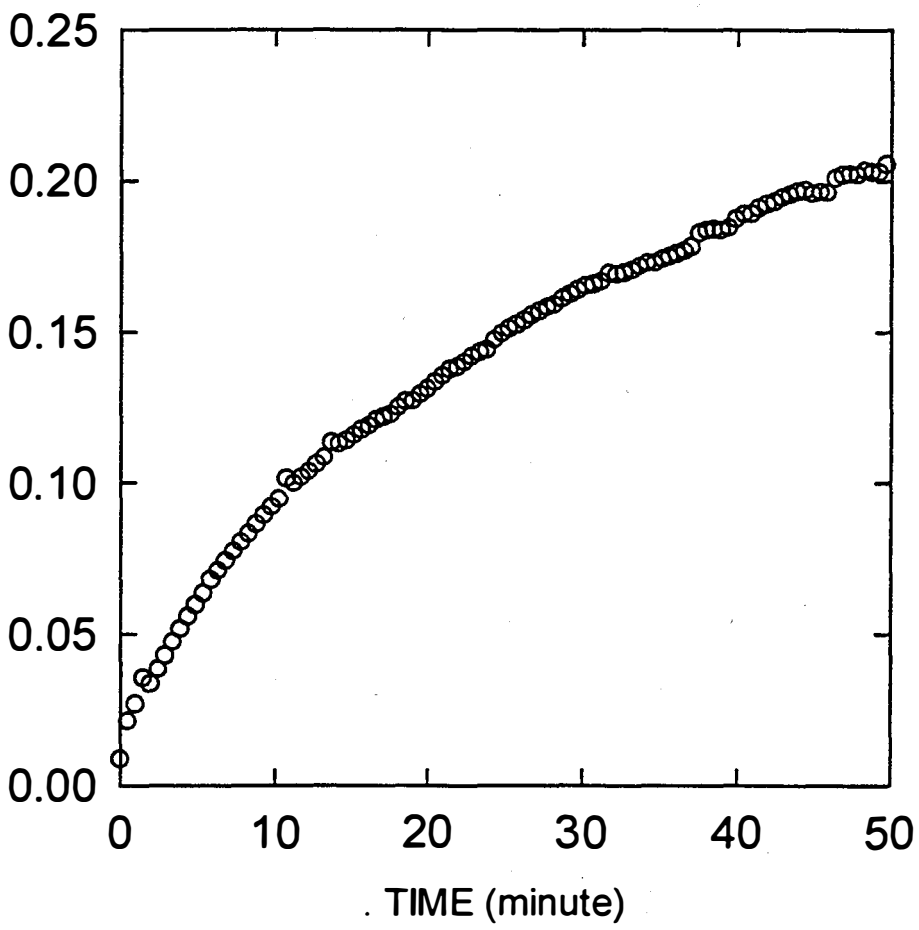

Fig. 58 Si-H volume fraction versus time deduced from an RTSE analysis of data collected during filament-generated H_2-treatment of an a-Si:H i-layer at 250°C. The surface roughness remained constant throughout this process.

i-layer during exposure to filament-generated atomic H at 250°C. In this case, no significant increase in surface roughness is detected during the exposure, and ~1000 s is required before the Si-H content reaches one-half its saturation value. (The saturation value is reached after 60 min.) We also note that infrared and SIMS measurements reveal that the additional incorporated H-content in at.% is ~3-5 times lower than the Si-H bond volume fraction deduced from RTSE. In Fig. 59, the corresponding results for the i-layer H_2-plasma treatment is shown. In this case, only ~5 s is required before the Si-H volume fraction reaches one-half its saturation value. (Saturation is reached after 30 s in this case.) In contrast to the results obtained for the filament treatment, significant roughening occurs over time. The roughness increases from its initial value of 25Å to 60Å after the two minute exposure. The role of the roughening effect on the nucleation of the p-layer is unclear. In future work, we plan to compare the nucleation and growth of p-layers on i-layers exposed to H_2 plasma and filament treatments.

In an attempt to understand the nature of the H_2 plasma-reduced roughening effect in Fig. 59 (bottom), we performed atomic force microscopy (AFM) on i-layers exposed to the H_2 plasma. Figure 60 shows 1x1 μm_2 tapping mode AFM images of a control i-layer (top) and an H_2-plasma-treated i-layer (bottom). All such images reveal rms roughness values of 11Å, and no differences between the H_2-treated and control surfaces were detected within the resolution limit of the AFM (~100 Å; controlled by the tip). This suggested that the H_2 plasma-induced roughening of the a-Si:H i-layer surface occurs at very small lateral scales, most-likely at the atomic level. It is possible that such atomic scale roughness is the effect that leads to a high p-layer nucleation density; however future studies are needed to lend further support to this idea. The observations of Fig. 60 are also important for the accurate analysis of the RTSE data to be discussed next.

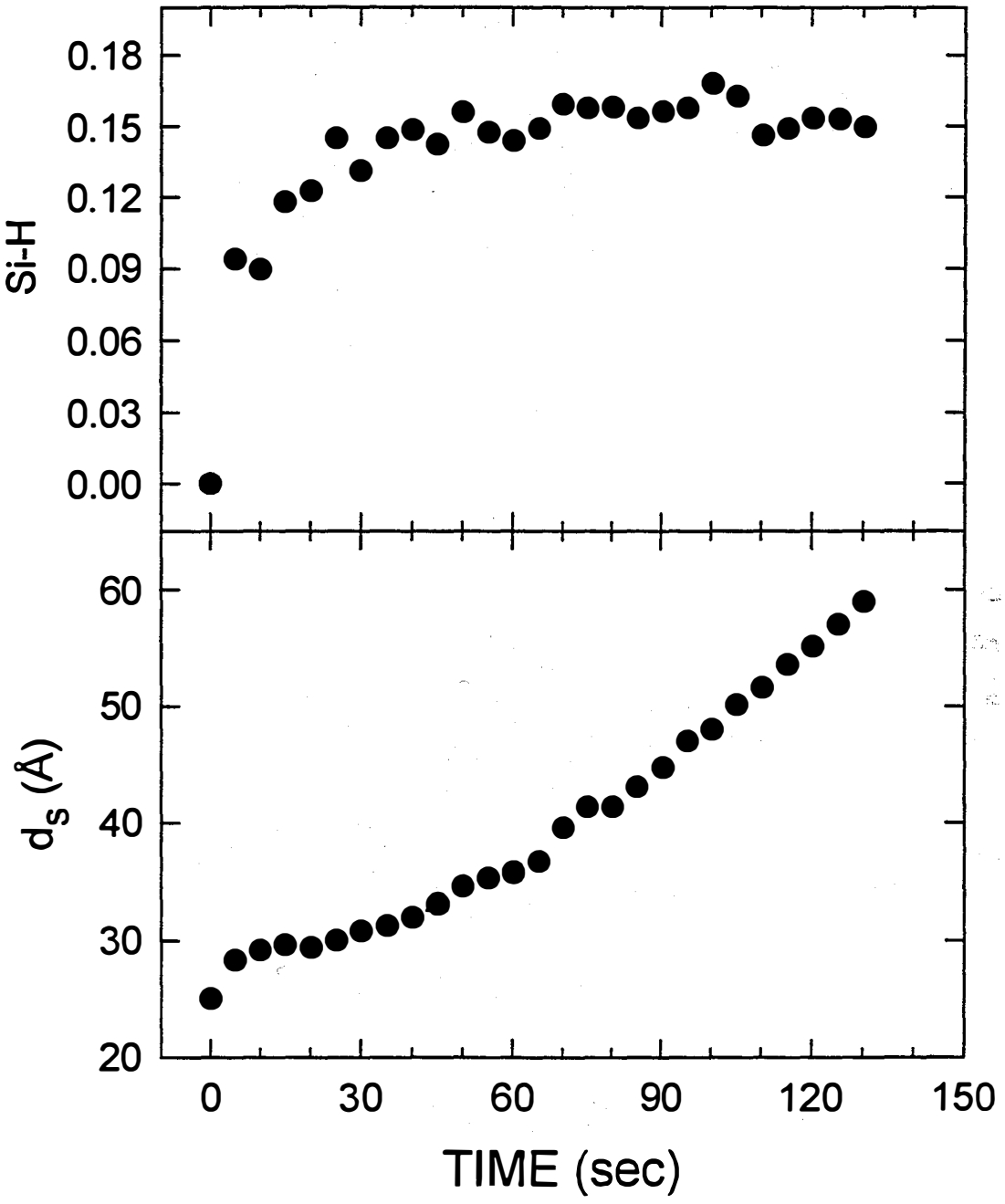

Fig. 59 Si-H volume fraction and surface roughness layer thickness versus time deduced from an RTSE analysis of data collected during H_2-plasma treatment of an a-Si:H i-layer. The plasma conditions are the same as those used for i-layer treatments in the n-i-p solar cells of Table 10.

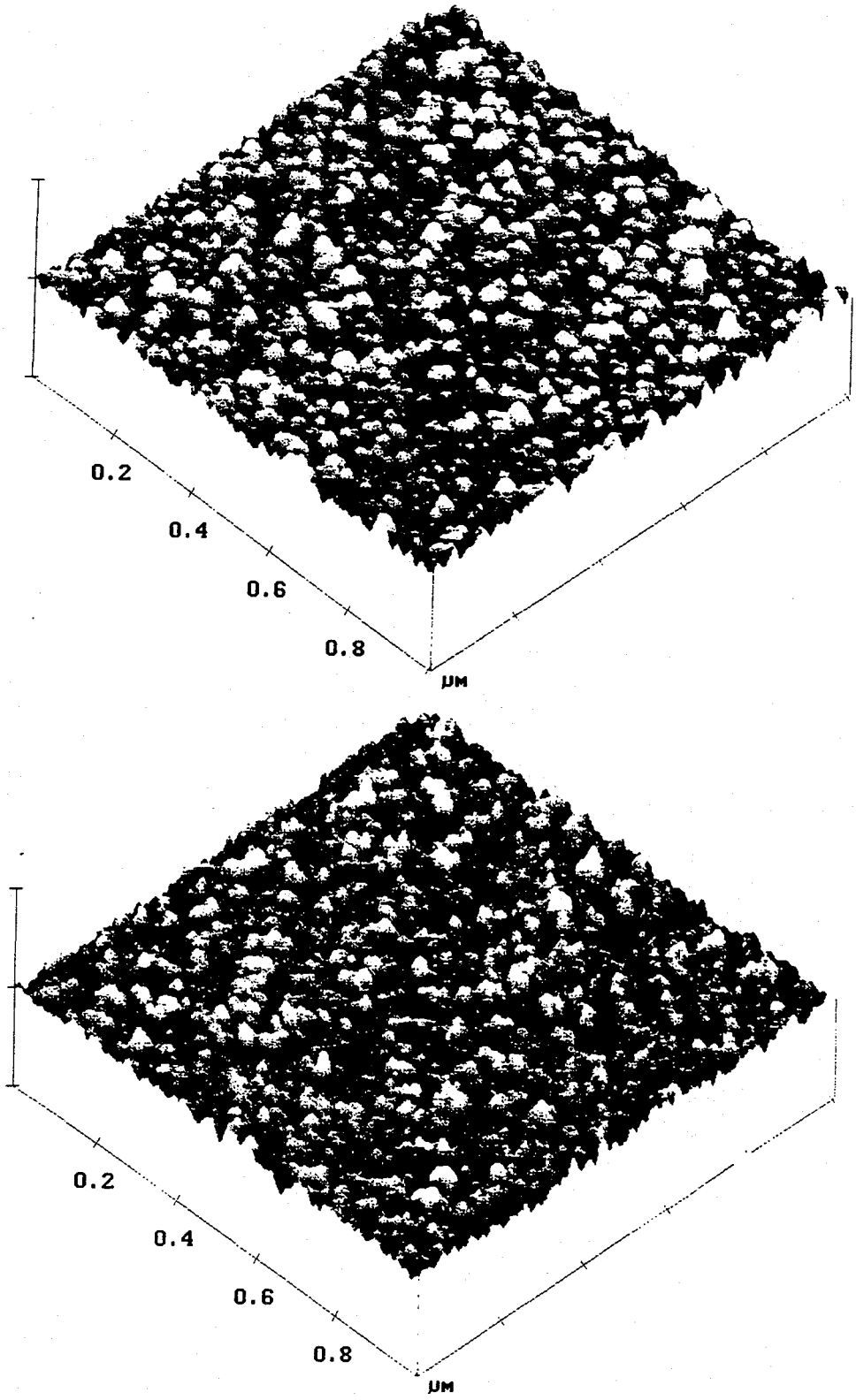

Figure 60 AFM images over a 1x1 μm^2 area, obtained in tapping mode, for an i-layer used as a control (top) and an i-layer treated with an H_2-plasma. The two images reveal rms roughness values of 11Å.

5.4 Real Time Spectroscopic Ellipsometry Characterization of Top Junction Formation for the n(a-Si:H)-i(a-Si:H)-p(μc-Si:H) Solar Cell

In Sec. 4, we described the development of mixed-phase μc-Si/a-$Si_{1-x}C_x$:H p-type films using high H_2 dilution in the PECVD growth process. These films were also incorporated into n-i-p solar cells. In Secs. 4 and 5.3, several capabilities for characterizing the p-layer process were developed. First, we applied ex situ SE to characterize the crystallinity of thick microcrystalline p-layers, using (i) an effective medium theory to estimate the crystalline Si content, and (ii) a critical point analysis of the E_1 and E_2 transitions to estimate relative crystallite sizes. Second, we developed a very simple analysis to characterize the nucleation behavior for microcrystalline p-layer on i-layer deposition based on real time SE. In this simple analysis, we plot the void volume fraction (f_v) versus p-layer thickness (d) assuming a one-layer model for the i/p structure. The thickness at which f_v drops through 0.5 is an approximate measure of the thickness at which p-layer nuclei (assumed to be crystallites) make contact. This critical thickness d_c has been observed to correlate with V_{oc}. The apparent origin of this correlation is that when d_c is very high (>100Å), the film is expected to be incompletely coalesced after 200Å, the optimum p-layer thickness, and this can lead to the low V_{oc}.

The simple RTSE analysis in which f_v is determined as a function of d in the early nucleation stage of the microcrystalline p-layer is important because of the correlation with V_{oc}; however, the model lacks two critical features. First, we need to determine the final effective thickness of the p-layer, which in most cases is modeled using an interface roughness layer, a bulk coalesced layer, and a surface roughness layer on top. Earlier results in Sec. 4 have demonstrated the need for accurate thickness control for our wide-gap a-Si:H:C p-layers in order to optimize cell performance. Second, we also need to determine the optical properties of the p-layer in the actual device configuration, which will not necessarily be the same as those in the thick layers due to a thickness dependence of the grain size and the overall microstructure. A preview of these results was given in Sec. 4.3.

As a result, we have developed a detailed analysis of microcrystalline p-layer growth on the i-layer, including a H_2-plasma pretreatment, which allows us to determine not only the layer thicknesses throughout the growth process, but also the optical properties of the p-layer in the device configuration. Figure 61 is a multi-part figure that summarizes the microstructural evolution not only during the H_2 plasma pretreatment of the i-layer, but also during p-layer growth on the modified i-layer for an n-i-p solar cell. The i-layer of this cell was prepared at 200°C without H_2-dilution at an rf power density of 70 mW/cm^2 and a pressure of 0.18 Torr. The p-layer was prepared from a gas flow ratio of SiH_4:CH_4:TMB:He:H_2 of 0.6:0.4:0.2:10:200, with an rf power density of 700 mW/cm^2, and a pressure of 0.90 Torr. A 133 s H_2 plasma treatment was performed between the i- and p-layer preparation using conditions identical to that of p-layer growth, but in the absence of the SiH_4, CH_4, and TMB:He gases. As noted in the previous section, the H_2 plasma treatment serves to increase the nucleation density which in turn leads to an increase in V_{oc}.

In Fig. 61(a), we show the evolution of the Si-H bond volume fraction versus time measured within the top ~200-250 Å of the i-layer during H_2 plasma exposure. The Si-H bond volume fraction is proportional to the increase in the number of Si-H bonds per unit volume and is a factor of ~3-5 higher than the increase in the H content in at.%. Thus, the rapid increase in the Si-H volume fraction to 0.14 indicates an increase in the H-content in the near-surface by 3.5±1 at.%. This hydrogenation effect is rapid and follows reaction limited kinetics with a rate constant of about 15 s. Figure 61(b) shows the surface roughness evolution on the i-layer during exposure to the H_2 plasma. Before the plasma exposure, the roughness thickness is 28Å. This roughness essentially arises from the modulations on the Cr film which is used as the back contact. There is little roughness increase (~5Å) in the first 60 s when the atomic H from the plasma penetrates the i-layer and the hydrogenation effect saturates [see Fig. 61(a)]. However, the roughness builds up on a longer time scale and increases linearly with time, reaching a thickness of 51Å after 133 s. The AFM results of Fig. 60 show that this roughness exists on a very small lateral scale. In fact, we suggest that the additional 23Å roughness induced by the H_2 plasma treatment consists of a layer of atomic-scale surface-connected microvoids conformally

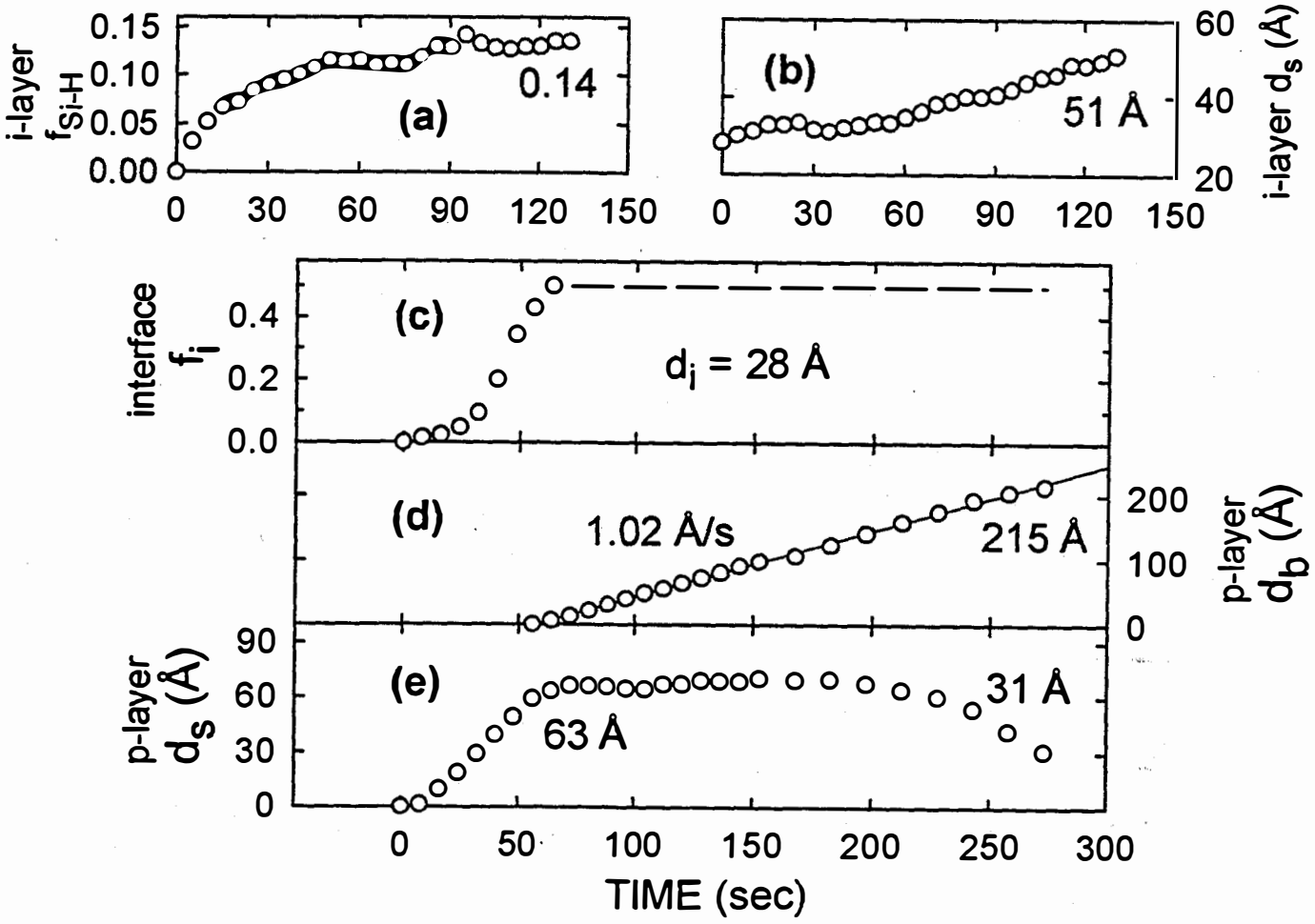

Figure 61 Microstructural evolution for an n-i-p solar cell deduced from real time SE data collected during (a-b) H_2 plasma treatment of the i-layer and during (c-e) p-layer growth. The p-layer was prepared from gas flow ratios of SiH_4:CH_4:TMB:He:H_2 given by 0.6:0.4:0.2:10:200, with an rf power density of 700 mW/cm^2, and a pressure of 0.9 Torr. A 133 s H_2 plasma treatment was performed between the i- and p-layer preparation using conditions identical to that of p-layer growth, but in the absence of the SiH_4:CH_4 and TMB:He gases. At the top, the time evolution of (a) the Si-H bond volume fraction measured within the top ~200-250Å of the i-layer and (b) the surface roughness layer thickness are plotted, both obtained during H_2 plasma exposure. In (c)-(e), the microstructural evolution of the p-layer is plotted including (c) the filling of the modulations in the i-layer surface roughness by p-layer material, (d) the evolution of the p-layer bulk thickness, and (e) the evolution of the p-layer surface roughness. Accounting for the material in all three layers of the p-layer structure (bulk, interface, and surface), yields a final effective thickness of 244Å.

covering the 28Å thick modulations of the i-layer surface. Two other effects besides H-modification (top ~200Å) and microvoid formation (top ~20Å) are expected to occur during the H_2 plasma treatment (based on our studies of filament-generated H-treatments). These two effects are more difficult to detect: (i) near-surface crystallization of the a-Si:H where the porosity is highest (top 10-20Å) and (ii) etching (or thickness reduction) of the i-layer. Further studies of H_2-plasma treatment of thinner i-layers will allow us to extract this information.

In Figs. 61(c)-(e), we show the microstructural evolution of the p-layer including (c) the filling of the long range, 28Å thick modulations in the i-layer surface by p-layer material (leaving the 23Å thick microvoid layer buried at the interface as suggested by the AFM results of Fig. 60), (d) the evolution of the bulk p-layer thickness, and (e) the evolution of the surface roughness on the p-layer. This combination of results shows a short "induction time" of ~10 s during which very little material forms. Then the p-layer begins to form as indicated by p-layer filling of the i-layer roughness and by the development of p-layer roughness which simulates nuclei. In the first 60 s, no bulk layer has formed and all that occurs during this period is roughness development and interface filling consistent with nucleation on a modulated surface. After 60 s, the first monolayers of the bulk film form. At this point the i-layer roughness is completely filled in and the surface roughness on the p-layer reaches its maximum. In the bulk film growth regime, the bulk p-layer increases linearly with thickness as the roughness first stabilizes, then decreases with time. The growth rate of the p-layer is found to be 1.02 Å/s. The final bulk and surface roughness thicknesses for the p-layer are 215 and 31Å, respectively. Adding the p-layer components of the three layers (bulk, interface, and surface), we arrive at an effective thickness of 244Å, which is higher than the intended value of 200Å. However, with this measurement we have calibrated the p-layer growth rate, and this provides a deposition time that will yield 200Å in the next run. Thus, further optimization of this cell structure may yield device performance improvements.

Figure 62 shows the results of the simplified analysis for the same p-layer growth as in Fig. 61. The simplified analysis neglects the roughness on the i-layer and treats the initial stage of growth in terms of a single layer model in which the nucleating film has a

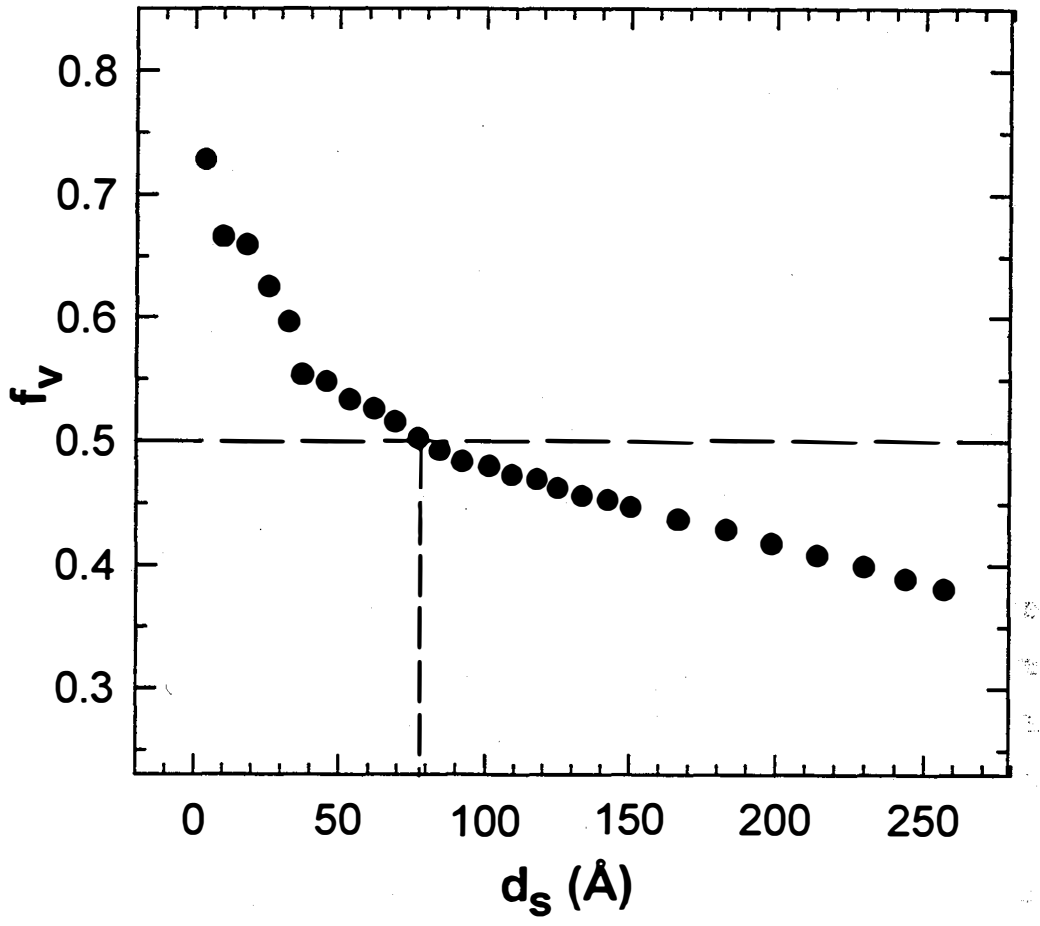

Figure 62 The void volume fraction versus thickness for the same p-layer as in Fig. 61 obtained in a simplified analysis of real time SE data collected during growth. The simplified analysis neglects the roughness on the i-layer and treats the initial stage of p-layer growth in terms of a single layer model in which the film has a variable void volume fraction. The thickness at which the void volume fraction drops below 0.5 is a measure of the p-layer nuclei contact thickness.

variable void volume fraction. The simplified analysis yields a p-layer thickness at which nuclei make contact of 78Å, whereas the more complete analysis yields 63Å. This provides an estimate of the possible error in the simplified analysis used earlier.

In addition to the microstructural changes that occur as shown in Figs. 61 and 62, we can also determine the optical properties associated with the H_2-plasma treated i-layer and the bulk p-layer. In both cases, the optical properties are characteristic of the processing temperature of 200°C. First in Fig. 63, we show the optical gap shift in the top 200-250Å of the i-layer that is induced by the 133 s H_2-plasma exposure. Corrections are made for both the microvoid and modulated roughness layers on the surface. Here, the optical gap is obtained by the Cody method of $\varepsilon_2^{1/2}$ extrapolation. The high energy data for the gap measurement are the most reliable since the low energy photons penetrate into the unmodified region (deeper than 250Å); thus, the curves tend to converge at low energy. From these data, we estimate an optical gap shift of 0.08±0.02 eV in the top of the i-layer whereby the $\varepsilon_2^{1/2}$ gap at 200°C increases from about 1.60 to 1.68 eV. This corresponds to an increase in the Tauc gap at 25°C from 1.78 to 1.86 eV. Such an effect is important in modeling the performance of the resulting solar cells. Second, in Fig. 64, we show the 200°C dielectric function and optical gap determination for the p-layer. Although the dielectric function shows no features of a c-Si structure (normally evident as a peak or shoulder near 3.3 eV), one observation suggests a difference between this material and conventional a-$Si_{1-x}C_x$:H:B. An $\varepsilon_2^{1/2}$ plot yields a gap of 2.04 eV, which is much higher than the 1.72 eV value observed for a similarly-prepared a-$Si_{1-x}C_x$:H:B material (the primary difference being that the H_2-dilution ratio is R=200). Thus, it is possible that this material is composed of very small nanocrystallites in an a-$Si_{1-x}C_x$:H matrix. The wider gap may be due in part to quantum size effects, and the extrapolated room temperature gap of ~2.1 eV would be consistent with red luminescence seen in Si nanocrystals.

In spite of the apparent desirable properties of the top junction, namely a H-modified near-surface i-layer with a room temperature $\varepsilon_2^{1/2}$ gap of 1.86 eV and a top microcrystalline p-layer with a room temperature absorption onset of 2.1 eV, it is surprising that the V_{oc} of the cell is as low as it is (0.85 eV). There are several possible reasons for this, which will be explored in future studies. First, it is possible that, in

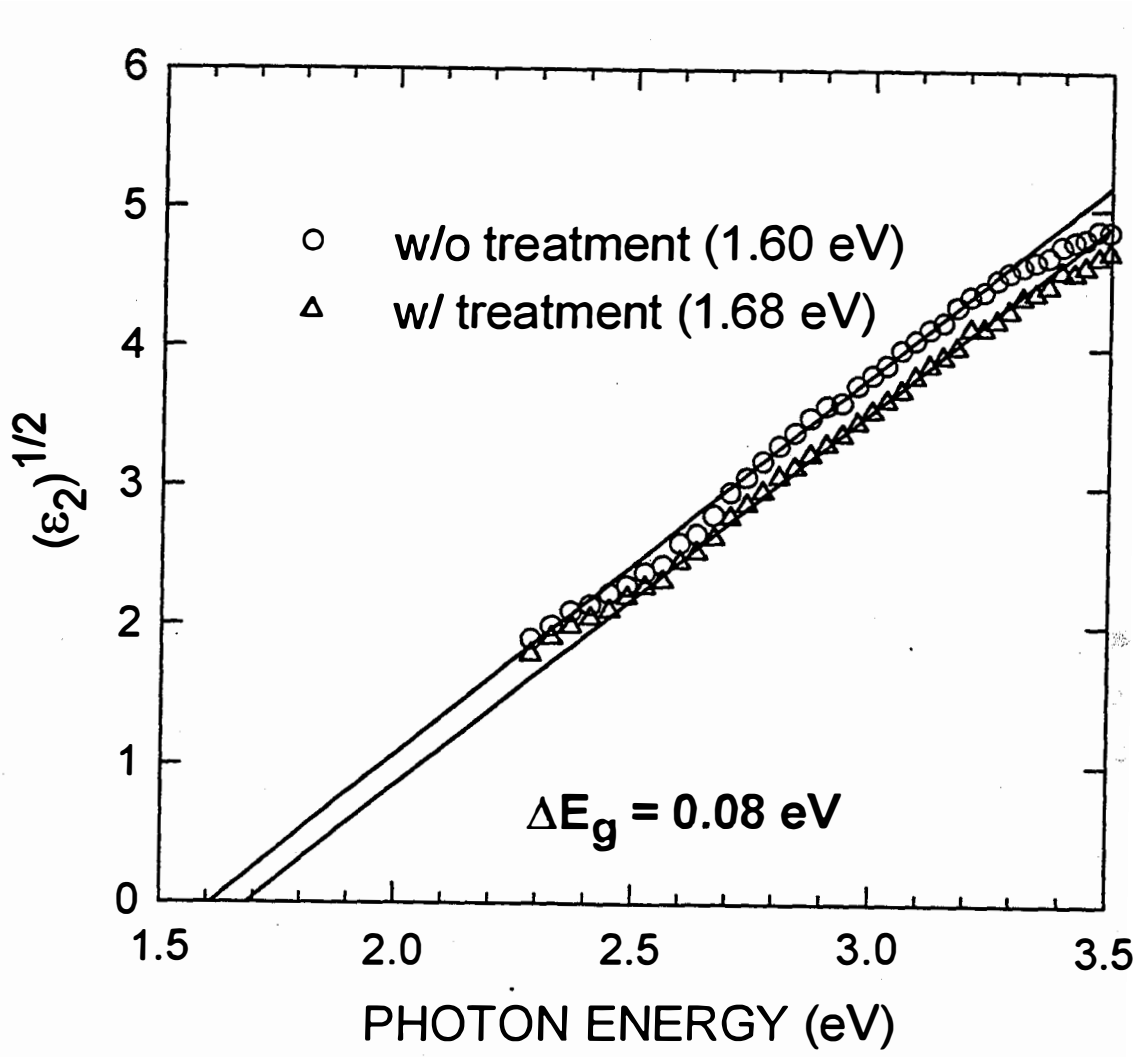

Figure 63 Optical gap shift within the top 200-250Å of the i-layer induced by the 133 s H_2-plasma exposure of Fig. 61. Here, the optical gaps are obtained at 200°C from real time SE data by extrapolation of $\varepsilon_2^{1/2}$. The RTSE data were collected before and after H_2 plasma exposure. The high energy ε_2 data for the gap measurement are most reliable since the low energy photons penetrate into the unmodified region. For this reason, the two curves converge at low energy.

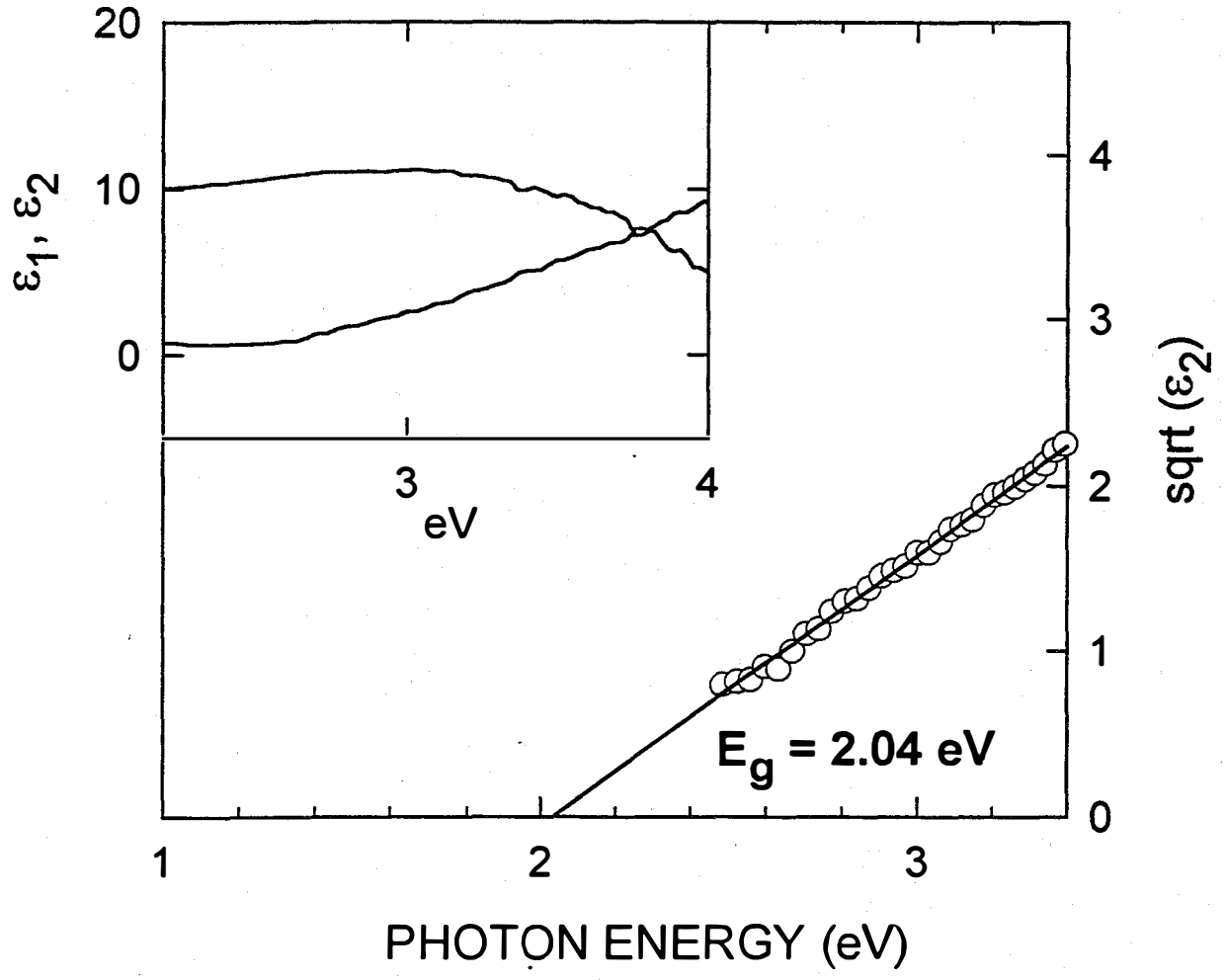

Figure 64 Dielectric function at 200°C and optical gap determination for the p-layer of Fig. 61. As usual, the optical gap is obtained by extrapolation of $\varepsilon_2^{1/2}$.

addition to widening the i-layer gap in the top 200-250Å, the H_2 plasma treatment damages the near-surface of the i-layer. Second, the final effective thickness of the p-layer for this n-i-p cell is higher than expected (~250 vs. 200 Å). Third, although the p-layer gap is quite high, the p-layer properties may not be optimum. For example, the crystallites may be isolated in a defective, lower conductivity a-$Si_{1-x}C_x$:H phase as indicated in Sec. 4. In the future, we plan to optimize (i) the H-treatment for nucleation enhancement of the p-layer while minimizing damage, (ii) the p-layer thickness, and (iii) the p-layer properties. In the course of the latter studies, we expect to shift from the TMB dopant gas source to BF_3.

The structural evolution for the microcrystalline p- and n-layers shown in Figs. 55 and 61, respectively, is quite complex. As a result, it is important to compare the final roughness values obtained from the SE analyses with the corresponding results from AFM image analyses. As an example of the AFM data obtained in this study, Fig. 65 shows an image over a 1x1 μm^2 area for the n-type microcrystalline Si surface of the p-i-n cell discussed in the last section. The in-plane and out-of plane scales are the same as those in Fig. 60, allowing easy comparison of the surface roughness on the i- and n-layers. We find that the n-type microcrystalline layer is considerably rougher than the i-layer; the rms values for these surfaces are 29 Å and 11 Å, respectively. Figure 66 shows a correlation between the roughness layer thickness deduced by real time SE and the rms roughness from AFM. Films of a-$Si_{1-x}C_x$:H are designated by the circles and exhibit a linear correlation given by $d_S(SE) = 1.5 d_{rms}(AFM) + (4\ Å)$. Results for the two microcrystalline doped layers, studied in the previous two sections, are depicted as the squares. These results obey a trend with a similar slope to that of the amorphous layers, but with an SE-deduced roughness thickness that is ~5-10 Å greater. The origin of this offset is unclear; however, we can conclude that the SE results for roughness on the microcrystalline layers, as obtained in Figs. 55 and 61, are in error by no more than 10 Å. This conclusion gives us greater confidence in the validity of the overall model developed in Secs. 5.2 and 5.4.

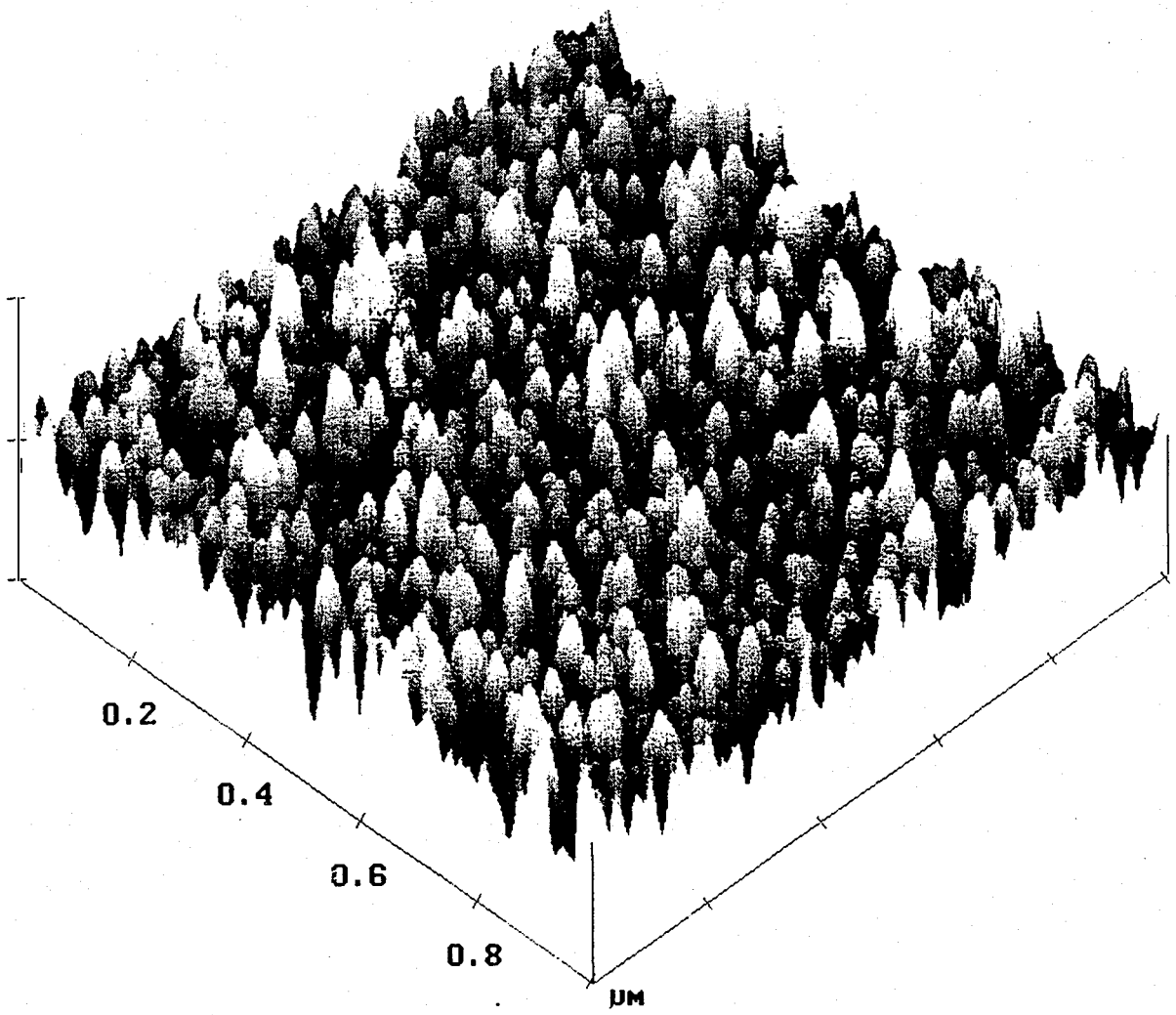

Figure 65 AFM image over a 1x1 μm^2 area for the n-type microcrystalline Si surface at the top of the p-i-n cell of Figs. 55 and 56. The in-plane and out-of plane scales are the same as those in Fig. 60, allowing easy comparison of the surface roughness on the i- and n-layers. We find that the n-type microcrystalline layer exhibits an rms roughness value of 29Å.

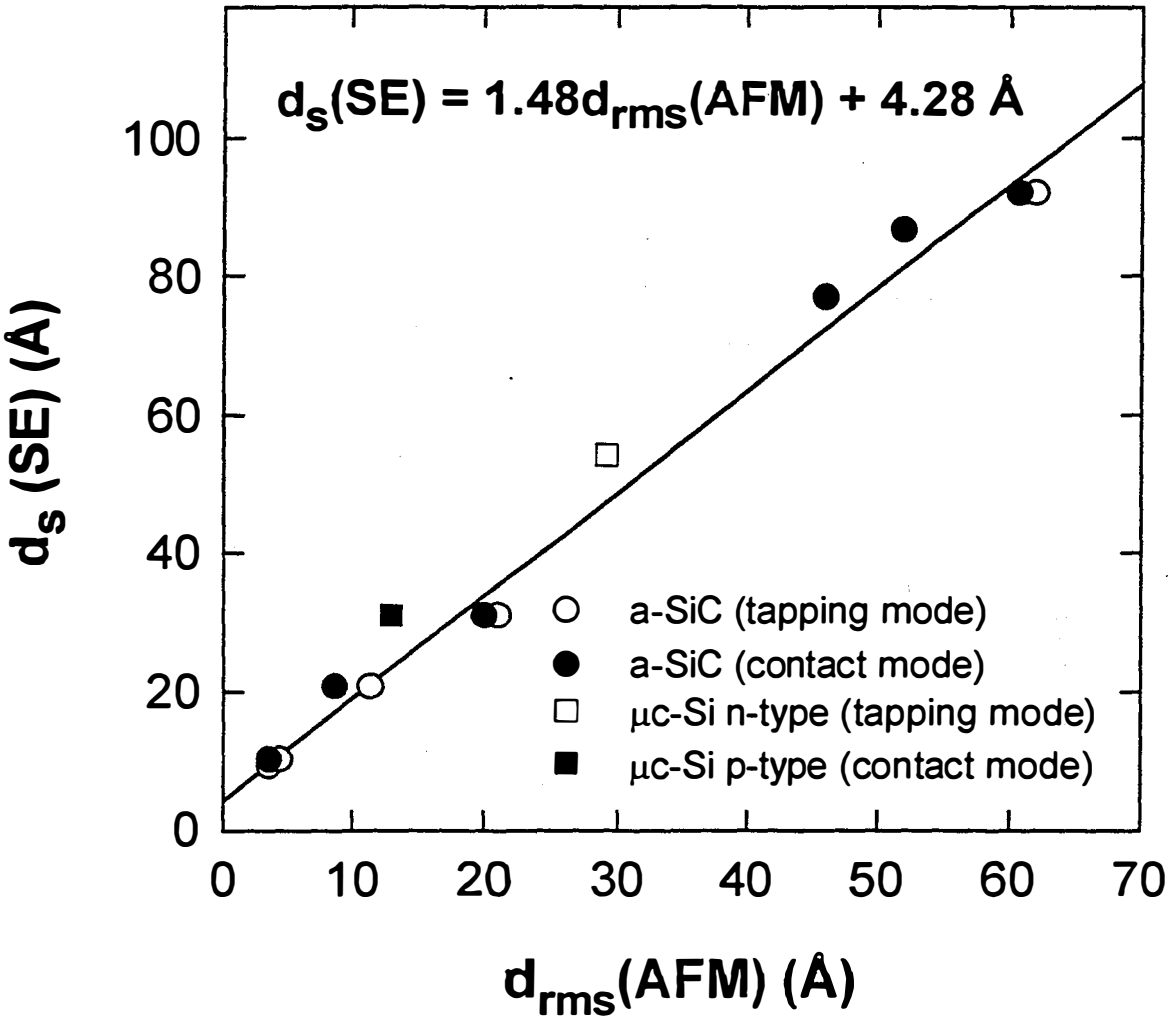

Figure 66 Correlation between the roughness layer thickness deduced by real time SE and the rms roughness from AFM. Films of a-$Si_{1-x}C_x$:H are designated by the circles and exhibit a linear correlation given by $d_S(SE) = 1.5d_{rms}(AFM)$ + (4 Å). Results for the two microcrystalline doped layers of Figs. 55 and 61 are depicted as the squares. These latter results obey a trend with a similar slope to that of the amorphous layers.

5.5 Role of Top Interfaces in Limiting V_{oc}

As reported in Sec. 3, the possible contributions of the p/i interface regions, the built-in potential, V_{bi}, and the bulk i-layer on the open circuit voltage, V_{oc}, of p-i-n solar cell structures were identified. The V_{oc} vs. light intensity characteristics can be used to identify these contributions. A comparison between a "high V_{oc}" USSC n-i-p solar cell and a (PSU n-i)/(USSC p/ITO) cell is shown in Fig. 67, where the V_{oc}'s are plotted as a function of white light illumination as well as blue and red light. It is interesting to note that there is complete superimposition of results obtained with blue, red, and white light. The light intensity range under investigation spans from 10^{-5} to about 50 times AM1. The V_{oc}'s for the USSC and PSU cells at AM1 are 1.04V and 0.96V, respectively, while the V_{oc}'s at ~50AM1 are 1.13V and 1.07V, respectively. As indicated in Sec. 6, AMPS simulation results show that for light intensities less than ~0.1AM1, the factors limiting the V_{oc} are mainly due to the bulk contribution, which in high quality materials is very sensitive to the mobility gap. Above ~0.1AM1, the dominant factors limiting the V_{oc} performance are due to the defective p/i interface regions. Although the contributions due to the V_{bi} depend on its values, such effects are expected to be felt beyond AM1. With those results in mind, the V_{oc} vs. light intensity characteristics in Fig. 67 show that the USSC cell has a bulk i-layer with a significantly wider mobility gap than that of PSU cell. However, because of the differences in the slope of the curves below ~AM1 where it is smaller for the USSC cell, the relative contributions from the p/i interface regions in limiting V_{oc} cannot be clearly seen. At this point, the curving-over observed for V_{oc} above AM1 for both cells cannot be identified in terms of the limitations that are imposed on V_{oc} by either the p/i interface or V_{bi}. More detailed analysis is being carried out on different cells to improve the ability to quantify such contributions.

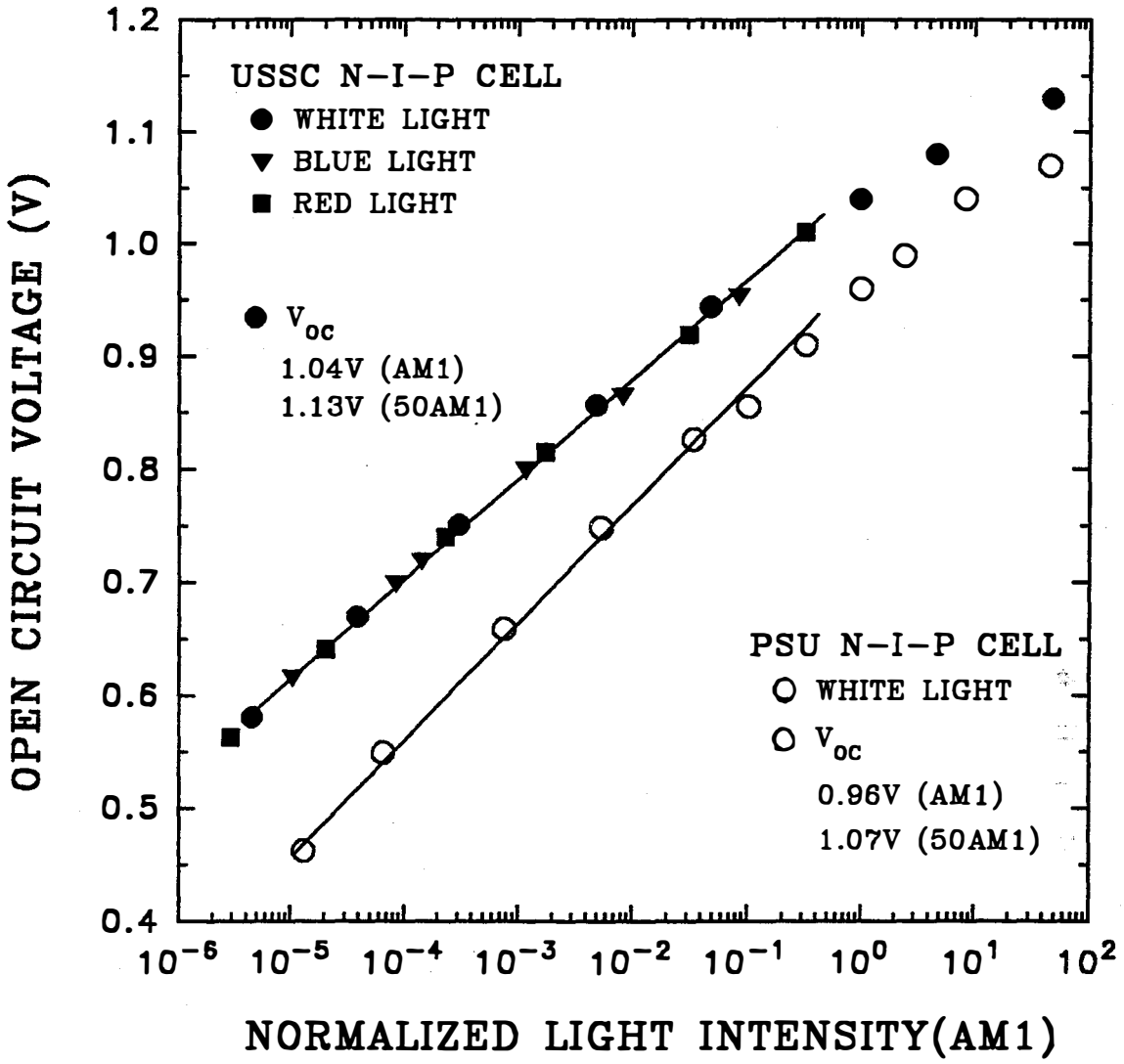

Figure 67 The dependence of the open circuit voltage, V_{oc}, on light intensity for a USSC n-i-p cell and a PSU n-i/ USSC p/ITO cell. The light intensity range spans from 10^{-5} to ~50 times AM1.

5.6 Compositional Grading at the p-i Interface in p-i-n Cells

In Phase I, we described the performance parameters of our first solar cell prepared with an undoped wide-bandgap graded layer at the *i*-layer side of the *p/i* interface. Such "buffer" layers are deposited by continuously changing the SiH_4 and CH_4 flows to provide a step in the optical gap at the *p/i* interface followed by a gradual decrease into the *i*-layer (see, for example, Figure 68). For our current control cells, the *p*- and *i*-layers are prepared at 200°C with a $[CH_4]/[SiH_4]$ ($\equiv$Z) gas flow ratio of Z=2/3, leading to *p*- and *i*-layer gaps given by E_{2000}=1.89 and 1.94 eV, respectively. We found that an intended 200 Å graded layer, with Z decreasing from 3/2 to 2/3 as shown in Figure 68, incorporated between the *p*-layer and a 2000 Å thick a-$Si_{1-x}C_x$:H wide bandgap *i*-layer of the solar cell, increased the observed initial V_{oc} on specular SnO_2 from 0.93 to 0.96 V. A small drop in fill-factor led to equal overall performance compared with a control cell also on specular SnO_2, but without the graded layer. A significant increase in cell performance which we do not understand at present was observed for the corresponding co-deposited cell on specular ZnO. These results are repeated in the first and second sections of Table 16.

We have extended this work to larger thicknesses and even wider gap graded layers in order to obtain a reasonable data base from which one can model the cell performance characteristics. Although the cell performance will deteriorate in the limit of very thick or very widegap interface layers, the parameter variation by which this occurs will provide insights into whether our cell modeling is simulating reality. We prefer to do this for thicker, macroscopic layers in which the trends are not subtle nuances, but significant variations (even if they are detrimental).

The results obtained so far are tabulated in Table 16, and the variations in cell parameters with interface layer thickness and optical gap gradient are included in Figs. 69 and 70. In our studies thus far, we have compared cells with intended 200 Å and 400 Å interface layers, and with flow ratio variations of Z=3/2$\rightarrow$2/3 and Z=4/1$\rightarrow$2/3. Cells on specular SnO_2 and ZnO were co-deposited, and thus provide important information on the effect of the top TCO/*p* contact. Figure 69 shows that an ~30 meV increase in V_{oc} with

Table 16 Performance parameters of a-$Si_{1-x}C_x$:H *p-i-n* solar cells with 2000 Å *i*-layers, prepared using different undoped, widegap-graded layers adjacent to the *p/i* interface. The variable parameters include the initial value of Z=[CH_4/[SiH_4] adjacent to the *p/i* interface -- the final value is fixed at 0.67 -- and the intended thickness of the graded layer. Also given are the parameters of a control cell prepared under the same conditions but without any graded layer. Cells were prepared on specular SnO_2 and ZnO coated glass substrates.

PREPARATION	SUBSTRATE	V_{oc} (V)	J_{sc} (mA/cm^2)	FF	Eff. (%)
Z = 0.67, R = 5	specular SnO_2	0.93	5.6	0.62	3.2
	specular ZnO	0.89	6.7	0.52	3.1
intended 200 Å Z = 1.5 to 0.67	specular SnO_2	0.96	5.7	0.60	3.2
	specular ZnO	0.92	7.4	0.56	3.8
intended 400 Å Z = 1.5 to 0.67	specular SnO_2	0.95	5.5	0.51	2.7
	specular ZnO	0.92	6.8	0.50	3.1
intended 200 Å Z = 4.0 to 0.67	specular SnO_2	0.94	5.5	0.42	2.1
	specular ZnO	0.92	5.5	0.28	1.4
intended 400 Å Z = 4.0 to 0.67	specular SnO_2	0.95	5.1	0.22	1.1
	specular ZnO	0.94	1.1	0.20	0.2

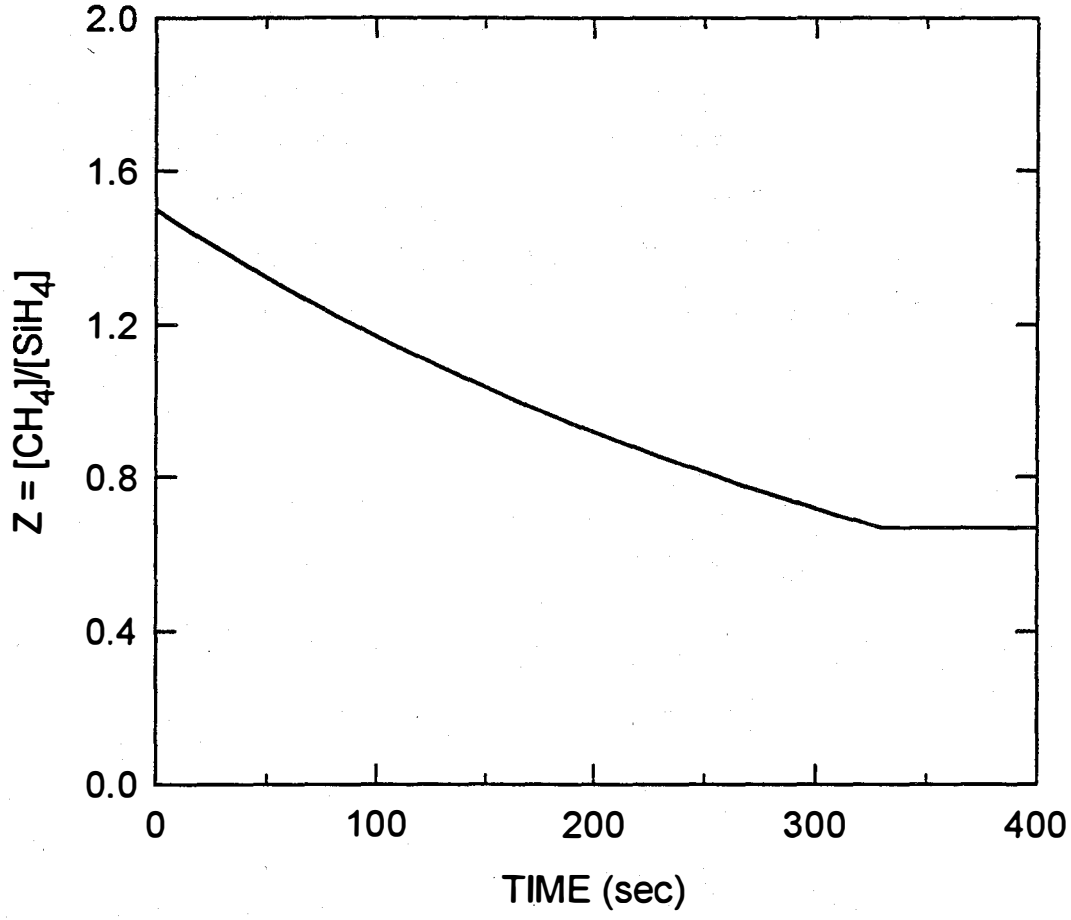

Figure 68 The ramp in the $[CH_4]/[SiH_4]$ gas flow ratio as a function of time used to generate the intended 200Å undoped, graded layer adjacent to the *p/i* interface for the a-$Si_{1-x}C_x$ cell of the second entry of Table 16.

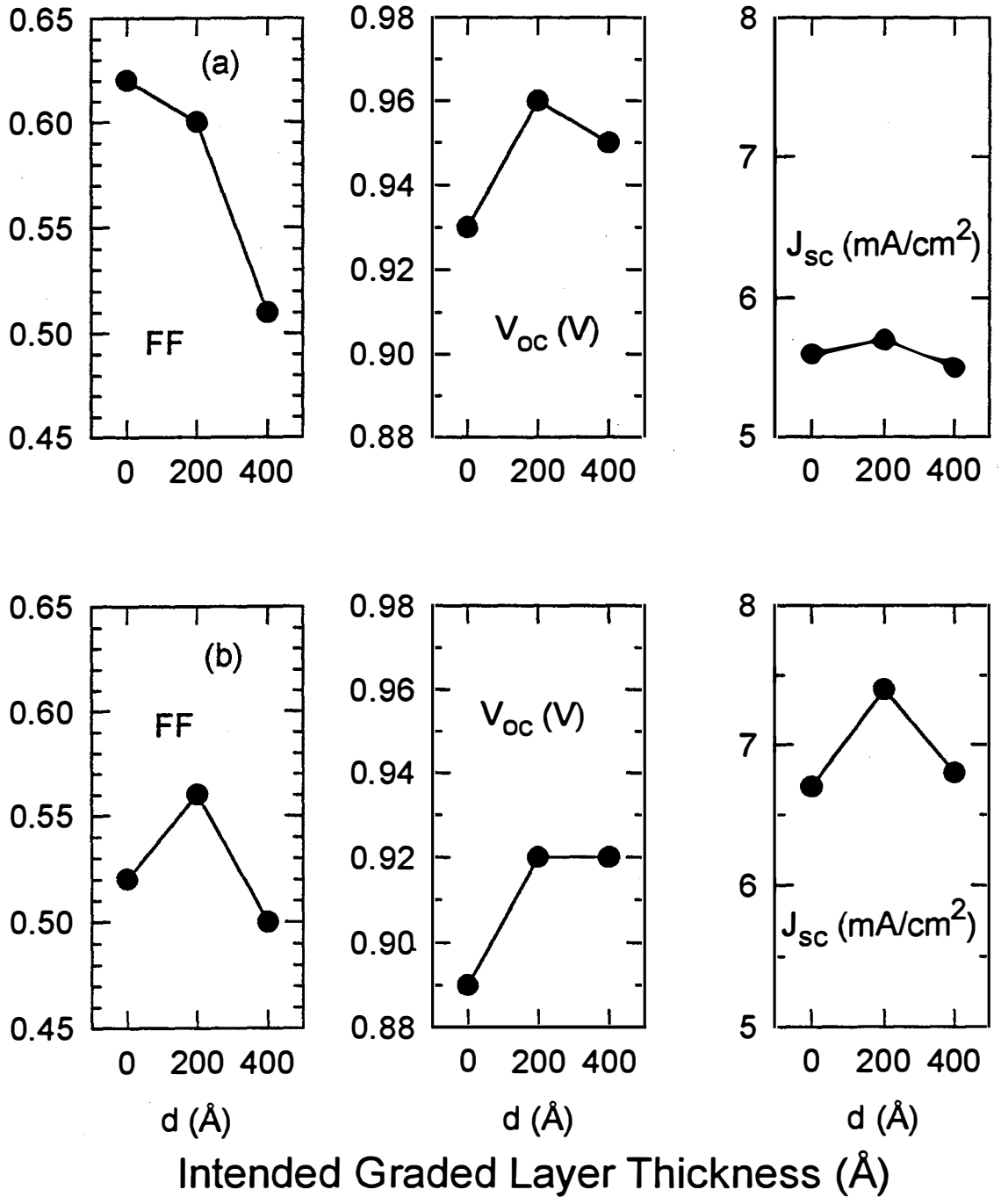

Figure 69 Variation in cell parameters as a function of the intended interface layer thickness for a-$Si_{1-x}C_x$:H solar cells prepared on specular (a) SnO_2 and (b) ZnO. For both intended thicknesses of 200 and 400 Å, the optical gap discontinuity relative to the *p*-layer starts at ~0.10 eV next to the *p/i* interface and drops throughout the graded layer to ~0.05 eV, the value at the *i*-layer.

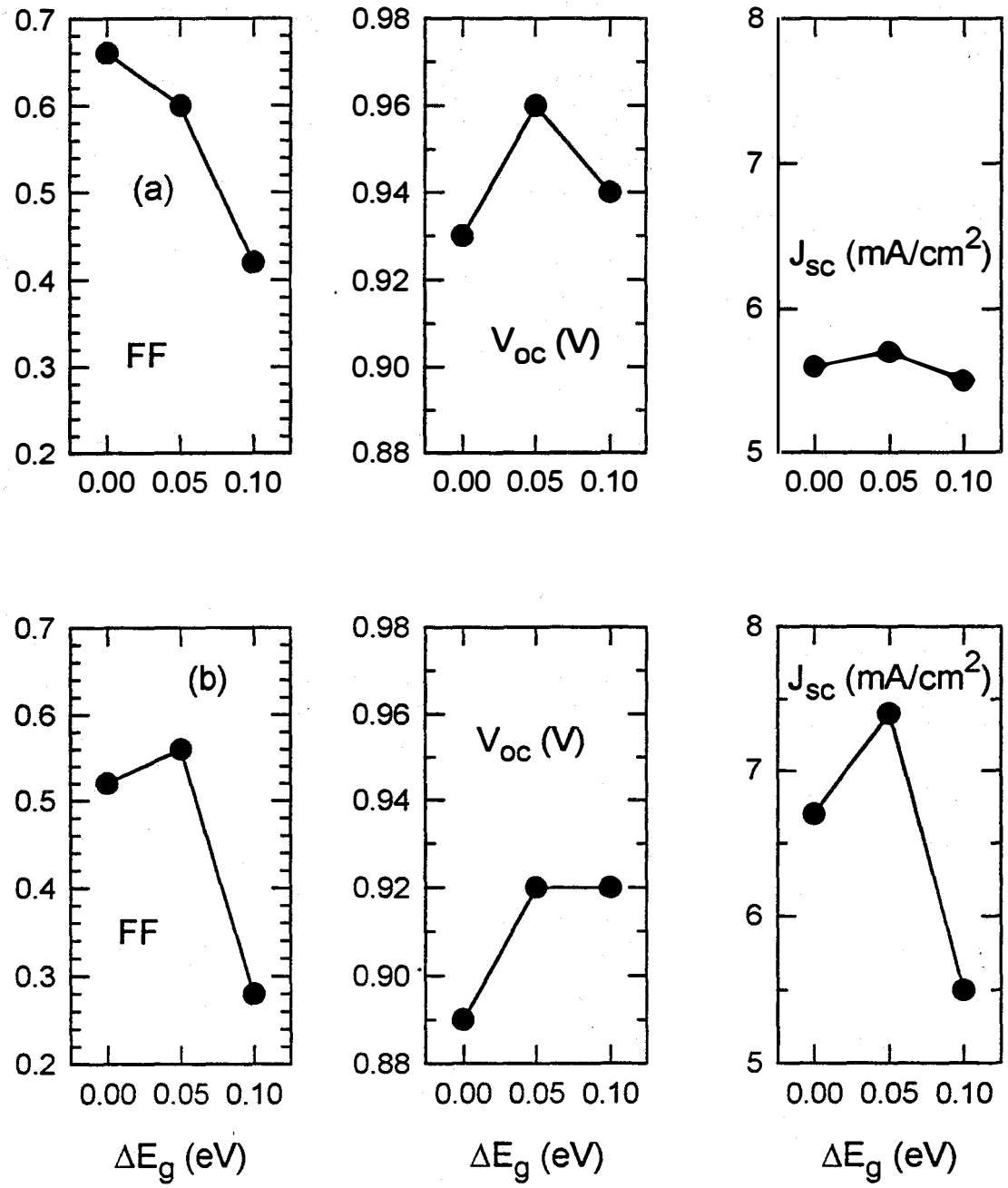

Figure 70 Variation in the a-$Si_{1-x}C_x$:H solar cell parameters as a function of the optical gap gradient over the graded *p/i* interface layer for cells prepared on specular (a) SnO_2 and (b) ZnO. When the band gap gradient is non-zero, the intended thickness of the interface layer is fixed at 200 Å.

the addition of an intended 200 Å interface layer is common to both TCO substrates, and this is one feature that should be sought out in any simulation of the data. As the interface layer thickness is increased, however, there appears to be no significant degradation in V_{oc}. The variation in fill-factor is interesting in that it depends on the TCO. There is a steady degradation from 0.62 to 0.51 for the SnO_2 as the graded layer thickness is increased to 400 Å; however, for ZnO there is a well-defined maximum of 0.56 for a layer thickness of 200 Å. Because of the rather coarse grid used in these experiments, it may be possible to optimize the fill factor with mode detailed studies.

Figure 70 shows the variation in cell parameters with the optical gap gradient throughout the intended 200 Å graded layer. For $\Delta E_g = 0$, there is a doping-induced step in the optical gap of ~+0.05 eV from the *p*- to the *i*-layer, even without the interface layer. Thus for the graded interface layers, the optical gap steps at the interface are ~0.10 and 0.15 eV for cells prepared with flow ratio variations of Z=3/2→2/3 and 4/1→2/3, respectively. The changes in the gaps over the intended 200 Å graded layers are thus 0 eV, ~0.05 eV and ~0.10 eV (see results below) for the control cell and for the cells prepared with flow ratio variations of Z=3/2→2/3 and 4/1→2/3, respectively. Figure 70 reveals first a gradual and then very rapid decrease in fill-factor with increasing optical gap gradient for the SnO_2 TCO. The interesting result here is for the cells on ZnO in which the fill-factor first increases for small gap gradients and then decreases. V_{oc} also shows an increase for a small optical gap gradient, but degrades for larger gradients only for the SnO_2 TCO.

In order to understand these trends, we need accurate inputs to the solar cell modeling. This includes depth profiles from the *p/i* interface of (i) the conduction and valence band edges (relative to the *p*- and *i*-layer edges), (ii) the spectrum in the absorption coefficient, and (iii) the defect state density that controls the recombination. We have been actively pursuing (i) and (ii) using RTSE. In fact for all the cells in Table 16 and Figs. 69 and 70, RTSE was performed throughout the cell preparation. The conventional method of ellipsometric data modeling for a continuously graded layer involves splitting the layer into several ~20 Å slices and using optical multilayer analysis. Instead, we have developed a new procedure based on RTSE in which we track only the near surface structure and optical properties, combining the past history of deposition into

a "pseudo-substrate" characterized by a pseudo-dielectric function that simulates the underlying multilayer structure. With this approach, we can determine: (i) the dielectric function of the top ~20 Å of the bulk film (which is a continuous function of time during graded layer preparation), (ii) the surface roughness layer thickness on top of the bulk film, and (iii) the instantaneous deposition rate. By integrating the instantaneous deposition rate over time during graded layer formation, a depth profile in the full dielectric function can be determined. The mathematical procedure is described in detail in our published work.

The depth profile in the dielectric function $\varepsilon=\varepsilon_1+i\varepsilon_2$ is not particularly useful in itself. However, by extrapolating the linear behavior in $(\varepsilon_2)^{1/2}$ vs. photon energy to zero in the region of the absorption onset, a measure of the optical gap (*i.e.*, via the Cody method) can be obtained. This method is preferred over the Tauc method since the linearity in $(\varepsilon_2)^{1/2}$ extends over a wider range of ε_2. With the Tauc method, $(\varepsilon_2 E^2)^{1/2}$ shows significant upward curvature with photon energy E. As a result the Tauc gap derived from spectroscopic ellipsometry (SE) data at high ε_2 is significantly larger than that derived from T&R data collected at low ε_2. The Cody method does not suffer from this problem, giving optical gap values from T&R and SE that are similar. However, the optical gap by the $(\varepsilon_2)^{1/2}$ method is typically ~0.08-0.10 eV lower than the Tauc gap from T&R measurements. The final conclusion of these considerations is that one can extract a depth profile in the optical gap from the depth profile in ε. This gap is extracted using the $(\varepsilon_2)^{1/2}$ (or Cody method) and is characteristic of the deposition temperature, which for the cells of Table 16 and Figures 69 and 70, is 200°C. Because of the red-shift of the gap with increasing temperature, as well as the difference between the Tauc and Cody methods, the measured gap profile in the solar cells is displaced to the red from the room-temperature Tauc (T&R) gap by ~0.18 eV.

Another approach will be described to determine the optical gap profile. This alternative is more definitive and yields a higher precision gap profile since it avoids the linear gap extrapolation for each (ψ, Δ) spectrum collected during graded layer formation. The alternative approach first involved preparing a selected set of three a-$Si_{1-x}C_x$:H

samples versus $Z=[CH_4]/[SiH_4]$ and characterizing them by real time SE. All other deposition parameters were fixed at the values used to deposit the graded layers. The substrate temperature was 200°C, the H_2-dilution ratio R was given by $R=[H_2]/\{[SiH_4]+[CH_4]\}=5$, with separate $\{[SiH_4]+[CH_4]\}$ and $[H_2]$ flows of 5 and 25, respectively. These flow conditions lead to a H_2 partial pressure of ~0.18 Torr and a total gas pressure of 0.21 Torr. These in fact are the fixed conditions used to prepare the graded layers (Z being the only variable). The resulting three samples represent discrete states through which the graded layer passes.

In addition to real time SE characterization, *ex situ* x-ray photoelectron spectroscopy and transmission & reflection spectroscopy was used to determine the C-content x for these three samples, yielding x=0.05 for Z=0.67, x=0.10 for Z=1.5, and x=0.22 for Z=4. From real time SE, the dielectric functions at 200°C for these films are also determined as shown in Fig. 71. Figure 72 shows three measures of the room temperature optical gaps, E_{2000}, the Tauc gap, and the gap by $\varepsilon_2^{1/2}$ extrapolation, all deduced from the T&R measurements, in this case plotted versus x. The solid lines in Fig. 72 are second order polynomial fits (coefficients in order of increasing order are given in the Figure). With these relationships between the C-content and the gaps, all we need now is a way to extract the C-content from the dielectric function, and we will be able to use the depth profile in the dielectric function to extract the depth profiles in the C-content and optical gap.

In order to extract the C-content from the dielectric function using a least-squares regression analysis method, we must develop a method to generate the dielectric function of the a-$Si_{1-x}C_x$:H material that makes up the graded layer for any value of x, even those values for which discrete samples are not available. In order to do this, we first fit the dielectric functions of the three samples, as well as a fourth for which x=0 and Z=0, using the general formula provided by Forouhi and Bloomer (F-B) [Phys. Rev. B34, 7018 (1986)]. Although the physical meaning of the F-B formulas have been questioned recently, here we use the formulas only as a convenient mathematical parameterization scheme. The resulting fits provide a set of five photon energy-independent parameters related to the electronic structure of the material. The fits using this formula are given as

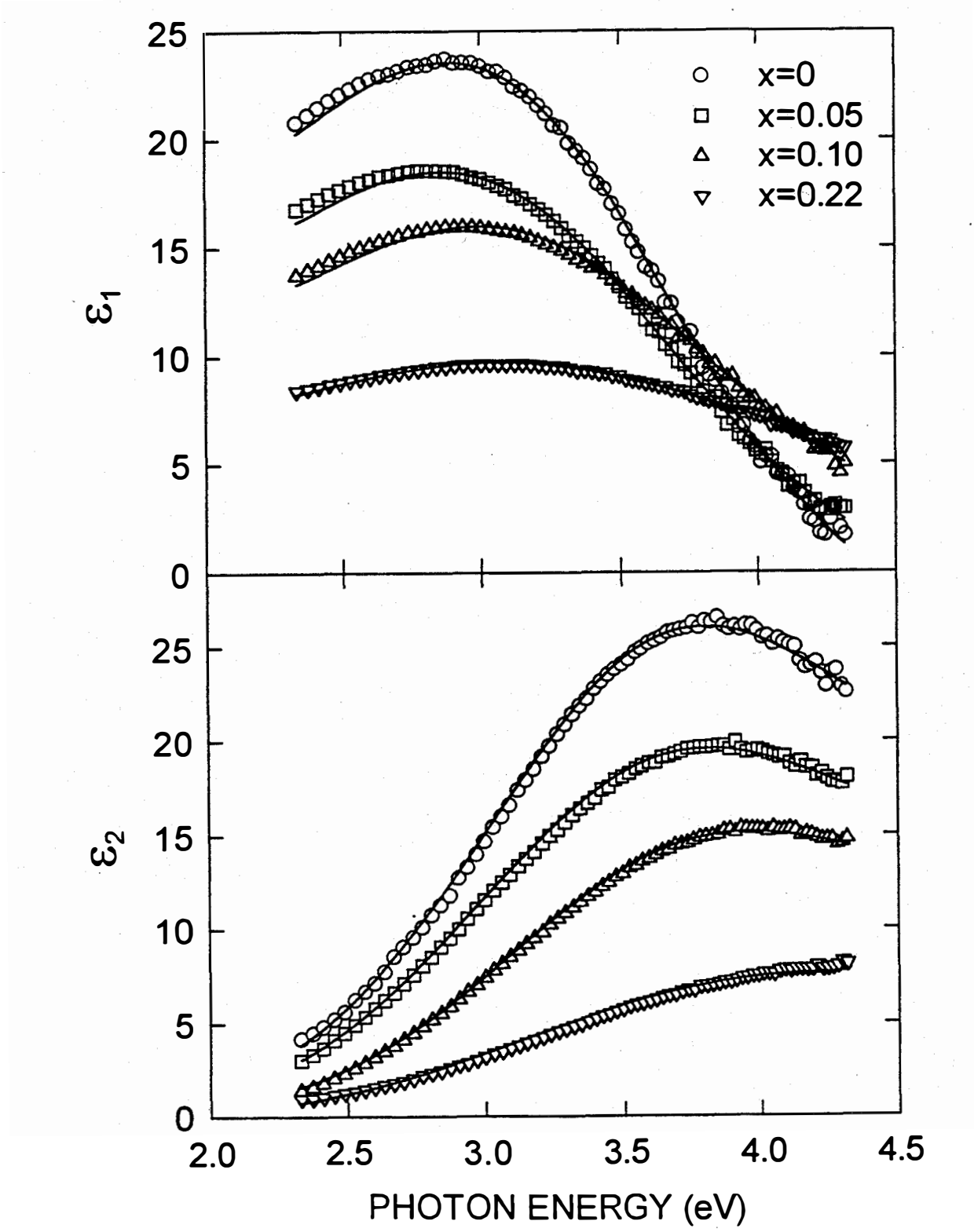

Figure 71 Dielectric functions at 200°C for a-$Si_{1-x}C_x$:H alloys with different values of x, deduced in an analysis of real time spectroellipsometry data collected during the preparation of a series of 700-1100Å thick alloy films in a multilayer stack on the same c-Si substrate. The solid lines are calculated from the best-fit photon energy-independent parameters plotted in Fig. 73.

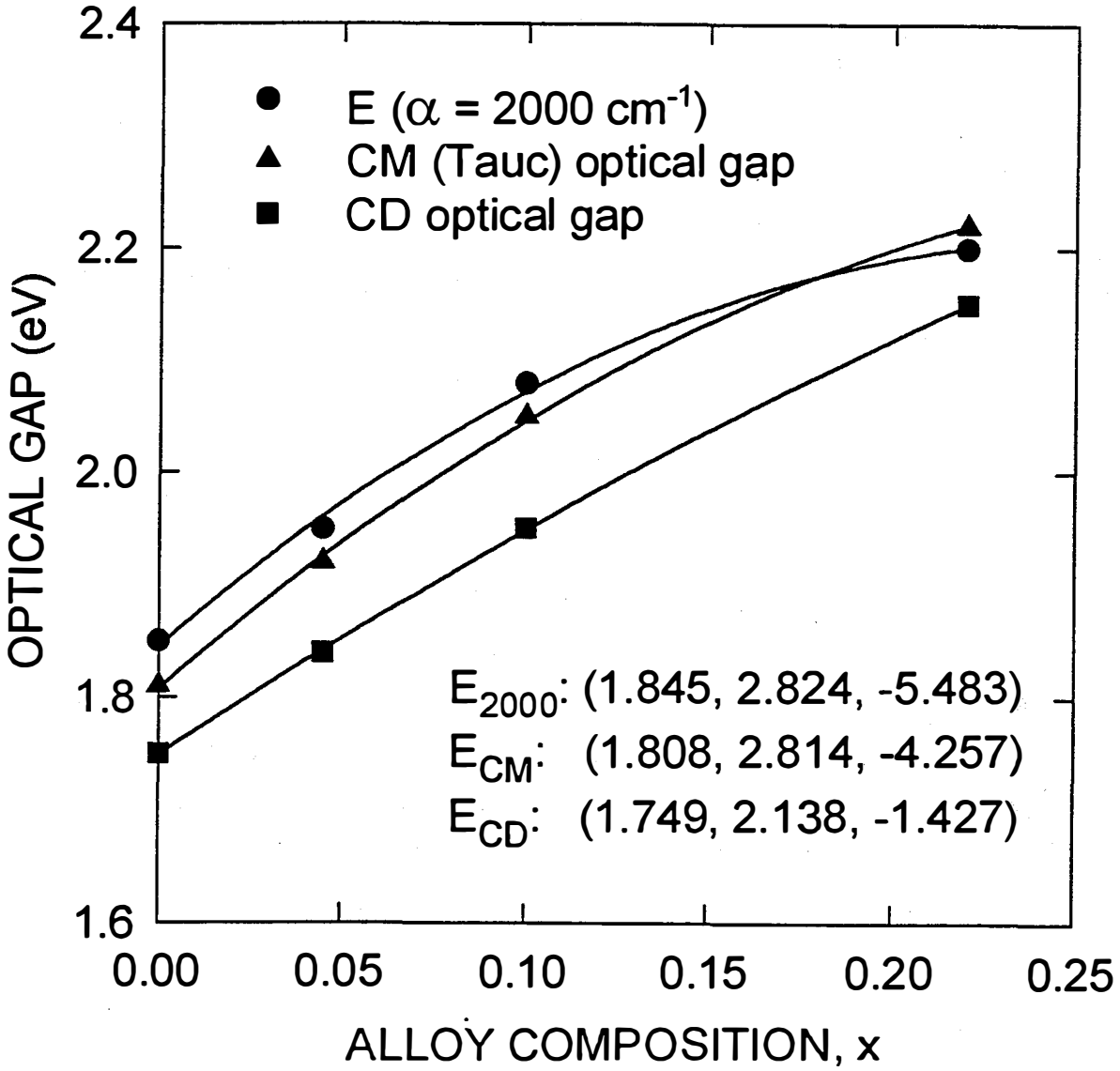

Figure 72 Three measures of the room temperature optical gap for a-$Si_{1-x}C_x$:H films plotted as a function of x, all deduced from Transmission & Reflection measurements. These measures include (i) E_{2000}, an empirical measure of the gap, defined as the photon energy at which the absorption coefficient is $2000cm^{-1}$, (ii) the Tauc gap, obtained by extrapolation of $(\alpha nE)^{1/2}$ vs. E to zero ordinate, and (iii) the gap obtained by extrapolation of $\varepsilon_2^{1/2}$ vs. E. The solid lines are second-order polynomial fits to the data values. The polynomial coefficients are given in order of increasing order at the bottom.

the solid lines through the data points in Fig. 71. The best fit values of the five parameters are plotted for the four samples versus x in Fig. 73. The solid lines in Fig. 73 are second order polynomial fits to the five parameters versus x. The 15 coefficients of these polynomials completely specify the dielectric function of a-$Si_{1-x}C_x$:H for $0 \leq x < 0.25$. For example, to generate the dielectric function for a-$Si_{0.85}C_{0.15}$:H, one simply evaluates the polynomials that describe each of the five F-B parameters at x=0.15, and this provides values for the parameters that can be plugged into the F-B formulas. The advantage of this approach is that it provides a smooth interpolation method for dielectric function generation.

Having established a relationship between the C-content and the dielectric function through the F-B parameterization, we can incorporate this approach into a least-squares regression analysis of real time SE data. With this enhancement, the best fit C-content in the near-surface (top 20 Å) of the graded layer, along with the surface roughness layer thickness and the instantaneous deposition rate can be determined as a function of time. Figure 74 shows the final results obtained from an analysis of the data for the intended 200 Å thick graded layer of the solar cell listed in the second entry in Table 16. In this cell, the V_{oc} was highest in the initial state among all of our wide-gap cells prepared to this point. The results of Fig. 74 show a gradual decrease in the C-content by $\Delta x \sim 0.05$ over the 325 s time period during which Z is decreased from 1.5 to 0.67 (see Figure 71). The surface roughness layer remains constant throughout the process at ~11.5±1.5 Å, in consistency with measurements of separate layers. The instantaneous deposition rate shows a weak maximum ~150-200 s into the gradient at which point $Z \approx 1$. By integrating the instantaneous deposition rate in Fig. 74, we can derive the depth profile in the C-content as shown in Fig. 75. In this figure, zero thickness corresponds to the *p/i* interface. The result is interesting in that the intended graded layer thickness was 200 Å; however, the actual thickness is significantly larger, ~370 Å. This information along the room temperature optical gap profiles given in Figure 76 deduced from the relationship in Fig. 72, provide important inputs for solar cell modeling.

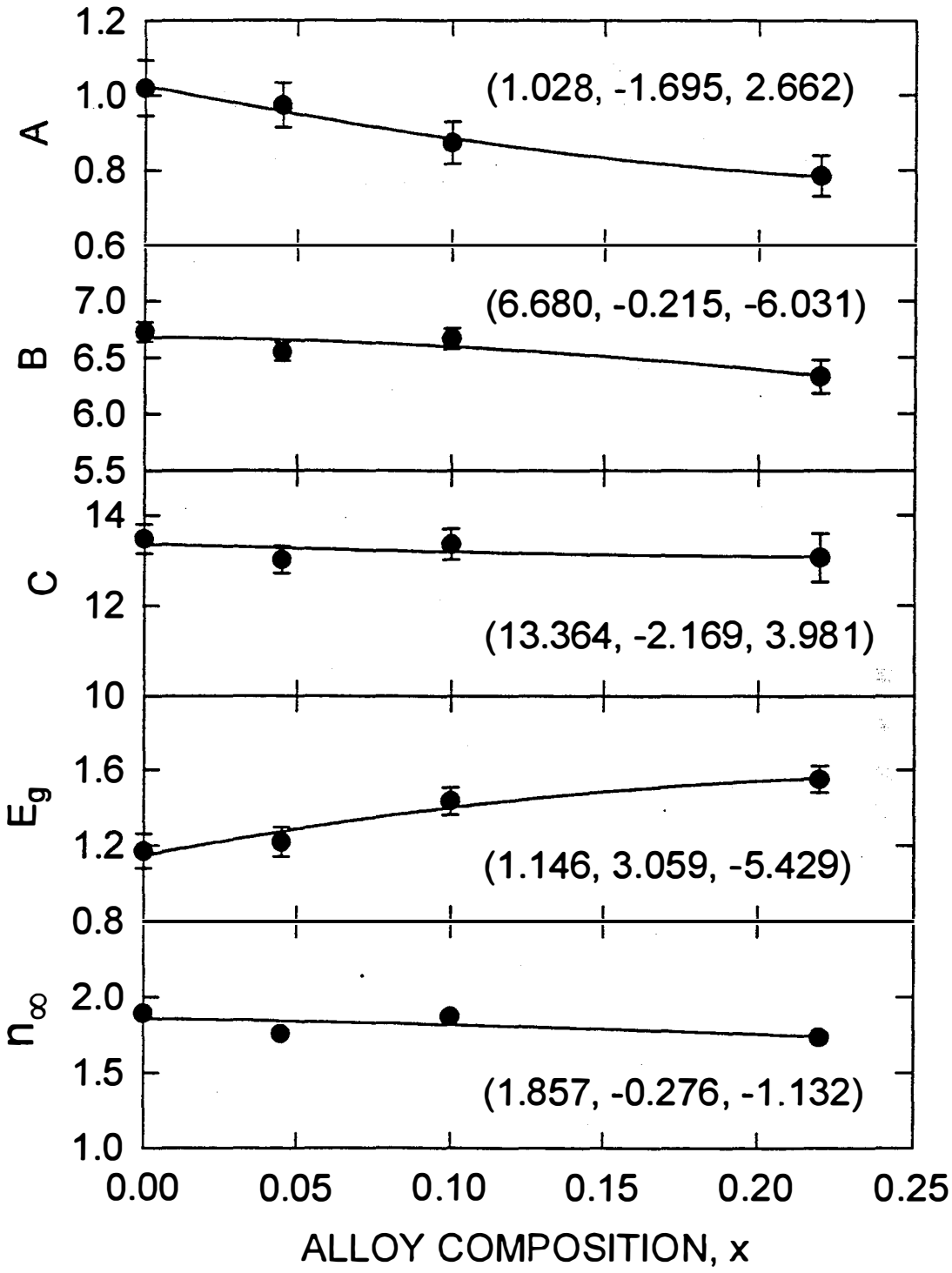

Figure 73 Photon energy-independent parameters in the formulas developed by Forouhi and Bloomer, plotted as a function of alloy composition x (points) for a-$Si_{1-x}C_x$:H. These values were obtained from the fits shown in Fig. 71. The solid lines are second-order polynomial fits to the data values that allow one to calculate the dielectric function of a-$Si_{1-x}C_x$:H for any value of x. The polynomial coefficients are provided in order of increasing order for each parameters.

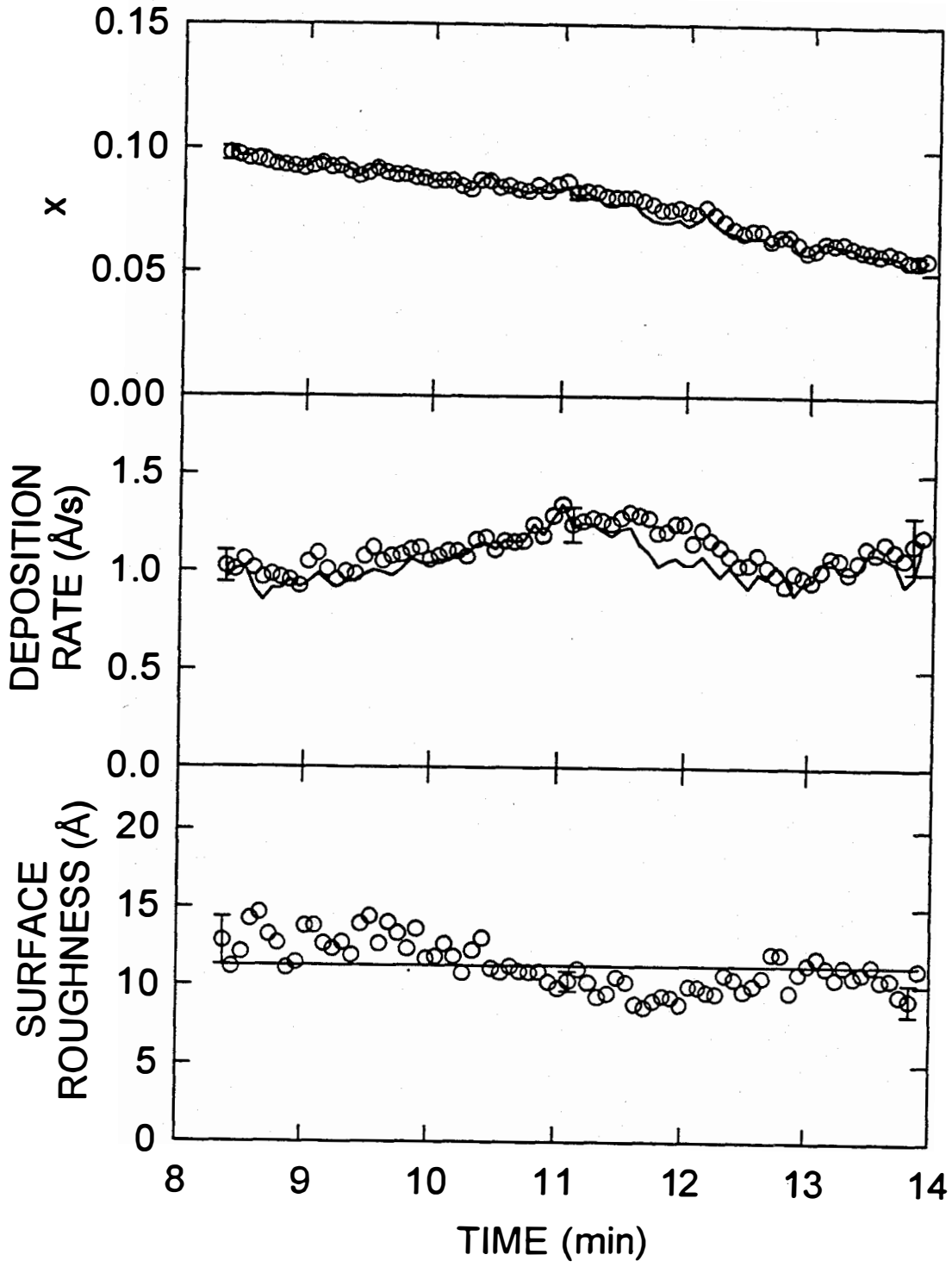

Figure 74 Time evolution of the alloy composition (x), the deposition rate, and the surface roughness layer thickness deduced from real time spectroellipsometry data collected during the preparation of a compositionally-graded a-$Si_{1-x}C_x$:H layer. To obtain the composition gradient, the gas flow ratio Z was varied as shown in Fig. 68. The solid lines in the top and center panels were calculated assuming a fixed surface roughness layer of 11.5 Å (horizontal line in lower panel).

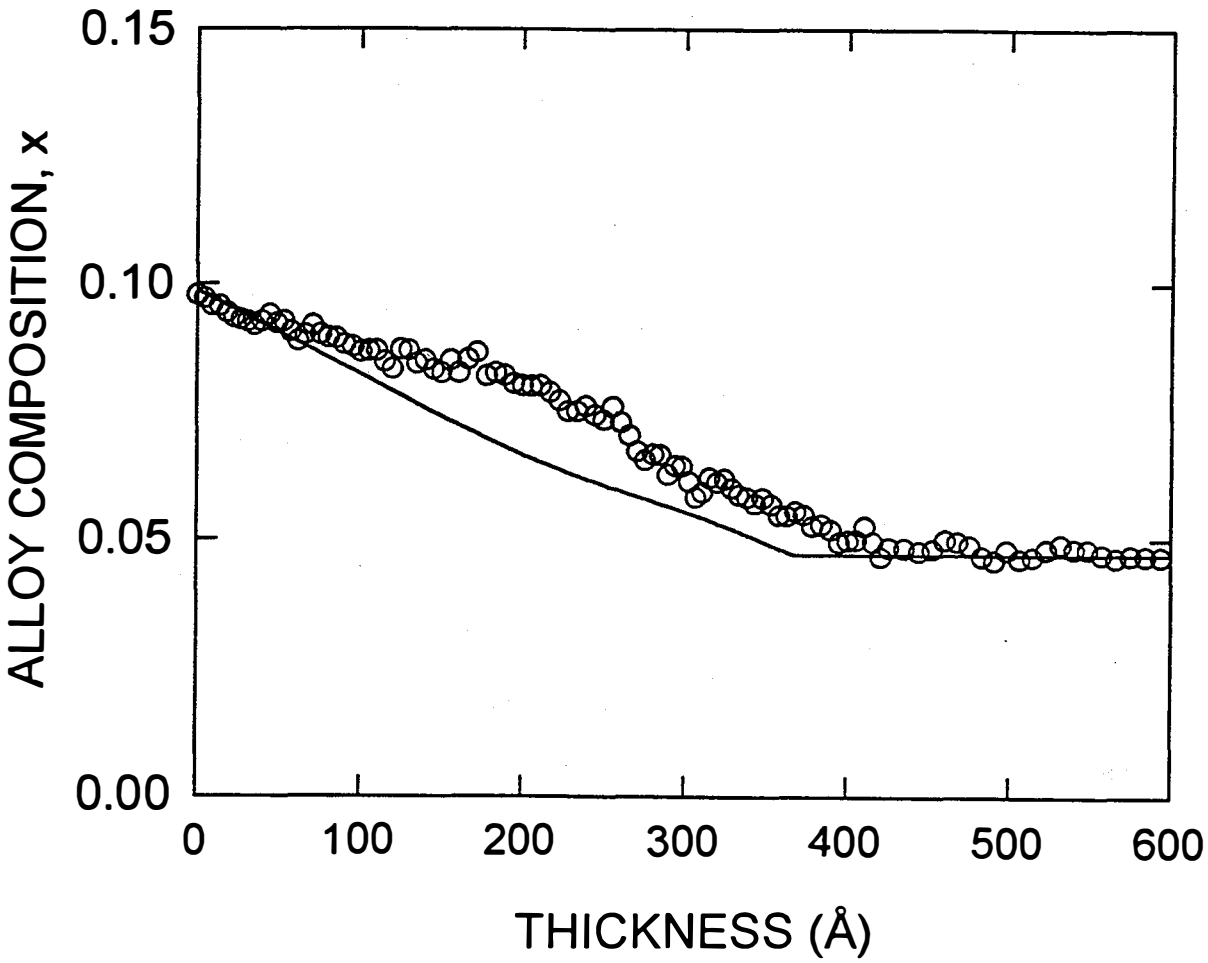

Figure 75 Alloy composition, plotted as a function of distance from the interface to the p-layer (formed at t=8.3 min in Fig. 74) for the compositionally-graded a-$Si_{1-x}C_x$:H whose preparation and analysis has been described in Figs. 68 and 74. The solid line is a prediction based on the assumption that the alloy composition in the film instantaneously responds to the flow ratio in accordance with the relationship of Fig. 68, assuming the deposition rate variation in Fig. 74 (with variable roughness).

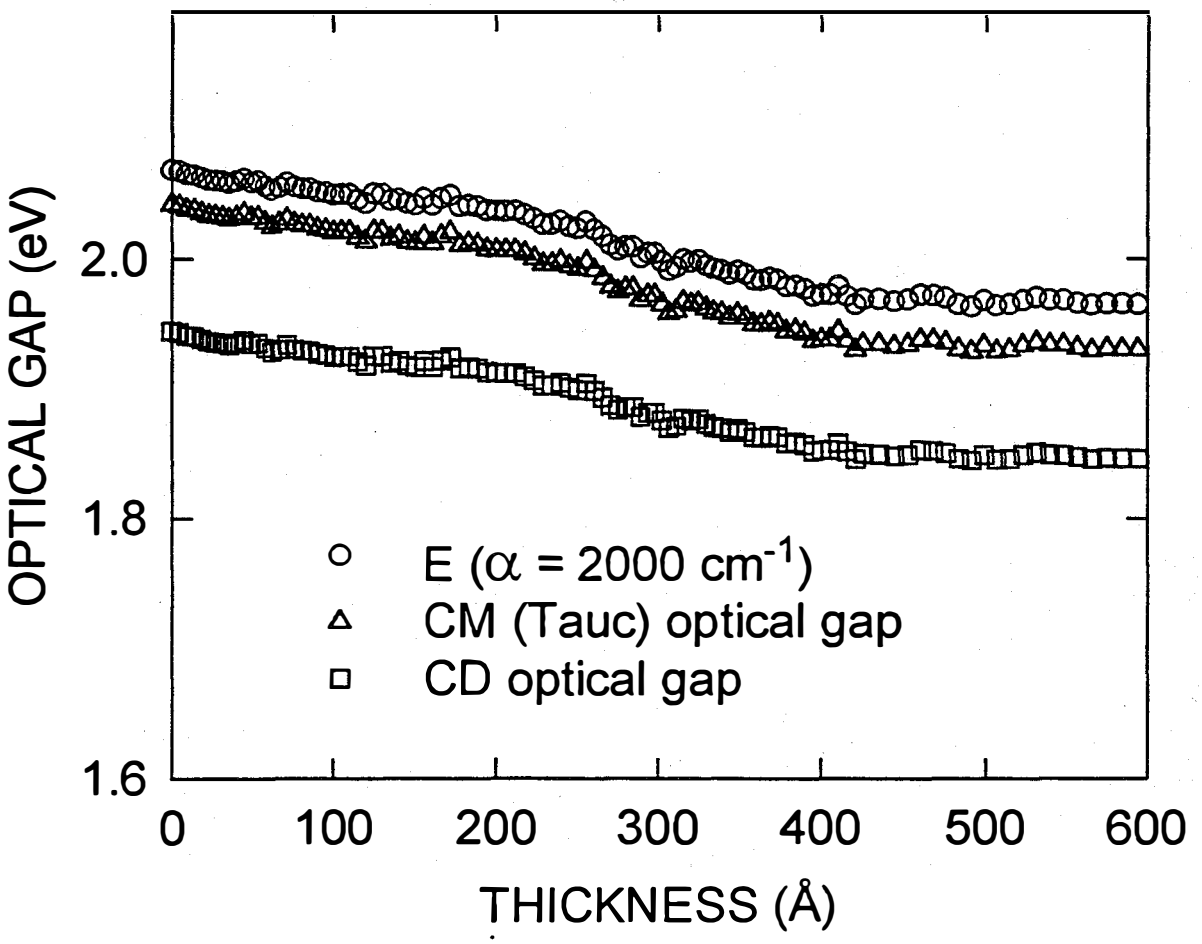

Figure 76 Three measures of the optical gap at room temperature, plotted as a function of distance from the interface to the p-layer (formed at t=8.3 min in Fig. 74) for the compositionally-graded a-$Si_{1-x}C_x$:H whose preparation and analysis has been described in Figs. 68 and 74.

There are several future refinements that need to be made in order to fully develop property profiles in solar cell modeling. First, we must be able to extract from the optical gap gradient the gradients in the valence and conduction band offsets relative to the *i*-layer band edges. This will require accurate information from photoemission measurements which may not be currently available. Second, we must be able to extract the depth profile in the room temperature absorption spectrum from the depth profile of the optical gap. This capability has actually been developed recently in our research. Third, we need to input defect density profiles for the graded layer. These must be obtained using sub-bandgap absorption measurements of individual films, extracting the density of defect states, which are then correlated with the value of Z and the optical gap. From such a correlation, the gradient in the optical gap can be used to predict the gradients in the defect densities of states. With these refinements, one will have sufficient information to determine whether the existing solar cell models contain the essential physics needed to understand the impact of *p/i* interface buffer and graded layers.

6. Device Modeling

6.1 Schottky Barrier Solar Cell Structures

In Phase II a new approach to device modeling using AMPS was taken. This approach is less ambitious than originally proposed due to the absence of reliable input parameters which has limited the ability of AMPS to make reliable, quantitative predictions about the directions for improving the performance and stability of solar cells. This is particularly true for the p/i interface regions which are generally included in such modeling, but whose parameters have not yet been established in any detailed studies. In this new approach the modeling of solar cell structures is carried out first to establish material parameters that are self-consistent with those derived in detailed studies on intrinsic material thin films. This is currently being done with the Schottky barrier solar cell structures, which do not have the uncertainties introduced by the p/i interface regions. The

work carried out in the EPRI program has shown that self-consistent analysis can only be achieved by including charged defects and that useful "operational" parameters can be obtained using a three-Gaussian distribution. The analysis being carried out in Phase II relies heavily on the work being done in that program. Both the dark I-V's and QE's in these Schottky barrier structures are very sensitive to the bulk, and in particular to its light induced changes. Thus, they are very useful in the "fine-tuning" of the thin film material parameters for the self-consistent modeling of p-i-n cells with AMPS.

Modeling with AMPS is currently being utilized to obtain insights into the degradation of cells fabricated with undiluted materials. Examples of such analyses are illustrated in Figs. 77 and 78 where the dark I-V's and QE's are shown in the annealed state and after degradation for 20 hours with AM1 illumination through the TCO. The symbols are experimental results and the solid lines are fits obtained with a three-Gaussian defect distribution such as that used in the analysis of the thin film materials results. In this case the densities of charged defects increase from $5x10^{15}/cm^3$ to $7x10^{16}/cm^3$ and the neutral dangling bond defects from $5x10^{15}/cm^3$ to $1x10^{17}/cm^3$. It is important to note here that the three orders of magnitude change in the dark I-V of Fig. 77, which is more than one hundred times larger than that seen for the p-i-n's, can still be fitted with these distributions of gap states. In addition, similar changes in dark I-V and QE characteristics of Schottky barrier solar cell structures are observed after light soaking even with ~0.4μm thick structures.

Modeling with AMPS is also being utilized to obtain insights into the degradation of cells fabricated with diluted materials. Examples of such analysis are illustrated in Figs. 79, 80 and 81 where the dark I-V's and QE's are shown in the annealed state, after 30 seconds fast degradation, and in the stabilized degraded state obtained with AM1 illumination through the TCO. The Schottky barrier cell for these studies is 0.5μm thick with a 200°C diluted a-Si:H i-layer material. In Fig 79, the symbols denote the experimental results and the solid lines denote fits obtained with a three-Gaussian defect distribution such as that used in the analysis of the thin film materials results. The large sensitivity of the far forward I-V's in Schottky barrier solar cell structures to the light induced changes can be clearly seen in Fig 79 by the 3-4 orders of magnitude decrease in

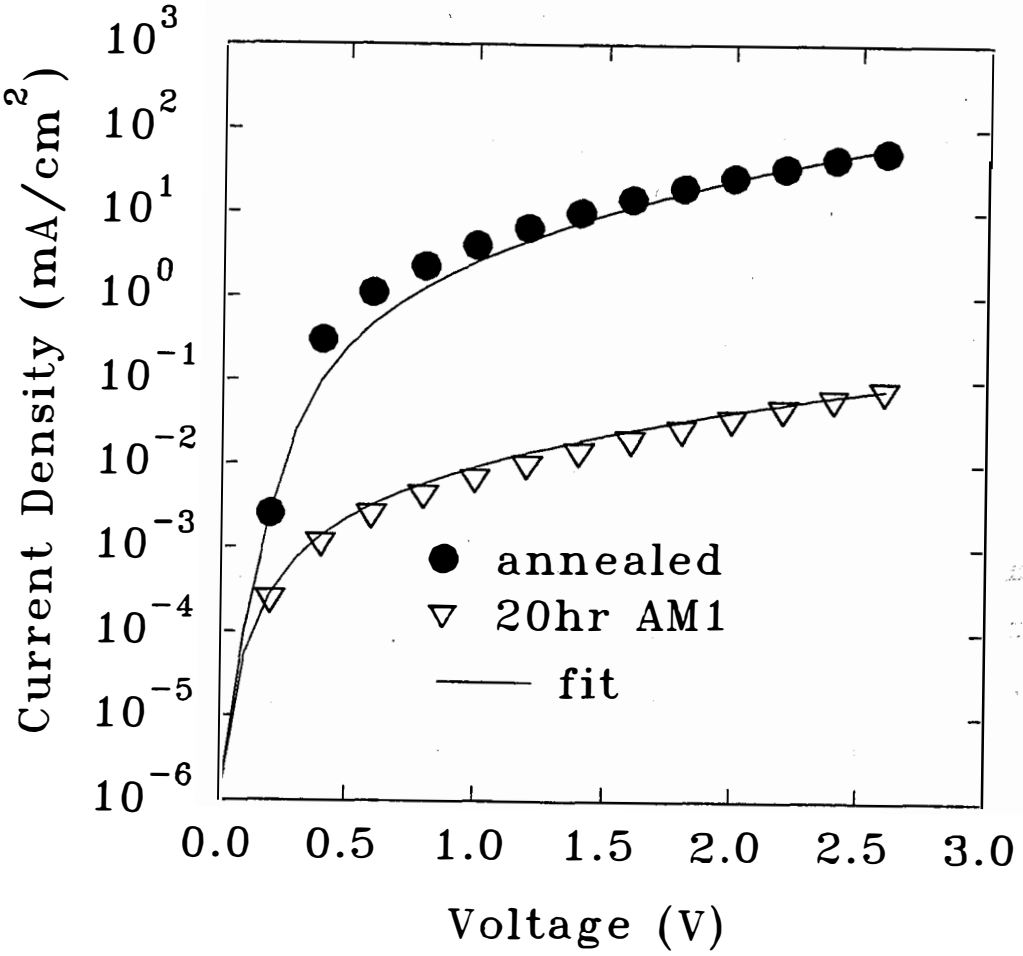

Figure 77 Dark I-V's of a 1μm thick n-i Schottky barrier structure in the annealed and degraded states.

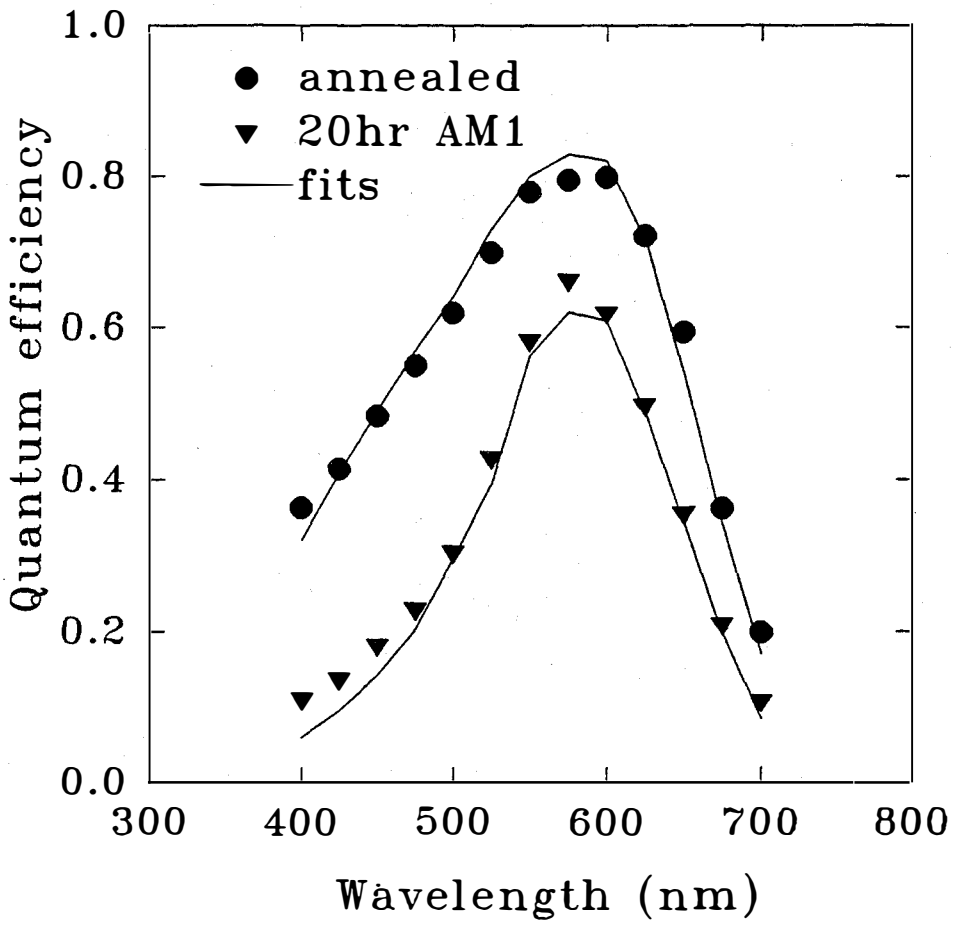

Figure 78 QE's of a 1μm thick n-i Schottky barrier structure in the annealed and degraded states.

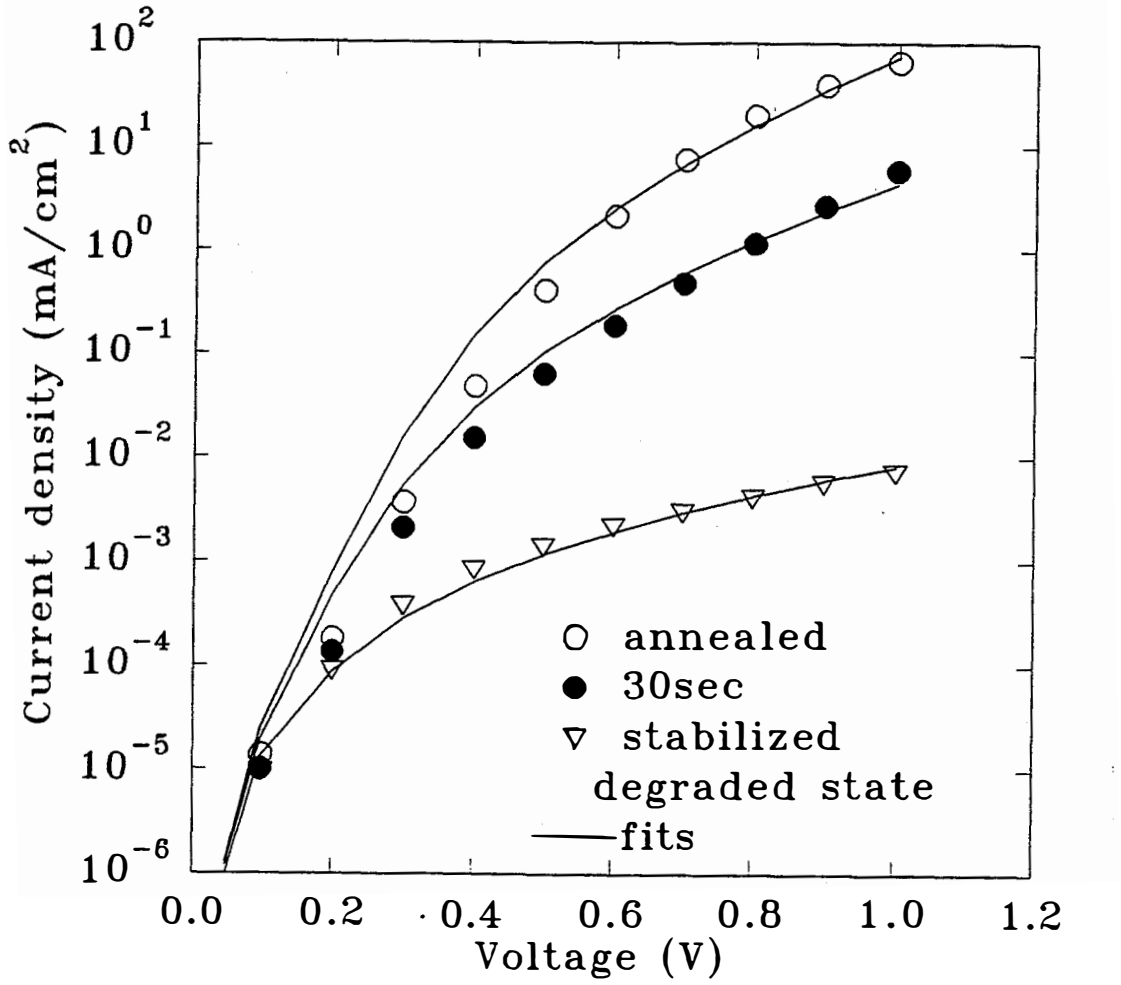

Figure 79 Forward I-V characteristics for a 0.5μm thick Schottky barrier solar cell structure in the annealed state, after 30 seconds of AM1 illumination, and in the stabilized degraded state. The symbols are the experimental results. The solid lines are best fits using the same material parameters as in SAM.

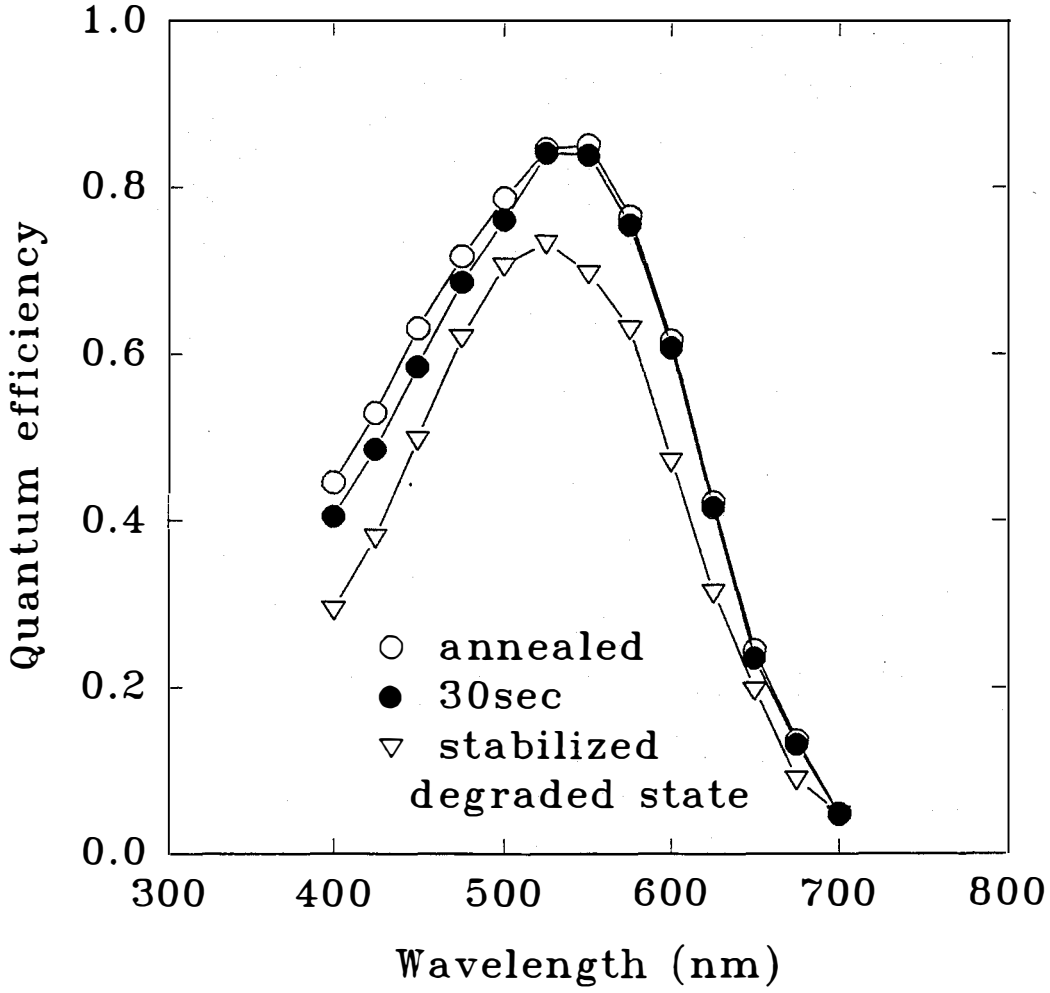

Figure 80 Quantum efficiency characteristics for a 0.5μm thick Schottky barrier solar cell structure in the annealed state, after 30 seconds of AM1 illumination, and in the stabilized degraded state. The symbols are the experimental results.

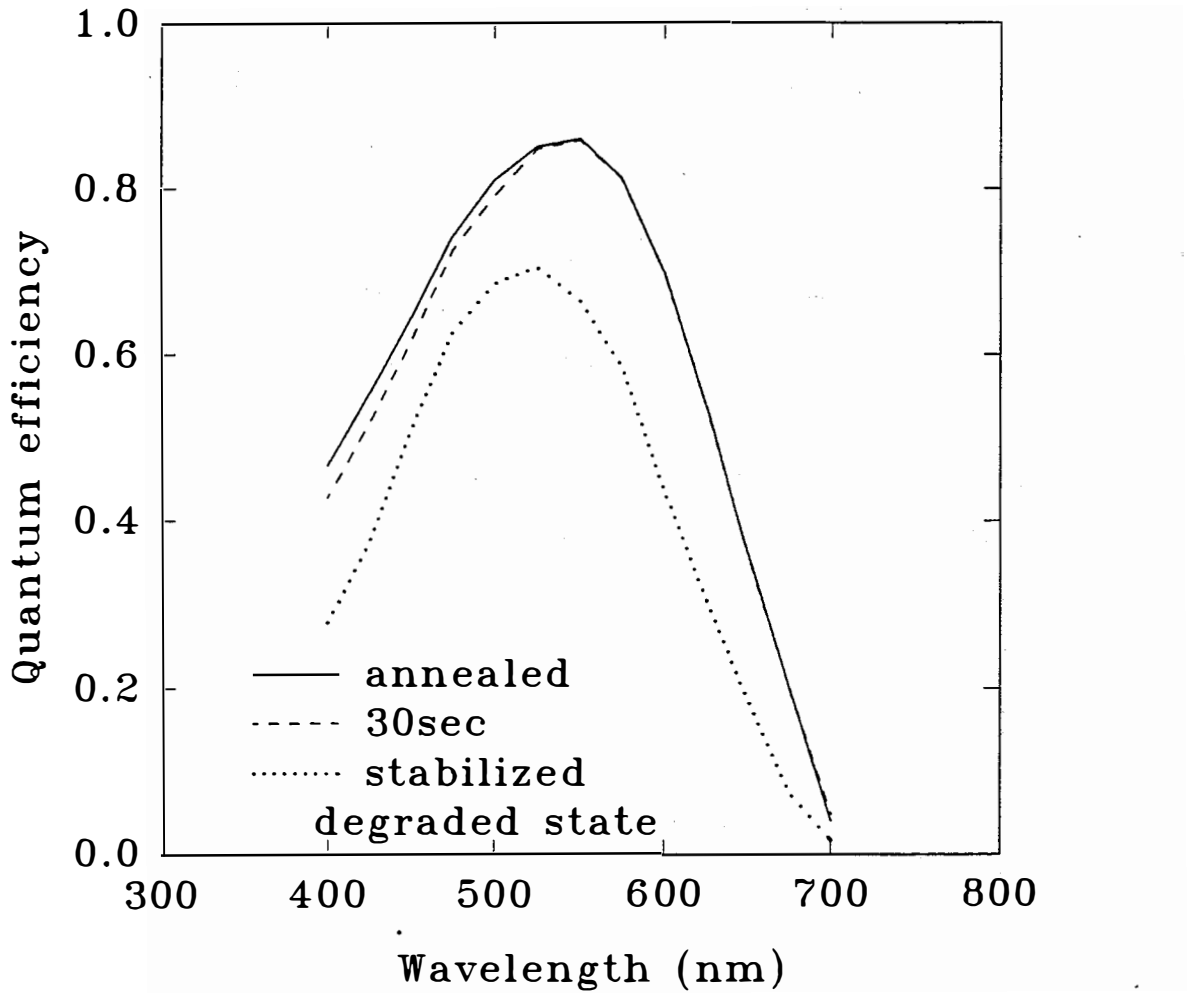

Figure 81 Simulation results of the quantum efficiency characteristics for a 0.5μm thick Schottky barrier solar cell structure in the annealed state, after 30 seconds of AM1 illumination, and in the stabilized degraded state.

current density from the annealed state to the stabilized degraded state. The far forward I-V's in this structure drop by about one order of magnitude after only 30 seconds of AM1 illumination, a change which is similar to that found in the photoconductivities and electron mobility lifetime products in the corresponding i-layers. The fits shown in Fig. 79 as the solid lines are obtained for the annealed and stabilized degraded states using AMPS with virtually identical defect state parameters as those used to fit the thin film materials results. The densities of the defect states are $D^+=8x10^{15}$ cm^{-3}, $D^0=7x10^{15}$ cm^{-3}, and $D^-=8x10^{15}$ cm^{-3} in the annealed state; $D^+=1.2x10^{16}$ cm^{-3}, $D^0=7x10^{15}$ cm^{-3}, and $D^-=1.2x10^{16}$ cm^{-3} after 30 seconds of AM1 illumination; and $D^+=9x10^{16}$ cm^{-3}, $D^0=2x10^{17}$ cm^{-3}, and $D^-=9x10^{17}$ cm^{-3} in the stabilized degraded state. The 30 second degradation is consistent with the small changes in densities of D^+, D^- and no change in D^0 as indicated by the subgap absorption results.

A simulation of the degradation in the quantum efficiency for this Schottky barrier structure was also carried out and the results are shown in Fig. 80. In contrast to the large changes in the far forward I-V's, after 30 seconds of AM1 illumination, the quantum efficiencies between the wavelengths of 400nm to 550 nm degraded only very slightly with virtually no change at longer wavelengths. In the stabilized degraded state, both the blue and red responses decreased significantly. These results are consistent with the changes observed in the subgap absorption and the gap state parameters derived from the material analysis and from forward I-V modeling. In the latter cases, there is a rapid increase in the densities of D^+ and D^- states but virtually no change in D^0 states in the initial stages of light-induced degradation. The modeling results of the quantum efficiencies are shown in Fig. 81 using AMPS with the same material parameters as those used in forward I-V modeling. As can be seen, these results agree well with the experimental data. The important role of charged defects is clearly evident in the analysis of the kinetics of light induced changes. These changes cannot be explained by considering only increases in D^0 as measured by CPM, as is often postulated. Self-consistent analysis of the light-induced degradation in films is obtained however by using a three gaussian distribution of D^+, D^0, and D^- states. Using these derived parameters for the charged and neutral gap states in

AMPS, it is possible to establish direct correlations between the degradation kinetics in Schottky barrier structures and corresponding thin films.

Even though the amphoteric nature of silicon dangling bonds is not directly included in the analysis discussed here, the charged defect states are taken into account by having three rather than the two gaussian distribution of states . By self-consistently fitting a wide range of results on both material and Schottky barrier structures, "operational" material parameters could be obtained which are useful in establishing more reliable and quantitative correlations between p-i-n and n-i-p solar cell performance and their bulk materials.

6.2 p-i-n and n-i-p Cell Performance Limitations

In parallel, AMPS is being used for devices whose materials have not yet been fully characterized or "fine-tuned". This research is carried out in an attempt to identify the potential contributions of the various mechanisms limiting the performance of different cell structures. An example of this is the study of the factors limiting V_{oc} as discussed in Sec. 3. The contributions of these mechanisms will be quantified after reliable material parameters are established. Similar analysis will be carried out on the customized cells once more information is available about the material parameters for the diluted and undiluted i-layers.

The simulations obtained using AMPS shown in Fig. 82 include the dependence of V_{oc} on the intensity of illumination in cells having the same V_{bi} (1.3V), densities of states ($D^+= 8x10^{15}$, $D^o= 6x10^{15}$, and $D^-= 8x10^{15}/cm^3$), but different mobility bandgaps of 1.84 and 1.8 eV. In these simulations, no additional defects were introduced in the p/i interface regions. It is clearly seen that for light intensities up to 100AM1, a higher bandgap in the bulk i-layer leads to a higher V_{oc} , where $\Delta V_{oc} \approx \Delta E_{\mu}$. Above 100AM1 the shape of V_{oc} vs light intensity begins to bend over due to the possible limitations imposed by the exponential band tails and/or V_{bi}. According to the simulations, J_{sc} is proportional to the illumination intensity below 100AM1, which is also found experimentally, so that an exponential dependence of V_{oc} on the flux is expected when $V_{oc} \approx nkT[\exp(J_{sc}/J_o)]$.

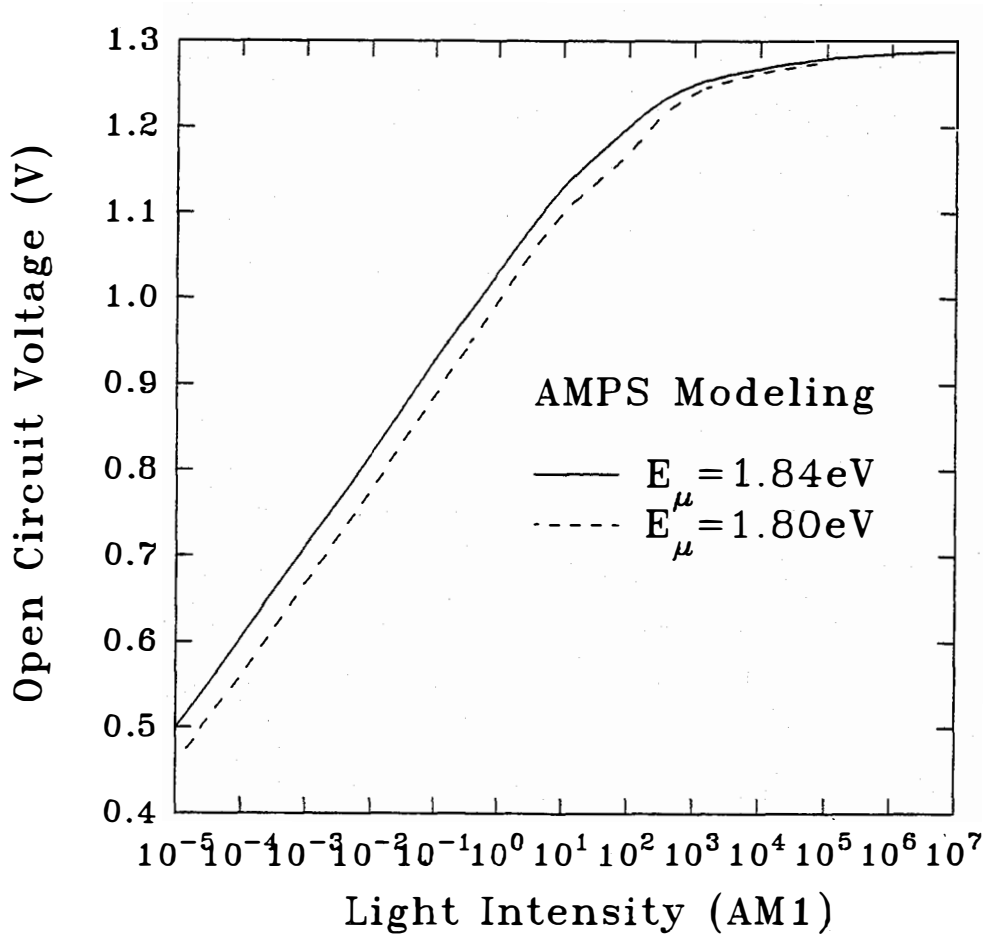

Figure 82 The dependence of V_{oc} on the normalized light intensity obtained by AMPS modeling for two p-i-n cells that incorporate i-layers having different bandgaps.

In cases where there are no additional effects due to defects at the p/i interface , the value of n can be related to bulk recombination which depends on the densities and distribution of defect states in the bulk i-layer.

As discussed in Sec. 3, p/i interface regions and V_{bi}'s can also affect the open circuit voltages of p-i-n solar cell structures. This issue was addressed by carrying out additional simulations on the cell with the material having E_{μ}=1.84 eV in order to assess the possible effects of V_{bi} and p/i interfaces. In one of the cases shown, V_{bi} was decreased from 1.30 to 1.15V and in the other a 100Å thick defective p/i interface layer was introduced with defect densities of around $5x10^{17}/cm^3$. These results are shown in Fig. 83, where as expected it can be seen that the defective p/i interface is very effective in decreasing V_{oc}. At light intensities starting from around 0.1AM1, V_{oc} deviates from the simple exponential behavior so that at AM1 it drops from 1.03V to 0.96V. On the other hand, when V_{bi} decreases from 1.30V to 1.15V, its effects begin to set in at a light intensity around AM1, where the drop of V_{oc} is about 20meV. Furthermore, in the light intensity regime from about AM1 to 100AM1, the effects of the p/i interfaces also appear to be stronger limiting factors. At low light intensities below about 0.1AM1, the effects of bulk i-layers seem to be the dominant factors in determining V_{oc} as in Fig. 82 with the effects of the p/i interface regions and V_{bi} becoming insignificant.

For comparison, the experimental results are shown as the symbols in Fig. 83 for the p(a-SiC:H)-i(a-Si:H)-n(μc-Si) and n(μc-Si)-i(a-Si:H)-p(μc-Si) cells discussed in Sec.1. These initial simulation results appear to indicate that the difference in V_{oc}'s of these two cells is more likely to be due to differences in their p/i interface regions rather than V_{bi}, but at this point this condition is based solely on qualitative analysis without any confirmation involving a wide range of material parameters.

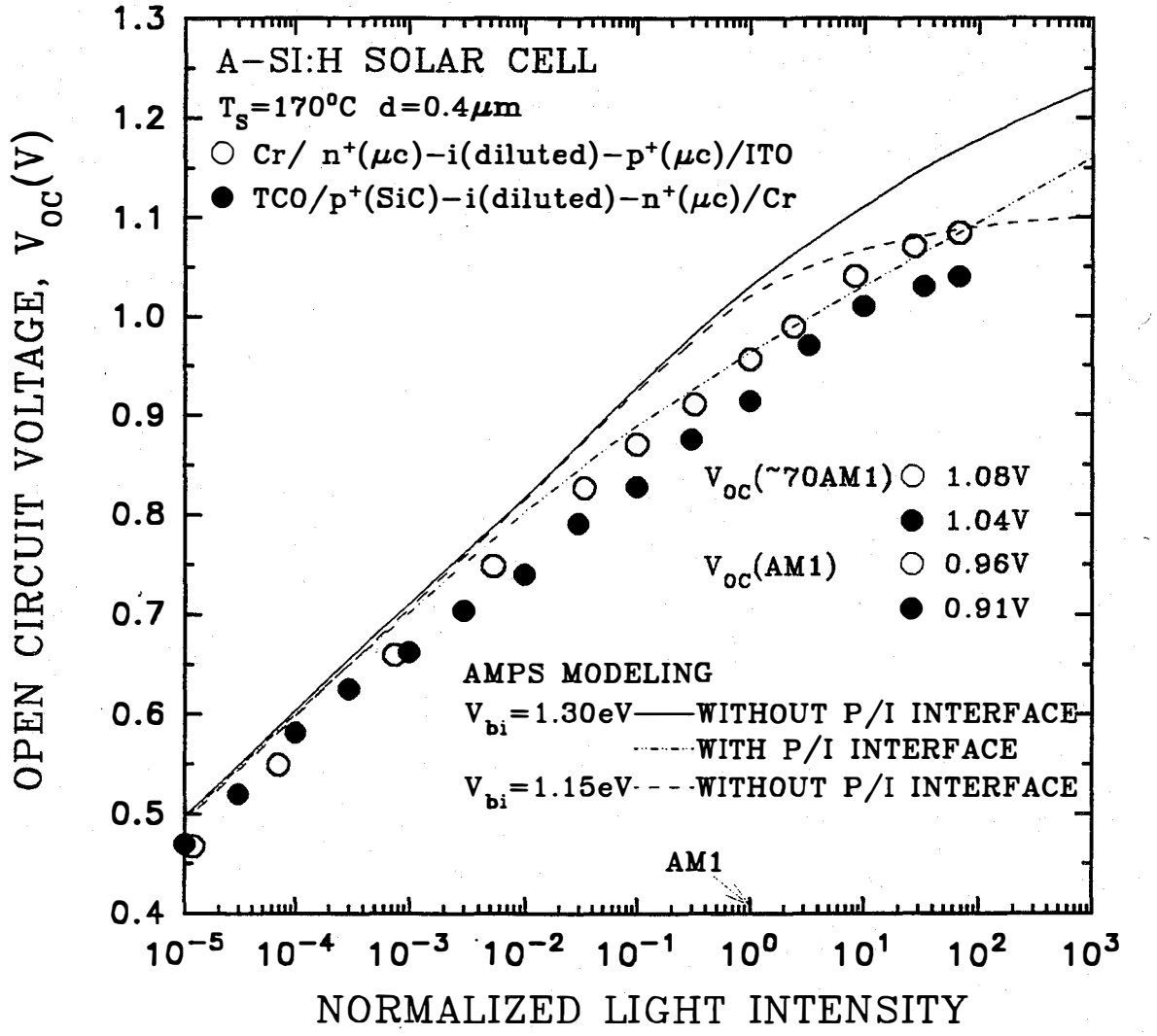

Figure 83 The dependence of V_{oc} on the normalized light intensity. Values for one p-i-n cell and one n-i-p cell are shown as the symbols, together with three AMPS modeling fits shown as the lines. In the AMPS modeling, a change of V_{bi} and the effect of the p/i interface are investigated.

7. Publications

1] "Stability of a-Si:H Solar Cells and Corresponding Intrinsic Materials Fabricated Using Hydrogen Diluted Silane", Y.Lee, L.Jiao, H.Liu, Z.Lu, R.Collins and C.R.Wronski, *25th IEEE Photovoltaic Specialists Conference, May, 1996, Washington D.C., USA* (IEEE, 1996), pp. 1165-1168.

2] "Importance of Charge Defects in a-Si:H Materials and Solar Cell Structures", L.Jiao, H.Liu, S.Semoushikina, Y.Lee and C.R.Wronski, *25th IEEE Photovoltaic Specialists Conference, May, 1996, Washington D.C., USA* (IEEE, 1996), pp. 1073-1076.

3] "Light-Induced Degradation In Different p-i-n and n-i Shottky Barrier Solar Cell Structures", H.Liu, Y.Lee, T.Jamali-beh, Z.Lu, R.Collins and C.R.Wronski, *25th IEEE Photovoltaic Specialists Conference, May, 1996, Washington D.C., USA* (IEEE, 1996), pp. 1125-1128.

4] "Internal Photoemission on a-Si:H Schottky Barrier Revisited" I.S.Chen and C.R. Wronski, *J. of Non- Cryst. Solids*, pp. 58 (1995).

5] "Analysis of Non-Uniform Creation of Light Induced Defects in Schottky Barrier Solar Cell Structures", H.Liu, C.T.Malone, C.M.Fortmann and C.R.Wronski, *(MRS Pittsburgh,1995)* Vol.377, pp. 687.

6] "Effect of White and Red Light Illumination on the Degradation of a-Si:H Solar Cells", T.Jamali-Beh, I.S.Chen, H.Liu, Y.Lee and C.R.Wronski, *(MRS Pittsburgh,1995)* Vol.377 pp. 627.

7] "Amorphous silicon technology: Coming of age", C.R.Wronski, *Solar Energy Materials and Solar Cells* 41/42(1996) pp. 427.

8] "Characterization of Semiconductor Heterojunctions Using Internal Photoemission", I.S.Chen, T.N.Jackson and C.R.Wronski, *J.Appl. Phys.* V.79, No.11, 1996, June, pp8470.

9] "A Novel Approach to the Analysis of Sub-bandgap Absorption in a-Si:H Based Materials", I.S.Chen, L.Jiao, R.W.Collins and C.R.Wronski, *J. of Non-Cryst. Solids*, 198-200(1996) pp. 391.

10] "Distribution of Charged Defects in a-Si:H n-i Schottky Barrier Solar Cells", H.Liu, L.Jiao, S.Semoushkina and C.R.Wronski, *J. of Non-Cryst. Solids*, 198-200(1996) pp391.

11] "Optical Properties of Ultrathin Crystalline and Amorphous Silicon", H.V. Nguyen, Y. Lu, S. Kim, M. Wakagi, and R.W. Collins, *Physical Review Letters* 74, pp. 3880-3883 (1995).

12] "A Real Time Spectroellipsometry Study of Hydrogenated Amorphous Silicon p-i-n Solar Cells: Characterization of Microsctructural Evolution and Optical Gaps", J. Koh, Y. Lu, S. Kim, J.S. Burnham, C.R. Wronski, and R.W. Collins, *Applied Physics Letters* 67, pp. 2669-2671 (1995).

13] "Optical Characterization of Continuous Compositional Gradients in Thin Films by Real Time Spectroellipsometry", S. Kim and R.W. Collins, *Applied Physics Letters* 67, pp.3010-3012 (1995).

14] "Correlation of Real Time Spectroellipsometry and Atomic Force Microscopy Measurements of Surface Roughness on Amorphous Semiconductor Thin Films", J. Koh, Y. Lu, C.R. Wronski, Y. Kuang, R.W. Collins, T.T. Tsong, and Y.E. Strausser, *Applied Physics Letters* 69, pp. 1297-1299 (1996).

15] "Real Time Spectroellipsometry Characterization of Optical Gap Profiles in Compositionally- Graded Semiconductor Structures: Applications to Bandgap Engineering in Amorphous Silicon-Carbon Alloy Solar Cells", S. Kim, J.S. Burnham, Joohyun Koh, L. Jiao, C.R. Wronski, and R.W. Collins, *Journal of Applied Physics* 80, pp. 2420 (1996).

16] "Real Time Diagnostics of Thin Film Growth: Introduction and General Discussion", R.W. Collins, in Handbook of Thin Film Process Technology, Part D0, edited by D.A. Glocker and S.I. Shah (IOP, Philadelphia, 1995), p. D0:1-10.

17] "Optical Properties of Solids", R. W. Collins and K. Vedam, Encyclopedia of Applied Physics, Vol. 12, edited by G.L. Trigg (VCH, New York, 1995) pp. 285-336.

18] "Real Time Spectroellipsometry Characterization of the Fabrication of Amorphous Silicon Solar Cells", R. W. Collins, Yiwei Lu, Sangbo Kim, and C.R. Wronski, in Semiconductor Characterization: Present Status and Future Needs, edited by W.M. Bullis, D.G. Seiler, and A.C. Diebold (AIP, New York, 1995), pp. 517-521.

19] "Spectroscopic Ellipsometry with Multichannel Detection: Applications in Real Time Monitoring of Optical Coatings", R.W. Collins and Sangbo Kim, in Optical Interference Coatings, Vol. 17, 1995 Technical Digest Series (Optical Society of America, Washington DC, 1995) pp. 210-212.

20] "Preparation and Optical Properties of Ultrathin Silicon Films", R.W. Collins, H.V. Nguyen, I. An, Y. Lu, and M. Wakagi, Mater. Res. Soc. Symp. Proc. 358, pp.763-768 (1995).

21] "Real Time Monitoring of Amorphous Silicon Solar Cells: Evolution of Microstructure and Optical Properties" R.W. Collins, Y. Lu, S. Kim, I.-S. Chen, Y. Lee, and C.R. Wronski, in Technical Digest of the 8th Sunshine Workshop on Thin Film Solar Cells (MITI-NEDO, Tokyo, 1995) pp. 53-60.

22] "Quantitative Correlation between a-Si:H Material and Solar Cell Properties" C.R. Wronski, I.-S. Chen, M. Gunes, T. Jamali-beh, H. Liu, and R.W. Collins, in Technical Digest of the 8th Sunshine Workshop on Thin Film Solar Cells (MITI-NEDO, Tokyo, 1995) pp. 35-42.

23] "Real Time Monitoring of Amorphous Silicon Solar Cell Fabrication", Y. Lu, S. Kim, J. S. Burnham, I.-S. Chen, Y. Lee, Y. E. Strausser, C. R. Wronski, and R. W. Collins, Mater. Res. Soc. Symp. Proc. 377, pp. 603-608 (1995).

24] "Characterization of Compositional Gradients in Amorphous Semiconductor Thin Films by Real Time Spectroscopic Ellipsometry", S. Kim and R. W. Collins, Mater. Res. Soc. Symp. Proc. 377, pp. 15-20 (1995).

25] "Characterization of Amorphous Silicon Solar Cell Preparation Processes by Real Time Spectroscopic Ellipsometry", R.W. Collins, J.Koh, Y. Lu, S. Kim, J.S. Burnham, and C.R. Wronski, 25th IEEE Photovoltaiocs Specialists Conference, May 1996, Washington DC, USA, (IEEE, 1996), pp. 1035-1040.

26] "Insights into Deposition Processes for Amorphous Semiconductor Materials and Devices from Real Time Spectroscopic Ellipsometry", R.W. Collins, J.S. Burnham, S. Kim, J. Koh, Y. Lu, and C.R. Wronski, *J. Non-Cryst. Solids* 198-200, pp981-986 (1996).

27] "A Comparison of the Optical Properties of Ultrathin Amorphous and Crystalline Silicon Thin Films", H.V. Nguyen, S. Kim, Y. Lu, M. Wakagi, and R.W. Collins, *J. Non-Cryst. Solids* 198-200, pp. 853-856 (1996).

28] "Multichannel Spectroscopic Ellipsometry", R.W. Collins and H.V. Nguyen, "Proccedings of the Workshop on Highlights of Light Spectroscopy on Semiconductors: HOLSOS-95", Frascati-Roma, Italy, September 11-12, 1995 (in press).

29] "Advances in the Characterization of Compositionally-Graded Layers in Amorphous Semiconductor Solar Cells by Real Time Spectroellipsometry", R.W. Collins, S. Kim, J. Koh, J.S. Burnham, I.-S. Chen, and C.R. Wronski, Mater. Res. Soc. Symp. Proc (in press, 1996).

30] "Structural Evolution of Top-Junction a-Si:C:H:B and Mixed-Phase (Microcrystalline Si) - (a-$Si_{1-x}C_x$:H) p-Layers in a-Si:H n-i-p Solar Cells", J. Koh, J.S. Burnham, Y. Lee, H. Liu, I.-S. Chen, C.R. Wronski, and R.W. Collins, Mater. Res. Soc. Symp. Proc (in press, 1996).

31] "In Situ Observation of Surface of Semiconductive Thin Films Using Spectroscopic Ellipsometry", R.W. Collins, I. Shimizu, *Applied Physics* [Japan Society of Applied Physics] 65, pp. 237-243 (1996).

REPORT DOCUMENTATION PAGE

Form Approved
OMB NO. 0704-0188

Public reporting burden for this collection of information is estimated to average 1 hour per response, including the time for reviewing instructions, searching existing data sources, gathering and maintaining the data needed, and completing and reviewing the collection of information. Send comments regarding this burden estimate or any other aspect of this collection of information, including suggestions for reducing this burden, to Washington Headquarters Services, Directorate for Information Operations and Reports, 1215 Jefferson Davis Highway, Suite 1204, Arlington, VA 22202-4302, and to the Office of Management and Budget, Paperwork Reduction Project (0704-0188), Washington, DC 20503.

1. AGENCY USE ONLY (Leave blank)	2. REPORT DATE	3. REPORT TYPE AND DATES COVERED
	January 1997	Annual Technical Report, 15 July1995 - 15 July 1996

4. TITLE AND SUBTITLE

Wide Band Gap Solar Cells with High Stabilized Performance; Annual Technical Report, 15 July 1995 - 15 July 1996

5. FUNDING NUMBERS

C: XAN-4-13318-03
TA: PV704401

6. AUTHOR(S)

Wronski, C.R.; Collins, R.W.; Fujiwara, H.; Jiao, L.; Lee, Y.; Semoushkina, S.; Kim, S.; Lu, Z.; Liu, H.; and Koh, J.

7. PERFORMING ORGANIZATION NAME(S) AND ADDRESS(ES)

Pennsylvania State University
University Park, Pennsylvania

8. PERFORMING ORGANIZATION REPORT NUMBER

9. SPONSORING/MONITORING AGENCY NAME(S) AND ADDRESS(ES)

National Renewable Energy Laboratory
1617 Cole Blvd.
Golden, CO 80401-3393

10. SPONSORING/MONITORING AGENCY REPORT NUMBER

SR-520-22364

DE97000103

11. SUPPLEMENTARY NOTES

NREL Technical Monitor: B. von Roedern

12a. DISTRIBUTION/AVAILABILITY STATEMENT

12b. DISTRIBUTION CODE

UC-1260

13. ABSTRACT *(Maximum 200 words)*

This report describes work done in Phase II of this subcontract. In their work on materials stability, researchers found that a-Si:H films deposited with H_2-dilution of SiH_4 gas not only show lower defect densities in the annealed state than the a-Si:H films prepared with pure SiH_4, but also better stability against light soaking. The improvement in material stability is found to translate directly into an improvement in device quality. In other work, researchers demonstrated that, while in the annealed state a-$Si_{1-x}C_x$:H *i*-layers prepared with H_2-dilution of source gases (i.e., $SiH_4 + CH_4$) exhibit similar photoconductive properties to those of H_2-diluted a-Si:H materials, the gains made through H_2-dilution are largely lost in the degraded state. In investigations of the dependence of *p-i-n* solar cell performance, they found that the open-circuit voltage of the cell increases at lower *i*-layer deposition temperatures as the bandgap of the *i*-layer is widened, and such an increase is more profound in cells prepared with H_2-diluted *i*-layers. Another area of work is discussed in which researchers developed novel wide gap amorphous and microcrystalline p-layers prepared using H_2-diluted and undiluted mixtures of SiH_4, CH_4, and $B(CH_3)_3$ (TMB) that are to be incorporated as the top layer in the *n-i-p* solar cell configuration. In their work on solar cell interfaces, they discuss their extended studies of the p/*i* interface to small sub-monolayer level discontinuities observed in the real-time ellipsometry trajectories for interfaces formed with TMB *p*-layers. Finally, they discuss their new approach to device modeling that is less ambitious than originally proposed because of the absence of reliable input parameters. In this approach, the modeling of solar cell structures is carried out first to establish material parameters that are self-consistent with those derived in detailed studies on intrinsic material thin films.

14. SUBJECT TERMS

photovoltaics ; amorphous silicon ; solar cells ; materials stability ; device modeling ; wide band gap materials ; hydrogen dilution

15. NUMBER OF PAGES
184

16. PRICE CODE

17. SECURITY CLASSIFICATION OF REPORT	18. SECURITY CLASSIFICATION OF THIS PAGE	19. SECURITY CLASSIFICATION OF ABSTRACT	20. LIMITATION OF ABSTRACT
Unclassified	Unclassified	Unclassified	UL